The work presented in this thesis is original and not plagiarised from any third party. The author of the work is Khalil Rhazaoui, and all else is appropriately references as per the Imperial College requirements and guidelines.

# Solid Oxide Fuel Cell microstructure and performance modeling

Written by

Khalil Rhazaoui

MSc. BEng. DIC

Philosophical Doctorate Thesis

Imperial College of London

October 2013

Supervised by:

Prof. N. P. Brandon
Prof. C. S. Adjiman
Dr. Q. Cai

# Abstract

The fundamental operation of Solid Oxide Fuel Cells (SOFCs) relies on the liberation of electrons at reaction sites within porous electrodes. These reaction sites, or triple-phase boundary (TPB) points, must be percolated to allow for reactants and products to flow to and from these sites.

Due to the fact that electrochemical reactions in composite electrodes are dependent on the presence of TPB sites, a direct link exists between SOFC electrode microstructures and electrochemical performance. Recently, the development of advanced tomography and imaging techniques has allowed for this link to be better understood and quantified.

This thesis presents the development of a novel effective conductivity model (ResNet) for 3D composite, anisotropic microstructures in the context of Ni-YSZ electrode characterization. The ResNet model is first used to derive the effective conductivity of simple structures, conductivities of which can be found in the literature. Good agreement was found in this initial study.

The model is then used to compute the effective conductivities of more complex synthetic microstructures, comparing model outputs to those given by COMSOL Multiphysics, a commercial modeling platform. It was found that for a sufficiently high resolution, both models converge to the same results. Varying the discretization resolution allowed for an optimum discretization resolution to be determined, based on the mean particle size used for fabrication.

The introduction of Volume Elements into the ResNet model is then presented, and the optimum aggregation resolution is extracted from a set of simulations. This allowed for the analysis of a real SOFC anode microstructure to be carried out, and underlined the importance of selecting a microstructure sample of a size that can be considered representative of the entire electrode.

After a series of simulations on synthetically generated microstructures, several microstructural parameters are varied to carry out a sensitivity analysis on the effective conductivities and current densities of the microstructures. This analysis yielded an optimum ratio of 7 particles per structure length for microstructure size representativeness.

Using the parameters derived from the studies presented in this thesis, the effective conductivities of two experimental Ni/10ScSZ anodes are extracted using the ResNet model and compared to their experimentally determined values. Excellent agreement was obtained, validating the ResNet model and associated work.

In a final instance, it was shown that using the ResNet model in the electronic phase in conjunction with the VOF model developed by Golbert et al. does not yield a noticeable

difference in current density output when compared to results obtained without using the ResNet. When applied to the ionic phase however, using the ResNet model in conjunction with the VOF model is found to predict as much as 50% lower computed area current densities than when the volume fraction average model is used.

# Acknowledgements

This thesis, alongside the 3 years of work that it took to complete, would not have been possible with the invaluable help and support of a network of co-workers, friends and family.

Firstly I would like to thank my supervisors Prof. Nigel Brandon, Prof. Claire Adjiman and Dr. Qiong Cai who have been a critical source of advice and guidance. I am also grateful for funding provided by the EPSRC Supergen Fuel Cells program.

I would like to thank a number of colleagues who have played a key role in making this work possible: Dr. Farid Tariq and Dr. Masashi Kishimoto, whose work on SOFC anode tomography and imaging techniques allowed for a validation of the presented model, and more importantly for promoting the further understanding between the microstructural parameters and electrochemical performance of SOFC anodes.

Dr. Qiong Cai and Dr. Josh Golbert for having developed the VOF model used in this thesis, and Dr. Mahendra Somalu for working on the experimental side of this thesis and allowing for a validation to be carried out. Special thanks goes to Dr. Qiong Cai for her time and patience through two pregnancies in the better understanding and operation of the VOF model.

I would like to thank Prof. David Caplin and Dr. Gary Perkins from the Physics Department of Imperial College London for their contribution towards a better understanding of current behaviour in non-uniform structures.

My gratitude also goes to all the members of the Brandon research group and Leena Lindholm-White for having made these three years enjoyable and for all the help and support they gave me.

Finally, I would like to extent my thanks and love to my parents who have always been there no matter what.

# Contents

# Figures -

shows a magnified view of the equipotential lines going through the structure at the upper-left boundary.

Figure 3.8 - Equivalent resistance of a cone as a function of its smallest radius. The black squares denote the analytical results, results given by averaging the conductivity of pure nickel to the volume fraction of nickel in the discretized structure are denoted by the red circles and the others are results given by the ResNet model using varying numbers of voxels to describe the cone.

Figure 3.9 –Equivalent resistance of four cones with slopes varying from 0.3 to 0.45. The lines show the analytical solution given by Equation 3.1, and the data points show the equivalent solution given by the ResNet model for each cone at the different discretization resolutions.

Figure 3.10- Graphical representation of the conical structure under study with relevant dimensions. When used in the ResNet model, the cylinder is discretized within a cuboid of length 2μm in which the volume not occupied by the conical structure is defined as an arbitrary material of conductivity $1x10^{-8}$ S/μm.

Figure 3.11 – Equivalent resistance of eight conical structures with smaller radii varying from 0.4 to 0.15 μm in steps of 0.05 μm, (a) showing results for $R_{vary}$ = 0.4 μm, (b) for $R_{vary}$ = 0.35 μm, (c) for $R_{vary}$ = 0.3 μm, (d) for $R_{vary}$ = 0.25 μm, (e) for $R_{vary}$ = 0.2 μm and (f) $R_{vary}$ = 0.15 μm respectively. Square symbols indicate the equivalent resistances given by the ResNet model for each cone at the different discretization resolutions and the circle symbols indicate the equivalent resistances given by COMSOL at the corresponding mesh resolutions.

Figure 3.12 - Graphical representation of the discretization process employed by the ResNet model and the meshing approach employed by COMSOL. (a) The original structure as used in COMSOL; (b) the discretized form, with a coarse resolution of 8192 voxels and a fine resolution of 1769472 voxels for use by the ResNet model; (c) the meshed form showing a coarse resolution of 8632 mesh elements and a fine resolution of 1815465 mesh elements for use in COMSOL.

Figure 3.13 – Equivalent resistance of six sets of two semi-spheres in contact with length of overlap varying from 0 to 0.4 μm. (a) shows the results for γ = 0.4 μm, (b) for γ = 0.3 μm, (c) for γ = 0.2 μm, (d) for γ = 0.1 μm, (e) for γ = 0.05 μm and (f) for γ = 0 μm. The square symbols

indicate the equivalent resistances given by the ResNet model for each structure at the different discretization resolutions, and the circle symbols show the equivalent resistances given by COMSOL at the corresponding mesh resolutions.

Figure 3.14 - Graphical representation of the four quarters of spheres under study with relevant dimensions. When used in the ResNet model, the structure is discretized within a cuboid of length 1μm in which the volume not occupied by the spherical structure is defined as an arbitrary material of conductivity $1x10^{-8}$ S/μm.

Figure 3.15 – Equivalent resistance between the opposite faces of six sets of four quarter-spheres in contact with radius varying from 0.62 to 0.52 μm in steps of 0.02 μm. (a) shows results for the case where R = 0.62 μm, (b) where R = 0.6 μm, (c) where R = 0.58 μm, (d) where R = 0.56 μm, (e) where R = 0.54 μm and (f) the case where R = 0.52 μm respectively. The square symbols indicate the equivalent resistances given by the ResNet model for each structure at the different discretization resolutions, and the circle symbols show the equivalent resistances given by COMSOL at the corresponding mesh resolutions.

Figure 3.16 - Graphical representation of the sphere array under study made by agglomerating the structures illustrated in Figure 3.14. When used in the ResNet model, the structure is discretized within a cuboid of length 4μm in which the volume not occupied by the spherical structure is defined as an arbitrary material of conductivity $1x10^{-8}$ S/μm.

Figure 3.17 - Equivalent resistance of a sphere array as illustrated in Figure 3.16, with a radius of 0.56 μm. The square symbols show the equivalent resistance given by the ResNet model for each structure at the different discretization resolutions and the circle symbols show the equivalent resistance given by COMSOL at the corresponding mesh resolutions.

Figure 3.18 – Graphical representation of the particle distribution in a structure of uniform length 5 μm and particle diameter 1 μm post-sintering. Green spheres represent nickel particles, blue spheres represent YSZ particles and red spheres represent pore particles. In this case 40% of the volume occupied in the structure represents Nickel.

Figure 4.6- Graphical representation of the electrodes 3 and 4 of case 2. a) and b) show electrode 3 and in b) the purple shows the connected nickel paths in the direction in which the conductivity is being considered. c) and d) show electrode 4, and in d) the yellow shows the connected nickel paths in the direction in which the conductivity is being considered.

Figure 4.7- Graphical representation of the connected pathways of electrodes 3 and 4 of case 2, illustrated respectively by i) and ii). a shows the percolated structures of the electrodes, b shows the skeleton of the electron path through the electrodes in green superimposed on the structure, and c shows the skeleton of the electron paths alone. The red arrows show the x-axis, the green arrows show the y-axis and the blue arrow the z-axis. The red circles show the charge-limiting bottle-necks of electrode 4, yielding a lower conductivity.

Figure 4.8- Graphical representation of a 2 dimensional slice of structure 3 used in Case 2. The slice selected is comprised of 20x20 voxels, which are aggregated into 1 VE (a), $2^2$ VEs (b), $4^2$ VEs (c), $5^2$ VEs (d), $10^2$ VEs (e) and $20^2$ VEs (f). In each case, i) shows the original structures superimposed by the VE aggregation layout, and ii) shows the aggregated structure. Green blocks represent voxels, or VEs, that show conducting pathways in the x and y directions, blue blocks represent VEs that only have conducting pathways in the x direction, and yellow blocks represent VEs that only have conducting pathways in the y direction. The red arrows show conducting pathways in the aggregated structures which are conductive in the x direction, and the red crosses mark the structures which are not conductive in the x direction.

Figure 4.9- Graphical representation of the reconstructured microstructure extracted from a Ni/10ScSZ anode sample with 30% nickel content. The red arrow represents the x-axis, the green arrow the y-axis and the blue arrow the z-axis. Red portions of the microstructure represent nickel particles, green portions represent ScSZ particles and the empty areas represent pores.

Figure 4.10- Graphical representation of the nickel network extracted from a Ni/10ScSZ anode sample with 30% nickel content. The red arrow represents the x-axis, the green arrow the y-axis and the blue arrow the z-axis. The full network is illustrated by i) in contrast to the percolated particles shown in ii). a shows a shaded view of the structures, b a transparent view of the structures overlaid with the skeletonized paths of this network, and c the skeletonized paths alone.

aggregation resolutions of $2^3$ voxels per VE, $5^3$ voxels per VE and $10^3$ voxels per VE are compared. All conductivities presented are computed in the x-direction.

Figure 5.10 - Variation of effective conductivity of Ni/10ScSZ anode films measured at 700$^o$C as a function of Ni content and sinter temperature as reported by Somalu et al. (Somalu et al., 2011) compared to the effective conductivity of 2 samples taken from these anodes as computed by the ResNet model, following FIB segmentation and image reconstruction. The samples were cut to sizes of 10.95×10.95×10.95 μm, and constituted $365^3$ voxels. Also presented are the effective conductivities as computed by the ResNet model as a function of nickel volume fraction for synthetic structures with an L/D ratio of 7, particle diameters of 1 μm and a fixed porosity of 41.2%. All conductivities presented are computed in the x-direction.

Figure 5.11 - Effective conductivity as a function of sintering coefficient for structures with an L/D ratio of 7, particle diameters of 1 μm and a 43.5% volume content of nickel, 35% volume content of YSZ and 21.5% porosity.

Figure 5.12 - Effective conductivity as a function of L/D for families of structures with a 20.1% nickel content, 38.7% YSZ content, 41.2% porosity and comprising particles of diameter 1 μm.

Figure 5.13 – Area current density as a function of L/D for families of structures with a 43.5% volume content of nickel, 35% volume content of YSZ and 21.5% porosity for four different particle sizes.

Figure 5.14 - Area current density as a function of electronic conductivity for families of structures with an L/D ratio of 2, a 43.5% volume content of nickel, 35% volume content of YSZ, 21.5% porosity and particles of diameter 1 μm.

Figure 5.15 – Effective ionic conductivity as a function of L/D for families of structures with a 43.5% volume content of nickel, 35% volume content of YSZ and 21.5% porosity with particles of diameter 1 μm. All conductivities presented are computed in the x-direction.

Figure 5.16 – Area current density as a function of L/D for families of structures with a 43.5% volume content of nickel, 35% volume content of YSZ and 21.5% porosity with particles of diameter 1 μm. The VOF model is initially employed using volume fraction averaged ionic

# Tables -

# Nomenclature -

## Symbols

| | | |
|---|---|---|
| $A$ | = | Anode cross-sectional area ($m^2$) |
| $a$ | = | Charge transfer coefficient |
| $\beta$ | = | Butler-Volmer equation constant |
| $D$ | = | Particle diameter (m) |
| $\delta$ | = | Volume element size (m) |
| $D$ | = | Diffusivity ($m^2/s$) |
| $E$ | = | Potential (V) |
| $\varepsilon$ | = | Phase volume fraction |
| $E^o$ | = | EMF for standard temperature at given pressure (V) |
| $E_R$ | = | Reversible cell potential (V) |
| $F$ | = | Faraday's constant (C/mol) |
| $f$ | = | Phase volume fraction |
| $\eta_{act}$ | = | Activation polarization (V) |
| $\eta_{con}$ | = | Concentration polarization (V) |
| $\eta_{ohm}$ | = | Ohmic polarization (V) |
| $h$ | = | Height (m) |
| $i$ | = | Current (A) |
| $j$ | = | Current density ($A/m^2$) |
| $j_L$ | = | Limiting current density ($A/m^2$) |
| $j_o$ | = | Exchange current density ($A/m^2$) |
| $\gamma$ | = | Overlap length (m) |

| | | |
|---|---|---|
| $k$ | = | Reaction rate constant |
| $L$ | = | Electrode length (m) |
| $l$ | = | Voxel length (m) |
| $N$ | = | Number of voxels/VEs |
| $n$ | = | Number of electrons |
| $P$ | = | Pressure (Pa) |
| $\rho$ | = | Resistivity (Ω/m) |
| $\rho_{TPB}$ | = | Triple-phase boundary density ($m/m^3$) |
| $q$ | = | flux ($m^3/s$) |
| R | = | Universal gas constant (J/mol.K) |
| $R$ | = | Resistance between voxels (Ω) |
| $r$ | = | Resistance of material inside voxel (Ω) |
| $rad$ | = | Radius (m) |
| $S$ | = | Resistance of a VE (Ω) |
| σ | = | Effective conductivity (S/m) |
| $T$ | = | Temperature (K) |
| $v$ | = | Stochiometric coefficient |
| $X$ | = | Entries of VE resistance matrix |
| $x$ | = | Entries of voxel resistance matrix |
| $x$ | = | Dimension along x-axis (m) |
| y | = | Dimension along y-axis (m) |
| $z$ | = | Dimension along z-axis (m) |
| $\zeta$ | = | Overpotential (V) |
| $z$ | = | Number of moles |

## Acronyms

| | | |
|---|---|---|
| AFC | = | Alkaline fuel cell |
| CGO | = | Cerium gadolinium oxide |
| CON | = | Concentration |
| DEM | = | Discreet element method |
| FC | = | Fuel cell |
| GDC | = | Gandolinium doped ceria |
| HPC | = | High performance computer |
| LBM | = | Lattice Boltzman method |
| LSCM | = | Lanthanum strontium manganese chromite |
| MCFC | = | Molten carbonate fuel cell |
| Ni | = | Nickel |
| OX | = | Oxidizing agent |
| PAFC | = | Phosphoric acid fuel cell |
| PEMFC | = | Proton exchange membrane fuel cell |
| PO | = | Pore |
| RD | = | Reducing agent |
| SDC | = | Samaria doped ceria |
| SOFC | = | Solid oxide fuel cell |
| STO | = | Strontium titanium oxide |
| TPB | = | Triple-phase boundary |
| VOF | = | Volume of fluid |
| VE | = | Volume element |
| YSZ | = | Yttria-stabilized zirconia |

## Subscripts

| | | |
|---|---|---|
| CO | = | Carbon monoxide |
| *d* | = | Dimension |
| *eff* | = | Effective |
| *eq* | = | Equilibrium |
| *el* | = | Electronic |
| $H_2$ | = | Hydrogen |
| $H_2O$ | = | Water |
| *io* | = | Ionic |
| $O_2$ | = | Oxygen |
| *oe* | = | Standard potential |
| *po* | = | Pore |
| *ve* | = | Volume element |
| *vox* | = | Voxel |

# Chapter 1 – Introduction

## 1.1– The drive towards sustainable energy sources

A global trend towards developing and using "greener" ways to generate energy has been clearly felt for the past two decades, due in most part to the general consensus of the scientific community on the negative effects of man-made $CO_2$ emissions together with concerns over the security of existing fossil fuel supply. As the world strives to decarbonise power generating and production processes, it has been recognized that the development and implementation of alternative energy technologies play a key role in reaching the targets put forward by the Kyoto protocol (United Nations, 1997).

The second article of the United Nations Framework convention on Climate Change (Brazil. *United Nations Framework convention on Climate Change* 1992) underlines the importance of stabilizing greenhouse gas concentrations in the atmosphere at a level that would prevent dangerous anthropogenic interference with the climate system. Article 4(c), which underlines the importance of international research efforts towards reaching this objective, has incentivized governments across the developed world to dedicate more resources to the field of alternative energy technology development.

With most of the research efforts driven by this incentive having been used to improve the efficiency and availability of renewable energy generating devices (Mench, 2008), fuel cells offer very high efficiency electrical power generation and the ability to use a variety of fuels with low levels of associated emissions such as particulates, $NO_x$, $SO_x$, etc. (Mench, 2008).

## 1.2– An introduction to Fuel Cells

While the recent flurry of activity by the scientific community has brought the Fuel Cell into the public eye, it is not a recent innovation. Their origins can be traced back to the work of Sir William Robert Grove , a Welsh lawyer born in 1811 who later applied himself to the mastery of

science (Mench, 2008). In 1843 W. R. Grove published a diagram and made a primitive model known as the "Grove Gas Battery" (Mench, 2008).

Wilhelm Ostwald went on to describe Grove's gas battery as "of no practical importance but quite significant for its theoretical interest" in a journal entitled *Electrochemistry: History and Theory*, published in 1896 (Mench, 2008).

It was not until 1959 that a fuel cell with a sizable power output – 5kW – was developed by British Engineer Francis Thomas Bacon (Britannica, 2013). Bacon's fuel cell used a different technology than Grove in his earlier design. Bacon used electrodes of nickel in a solution of potassium hydroxide, naming his invention the "Bacon Cell". Fuel cells of this type are today known as "Alkaline Fuel Cells", and of the most common types found in industry (Stolten, 2010).

The application of fuel cells started in 1959 with the development of the very first fuel cell vehicle by Harry Karl Ihrig who built a 15 kW fuel cell tractor for Allis-Chalmers. The fuel cell used was alkaline and incorporated a potassium hydroxide electrolyte, and the tractor produced 20 hp power (Stolten, 2010).

The first experiments on solid electrolytes were conducted by Baur, a Swiss scientist, and his colleague Preis in the late 1930s (Stambouli & Traversa, 2002) using materials such as zirconium, yttrium, cerium, lanthanum and tungsten oxide amongst others. The first ceramic fuel cell was operated in 1937 (Baur & Preis, 1937) at 1000$^{o}$C. Monazite sand was added to a mix of sodium carbonate, tungsten trioxide and soda glass by Russian scientist Davtyan in the late 1940s in order to increase the conductivity and mechanical strength of the cell (American history, 2004). Due to unwanted chemical reactions though, the design lived a short life. By the late 1950s a coalition of the Central Technical Institute in the Hague, Netherlands, Consolidation Coal Company in Pennsylvania and General electric in Schenectady, New York, accelerated the research into SOFCs (American history, 2004). In 1959 a discussion concluded that problems with solid electrolytes included relatively high internal electrical resistance, melting and short-circuiting due to semi-conductivity (American history, 2004). However due to the fact that it was one of the only fuel cell technologies which promised a high-temperature cell tolerant of carbon monoxide with a stable solid electrolyte, interest remained in the concept. In 1962 researchers at

Westinghouse experimented with a cell using zirconium oxide and calcium oxide, developing the first cathode-supported tubular SOFC (American history, 2004). Based on this design, Westinghouse successfully produced and tested a number of 5-250 kW sized SOFC power systems from the 1980s to the 1990s (American history, 2004). Since then, the work on SOFCs has continued with increasing intensity and a recent report noted more than 50 companies working on these fuel cells including Ceres Power and Rolls Royce FCS in the UK, Siemens and Ezelleron in Germany, Hexis in Australia, AMI and Chevron in the USA.

## 1.3– Comparison of Fuel Cell technologies

At the time of writing this thesis, five dominant types of fuel cells have been developed, each with specific advantages and drawbacks making them suitable for a wide variety of applications. These include Proton Exchange Membrane Fuel Cells (PEMFCs), also known as Polymer Electrolyte Membrane Fuel Cells, Alkaline Fuel Cells (AFCs), Phosphoric Acid Fuel Cells (PAFCs), Molten Carbonate Fuel Cells (MCFCs) and Solid Oxide Fuel Cells (SOFCs). Details of each type of fuel cell (FC) are described briefly in Table 1.1.

SOFCs are stable, capable of internally reforming fuels, and have a relatively high power output and efficiency compared to other types of FCs. Furthermore, they are much cheaper to produce due to the fact that they do not require expensive catalysts to operate. However, a better understanding of the effect microstructural parameters have on overall cell operation is required in order to reduce operating temperatures, which currently pose engineering difficulties during operation; SOFCs are therefore the focus of this thesis.

It is clear from the literature that immense progress has been made with regards to decreasing manufacturing costs of SOFCs as well as improving life ratings and efficiency in the past few decades. To give a better understanding of the issues faced by researchers and developers in making SOFCs more commercially viable, the next sections will explain the basic operation of SOFCs as well as give an overview of the components required for operation and the materials used during fabrication.

Table 1.1 – Comparison of fuel cell technologies (US Department of Energy, 2013)

| Fuel Cell Type | Common Electrolyte | Operating temperature | Typical Stack Size | Efficiency | Applications | Advantages | Disadvantages |
|---|---|---|---|---|---|---|---|
| PEM | Perfluoro sulfonic acid | 50-100° C<br><br>Typically 80° C | <1kW-100kW | 60% Transpor-tation<br><br>35% stationary | -Backup power<br>-Portable power<br>-Distributed generation<br>-Transportation<br>-Speciality vehicles | -Solid electrolyte reduces corrosion and electrolyte management problems<br>-Low temperature<br>-Quick start-up | -Expensive catalysts<br>-Sensitive to fuel impurities<br>-Low temperature waste heat |
| AFC | Aqueous solution of potassium hydroxide soaked in a matrix | 90-100° C | 10-100kW | 60% | -Military<br>-Space | -Cathode reaction faster in alkaline electrolyte, leads to high performance<br>-Low cost components | -Sensitive to $CO_2$ in fuel and air<br>-Electrolyte management |
| PAFC | Phosphoric acid soaked in a matrix | 150-200°C | 400kW<br><br>100kW module | 40% | -Distributed generation | -Higher temperature enables CHP<br>-Increased tolerance to fuel impurities | -Pt catalyst<br>-Long start-up time<br>-Low current and power |
| MCFC | Solution of lithium, sodium, and/or potassium carbonated soaked in a matrix | 600-700°C | 300kW-3MW<br><br>300kW module | 45-50% | -Electric utility<br>-Distributed generation | -High efficiency<br>-Fuel flexibility<br>-Can use a variety of catalysts<br>-Suitable for CHP | -High temperature corrosion and breakdown of cell components<br>-Long start-up time<br>-Low power density |
| SOFC | Yttria-stabilized zirconia | 500-1000°C | 1kW-2MW | 60% | -Auxiliary power<br>-Electric utility<br>-Distributed generation | -High efficiency<br>-Fuel flexibility<br>-Can use a variety of catalysts<br>-Solid electrolyte<br>-Suitable for CHP & CHHP<br>-Hybrid/GT cycle | -High temperature corrosion and breakdown of cell components<br>-High temperature operation requires long start-up time and limits |

## 1.4– Fundamentals of SOFCs

SOFCs stand out from other fuel cell technologies in many respects. Firstly, they can operate at high temperatures, up to 1000$^{o}$C, significantly hotter than any other fuel cell category. This high operating temperature of SOFCs allow for conventional hydrocarbon fuels to be reformed directly into hydrogen and carbon monoxide within the SOFC itself (Lee et al., 1990), and the fact that they are not poisoned by CO, which is used as a fuel, allows SOFCs to readily use fossil fuels. Another advantage given by this high operating temperature is that no precious metal catalyst is needed, and metals such as nickel can be used instead.

However these high operating temperatures also pose some disadvantages and challenges. Start-up times can be an issue in some configurations, and the thermal stresses induced in start and stop cycles mean that SOFCs are more suitable for use in stationary applications where these cycles are minimized (Singhal & Kendall, 2003).

Secondly, they are composed entirely of solid-state materials. This means that there is no fundamental restriction on the cell configuration. Westinghouse Electric Corporation had been developing tubular cells, also called rolled tubes, from the late 1950s till the late 1990s (Stambouli & Traversa, 2002). Nowadays, companies such as Ezelleron and Acumentrics continue to pursue the development of these types of cells due to their relative ease of fabrication and resistance to thermal cycling. Table 1.2 illustrates various types of SOFC design as adopted by a selection of companies.

Table 1.2 – SOFC design variations

| | |
|---|---|
| 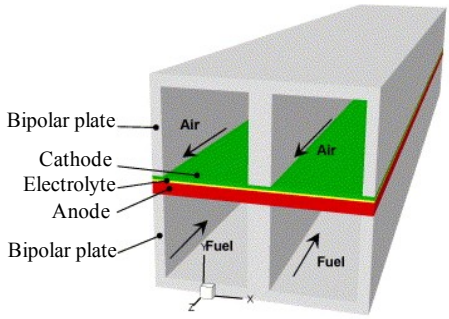 | Conventional Planar SOFC (Hwang et al., 2005) |
| 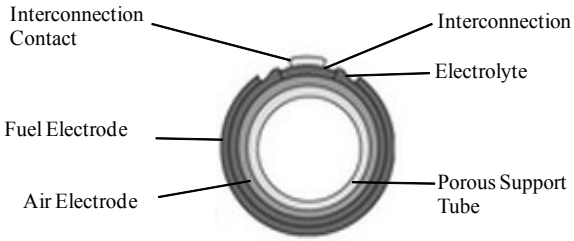 | Siemens Thin-wall PST SOFC (Henne, 2007) |
| 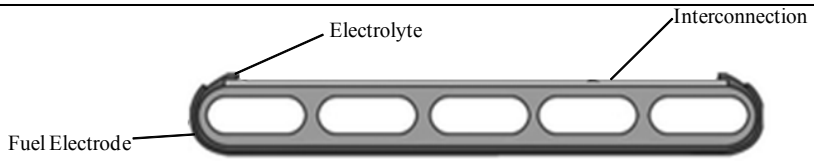 | Siemens HPD5-R1 SOFC (Henne, 2007) |
|  | Anode supported planar SOFC fuel cell (Shi et al., 2007) |
| 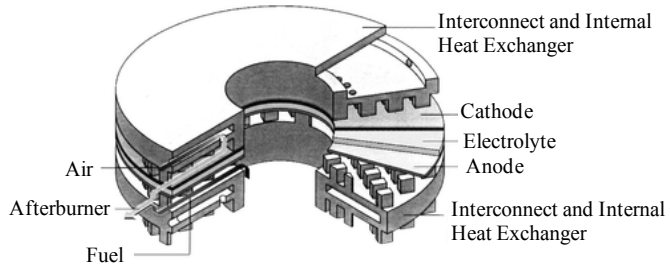 | HEXIS SOFC (Schuler & Nerlich, 2006) |
| 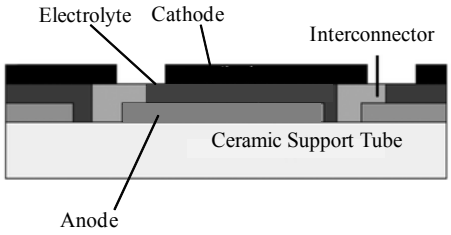 | Rolls-Royce SOFC (Travis et al., 2006) |

### 1.4.1 – SOFC basic operation

A SOFC consists of two electrodes, the anode and the cathode, sandwiched around a dense ceramic electrolyte. Hydrogen rich fuel is fed into the anode and oxygen, from the air, enters the cathode. Inside the anode, oxygen ions leaving the electrolyte react with the oxidized fuel which releases electrons. On the cathode side of the cell which is exposed to air, the absorption of oxygen creates a concentration gradient from the cathode to the anode. A charge balance is maintained in the cell by electrically connecting both electrodes, allowing a continuous flow of electrons and oxygen ions from cathode to anode. This generates useful electrical power from the combustion of the fuel, with pure water and heat as the only by-product of the reaction when hydrogen is used to fuel the reaction. Figure 1.2 illustrates the fundamental layout and reactions that define a SOFC.

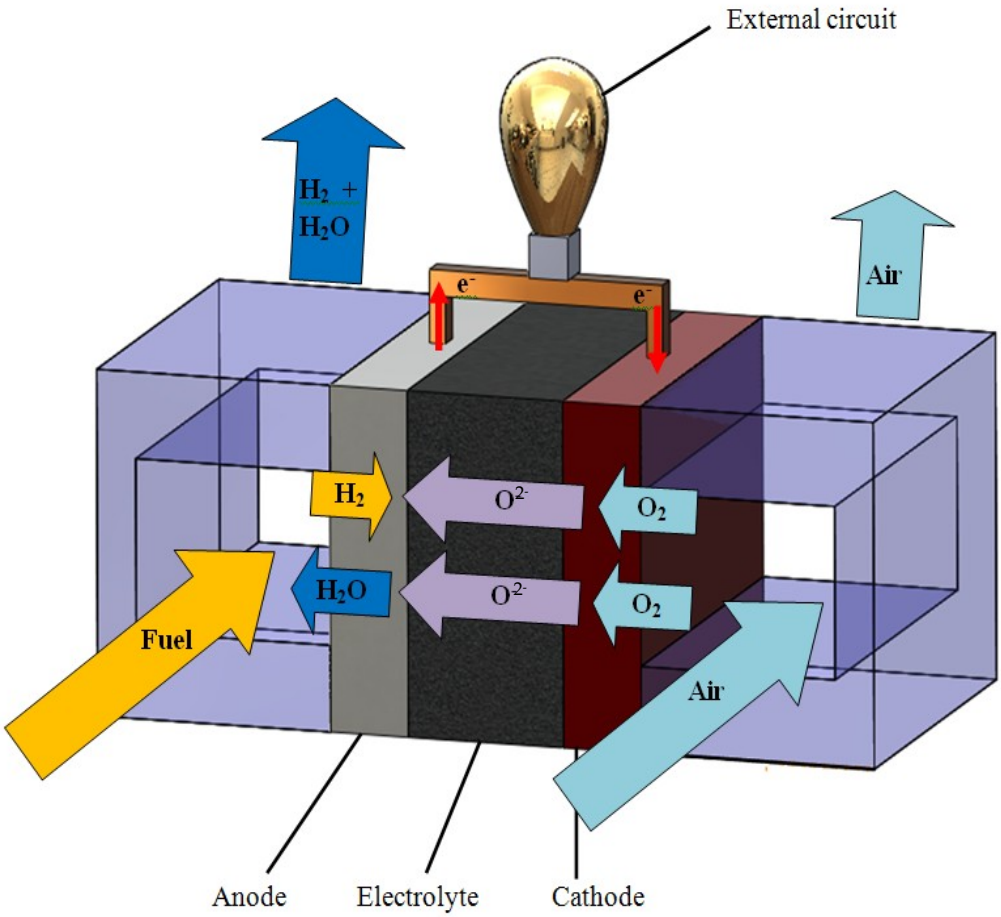


Figure 1.1 – Solid Oxide fuel cell (SOFC) operating principle.

The reactions inside the SOFC are:

| | |
|---|---|
| Anode | $H_2 + O^{2-} \rightarrow H_2O + 2e^-$ |
| Cathode | $0.5O_2 + 2e^- \rightarrow O^{2-}$ |
| Overall Reaction | $H_2 + 0.5O_2 \rightarrow H_2O$ |

When conventional fuels are used in SOFCs however, the process is not as clean and harmful emissions do exist. When using diesel or methanol for instance, SOFCs linked to remote power generation units were recorded to produce approximately 0.27 g/kWh of $NO_x$, 0.34 g/kWh of $SO_x$, 0.048 g/kWh of CO, 0.59 g/kWh of NMHC, 0.005 g/kWh of PM, as well as 680.1 g/kWh of $CO_2$ and 0.11 g/kWh of $CH_4$ (Hoogers, 2002). These emissions are however lower by almost 90% on average than when conventional combustion engines are used (Hoogers, 2002).

### 1.4.2 Electrochemical principles of SOFCs

The electrochemical reactions taking place in fuel cells determine the ideal performance of these cells. These are discussed in more detail in section 1.4 of this Chapter.

Some of these cell types are limited by the requirements of noble metal electrocatalysts to enable optimum reaction rates at the anode and cathode. Furthermore, carbon monoxide can poison noble metal electrocatalysts like platinum in low-temperature fuel cells, but can also serve as a fuel in high-temperature fuel cells where catalysts such as nickel or other oxides can be used instead.

The most common way to represent the ideal performance of a fuel cell is to define it by the Nernst potential, represented as cell voltage. Full cell reactions at the anode and cathode and their corresponding Nernst equations (Simons, King & Prokopius 1982; Cairns & Liebhafsky, 1969) are given in Table 1.1 in which R is the universal gas constant, F the Faraday constant, $E$ the equilibrium potential and $E^0$ the standard potential.

Table 1.3 – Relationship between different fuel cell reactions and their corresponding Nernst equations, derived from Gibb's free energy change.

| Fuel cell reaction (cathode → anode) | Nernst equation |
|---|---|
| $H_2 + ½\ O_2 \rightarrow H_2O$ | $E = E^0 + \left(\frac{RT}{2F}\right) \ln \left[\frac{[H_2][O_2]^{\frac{1}{2}}}{[H_20]}\right]$ |
| $H_2 + ½\ O_2 + CO_2 \rightarrow H_2O + CO_2$ | $E = E^0 + \left(\frac{RT}{2F}\right) \ln \left[\frac{[H_2][O_2]^{\frac{1}{2}}\ [CO_2]}{[H_20][CO_2]}\right]$ |
| $CO + ½\ O_2 \rightarrow CO_2$ | $E = E^0 + \left(\frac{RT}{2F}\right) \ln \left[\frac{[CO][O_2]^{\frac{1}{2}}}{[CO_2]}\right]$ |
| $CH_4 + 2O_2 \rightarrow 2H_2O + CO_2$ | $E = E^0 + \left(\frac{RT}{8F}\right) \ln \left[\frac{[CH_4][O_2]^2}{[H_2O]^2[CO_2]}\right]$ |

The Nernst equation represents the relationship between the ideal standard potential $E^0$ of the fuel cell reaction and the ideal equilibrium potential $E$ at different temperatures and partial pressures of the reactants and products. With a known ideal potential at standard conditions, the equations in Table 1.1 can be derived further to find the equilibrium potential at other temperatures and pressures (Simons, King & Prokopius 1982).

The Nernst equation is derived from two forms of the Gibbs free energy change equation, defining how much energy is required to break the bonds between two elements during a chemical reaction:

$$\Delta G = -RT\ln k \tag{1.1}$$

$$\Delta G = -zFE \tag{1.2}$$

where z is the number of moles of electrons exchanged in the reaction, $F$ is Faraday's constant, $R$ the universal gas constant, $E$ the electrical driving force, and $k$ is the equilibrium constant for the reaction (Mench, 2008). Combining Equations 1.1 and 1.2, and substituting $k$ for its original form yields the equations shown in Table 1.3.

The ideal standard potential of a hydrogen/oxygen fuel cell is 1.229 V with the product as liquid water, and 1.18 V for water as a gaseous product. This standard potential is usually referred to as the oxidation potential for hydrogen ($H_2$), also expressed as the Gibbs free energy of the reaction between hydrogen and oxygen. The change in standard Gibbs free energy is proportional to the ideal cell potential, and it can be seen that the Gibbs free energy increases alongside a decrease of cell temperature. The difference between the ideal and actual performance of a fuel cell is quite pronounced, especially when considering the potential current response of a fuel cell. Shown in Figure 1.2 is the actual and ideal response of a fuel cell.

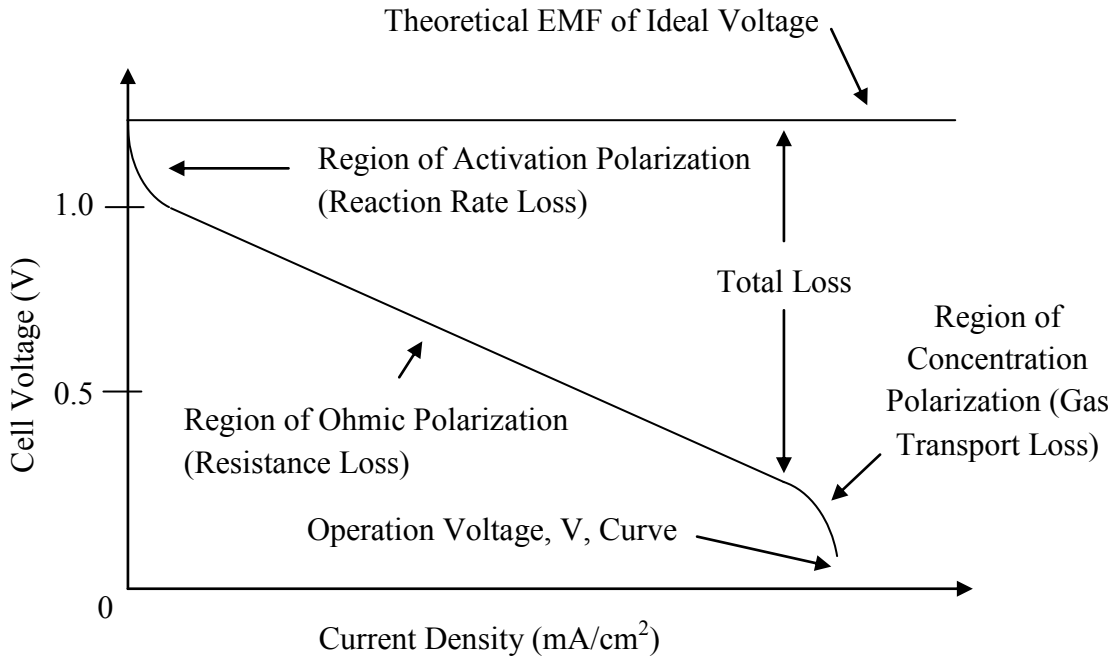


Figure 1.2 – Theoretical and actual performance of a fuel cell against potential current response.

When current is drawn from a cell, electrical energy is obtained but the actual cell potential is lowered from the equilibrium potential due to irreversible losses caused by various processes. These losses, which are usually called polarization or over potential losses, can be attributed to activation polarization, gas concentration polarization and ohmic polarization (Stolten, 2010).

In low current regions, the activation loss dominates, as in this region activation energy barriers must be over-come before current and ions can flow. This loss is directly proportional to current

flow magnitude. In high current regions, the concentration loss dominates. In these regions, the current flow is commonly modelled using the Butler-Volmer equation, looked at in more detail later in this section, derived from the fundamental Gibb's free energy change during oxidation and reduction

$$j = j_0 \left\{ e^{\left(\frac{-a_{RD} F\eta}{RT}\right)} - e^{\left(\frac{a_{OX} F\eta}{RT}\right)} \right\} \tag{1.3}$$

where $a$ is the charge transfer coefficient, $j$ the current density, $j_0$ the exchange current density and $\eta$ the overpotential (Golbert et al., 2008; Stolten, 2010). The activation polarization of a fuel cell can be represented as

$$\eta_{\text{act}} = \frac{RT}{anF} \ln\left(\frac{j}{j_0}\right) \tag{1.4}$$

where $\eta_{\text{act}}$ is the activation polarization, $a$ the charge transfer coefficient, $j$ the current density and $j_0$ the exchange current density (Bard & Faulkner, 2001). The activation polarization is caused by the slow electrochemical reactions at the electrode surface where the fuel/product molecules are reduced or oxidized. This polarization is directly related to the rate at which the fuel or oxidant is reduced or oxidized. The reacting species must overcome the activation barrier in the case of a fuel cell (Bard & Faulkner, 2001).

With increasing current density, Ohmic losses become important, defined as

$$\eta_{\text{ohm}} = iR_c \tag{1.5}$$

where $\eta_{ohm}$ is the ohmic polarization and $R_c$ the cell resistance (Bard & Faulkner, 2001). This is the first case where the resistance of a cell is mentioned as being important to the calculations used to predict its performance, and this will be investigated in much more detail in later Chapters. The only way to effectively reduce these losses is to modify the geometry of the electrolyte and electrodes to allow shorter electronic and ionic path lengths through these structures, or by selecting materials with higher conductivity (Bard & Faulkner, 2001).

When entering the region of high current densities or low gas partial pressures, mass transport losses, or concentration polarization, becomes dominant (Stolten, 2010). In these cases it is increasingly difficult for the reactant flow to reach the fuel cell reaction sites. The concentration polarization can be expressed as

$$\eta_{con} = \frac{RT}{n\mathrm{F}} \ln\left(1 - \frac{j}{j_L}\right) \tag{1.6}$$

where $\eta_{con}$ is the concentration polarization and $j_L$ is the limiting current density (Bard & Faulkner, 2001). A concentration gradient is formed in the system following the consumption of reactant gas at the electrode through the electrochemical reactions, which cause a drop in local partial pressures of the reacting gas. The rate of diffusion of gas in electrode pores, and the removal of reaction products out of the system, are all processes responsible for concentration polarization losses.

Figure 1.3 gives a representation of the various contributions to polarization losses in a typical fuel cell, regardless of the type. The direct consequence of concentration polarization with regards to current flow in a fuel cell is the increase the anode potential and the decrease in cathode potential. A result of this is a reduction in overall cell voltage.

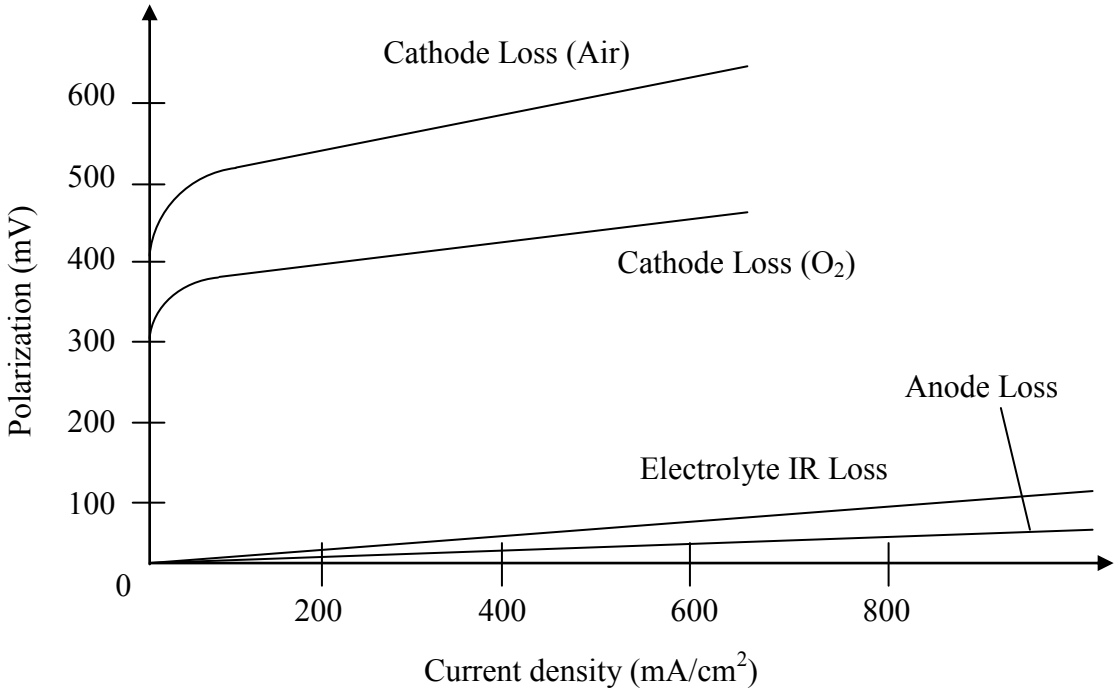

Figure 1.3 – Origin of polarization losses in a fuel cell (Knibbe et al., 2010)

The Butler-Volmer equation (formally named the Butler-Erdey-Gruz-Volmer equation) is the fundamental equation of electrode kinetics that describes the exponential relationship between the current density and the electrode potential of a fuel cell electrode. Based on this model, the reversible electrode potential, also called the equilibrium electrode potential, can be defined.

Erdey-Gruz and Volmer published a seminal paper in 1931 (Erdey-Gruz & Volmer, 1931) where they elucidated the "hydrogen overpotential" by using a kinetic model for the electrode processes when the charge transfer step, i.e. the electrode reaction, is the rate-determining process. Although the names used for this model vary in the literature and the definition itself ambiguous in light of the historical facts, the most acceptable form of the current-electrode potential equation that may be called the Butler-Volmer equation for a one-step, one-electron process can be derived as follows.

It is understood that current can be defined in terms of the charge of all electrons flowing in a certain direction, as given by

$$i = n\mathrm{F}j \tag{1.7}$$

where $j$ is the flux of reactant per unit area in mol/cm$^2$ (Bard & Faulkner, 2001). The reaction at each electrode is determined by $k_F$ and $k_B$, respectively the forward and backward rate coefficients in s$^{-1}$. The forward and backward fluxes of reactants per unit area are therefore given by:

$$j_F = k_F c_{OX} \tag{1.8}$$

$$j_B = k_B c_{RD} \tag{1.9}$$

in which $C_{OX}$ and $C_{RD}$ are the surface concentrations of oxidants and reductants respectively, and $j_F$ and $j_B$ are the forward and backward fluxs of reactants per unit area in mol/cm$^2$ (Bard & Faulkner, 2001). The net current produced by an electrode is the difference between the current densities at that respective electrode, and can be expressed as:

$$i = nF(k_F c_{OX} - k_B c_{RD}) \tag{1.10}$$

The given reaction rate coefficients are functions of temperature and Gibb's free energy change as shown in the following equation, called the Erying equation (Erying, 1935):

$$k = \frac{k_{Bo}T}{h} e^{\left(\frac{-\Delta G}{RT}\right)} \tag{1.11}$$

where $j$ is the reaction rate constant in Js/m$^2$kg, or s$^{-1}$, $h$ is Plank's constant being $6.626\times10^{-34}$ m$^2$kg/s and $k_{Bo}$ is Boltzmann's constant being $1.381\times10^{-23}$ J/K (Bard & Faulkner, 2001). The respective forward and backward reaction rate coefficients can now be found by determining the

Gibb's free energy changes for the forward reduction and backward oxidation reactions, as given by

$$\Delta G_F = \Delta G_{CH} + a_{RD} FE \tag{1.12}$$

$$\Delta G_B = \Delta G_{CH} - a_{OX} FE \tag{1.13}$$

in which $\Delta G_F$ is Gibb's free energy change for the forward reaction in J/mol, $\Delta G_B$ is Gibb's free energy change for the backward reaction in J/mol, $\Delta G_{CH}$ is the chemical part of Gibb's free energies in J/mol, $a_{RD}$ is the transfer coefficient for the electrical term of Gibb's free energy during a reduction and $a_{OX}$ is the transfer coefficient for the electrical term of Gibb's free energy change during an oxidation (Bard & Faulkner, 2001).

Therefore the respective forward and backward reaction coefficient rates are given by

$$k_F = k_{0,F} e^{\left(\frac{-a_{RD} FE}{RT}\right)} \tag{1.14}$$

$$k_B = k_{0,B} e^{\left(\frac{-a_{OX} FE}{RT}\right)} \tag{1.15}$$

Substituting the previous equations into the definition of current yields

$$i = nF \left\{ k_{0,F} e^{\left(\frac{-a_{RD} FE}{RT}\right)} c_{OX} - k_{0,B} e^{\left(\frac{-a_{OX} FE}{RT}\right)} c_{RD} \right\} \tag{1.16}$$

At equilibrium, the net current is zero and the current densities are both equal to the exchange current density, given by

$$i_0 = nFk_{0,F}e^{\left(\frac{-a_{RD}FE}{RT}\right)}c_{OX} = nFk_{0,B}e^{\left(\frac{a_{OX}FE}{RT}\right)}c_{RD} \quad (1.17)$$

By combining both of the above equations, we can derive the Butler-Volmer equation as being (Bard & Faulkner, 2001)

$$i = i_0\left\{e^{\left(\frac{-a_{RD}F\eta}{RT}\right)} - e^{\left(\frac{a_{OX}F\eta}{RT}\right)}\right\} \quad (1.18)$$

The over-potential is expressed as

$$\eta = \eta_{act} + \eta_{ohm} + \eta_{con} \quad (1.19)$$

In the work presented in this thesis, the exchange current density is used as an input to the model and is obtained experimentally from impedance measurements on cells under specific conditions. The over-potential is also an input parameter, matched to that used experimentally, meaning that the activation, ohmic and concentration over-potentials are indirectly taken into account by the electrochemical model presented in section 1.10.

### 1.4.3 – SOFC components overview

As stated previously, an SOFC is comprised of an anode and a cathode either side of a ceramic electrolyte.

The principle function of the electrode is to enable the reaction of the fuel, oxygen, and the electrolyte, without degradation through those reactions and/or corrosion. A key role of the

electrode is to bring into contact the three phases; the gaseous fuel, the solid electrolyte and the electrode itself (Stolten, 2010).

The electrolyte is often the component which limits the operating temperature of the fuel cell, and plays the role of an electronic insulator to prevent the conduction of electrons between both electrodes (Mench, 2008). The main role played by the electrolyte is the conduction of ions from one electrode to the other to maintain overall electrical charge balance.

The cathode, defined as the positive terminal of the cell, distributes the supplied oxygen to the cathode/electrolyte interface, catalyses the oxygen reduction charge transfer reaction to form oxide ions, and transports electrons coming from the external circuit (Mench, 2008).

The anode, defined as the negative electrode, distributes fuel gas to the anode/electrolyte interface, catalyses the reaction between the fuel and oxide ions, and transports electrons released to the external circuit (Mench, 2008).

In recent years, there have been intensive studies on the anode of SOFCs on a variety of disciplinary fronts, such as materials, surface science, catalysis and electrochemistry (Mench, 2008). The relationship between microstructure and performance has been a particular area of interest due to the complexity of the reactions taking place and the relative lack of control with regards to the nature and number of reaction sites within the anode, a driving parameter of the performance of the entire cell. This thesis will attempt to contribute in better understanding the relationship between the microstructure of an SOFC anode and cell performance.

### 1.4.4 – SOFC component requirements and materials

Each component of the SOFC serves several particular functions, and as a consequence must meet certain requirements. The next sub-sections will give a description of the characteristics required for each component, as well as a brief overview of some materials used to fabricate SOFC electrolytes and cathodes. A more in-depth analysis of the research undertaken on materials used for the fabrication of SOFC anodes will follow in order to provide a comprehensive understanding of the current state of research on suitable anode materials.

Anodes being the “fuel” electrode of the cell, where the microstructure plays an essential role in the performance of the entire cell, the work presented in this thesis is focused on anodes.

#### 1.4.4.1 – Electrolyte

SOFC electrolytes need to be ionically conductive, chemically stable in order to avoid unwanted reactions, and mechanically strong enough to undergo the thermal and stress cycles without failure. Furthermore, the electrolyte material must be sinterable to provide conducting pathways for the transport of ions.

The most widely used material for SOFC electrolytes is yttrium-doped zirconium oxide (YSZ) due to its high ionic conductivity, chemical stability and reasonable mechanical strength (Stolten, 2010). However, YSZ is known to have a low ionic conductivity at temperatures below 750$^{o}$C, rendering its use problematic in lower temperature SOFCs (Stolten, 2010). In order to resolve this problem, manufacturers have decreased the electrolyte thickness and used alternative materials to replace the yttrium (Stonlten, 2010). A recent replacement for YSZ is scandium-doped zirconia which has a higher conductivity than YSZ but a higher cost, and problematic ageing effects of scandium-doped zirconium oxide have been a concern. Other options for SOFC electrolyte materials are gadolinium or samarium-doped cerium oxide, which exhibit a higher oxide ion conductivity compared to materials based on zirconia (Weber, 2004). On the other hand, cerium oxide based materials at high temperatures under reducing conditions show electronic conductivity and dimensional change, neither desired electrolyte characteristics (Weber, 2004). Operating at temperatures under 600$^{o}$C surmounts this problem, and companies such as Ceres Power Limited in the UK have successfully used ceria-based materials in the fabrication of electrolytes.

Different mixtures of oxides provide the opportunity to develop and explore other oxide ion conducting electrolytes. A mixture containing gallium oxide for example has attracted attention for use as an electrolyte. This mixture however has two principal drawbacks; the uncertain cost of gallium and uncertain chemical and mechanical stability of the oxide. Despite these issues however, Mitsubishi Materials Corporation in Japan is using this as an electrolyte in their

successfully built and tested SOFC systems with power ratings of up to 10kW (Kumar & Priya, 2012).

### 1.4.4.2 – Cathode

The electrochemical reduction of oxygen at the cathode involves a series of elementary reductions that involve the transfer of electrons, meaning that this part of an SOFC must meet the requirements of high electronic conductivity, high catalytic activity for oxygen dissociation and reduction, dimensional and chemical stability in environments found during cell performance and fabrication, compatibility and minimum reactivity with the electrolyte and interconnection, and thermal expansion properties that match with other cell components (Stolten, 2010). Additionally, the cathode must have a porous, stable microstructure to ensure the diffusion of gaseous oxygen through the cathode to the cathode/electrolyte interface. These specific requirements restrict the number of suitable materials for cathode fabrication.

A traditional material used for SOFC cathodes is doped lanthanum manganite. When substituted with low valence elements such as strontium or calcium, this material has low electronic resistance. Furthermore, the thermal characteristics of lanthanum manganite are compatible with YSZ, the material displays adequate electrocatalytic activity at higher temperatures, and is stable in the operating conditions of SOFC cathodes (Weber, 2004).

### 1.4.4.3 – Anode

The anode of SOFCs must be a good catalyst for the oxidation of fuel (hydrogen and carbon monoxide), must be electronically conductive, be stable in the reducing environments of the fuel, provide reaction sites for the electrochemical reactions to take place, have sufficient porosity to allow for the transport of fuel to these reaction sites and the products of the fuel oxidation away from them. The anode must also have matching thermal expansion coefficients with that of the interconnect and electrolyte, and be chemically stable with regards to the electrolyte and interconnect. On top of all of this, cost effectiveness is also an important consideration in

industry. Advanced SOFC designs place additional constraints on the anode; it must tolerate some exposure to oxidizing environments while also tolerating some hydrocarbon/sulphur species in the fuel stream when pure hydrogen is not used as the fuel.

For the oxidation of hydrogen and other fuels to take place in an SOFC anode, the fuel must be able to diffuse through the electrode and come in contact with the ionically conductive material, the electrons released must be able to leave through an electronically conductive material, and finally the water from the reaction must be able to leave the site and exit the electrode. These reaction sites are called triple-phase boundary sites, or TPB sites, and are illustrated in the following figure.

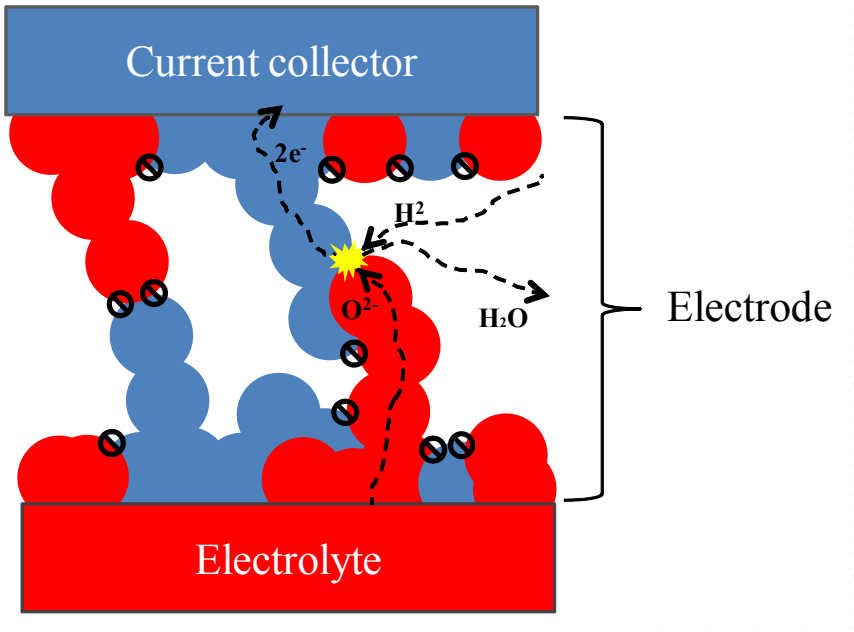


Figure 1.4 – Schematic 2D representation of SOFC anode showing active and inactive TPB sites. Blue particles are electronically conductive and red particles are ionically conductive. Dashed arrows show the percolated paths through which specific species can be transported. The black crossed circles mark inactive sites and the yellow star marks an active site.

The materials used in the fabrication of SOFC anodes therefore need to be a mix of ionically conductive materials, electronically conductive materials and be porous enough to allow for the diffusion of fuel gases and the products of oxidation.

A large portion of the research done on SOFC anode materials is based on the use of hydrocarbon fuels due to carbon deposition issues. The focus of this thesis are SOFCs operating using hydrogen as the fuel, so the following review will not take into account the work done on materials used to overcome the side-effects of using hydrocarbons to fuel the electrochemical reactions.

In the past decade a number of comprehensive reviews have been published in this area, for example those by Atkinson et al. (Atkinson et al., 2004), Tao et al. (Tao et al., 2004), Sun et al. (Sun et al., 2007) and Cowin et al (Cowin et al., 2011), and much of the information presented below is a collation of these works.

Nickel-based/YSZ cermet anodes, which are defined as the mixture of a ceramic (YSZ) and a metal (nickel), are a common choice for SOFC manufacturers due to the relatively cheap price of nickel, similar thermal expansion characteristics to YSZ, good electronic/ionic conductivity and high catalytic activity for hydrogen oxidation (Weber, 2004). However, Ni/YSZ is prone to nickel agglomeration during prolonged usage (Iwata, 1994) and has poor redox stability (Cassidy et al., 1996). The poor redox stability was shown to occur upon the re-oxidation in the anode as a result of the oxidation of nickel to nickel oxide, producing stresses at the anode-electrolyte interface (Faes et al., 2009; Laurencin et al., 2009) due to associated volume change. A modification of the microstructure and distribution of the YSZ and nickel phases in the anode (Kim et al., 2006; Waldbillig et al., 2005) was found to alleviate this stress induction. Although no solution was satisfactorily put forward for either of these problems, Ni/YSZ cermets are still a benchmark material in this field due to the lack of alternative high-performance anodes.

A selection of other materials based on $CeO_2$ have shown mixed electronic and ionic conductivity in reducing atmospheres (Cowin et al., 2011), and when doped the ionic conductivity was found to significantly increase, notably for Gd (GDC) and Sm (SDC) (Van Herle et la., 1996).

A great deal of research into alternative cermets for both cathodic and anodic purposes is focused on the fabrication of perovskite-type compounds (Martina et al., 2002; Tao et al., 2003; Huang et al., 2006) due to their ease of production, flexibility and variety of properties. The earliest example of an efficient and fully stable anode material under redox conditions is

$(La_{0.75}Sr_{0.25})Cr_{0.5}Mn_{0.5}O_3$ (LSCM) and was developed in 2003 (Tao & Irvine, 2003). LSCM is defined as a *p*-type semiconductor which can be utilized as both an anode and a cathode in a symmetrical SOFC (Bastidas et al., 2006). Although this material is stable, a relatively poor electronic conductivity and catalytic activity currently make it an inefficient SOFC anode at interim temperatures.

Strontium titanium oxide, $SrTiO_3$ (STO) is another material under extensive investigation, first proposed by Slater et al. in 1997 (Slater et al., 1997) for use as a potential anodic material for SOFCs. Although STO based anodes show good chemical and redox stability, they show low electronic conductivity in reducing conditions (Balachandran et al., 1981). In 2005, Kolodiazhni and Petric (Kolodiazhni & Petric, 2005) doped STO with niobium and yttrium and reported high conductivities in reducing atmospheres. Li et al. later reported high conductivities without adversely affecting the compound stability by doping the STO with yttrium and lanthanum (Li et al., 2007), but did not display a sufficiently high catalytic activity. In the past, both pyrochlore and tungsten bronze compounds were investigated as possible anode materials. The tungsten bronze alternative showed limited success in 1999 albeit displaying adequate electronic conductivities (Slater & Irvine, 1999). B-site doping allowed Ggadolinium titanate-based pyrochlores to be considered as alternative anode materials, initially having been developed for use as an electrolyte material, allowing for the mixed transport of electrons and ions (Sprague et al., 1999; Porat et al., 1997). However, subsequent research uncovered various deficiencies such as interfacial reactivity with YSZ, low electronic conductivity and redox instability (Holtappels et al., 2000).

In more recent years, researchers have been developing a number of new cermet anode materials using the fluorite structures from which electrolytes are commonly made. Qiao et al. (Qiao et al., 2007) used Ni/YSZ and Ni-$CeO_2$/YSZ as anodes and showed that at least 25 wt% of Ni is required to ensure a sufficiently high electronic conductivity. A decrease in cell polarisation resistance was observed with increases in ceria doping, meaning an increase in cell performance. The authors showed that the presence of nano-sized nickel oxide particles formed through the sintering process have a direct link to performance, meaning that the better dispersion of nickel particles with the YSZ phase had a more significant effect than the ceria doping.

Looking at SDC-based systems, Chen et al. (Chen et al., 2008) demonstrated that a volume percent of 50-60% of nickel is necessary for samples to meet anode material requirements based on electrical conductivity and TEC when fabricated using the urea-combustion sintering method. The authors also showed that material porosity and bend strength were highly dependent on Ni content, in spite of a lack of chemical reactivity between Ni and SDC. However the use of catalysts or other metals in the process gave varying results, meaning that additional investigations are required. Wang et al. investigated the addition of a SDC-Ru catalyst layer on top of a Nickel-SDC cermet and showed that the additional layer had no difference on the cell efficiency in wet hydrogen conditions, while analyses on copper-nickel composite anodes showed different results (Wang et al., 2008). The authors proposed that the high-catalytic activity of nickel is reduced in the copper-nickel composite.

A number of researchers expected the impregnation of an ionic conductive support with an electronic conducting phase to be effective in forming satisfactory anode materials. YSZ impregnated with LSCM formed stable and catalytically active anodes, as found by Zhu et al. (Zhu et al,.2010). These authors also noted that further impregnation with nickel or silver doubled cell performance. In some instances, using graded anodes was found to improve both cell stability and performance. A solid state composite of LSCM, copper and YSZ, coupled with two anode functional layers Ni/YSZ and Ni/ScSZ utilised as part of a graded anode, was shown by Ye et al. (Ye et al., 2008) to treble fuel cell power density over the parent Cu/LSCM/ScSZ anodes. However, in spite of the capacity of graded anodes to increase cell performance, the practicality of fabricating these materials renders them problematic for usage, and similar performance can be achieved using lower cost fabrication methods. Table 1.4 summarizes the principal findings mentioned in this section.

Table 1.4 – Advantages and disadvantages of some materials considered for use in the fabrication of SOFC anodes.

| Anode material | Advantage | Disadvantage |
|---|---|---|
| Nickel/YSZ | Poor catalytic activity and conductivity at interim temperatures | Prone to nickel agglomeration and poor redox stability after prolonged usage |
| LSCM | Stable for both anode and cathode use | Poor electronic conductivity and catalytic activity at interim temperatures |
| STO | Good chemical and redox stability | Low electronic conductivity in reducing conditions |
| Gandolinium-titanate based pyrochlores | Mixed ionic and electronic conductor | Interfacial reactivity with YSZ, low redox stability and electronic conductivity |
| LST | Higher conductivity than STO | Negligible catalytic activity for the oxidation of hydrogen |

This analysis presents only a fraction of the work that has been undertaken to identify alternative SOFC anode materials, with the challenges encountered underlining the importance the SOFC anode microstructure has on overall cell performance, on top of material chemical parameters and compatibility. It is indeed reported that the anode porosity, for example, is essential in the performance of the cell as it controls the mass transport within the anode (Suzuki et al., 2009; Qiong et al., 2011). This porosity can be controlled through changes in sintering temperature and the use of pore former particles such as graphite and starch. Suzuki et al. went on to show a direct correlation between the microstructure of the anode of an SOFC and its electrochemical performance when a tubular design is used. The size of the particles used was found to influence performance, with smaller particles enhancing the formation of a highly porous microstructure.

## 1.5– Link between SOFC anode microstructure and cell performance

It has been established in the literature that the microstructure of an SOFC electrode determines its performance as explained below, and a number of models have been developed with the goal of better understanding this relationship (Deng & Petric, 2004; Janardhana et al., 2008; Yuan et al., 2009; Ji et al, 2006; Martinez & Brouwer, 2008; Suzuki et al., 2008; Juhl et al., 1996; Chen et al., 2009; Chan et al, 2004; Kenney et al., 2007; Kenney et al., 2009; Sunde, 1996; Isolevich et al., 1999; Nam & Jeon, 2006; Deseure et al., 2005; Deseure et al., 2007; Ni et al., 2007; Li et al., 2006; Schneider et al., 2006; Schneider et al., 2007). Most modelling approaches are divided into two steps; the electrode generation itself, and the electrode performance simulation, usually requiring the solution of a system of equations describing the mass transport and electrochemistry.

A sample of recent research efforts in understanding the link between microstructural properties of SOFC electrodes and overall cell performance includes the work of Sim and co-workers (Sim et al., 2006), who established that the electrochemical properties of pure and composite electrodes are closely related to their microstructure. Jørgensen et al. (Jørgensen et al., 2001) showed that the less dense the electrode microstructure of a SOFC comprising a composite Lanthanum Strontium Manganate (LSM)-YSZ layer and two current collecting layers of LSM, the smaller the grains that compose it are, leading to a longer TPB line in the composite structure, in turn causing a decrease in polarization resistance with decreasing sintering temperature. The previously mentioned authors observe in their experiments that, if the composite structure is too dense, gas access to the composite-electrolyte interface and to LSM-YSZ contacts can be obstructed, reducing overall SOFC performance. Haanappel and co-workers (Haanappel et al., 2005) noted an increase in electrochemical performance following a grain size increase of the outer cathode current collector layer, with a peak performance using coarse LSM powder. From their experiments, Haanappel et al. conclude that the use of coarse LSM for the cathode current collector layer and non-calcined YSZ powder for the cathode functional layer simplifies the production route of SOFCs (Haanappel et al., 2005). In this study the YSZ was not treated thermally; calcination is a thermal treatment process used on ores and other solid materials to bring about thermal decomposition, phase transition or removal of volatile particles. It can be concluded from these studies that one of the determining parameters of the overall

performance of a SOFC is particle size**.** Experimental studies coupled with an analytical simulation model developed by Costamanga (Costamanga et al., 1998) proved that for thick electrodes, the optimum performance is obtained for a composition near to the percolation threshold of the electron conducting phase. On the other hand, for thin electrodes this optimum performance is obtained when the contact area between the two phases is maximized. Hence another determining parameter is the electrode thickness. Choi and co-workers established that the electrochemical performance of a composite SOFC is largely dependent on the length and amount of TPBs (Choi et al., 2001). Indeed, Choi et al. determine in their experiments that the better cathodic activity in composite electrodes results from a higher TPB population. Also demonstrated is that LSM particle growth deteriorates the long-term stability of composite electrodes.

All in all, microstructural parameters that were shown to directly influence the performance of an SOFC anode are particle size, particle neck size, porosity and volume fraction contents. These parameters all directly influence the TPB densities and locations, which must percolate to relevant boundaries in order to transport species and charges.

Percolation theory is a discipline that has attracted considerable attention in the past few decades, born in the field of mathematics, and the next section will present some of the work done and its applicability to SOFC anode analyses.

## 1.6– Percolation theory

Percolation theory focuses on the connectivity of bonds (or sites) of different critical phenomena, models and relevant quantities. The field was introduced to deal with random networks in mathematics, and has since been applied to most fields of natural science. In the case of SOFC materials particularly, percolation relies on the prediction of coordination number of particles, or the number of contacts between a certain particle and all neighbouring particles. Several models (Chen et al., 2009; Suzuki & Oshima, 1983; Bouvard & Lange, 1991) were developed to calculate coordination numbers based on particle sizes and compositions. Coordination numbers are related to percolation thresholds, defined as the minimum volume fraction of particles required for percolating clusters of particles of the same type to exist, and probability of

connection, the probability that a given particle belongs to a cluster of percolating particles of the same type, providing a connecting pathway for conduction. A number of papers have been published to estimate the coordination numbers for discreet mixtures of rigid spheres of uniform size (Bouvard & Lange, 1991; Chen et al., 2009; Suzuki & Oshima, 1983; Dodds, 1980).

Liu and Regenauer-Lieb (Liu & Regenauer-Lieb, 2011) applied percolation theory to microtomographic images to derive scaling laws to upscale microstructural properties. They report that, for near-isotropic samples such as sandstone, the approach works well. When strongly anisotropic structures are analyzed such as tree branches and deformed rock, the percolation threshold and fractal dimension can be assessed with accuracy. However, the uncertainty of the correlation length makes the determination of critical exponents inaccurate using this approach in strongly anisotropic media.

Bertei and Nicolella used percolation theory to predict the effective properties of composite electrodes for solid oxide fuel cells, such as TPB boundary length and mean hydraulic radius. (Bertei & Nicolella, 2011). The application of percolation theory to predict effective properties and morphological parameters of random packings of solid particles in SOFC materials such as ionic and electronic conductivity is found to be extensively used in the literature to study the effect of various microstructural parameters on these transport properties such as particle size and porosity (Nam & Jeon, 2006; Costamanga et al., 1998; Al-Raoush & Alsaleh, 2007; Bertei & Nicolella al., 2011; Kenney & Karan, 2007; Zhu & Kee, 2008; Bessler et al., 2010).

Other authors make use of percolation theory to analyze micro-CT scans to investigate the 3D interconnection, correlation function and shape of rock samples (Ikeda et al., 2000; Navarre-Stichler et al., 2009). Nakashima and Kamiya developed a model to analyze the tortuosity and pore connectivity of porous rocks (Nakashima & Kamiya, 2007), and determined the upscaled effective diffusivities as a function of porosity.

The formation and percolation of TPB sites are another domain in which percolation theory has been applied, for example by Martinez and Brouwer (Martinez & Brouwer, 2007) who showed that active TPB formation is found to be mostly dependent on the continuous and competing percolation of multiple phases.

Most of the authors mentioned above rely on computational tools and 3D synthetic microstructures to carry out their investigations. This is looked into in more detail is section 1.8 bellow. In the case of percolation theory, initially developed for mathematical analyses, the use of synthetic structures arises from the numerical nature of percolation theory. Researchers progressively turn towards computational methods and synthetic structures in a variety of other fields for specific reasons, as explained in the next section.

## 1.7– Motivation behind creating multi-scale models for fuel cells

Computational modelling plays an increasingly important role in academic and industrial research with the continuous advancements in computational hardware and software. For example in both automotive and aerospace R&D, both keystone industries of the worldwide economy, prototype development and optimization has almost completely been transferred from the workbench to the virtual drawing board. This has helped both industries and academic institutions maintain their competitive edge by undertaking orders of magnitude more analyses than would normally have been possible if they were limited to real life experiments.

An example of this is the emergence of a wide array of novel catalysts, supports and membranes based on materials at the nano-scale in the development of a variety of fuel cells, which has opened a number of exciting opportunities to accelerate materials-research developed by computational experiments, or "models". Many of these materials, if not all of them, can be characterized with first principle quantum mechanics methods in turn opening the door to *ab initio* descriptions and optimizations of materials properties using a bottom-up approach. To achieve this, the large amount of data involved must be transferred in a series of hierarchical simulations of increasing time- and length-scales than can be addressed with *ab initio* modelling alone.

The behaviour of fuel cells must be understood in the context of the complex interplay of assemblies and materials if a contribution is to be made to real-world applications of these devices, and to translate basic understanding into marketable products. The traditionally costly experiments carried out, for example long-term cell degradation tests, therefore need to be supported by a comprehensive strategy involving models of all length-scales ranging from

molecular dynamics to stack and system performance. Furthermore, some aspects of the behaviour of fuel cells are simply impossible to undertake with today's technologies, such as the *in operandi* visualization of the electrochemical double layer structure.

If simulation strategies developed for nano-and micro-scale based fuel cell material behaviours are to represent real-life operation modes, they must span a large length- and time-scale comprising many orders of magnitude. Due to the complexities of multi-scale calculations, predicting cell performance at larger scales is not achievable by simply extrapolating nano-scale simulation methods to increasingly larger systems. Instead, the integration of information of high-accuracy calculations at small length and time scales into large scale models to create multi-scale models capable of quantitatively simulating the behaviour of fuel cells as a whole. Figure 1.5 illustrates the interactions between each scale of the fuel cell system when modeled. Research efforts are currently being undertaken to achieve a successful multi-scale modelling approach capable of addressing the requirements of the world-wide industry and research communities (Henke et al., 2013).

Although there exists a wealth of experience throughout the world with respect to the development and application of individual software packages to tackle specific problems in materials-science and electrochemical modelling, simulations in this sector are presently far from being reliable whole system simulators. Indeed, a multitude of software packages, many of which are designed to be compatible with High Performance Computer (HPC) architectures, and are well adapted to perform particular challenging tasks. The comprehensive simulators required to system-level modelling effectively need to be able to describe the whole fuel cell systems at a functional level (usually macroscopic) on the basis of the components comprising these systems at the microscopic level involving nanometre length scales and picosecond time scales.

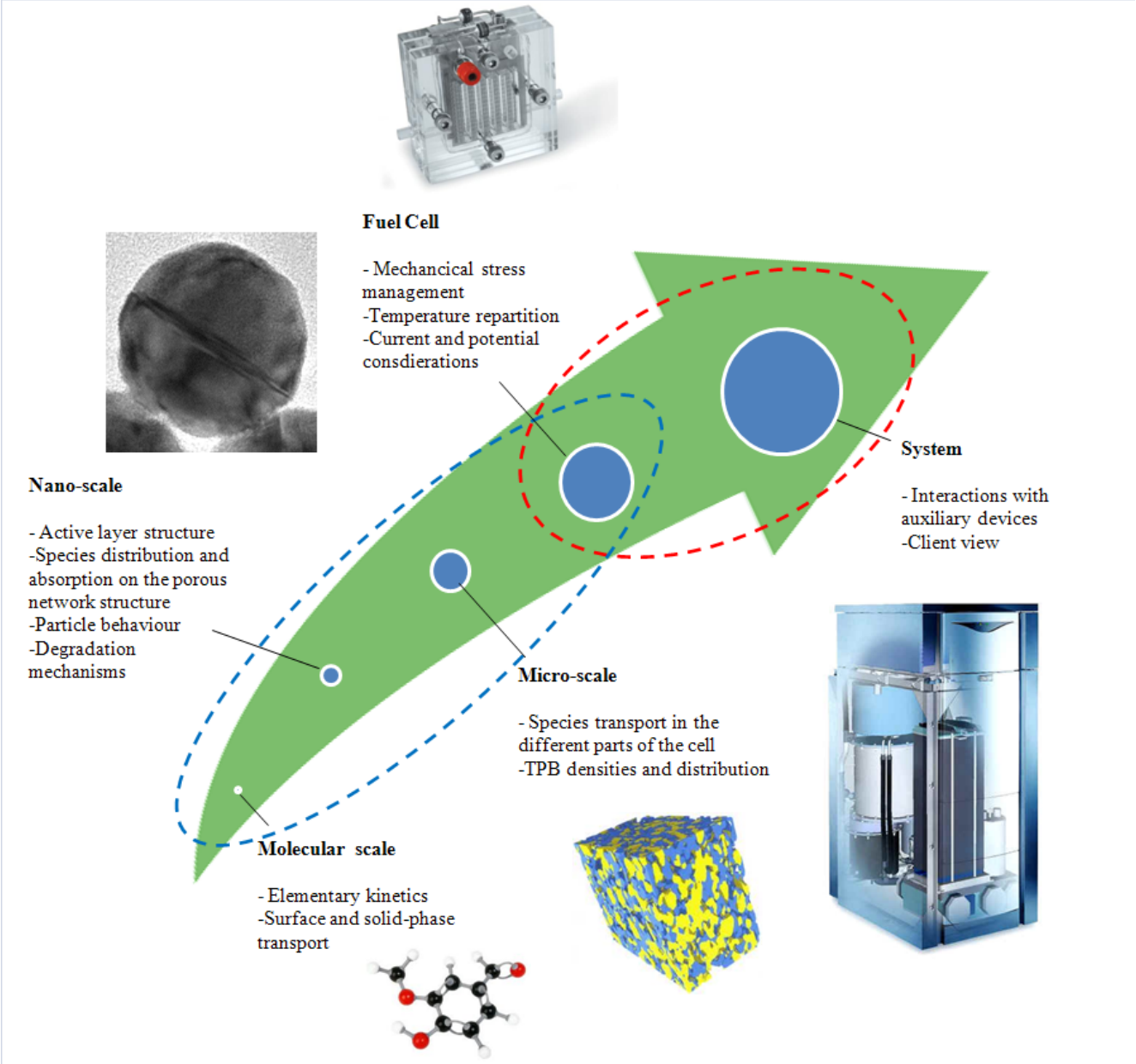


Figure 1.5 – Interaction between the different scales of the fuel cell system

This plethora of hardware and software made available to scientists around the world allows for the correlation between microstructural parameters and performance to be analyzed to an increasingly comprehensive extent. Some analyses however cannot be carried out in-situ, given current technological limitations, such as the real-time geometrical change of electrode microstructures during operation, for example. These types of analyses require the use of

synthetic 3D microstructures, which have been employed in a variety of other fields for similar reasons. Furthermore, the synthesis of a family of synthetic structures for the purpose of investigating the impact of varying a specific parameter characterizing these is generally a non-trivial and expensive task to carry out experimentally.

## 1.8– 3D synthetic microstructures

Researchers have been developing 3D synthetic microstructures in fields outside of the fuel cell industry, such as Faessel et al. who developed a 3D model of random fiber networks by means of experimental information to represent low density wood-based fiberboards and investigate the influence of internal architecture properties on local thermal conductivity (Faessel et al., 2005). Qing and Mishnaevsky presented a method for the automatic generation of 3D micromechanical Finite Element (FE) models of unidirectional long-fiber-reinforced composite (LFRC) to influence the strength distribution of fibers on the mechanical response and strength of the composites (Qing & Mishnaevsky, 2009). They report that three basic modeling approaches for composites can be distinguished; macroscopic modeling, where composites are often modeled as a single orthotropic material, or, at the laminate level, a single fully anisotropic material; mesoscopic modeling, where composites are typically considered as a single transverse isotropic or orthotropic material at the ply or lamina level; microscopic modeling, where the reinforcement material and the matrix are both modeled as deformable continua at the matrix/fiber level.

Although homogeneous models are numerically convenient when it comes to synthetic SOFC microstructure generation, their range of applicability is limited and they require many empirical parameters (Sunde, 2000). Alternative approaches include Monte-Carlo techniques in which the electrodes are initially generated as randomly packed spheres of various particle types, or the use of a fixed lattice structure. The result of this type of Monte Carlo generation is a random network of particles with numerous contact points between the different particle types (Kenney & Karan, 2007). Kenney et al. (Kenney et al., 2009) developed a 3D microstructure generation algorithm in which particles were randomly dropped into a domain of specified dimensions in which they were allowed to roll over other particles until they either came in contact with three other particles or the bottom of the domain. Desired phase volume fractions were enforced by

assigning a weighted probability to the particle selection. The authors also integrated a particle size distribution into their model.

Schneider et al. (Schneider et al., 2007) developed a different algorithm using the discrete element method (DEM). Particles were originally generated so as not to be in contact, and a force, defined as the sum of the contact forces given by a sintering model at the contact scale, was then applied to each particle. The new positions, velocities and accelerations of the particles at each time step were based on elastic interactions and calculated by means of a dynamic scheme in order to reach mechanical equilibrium.

Ali et al. (Ali et al., 2008) relied on the formation of "layers" of particles one upon another, starting with a base layer of ion conducting particles at one end of the electrode. In the algorithm of Golbert et al. (Golbert et al., 2007), particles are generated at randomized positions in the domain considered until two are found to be in contact. At this point every other new particle is generated so as to be in contact with at least two or more other particles, effectively building a particle cluster of increasing size until the specified domain is filled. Sintering is then represented by expanding the particles uniformly, a straight-forward numerical process, also used by Ali et al. in their model.

Suzue et al., presented a modelling scheme based on the stochastic reconstruction technique and the Lattice Boltzman Method (LBM) for the generation of SOFC anodes to assess their performance (Suzuke et al., 2008). The method starts by exploiting a cross-sectional microscopy image to obtain a two-dimensional phase map, and then two-point correlation functions are used to reconstruct a three-dimensional model microstructure. The LBM simulation then enables these authors to obtain the anodic polarization resistance of the reconstructed anode.

Most of these synthetic microstructures are generated with the aim of optimizing the design of SOFC anodes, and investigate the impact of varying operating conditions or microstructural parameters on the performance of the electrodes. One way to enable and facilitate the reactions driving SOFCs investigated by researchers is to facilitate the passage of ions, electrons and gases through the paths connecting the electrode/gas channel and electrode/electrolyte interfaces to the

TPBs. This is equivalent to providing as low a resistance as possible to, or equivalently, high values of the electronic and ionic conductivities and gas diffusivity, in the anode. A particular area of interest is the analysis of microstructural parameters affecting the effective transport properties of SOFC anodes. A challenging aspect of this investigation is that of determining the effective transport properties of entire electrodes for use in system-level models as well as stack performance prediction, amongst others. The mass and charge transfer paths being extremely tortuous and varied by nature renders predicting these effective transport properties non-trivial and time-consuming.

## 1.9– SOFC effective conductivity models

Maxwell was the first to develop an approximate expression for the effective conductivity of a dilute distribution of spheres (Maxwell, 1873). Bruggeman (Bruggeman, 1935) and Landauer (Landauer, 1952) then approximated this conductivity by solving implicit equations for the effective properties. Bruggeman's differential effective-medium estimate was extended by Archie who proposed an empirical law, Archie's power law (Archie, 1942). This equation is, to this day, frequently applied to porous media used in fuel cell applications and is given by:

$$\alpha_i^{eff} = \alpha_i \epsilon_i^n \tag{1.20}$$

where $\epsilon_i^n$ is the volume fraction of a given phase $i$ ($i = el$ for electronic or $i = io$ for ionic), $\alpha_i$ is the characteristic considered - here the conductivity, $\alpha_i^{eff}$ is the effective conductivity and $n$ is a pre-defined exponent, typically between 1.5 and 4 (Choi et al., 2010).

In more recent attempts, percolation theory was used to create models to predict the effective properties of composite electrodes for SOFCs (Schneider et al., 2007; Chen et al., 2009; Bertei & Nicollela 2011; Chen et al., 2004; Cai et al., 2005) such as their effective conductivities. These models rely on the concept of a coordination number, which represents the number of contacts that a certain particle has with neighboring particles, and a percolation probability, which represents the likelihood that particles are clustered in ways that form connected conduction pathways. The model developed by Bouvard and Lange (Bouvard & Lange, 1991), as reported

by Chen (Chen, 2009), has been widely used to estimate coordination numbers for binary systems. Suzuki and Oshima (Suzuki & Oshima, 1983, 1985, 1985) developed a similar model for multi-component mixtures. The draw-back of these types of models is their intrinsic dependence on statistically averaged results. If one wishes to determine the effective conductivity of a specific anode, results predicted by percolation theory may diverge from experimental results due to the heterogeneity of the microstructure within a given electrode.

Nam and Jeon presented a model to determine transport and reaction in intermediate temperature SOFC anode microstructure based on probabilities of percolation (Nam & Jeon, 2006). These authors reported an optimum anodic performance at electronic phase volume fractions lying between 40% and 50%, at sufficiently large electrode thicknesses. Schneider et al. proposed the discretization of their randomly generated microstructure into a mixed resistor network, each branch being assigned a value taken from the literature (Schneider et al., 2006). In their studies, they also reported an optimum electrode performance at 50% volume content of the electronic phase, but a higher electrode electronic conductivity at 60%. Sanyal et al. discretized their randomly generated structure using tetrahedral meshes that fully resolve the interior of the particles and their intersections (Sanyal et al., 2010). Current through the network is predicted by solving the charge-conservation equations, which is then used to compute the effective conductivities of these microstructures. The authors report that the computed conductivities are much lower than those predicted by percolation theory, which is resolved by adjusting the Bruggeman factor used in the percolation theory model from 1.5 to 3.5. Chen et al. and Bertei and Nicolella also use percolation theory to predict the effective conductivities of their microstructures (Chen et al., 2009; Bertei & Nicolella, 2011), and report the prediction of TPB lengths and hydraulic pore radii on top of transport properties.

A different approach was used by Hwang et al. who developed a multi-physics model coupling electrochemical kinetics with fluid dynamics to simulate the transport phenomena in mono-block-layer built (MOLB) SOFCs (Hwang et al., 2005). The conservation of mass, momentum, energy, species and electric charge is used by these authors as the base for the control volume-based finite difference method to carry out their calculations.

Other models treat SOFC composite anodes as resistor networks (Abel et al., 1997) in which solid electrolyte grains, metal particles, and pores are treated in a similar fashion. Sunde employed a similar approach (Sunde, 1995) where Kichoff's law of current conservation for a resistor network resulting from the scattering of predetermined fractions of electrolyte and electrode particles on the sites of a three-dimensional cubic lattice at random. He shows in his studies an abrupt rise in conductivity at a conducting particle volume fraction of 30%, correlated by the findings of Somalu and Brandon in their studies (Somalu & Brandon, 2011).

Jeon et al. (Jeon et al., 2005) have also developed a random resistor network model very similar to that of Sunde (Sunde, 1995) and Schneider et al. (Schneider et al., 2007) where particles are generated as perfect spheres of similar size, and reference Sunde's model to justify the use of a uniform neck size, or contact area between two particles, to determine the individual resistances attributed to each branch of the derived resistor network. A decrease in particle size for example increases the rate of electro-chemical reactions but decreases the rate of mass transport. Other authors who use resistor networks include Mari et al. (Mari et al., 2000). In their paper, the authors convert their structures to pixels, before a cubic grid is superimposed to the structure and the edges of the cube, and converted into discreet electrical circuits (RC parallel) that are reported to describe the electrical behaviours of the studied materials. Edges falling inside a certain grain are assigned either of the corresponding material impedances while those lying between particles are considered the material grain boundary contribution. The impedance of the three-dimensional resistance network is then calculated by minimizing the dissipated power, or by applying a transfer-matrix operation. This technique is based on iterative procedures where elements in the matrix are changed whenever a new electrical circuit is added, and the solving of a linear system finally yields the total impedance of the considered network.

Hussain et al. (Hussain et al., 2006) use a mathematical approach to solve the mass transport by diffusion, based on the assumption that the structure of the porous medium is isotropic, using the mean pore transport model (MPTM). Other authors such as Ni et al. (Ni et al., 2007) and Zhu and Kee (Zhu & Kee, 2008) also use a more mathematical approach to model the charge and mass transport through SOFC anodes, by using principles such as Ohm's law, the Dusty Gas Model, Darcy's law and the generalized Butler-Volmer equation. These authors also come to the

conclusion that a smaller particle size increases the electrochemical activity due to increased TPB lengths, although it impedes the transport of gases.

A different approach used in several papers (Choi et al., 2010; Mu et al., 2007) is to apply finite-element based methods on reconstructed 3D microstructures or synthetic 3D microstructures to which a mesh or computational grid is applied. Different types of grids have been studied such as 3D Cartesian grids, which are used in this thesis, octree grids and body-fitted/cut-cell type meshes amongst others (Choi et al., 2010). The algorithms used to analyze these grids vary, but are based on the same principle of a force driving the charge through a structure: some authors use the Fickian diffusion equation as the basis of their calculations (Choi et al., 2010) while others import their meshed structures into commercial platforms such as ANSYS (Mu et al., 2007), in which the calculations are based on charge-transfer or current conservation. This approach has led to satisfactory results, but the need for a high mesh resolution can result in high computational costs. This is especially pronounced in highly heterogeneous structures where contacts between bulks of particles of the same phase are very small. Furthermore, generating a grid which accurately represents the microstructure of such structures is not a trivial task (Choi et al., 2010).

To overcome this problem of computational cost, various numerical techniques have been used (Choi et al., 2011; Mari et al., 2000; Kishimoto et al., 2012) on 3D microstructures such as random walk calculations based on simulating the Brownian motion of a diffusing particle (Einstein, 1926), and continuum-based techniques which solve the Laplace equations. But these are yet to be validated against experimental data, and are prone to residual errors in the reconstruction process (Suzue et al., 2008; Mu et al., 2007).

Marinesk et al. (Marinesk et al., 2007) on the other hand use the general media approach and the sine-wave approximation to determine the electrical conductivity of composites in a broad range of metal content. These authors report a broad agreement with experimental measurements using this approach, and relatively important scattering between computed and experimentally derived results are attributed to the inaccuracy of the conductivity measurements as well as microstructural defects in the samples used.

The models presented above allow localized investigations to be carried out, and enable a variety of questions to be answered, giving significant insight into the link between the microstructure of SOFC anodes and cell performance. However, the models presented above suffer from various drawbacks, including the need to deal solely with either synthetic or experimental microstructures, or requiring the input of empirical parameters or prohibitive computational power to produce accurate results. A selection of microstructural features that have been examined in the literature are the influence of particle size (Ji et al., 2006; Nam & Jeon, 2006), porosity (Ji et al., 2006; Kenney & Karan, 2007; Golbert et al., 2007), and solid-phase fractions (Ji et al., 2006; Nam & Jeon, 2006; Golbert et al., 2007) on performance. One characteristic difficult to examine is that of particle size ratio, as many of the Monte-Carlo methods assume uniform particle sizes, but models have been recently developed to introduce particle size distributions (Kenney & Karan, 2007; Kenney et al., 2009; Choi et al., 2011).

In a model written by Golbert (Goblert et al., 2007), different particle sizes can be used to form a heterogeneous network of the composite materials. Mass transport and electrochemical reactions over this network can then be modelled. Mass transport presents an added difficulty due to the interstitial pores, but this is overcome by adopting the volume-of-fluid (VOF) method (Abel et al., 1997) which represents exact interface information by discrete volume data. Using this methodology, the heterogeneous network is divided into voxels, which are then aggregated into larger volume-of-fluid units. The characteristics of the microstructure are then captured using the phase volume fractions in a VOF unit, each containing a number of voxels. Free boundaries on which discontinuities exist in one or more variables, for example material interfaces or interfaces between fluid and deformable structures, are tracked and located. The phase fractions in a VOF unit $i$ are represented by $f_{i,\mathrm{pore}}$, $f_{i,io}$, and $f_{\mathrm{i,el}}$, for the pore, ionic and electronic phases, respectively, with their sum equal to 1. The characteristics of a VOF unit $i$, for example its conductivity $\kappa_i$, are assumed to be dependent on the characteristic values in the pure phases (e.g., $K_n^o$, $n$ = pore, io, el) and the phase fractions in that VOF unit:

$$K_i = \sum_n K_n^o f_{i,n}. \tag{1.21}$$

The transport phenomena are modeled for each phase separately and linked to the percolated TPB, where charge transfer occurs. Fickian diffusion is assumed for the transport of species in the microstructure. The VOF method is used to solve gas transport, oxygen ion transport, and electron transport in the three phases. In this model, charge-transfer is assumed to be the rate determining electrode process, and thus the Butler-Volmer equation is used to model electrochemical reactions. Details of the system equations, boundary conditions and input parameters are presented in the following section.

## 1.10 - The SOFC anode model and Volume-Of-Fluid approach (VOF)

In the model written by Golbert et al. (Golbert et al., 2007), particles can be generated synthetically by using a Monte-Carlo random packing process, followed by a sintering process represented by uniformly expanding the particles by a factor typically in the range of 1.2, making sure material properties remain consistent with the expansion. In the case of real microstructural data obtained through tomographic image capturing and enhancing techniques, the measured microstructure is used instead of the randomly packed system of spheres. The figure below illustrates the physical difference between a real and synthetic SOFC anode microstructure generated this way.

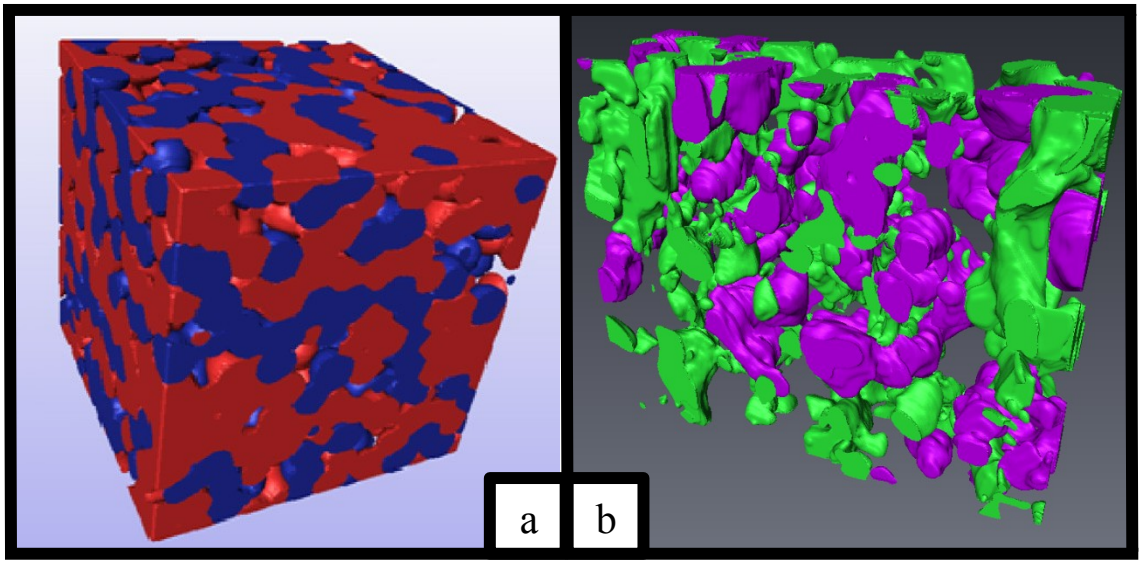


Figure 1.6 – Graphical representation of (a) a synthetic microstructure, and (b) a real Ni/YSZ microstructure with 20% Nickel. The red and blue phase represent respectively nickel and YSZ, and both structures are 5x5x5 μm in size.

The first step following the generation/importation of the desired type of microstructure (Figure 1.6) by Cai et al and Golbert et al. (Cai et al., 2011; Golbert et al., 2007) is the structure discretization into small cubic elements called voxels subsequently aggregated into Volume Elements (VEs) as shown in Figure 1.7.

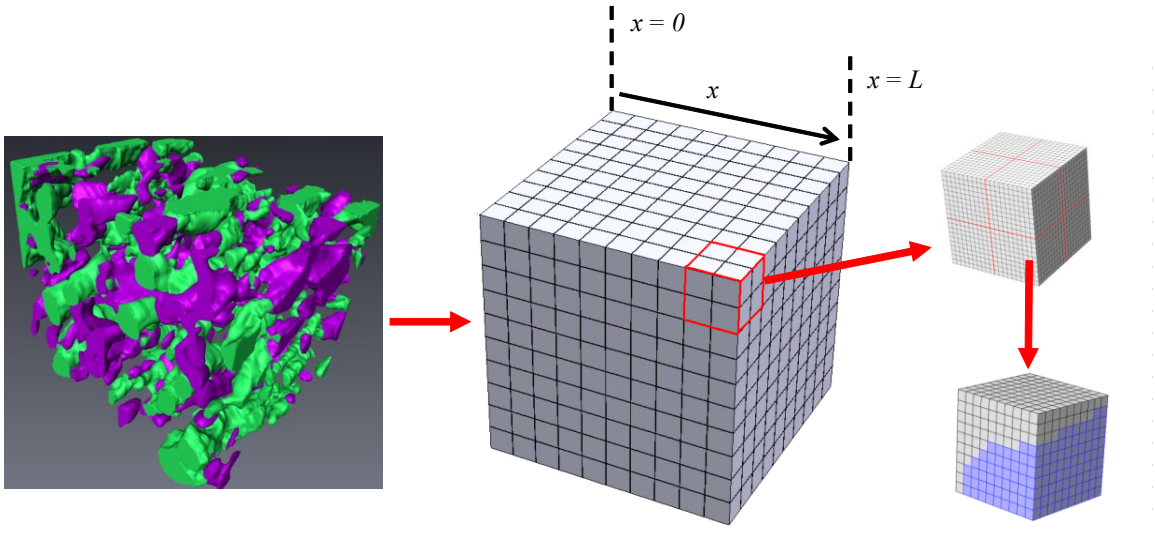


Figure 1.7 – Graphical representation of the discretization and aggregation process on a 20% Nickel SOFC anode microstructure sample.

The VE structure generation is initialized by dividing the system of voxels into cells of equal size. Phase fractions are then determined based on the position of the different spheres/material in relation to the position of the cells. Each cell is then given a TPB length density value following a percolation analysis of the entire voxelized structure using an in-house percolation algorithm (Shearing, 2009) based on the discretized structure and species masks to identify connected paths and percolation networks. This is discussed in detail in the work of Shearing (Shearing, 2009).

Once the percolated TPB paths have been isolated, the TPB density is calculated as the number of connected edges multiplied by the pixel length and divided by the voxel volume. In order to overcome the over-estimation that would arise from simply taking the voxels lengths as the actual TPB lengths, and the under-estimation that would arise from just approximating all the TPB lengths as straight lines, all the voxels neighbouring a TPB edge are counted and divided by four. Since some voxels appear for more than one edge but are only counted once, the calculated TPB length is reduced and the edges are smoothed out, giving a more realistic TPB length value (Golbert et al., 2007).

The transport phenomena are modelled in this framework for each phase separately and linked to the TPB where charge transfer occurs. Applying the VOF methodology, the considered heterogeneous network is modelled using the phase fractions in a voxel $i$, $f_{i,\,pore}$, $f_{i,\,io}$, and $f_{i,\,el}$ respectively representing the pore, ionic and electronic phase volume fractions in a VE $i$. The characteristics of a VE such as phase conductivities σ are assumed to be dependent on the characteristic's pure phase value as given in Equation 1.21. As each material can have a different conductivity for each species, systems with mixed conductivities are supported (for example intermediate-temperature SOFCs made with CGO). However, the conductivity of a VE is only dependent on the volume fraction of conductive material contained within the VE. This means that the heterogeneity of each VE is not taken into account in the charge transfer process. The first assumptions made are those of steady state and ideal gases in the pores, considering only the diffusion of $H_2$ and $H_2O$, the ionic and electronic potentials of the SOFC anode are modelled as:

$$\nabla(\sigma_{io}\nabla V_{io}) = -\rho_{TPB} j \tag{1.22}$$

$$\nabla(\sigma_{el}\nabla V_{el}) = 2\rho_{TPB}j \tag{1.23}$$

$$\nabla\left(\frac{D_{\mathrm{H_2O}}}{RT}\nabla P_{\mathrm{H_2O})}\right) = \frac{\rho_{TPB}j}{2F} \tag{1.24}$$

$$\nabla\left(\frac{D_{\mathrm{H_2}}}{RT}\nabla P_{\mathrm{H_2})}\right) = -\frac{\rho_{TPB}j}{2F} \tag{1.25}$$

where $\rho_{TPB}$ is the local TPB density in μm/μm$^3$, $j$ is the charge transfer current per TPB length, $D_{\mathrm{H2O}}$ and $D_{\mathrm{H2}}$ are the diffusion coefficients of $H_2O$ and $H_2$ respectively. In these equations, the constants are *R, T, F,* $V_{io}$ and $V_{el}$. Equations 1.22 and 1.23, where the electronic and ionic conductivities are taken into account by the model, show a direct relationship between the current produced by the anode and the phase conductivities. Coupled with the other equations defining the VOF model, a change of conductivity of either phase is predicted to directly affect the current density output under a certain threshold. Above this threshold, an increase of effective conductivity is not expected to have any effect on predicted current density, the rate limiting process would be the reaction rate.

It is assumed in this work that the current collector/electrode interface is at $x = 0$ (Figure 1.7) and the electrolyte/electrode interface which is electron insulating and impermeable to gas is as $x = L$ (Figure 1.7). In other words,

$$@x = 0 \qquad \frac{\partial V_{io}}{\partial x} = 0$$
$$V_{el} = V_{el}^0$$
$$P_{H_2O} = P_{H_2O,\infty}$$
$$P_{H_2} = P_{H_2,\infty}$$
$$@x = L \qquad V_{io} = 0$$
$$\frac{\partial V_{el}}{\partial x} = 0$$
$$\frac{\partial P_{H2O}}{\partial x} = 0$$

$$\frac{\partial P_H}{\partial x} = 0 \tag{1.26}$$

where $V_{io}$ is the ionic potential and $V_{el}$ the electronic potential. In this model all of the boundaries are assumed to be insulating. The current density is defined by the Butler-Volmer equation (Golbert et al., 2008) as

$$j = j_0 \left( e^{\left(\frac{2\beta F}{RT}\zeta\right)} - e^{\left(-\frac{2(1-\beta)F}{RT}\zeta\right)} \right) \tag{1.27}$$

where $\beta$ is assumed to be 0.5 and the overpotential $\zeta$ is defined as

$$\zeta = V_{eq} - (V_{io} - V_{el}) = V_{oe} + \frac{RT}{2F} \ln \left( \frac{P_{H_2} P_{H_2O,ref}}{P_{H_2O} P_{H_2,ref}} \right) - (V_{io} - V_{el}) \tag{1.28}$$

where the subscript *ref* refers to the virtual reference electrode and is defined as 1 atm of oxygen and 1 atm of hydroden and water. The standard potential, determined as a function of the Gibbs free energy change involved in the reaction is $V_{oc}$. $V_{eq}$ is the anodic equilibrium potential defined as

$$V_{eq} = V_{oe} - \frac{RT}{nF} ln \left( \frac{P_{H_2O}}{P_{H_2}} \right) \tag{1.29}$$

and $V_{oe}$ is the standard potential, determined as a function of the Gibbs free energy change involved in the reaction, taking the partial pressures of $H_2$, $H_2O$ and $O_2$ to be at standard pressure.

Substituting 1.13 into 1.12 yields a definition of the current density as a function of the state variables given as

$$j = j_0 \left( e^{\left(\frac{F}{RT}(V_{oe} - V_{io} + V_{el})\right)} \sqrt{\frac{P_{H_2}}{P_{H_2O}}} - e^{\left(-\frac{F}{RT}(V_{oe} - V_{io} + V_{el})\right)} \sqrt{\frac{P_{H_2O}}{P_{H_2}}} \right) \tag{1.30}$$

The overall system of equations is solved through the development of mass/charge balances for each VE surrounding the discretization points, equally distributed through the system. The discretization points are defined as being in the centroid of each VE as shown in the following figure. Furthermore, non-boundary VEs have a volume of $\delta^3$, VEs at the boundary faces have a volume of $\delta^3/2$, edge VEs have a volume of $\delta^3/4$ and VEs at the corners have a volume of $\delta^3/8$.

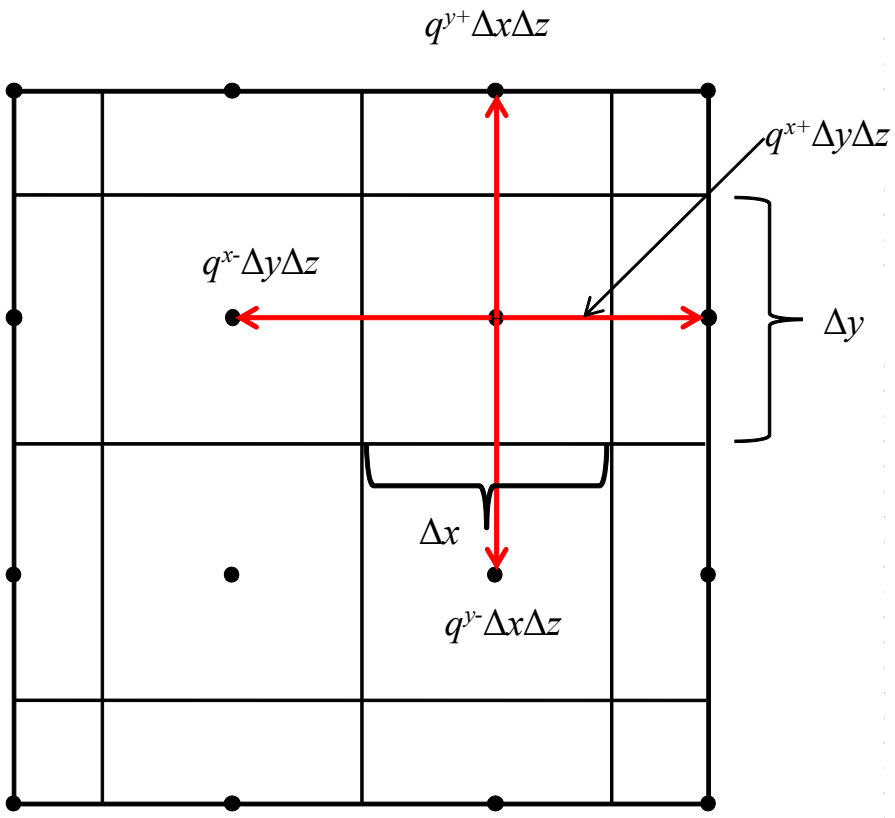


Figure 1.8 – Two-dimensional representation of the VE distribution used in the simulations. The red arrows show the fluxes between adjacent VEs.

This system of equations is solved by developing mass/charge balances for each voxel surrounding the discretization points, distributed equally through the system. Assuming steady state, the balance on a voxel centered on continuous point ($x,y,z$), equivalent to the discretet point ($i,j,k$) is given by

$$q_{i,j,k}^{x-}\Delta y\Delta z - q_{i,j,k}^{x+}\Delta y\Delta z + q_{i,j,k}^{y-}\Delta x\Delta z - q_{i,j,k}^{y+}\Delta x\Delta z + q_{i,j,k}^{z-}\Delta x\Delta y - q_{i,j,k}^{z+}\Delta x\Delta y = vj\Delta x\Delta y\Delta z \quad (1.31)$$

where $v$ is the stoichiometric coefficient in terms of current density $j$ and $q^{l-,+}{}_{i,j,k}$ is the flux across the VE face perpendicular to the $l$ axis ($l = \{x,y,z\}$). In the case where the VEs are cubic, the above equation becomes

$$\frac{q_{i,j,k}^{x-}}{\delta} - \frac{q_{i,j,k}^{x+}}{\delta} + \frac{q_{i,j,k}^{y-}}{\delta} - \frac{q_{i,j,k}^{y+}}{\delta} + \frac{q_{i,j,k}^{z-}}{\delta} - \frac{q_{i,j,k}^{z+}}{\delta} = vj \quad (1.32)$$

Due to the fact that diffusivities are not identical in adjacent VEs, care must be taken with regards to the flux out of a VE being the same as that entering an adjacent VE. In the case of two adjacent VEs ($i,j,k$) and ($i,j-1,k$) the flux across the shared interface of these VEs is given as function of the diffusivities specific to each VE by

$$q_{i,j,k}^{x-} = \frac{\sqrt{D_{i,j-1,k}D_{i,j,k}}}{RT}\frac{P_{i,j-1,k} - P_{i,j,k}}{\Delta x} \quad (1.33)$$

The use of a geometric average instead of an algebraic average prevents diffusion through a material interface as the solid diffusivity is zero, i.e. if instead of calculating the average diffusivity as $\sqrt{D_{i,j-1,k}D_{i,j,k}}$ we could calculate it as $\frac{D_{i,j-1,k}+D_{i,j,k}}{2}$, if one diffusion coefficient is 0 species could still diffuse across the interface as the average D would not be 0. By defining the flux at the x boundary ($x = 0$ at $j = 1$) the Dirichlet conditions are satisfied:

$$q_{i,1,k}^{x-} = \frac{D_\infty}{RT}(P_\infty - P_{i,1,k}) \quad (1.34)$$

Combining the above equation with the steady-state mass and charge transfer equation yields

$$\frac{2D_{\infty}}{RT\delta}\left(P_{\infty}-P_{i,1,k}\right)-2\frac{q_{i,j,1}^{x+}}{\delta}+\frac{q_{i,j,1}^{y-}}{\delta}-\frac{q_{i,j,1}^{y+}}{\delta}+\frac{q_{i,j,1}^{z-}}{\delta}-\frac{q_{i,j,1}^{z+}}{\delta}=vj \tag{1.35}$$

In the simulations of Golbert et al. (Golbert et al., 2008), $D_{\infty}$ is set to $10^5$. Using this definition instead of a hard constraint on $P_{i,1,k}$ avoids conflicts in VEs with two boundary conditions as the insulation, flux etc. constraints apply to the different sides of the VE separately. Insulation can therefore be applied to more than one side without problem.

The VOF approach however assumes that charge transfer is the limiting process, and that the behaviour of the current-voltage response of the cell according to the low-field Tafel approximation (Schneider et al., 2007) follows a straight line at low over-potentials. The gradient of the assumed straight line defines the charge-transfer resistance. Using an iterative approach, the electrochemical simulation can be used to match the low-overpotential gradient with experimentally derived charge transfer resistances. The model considers only electron transfer, and does not yet account for additional contributing processes such as absorption and surface diffusion. The approximation of electronic conductivity as currently used by Golbert et al. in the VOF model (Golbert et al., 2007) does not take into account the extremely heterogeneous and anisotropic nature of SOFC anode microstructures, yielding erroneous conductivities in instances where more than one phase occupies a VE.

Developing an accurate effective conductivity model is therefore understood to be technically important for the application of the VOF model, and can be validated with precise measurements made on real SOFC anode cermets.

## 1.11 – Conclusions

In this chapter, the motivation behind the push towards renewable energy sources is initially laid out, followed by an introduction to fuel cells. A brief history of these devices is presented, as well as a comparison of fuel cell technologies. The fundamentals of SOFCs are laid out, followed by an explanation of the basic operation of SOFCs and the electrochemical principles governing their performance. The requirements and properties of each SOFC component are

introduced, before the emphasis is put on the anode, the fuel electrode of the cell. Common materials used for the fabrication of the anode are presented, followed by an identification of the challenges researchers and industries meet in fabricating these SOFC anodes. The link between electrode microstructure and cell performance is analyzed and explained, before a literature review on percolation theory is presented. This review lays out the foundation for the motivation behind creating multi-scale models for fuel cells, after which a review on past and current 3D synthetic microstructure generations is presented. Most, if not all, research efforts in the domain of SOFC anodes are conducted with the aim of designing high-performing anodes. The culmination of the preceding sections is a review of current SOFC anode effective conductivity models. The tone is set for the need to develop an effective electronic conductivity model capable of analyzing real and synthetic structures that is computationally efficient and adaptable. In order to investigate the impact of the effective conductivity of SOFC anodes on overall cell performance, and validate the Volume-Of-Fluid approach employed by Cai et al. and Golbert et al. (Qiong et al., 2010; Golbert et al., 2007), and further validate the results obtained by Somalu et al. (Somalu et al., 2011) in their experimental determination of the effective conductivity of samples of anodes with increasing volume fraction contents of nickel, this VOF approach is explained. An effective conductivity model is presented in the next chapter, designed to meet the requirements laid out above and to be compatible with the electrochemical model developed by Golbert et al. (Golbert et al., 2007).

## 1.12 – References

Abel, T., Anninos, P., Zhang, Y., Norman & M. L. (1997) Modeling primordial gas in numerical cosmology. *New Astronomy* 2(3), 181-207.

Al-Raoush, R. & Alsaleh, M. (2007) Simulation of random packing of polydisperse particles. *Powder Technology* 176 (1), 47–55.

American History, 2004, *Fuel cells, origins*. [Online]. Available from: http://americanhistory.si.edu/fuelcells/so/sofcmain.htm [Accessed 01/07/2013]

Archie, G. E. (1942) The electrical resistivity log as an aid in determining some reservoir characteristics. *Transactions IME*, 146(1), 54-62.

Arnošt, D. & Schneider, P. (1995) Dynamic transport of multicomponent mixtures of gases in porous solids. *The Chemical Engineering Journal and the Biochemical Engineering Journal* 57(2), 91–99.

Atkinson, A., Barnett, S., Gorte, R. J., Irvine, J. T. S., McEvoy A. J., Mogensen, M., Singhal, S. C. & Vohs, J. (2004) Advanced anodes for high-temperature fuel cells. *Nature Materials* 3, 17-27.

Balachandran, U. & Eror, N. G. (1981) Electrical conductivity in strontium titanate. *Journal of Solid State Chemistry* 39(3), 351-369.

Bard, A., J. & Faulkner, L., R. (2001) *Electrochemical methods*, Phoenix, John Wiley & Sons Inc., 2nd Edition.

Bastidas, D. M., Tao, S. W. & Irvine, J. T. S. (2006) A symmetrical solid oxide fuel cell demonstrating redox stable perovskite electrodes. *Journal of Materials Chemistry* 16(1), 1603-1605.

Baur E & Preis H. Z. (1937) About Fuel Cell Chains with Fixed Ladders. *Elektrochem* 43(1), 727–32.

Bernuy-Lopez, C., Allix, M., Bridges, C. A., Claridge, J. B. & Rosseinsky, M. J. (2007) $Sr_2MgMoO_{6-\delta}$: Structure phase stability and cation site order control of reduction. *Chemical Materials* 19(1), 1035-1043.

Bertei, A. & Nicolella, C. (2011) Percolation theory in SOFC composite electrodes: Effects of porosity and particle size distribution on effective properties. *Journal of Power Sources* 196(22), 9429-9436.

Bessler, W. G., Gewies, S., Willich, C., Schiller, G. & Friedrich, K. A. (2010) Spatial distribution of electrochemical performance in a segmented SOFC: a combined modeling and experimental study. *Fuel Cells*, 10 (1), 411–418.

Bouvard, D. & Lange, F. F. (1991) Relation between percolation and particle coordination in binary powder mixtures. *Acta Metallurgica et Materialia* 39 (12), 3083–3090.

Bruggeman, D. A. G. (1945) Calculation of the various physical constat of heterogeneous substances. I. Delectric constants and conudctivities of mixtures of isotropic substances. *Annalen der Phsik* 24(1), 636-664.

Cai, Q., Adjiman, C. S. & Brandon, N. P. (2010) Investigation of the active thickness of solid oxide fuel cell electrodes using a 3D microstructure model. *Electrochemica Acta* 56(28), 10809-10819.

Cai, Q., Adjiman, C. S. & Brandon, N. P. (2011). Modelling the 3D microstructure and performance of solid oxide fuel cell electrodes: Computational parameters. *Electrochimica Acta* 56(16), 5804-5814.

Cai, W. Z., Tu, S. T. & Gong, J. M. (2005) A Physically Based Percolation Model of the Effective Electrical Conductivity of Particle Filled Composites. *Journal of Composite Materials* 40(23), 2131-2149.

Cairns, E. J. & Leibhafsky, H. A. (1969) *Fuel Cells and Fuel Batteries*. New-York, John Wiley & Sons.

Cassidy, M., Lindsay, G. & Kendall, K. (1996) The reduction of nickel/zirconia cermet anodes and the effects on supported thin electrolytes. *Journal of Power Sources* 61(2), 189-192.

Chan. S. H., Chen, X. J. & Khor, K. A. (2004) Cathode Micromodel of Solid Oxide Fuel Cell. *Journal of the Electrochemical Society*, 151(1), A164-A172.

Chen, X. J., Liu, A. L., Khor, K. A. & Chan, S. H. (2007) High-performance $(La,Sr)(Cr,Mn)O_3/(Gd,Ce)O_{2-\delta}$ composite anode for direct oxidation of methane. *Journal of Power Sources* 165(1), 34-40.

Chen, D., Lin, Z., Zhu, H. & Kee, R. J. (2009) Percolation theory to predict effective properties of solid oxide fuel-cell composite electrodes. *Journal of Power Sources* 191(2), 240–252.

Chen, M., Kim, B. H., Xu, Q., Nam, O. J. & Ko, J. H. (2008) Synthesis and performances of Ni–SDC cermets for IT-SOFC anode. *Journal of the European Ceramic Society* 28(15), 2947-2952.

Choi, H. W., Berson, A., Pharoah, J.G. & Beale, S.B. (2011) Effective transport properties of the porous electrodes in solid oxide fuel cells. *Journal of Power and Energy* 225(A2), 183-197.

Costamagna, P., Costa, P. & Antonucci, V. (1998) Micro-modelling of solid oxide fuel cell electrodes. *Electrochemica Acta* 43 (4), 375–394.

Cowin, P. I., Petit, C. T. G., Lan, R., Irvine, J. T. S. & Tao, S. (2011) Recent Progress in the Development of Anode Materials for Solid Oxide Fuel Cells. *Advanced Energy Materials* 1(3), 314-332.

Danilovic, N., Vincent, A., Luo, J. L., Chuang, K. T., Hui, R. & Sanger, A. R. (2009) Correlation of Fuel Cell Anode Electrocatalytic and ex situ Catalytic Activity of Perovskites $La_{0.75}Sr_{0.25}Cr_{0.5}X_{0.5}O_{3-\delta}$ (X= Ti, Mn, Fe, Co). *Chemical Materials*, 22(3), 957-965.

Deng, X. & Petric, A. (2004) Geometrical modeling of the triple-phase-boundary in solid oxide fuel cells. *Journal of Power Sources*, 140(2), 297-303.

Deseure, J., Bultel, Y., Dessemond, L. & Siebert, E. (2005) Theoretical optimization of a SOFC composite cathode. *Electrochemica Acta*, 50(10), 2037-2046.

Deseure, J., Bultel, Y., Schneider, L. C. R., Dessemond, L. & Martin, C. (2007) Micromodeling of Functionally Graded SOFC Cathodes. *Journal of the Electrochemical Society*, 154(10), B1012-B1016.

Dodds, J. A. (1980) The porosity and contact points in multicomponent random sphere packings calculated by a simple statistical geometric model. *Journal of Colloid Interface Science* 77 (2), 317–327.

Einstein, A. (1926) *Investigations on the theory of the brownian movement*. United States of America, Methuen Co.

Erdey-Gruz, T. & Volmer, M. (1931) *Zeitschrift fur Physikalische Chemie*, A157 (165).

Faessel, M., Delisée, c., Bos, F. & Castéra, P. (2005) 3D Modelling of random cellulosic fibrous networks based on X-ray tomography and image analysis. *Composites Science and Technology* 65(13), 1931–1940.

Faes, A., Nakajo, A., Hessler-Wyser, A., Dubois, D., Brisse, A., Modena, S. & Van Herle, J. (2009) RedOx study of anode-supported solid oxide fuel cell. *Journal of Power Sources* 193(1), 55-64.

Fisher, J. C. & Chuang, S. S. C. (2009) Investigating the $CH_4$ reaction pathway on a novel LSCF anode catalyst in the SOFC. *Catalysis Communications* 10(6), 772-776.

Ho., T. X., Kosinski, P., Hoffmann, A. C. & Vik, A. (2009) Modeling of transport, chemical and electrochemical phenomena in a cathode-supported SOFC. *Chemical Engineering Science* 64(12), 3000–3009.

Holtappels, P., Poulsen, F. W. & Mogensen, M. (2000) Electrical conductivities and chemical stabilities of mixed conducting pyrochlores for SOFC applications. *Solid State Ionics* 135(4), 675-679.

Hoogers, G. (2002) *Fuel cell technology handbook*, CRC Press, Florida.

Henke, M., Willich, C., Westner, C., Leucht, F., Kallo, J., Bessler, W., G. & Friedrich, K., A. (2013) A validated multi-scale model of a SOFC stack at elevated pressure. *Fuel Cells* 13(5), 773-780.

Henne, R. (2007) Solid oxide fuel cells: a challenge for plasma deposition processes. *Journal of Thermal Spray Technology* 16(3), 381-403.

Huang, T-J., Chou, C. L., Chen, W. J. & Huang, M. C. (2009) Coal syngas reactivity over Ni-added LSCF–GDC anode of solid oxide fuel cells. *Electrochemical Communications* 11(2) , 294-197.

Huang, Y. H., Xing, Z. L. & Goodenough, J. B. (2006) Double Perovskites as Anode Materials for Solid-Oxide Fuel Cells. *Science* 312, 254-257.

Hussain, M., M., Li, X. & Dincer, I. (2007) Mathematical modeling of transport phenomena in porous SOFC anodes. *International Journal of Thermal Sciences*, 46(1), 48–56.

Hwang, J. J., Chen, C. K. & Lai, D. Y. (2005) Detailed characteristic comparison between panar and MOLB-type SOFCs. *Journal of Power Sources*, 143(2), 75-83.

Ikeda, J., Nakano, S. & Nakashima, T. Y. (2000) Three-dimensional study on the interconnection and shape of crystals in a graphic granite by X-ray CT and image analysis. *Mineralogica Magazine* 64(5), 945-959.

Isolevich, A., Kornyshev, A. A. & Lehnert, W. (1999) Statistical geometry of reaction space in porous cermet anodes based on ion-conducting electrolytes: Patterns of degradation. *Solid State Ionics*, 124 (3), 221-237.

Iwata, T. (1996) Characterization of Ni-YSZ Anode Degradation for Substrate-Type Solid Oxide Fuel Cells. *Journal of the Electrochemical Soc*iety 143(5), 1521-1525.

Janardhana, V. M., Heuveline, V. & Deutschmann, O. (2008) Three-phase boundary length in solid-oxide fuel cells: A mathematical model. *Journal of Power Sources*, 178(1), 368-372.

Jeon, D. H.,Nam, J. H. & Kim, C-J. (2005) A random resistor network analysis on anodic performance enhancement of solid oxide fuel cells by penetrating electrolyte structures. *Journal of Power Sources* 139(2), 21-29.

Ji, Y., Yuan, K., Chung & J. N. (2006) Monte-Carlo simulation and performance optimization for the cathode microstructure in a solid oxide fuel cell. *Journal of Power Sources*, 165(2), 774-785.

Jørgensen, M. J., Primdahl, S., Bagger, C. & Mogensen, M. (2001) Effect of sintering temperature on microstructure and performance of LSM-YSZ composite cathodes. *Solid States Ionics*, 139(1) , 1-11.

Juhl, M., Primdahl, S., Manon, C. & Mogensen, M. (1996) Performance/structure correlation for composite SOFC cathodes. *Journal of Power Sources*, 61(1), 173-181.

Golbert, J., Adjiman, C. S. & Brandon, N. P. (2008) Microstructural modeling of SOFC anodes. *Ind Eng Chem Res* 47(1), 7693-7699.

Kenney, B. & Karan, K. (2007) Engineering of microstructure and design of a planar porous composite SOFC cathode: a numerical analysis. *Solid State Ionics*, 178 (4), 297–306.

Kenney, B., Valdmanis, M., Baker, C., Pharoah, J. G. & Karan, K. (2009) Computation of TPB length, surface area and pore size from numerical reconstruction of composite solid oxide fuel cell electrodes. *Jounral of Power Sources*, 189(2), 1051-1059.

Kim, G., Gross, M. D., Wang, W., Vohs, J. M. & Gorte R. J. (2008) SOFC Anodes Based on LST–YSZ Composites and on $Y_{0.04}Ce_{0.48}ZrM_{0.48}O_2$. *Journal of the Electrochemical Society* 155(4), B360-B366.

Kim, G., Lee, S., Shin, J. Y., Corre, G., Irvine, J. T. S.,Vohs, J. M. & Gorte, R. G. (2009) Investigation of the Structural and Catalytic Requirements for High-Performance SOFC Anodes Formed by Infiltration of LSCM. *Electrochemical Solid-State Letters* 12(3), B48-B52.

Kim, S. D., Moon, H., Hyun, S. H., Moon, J., Kim, J. & Lee, H. W. (2006) Performance and durability of Ni-coated YSZ anodes for intermediate temperature solid oxide fuel cells. *Solid State Ionics* 177(10), 931-936.

Knibbe, R., Ebbesen, S. D. & Mogensen, M. (2010) Origin of Polarization Losses in Solid Oxide Electrolysis Cells under High Current Density. *ECS Transactions* 28(26), 77-87.

Kobsiriphat, W., Madsen, B. D., Marks, L. D., Wang, Y. & Barnett, S. A. (2007) SOFC Anode Performance Enhancement through Precipitation of Nanoscale Catalysts. *10th International Symposium on Solid Oxide Fuel Cells, ECS Proceedings Series*, PV2007-7, 1339-1348, Pennington, NJ.

Kobsiriphat, W., Madsen, B. D., Wang, Y., Marks, L. D. & Barnett, S. A. (2009) $La_{0.8}Sr_{0.2}Cr_{1-x}Ru_xO_3$-$Gd_{0.1}Ce_{0.9}O_{1.95}$ Solid Oxide Fuel Cell Anodes: Ru Precipitation And Electrochemical Performance. *Solid State Ionics* 180(1), 252-257.

Kobsiriphat, W., Madsen, B. D., Wang, Y., Shah, M., Marks, L. D. & Barnett, S. A. (2010) Nickel- and Ruthenium-Doped Lanthanum Chromite Anodes: Effects of Nanoscale Metal Precipitation on Solid Oxide Fuel Cell Performance. *J. Electrochem. Soc.* 157(2), B279-B284.

Kolodiazhnyi, T. & Petric, A. (2005) The applicability of Sr-deficient m-type $SrTiO_3$ for SOFC anodes. *Journal of Electroceramics* 15(1), 5-11.

Kumar, G., V. & Priya, B., V. (2012) Power-management strategies for a grid-connected PV-FC hybrid system. *International Journal of Engineering Research & Technology* 1(8).

Landauer, R. (1952) The electrical resistance of binary metallic mixtures. *Journal of Applied Physics* 23(7), 779-784.

Laurencin, J., Delette, G., Morel, B., Lefebvre-Joud, F. & Dupeux, M. (2009) Solid Oxide Fuel Cells damage mechanisms due to Ni-YSZ re-oxidation: Case of the Anode Supported Cell. *Journal of Power Sources* 192(2), 344-352.

Lee, A. L., Zabransky, R. F. & Huber, W. J. (1990) Internal reforming development for solid oxide fuel cells. *Industrial and Engineering Chemical Research* 29 (5), 766-773.

Lee, S., Kim, G., Vohs, J. M. & Gorte, R. J. (2008) SOFC Anodes Based on Infiltration of $La_{0.3}Sr_{0.7}TiO$. *Electrochemical Society* 155(11), B1179-B1183.

Li, D. S., Saheli, G., Khaleel, M. & Garmestani, H. (2006) Quantitative perdiction of efective conductivity in anisotropic heterogeneous media using two-point correlation functions. *Computational Materials Science*, 38(1), 45-50.

Li, X., Zhao, H., Gao, F., Chen, F. & Xu, N. (2008) La and Sc co-doped $SrTiO_3$ as novel anode materials for solid oxide fuel cells. *Electrochemical Communications* 10(10), 1567-1570.

Li, X., Zhao, H., Shen, W., Gao, F., Huang, X., Li, Y. & Zhu, Z. (2007 )Synthesis and properties of Y-doped $SrTiO_3$ as an anode material for SOFCs. *Journal of Power Sources* 166(1), 47-52.

Li, X., Zhao, H., Xu, N., Zhou, X., Zhang, C. & Chen, N. (2009) Electrical conduction behavior of La, Co co-doped $SrTiO_3$ perovskite as anode material for solid oxide fuel cells. *International Journal of Hydrogen Energy* 34(15), 6407-6414.

Liu, J. & Regenauer-Lieb, K. (2011) Application of percolation theory to microtomography of structured media: Percolation threshold, critical exponents, and upscaling. *Physical Review E - Statistical, Nonlinear, and Soft Matter Physics* 83, 1-13.

Lu, X. C. & Zhu, J. H. (2007) Cu(Pd)-impregnated $La_{0.75}Sr_{0.25}Cr_{0.5}Mn_{0.5}O_{3-\delta}$ anodes for direct utilization of methane in SOFC. *Solid State Ionics* 178(25), 1467-1475.

Mari, C., M. & Dotelli, G. (2000) A random resistor model to forecast the electrical properties of crystalline ionic conductor composites. *Solid State Ionics* 136(1), 1315-1319.

Marina, O. A., Canfi eld, N. L. & Stevenson, J. W. (2002) Thermal, Electrical, and Electrocatalytical Properties of Lanthanum-Doped Strontium Titanate. *Solid State Ionics* 149(2), 21-28.

Marinesk , M., Pejonik, S. & Macek, J. (2007) Modeling of electrical properties of Ni-YSZ composites. *Journal of the European ceramic society* 27(3), 959-964.

Marrero-López, D., Peña-Martínez, J., Ruiz-Morales, J. C., Pérez-Coll, D., Martín-Sedeño, M. C. & Núñez, P. (2007) Applicability of $La_2Mo_{2-y}W_yO_9$ materials as solid electrolyte for SOFCs. *Solid State Ionics* 178(24), 1366-1378.

Martinez, A. S. & Brouwer, J. (2008) Percolation modeling investigation of TPB formation in a solid oxide fuel cell electrode–electrolyte interface. *Electrochimica Acta* 53(1), 3597–3609.

Maxwell, J. C, 1873, *Treatise of electricity and magnetism*. California, Oxford : Clarendon Press 1.

Mench, M. M. (2008) *Fuel cell engines*, John Wiley & Sons Inc.. New-Jersey.

Miller, D. N. & Irvine, J. T. S. (2010) B-site doping of lanthanum strontium titanate for solid oxide fuel cell anodes. *Journal of Power Sources* 196(17), 7323-7327.

Mu, D., Liu, Z. S.,Huang, C. & Djilali, N. (2007) Prediction of the effective diffusion coefficient in random porous media using the finite element method. *Journal of Porous Materials* 14(1), 49-54.

Nakashima, Y. & Kamiya, S. (2007) Mathematical Programs for the Analysis of Three-Dimensional Pore Connectivity and Anisotropic Tortuosity of Porous Rocks using X-ray Computed Tomography Image Data. *Journal of Nuclear Science Technolo*gy 44, 1233-1247.

Nam, J. H. & Jeon, D. H. (2006) A comprehensive micro-scale model for transport and reaction in intermediate temperature solid oxide fuel cells. *Electrochimica Acta* 51(1), 3446–3460.

Navarre-Sitchler, A., Steefel, C. I ., Yang, L., Tomutsa, L. & Brantley, S. L. (2009) Evolution of porosity and diffusivity associated with chemical weathering of a basalt clast. *Journal of Geophysical Research* 114(F2), F02016.

Ni, M., Leung & M. K. H., Leung, D. Y. C. (2007) Mathematical modeling of the coupled transport and electrochemical reactions in solid oxide steam electrolyzer for hydrogen production. *Electrochimica Acta* 52(24), 6707–6718.

Porat, O., Heremans, C. & Tuller, H. L. (1997) Stability and mixed ionic electronic conduction in $Gd_2(Ti_{1-x}Mo_x)_2O_7$ under anodic conditions. *Solid State Ionics* 94(4), 75-83.

Qiao, J., Sun, K., Zhang, N., Sun, B., Kong, J. & Zhou, D. (2007) Ni/YSZ and Ni–$CeO_2$/YSZ anodes prepared by impregnation for solid oxide fuel cells. *Journal of Power Sources* 169(2), 253-158.

Qing, H. & Mishnaevsky, L. (2009) Unidirectional high fiber content composites: Automatic 3D FE model generation and damage simulation. *Computational Materials Science* 47(2), 548–555.

Sanyal, J., Goldin, G. M., Zhu, H. & Kee, R. J. (2010) A particle-based model for predicting the effective conductivities of composite electrodes. *Journal of Power Sources,* 195(19), 6671–6679.

Schneider, L. C. R., Martin, C. L., Bultel, Y., Bouvard, D. & Siebert, E. (2006) Discrete modelling of the electrochemical performance of SOFC electrodes. *Electrochimica Acta* 52(1), 314–324.

Sim, K. Y., Bae, K. K., Kim, C. H., Park & K. B. 13-16 June 2006. Electrochemical performances of LSM/YSZ composite electrode for high temperature steam electrolysis. *16, WHEC*.

Slater, P. R. & Irvine, J. T. S. (1999) Niobium based tetragonal tungsten bronzes as potential anodes for solid oxide fuel cells: synthesis and electrical characterization. *Solid State Ionics* 120(4), 125-134.

Shearing, P. (2009) *Characterization of solid oxide fuel cell electrode microstructures in three dimensions*. PhD thesis. Imperial College London.

Shi, Y., Cai, N., Li, C., Bao, C., Croiset, E., Qian, J., Hu, A. & Wang, S. (2007) Modeling of an anode-supported Ni–YSZ|Ni–ScSZ|ScSZ|LSM–ScSZ multiple layers SOFC cell: Part I. Experiments, model development and validation. *Journal of Power Sources* 172(1), 235–245.

Schuler, A. & Nerlich, V. (2006) The Rebirth of HEXIS. *CD of the 7th European SOFC Forum*, Lucerne, A 061.

Simons, S. N., King, R. B. & Prokopius, P. R. (1982) Camara EH Symposium Proceedings Fuel Cells Technology Status and Applications. *Institute of Gas Technology*, Chicago, USA.

Slater, P. R., Fagg, D. P. & Irvine, J. T. S. (1997) Synthesis and electrical characterization of doped perovskite titanates as potential anode materials for solid oxide fuel cells. *Journal of Material Chem*istry 7(1), 2495-2498.

Somalu, M. R. & Brandon, N. P. (2011) Rheological Studies of Nickel/Scandia-Stabilized-Zirconia Screen Printing Inks for Solid Oxide Fuel Cell Anode Fabrication. *Journal of the American Ceramic Society* 95(4), 1220-1228.

Smith, B. H. & Gross, M. D. (2011) A highly conductive oxide anode for solid oxide fuel cell. *Electrochem. Solid-State Letters* 14, B1.

Sprague, J. J. & Tuller, H. L. (1999) Mixed ionic and electronic conduction in Mn/Mo doped gadolinium titanate. *Journal of the European Ceramic Society* 19(7), 803-806.

Stambouli, A. B. & Traversa, E. (2002) Solid oxide fuel cells (SOFCs): a review of an environmentally clean and efficient source of energy. *Renewable & Sustainable Energy Reviews* 6(1), 433-455.

Stauffer, D. & Aharony, A. (1994) *Introduction to Percolation Theory*; 2nd ed., Taylor & Frances Inc. London, 1994.

Stolten, D. (2010) *Hydrogen and Fuel Cells*. 3rd Edition. Weinheim, John Wiley & Sons Publishing.

Sun, C. &, Stimming, U. (2007) Recent anode advances in solid oxide fuel cells. *Journal of Power Sources* 171(2), 247-260.

Sunde, S. (1995) Calculation of Conductivity and Polarization Resistance of Composite SOFC Electrodes from Random Resistor Networks. *Journal of the Electrochemical Society* 142(4), L50-L52.

Sunde, S. (1996) Monte Carlo Simulation of Conductivity of Composite Electrodes for Solid Oxide Fuel Cells. *Journal of the Electrochemical Society*, 143(3), 1123-1132.

Suzue, Y., Shikazono, N. & Kasagi, N. (2008) Micro modeling of solid oxide fuel cell anode based on stochastic reconstruction. *Journal of Power Sources* 184(1), 52–59.

Suzuki, Z. H. T., Funahashi, Y., Yamaguchi, T., Fujishiro, Y. & Awano, M. (2009) Impact of Anode Microstructure on Solid Oxide Fuel Cells. *Science* 325, 852-855.

Suzuki, M. & Oshima, T. (1983) Estimation of the Co-ordination number in a Multi-Component Mixture of Spheres. *Powder Technology* 35 (2), 159–166.

Tao, S. W. & Irvine, J. T. S. (2003) A redox-stable efficient anode for solid-oxide fuel cells. *Nature Mater*ials 2(1), 320-323.

Tao, S. W. & Irvine, J. T. S. (2004) Discovery and characterization of novel oxide anodes for solid oxide fuel cells. *The Chemical Record* 4(1), 83-95.

Travis, R., P., Balestrino, C., Hill, R. & Bernardi, D. (2006) Development of a 1 MW SOFC System at Rolls-Royce Fuel Cell Systems. *CD of the 7th European SOFC Forum*, Lucerne, B 096.

United Nations. (1997) *Text of the Kyoto Protocol.* [Online]. Available from: http://unfccc.int/kyoto_protocol/items/2830.php [Accessed 15/01/2014]

US Department of Energy. (2013) *Home: Hydrogen and Fuel Cells: Fuel Cells*. [Online]. Available from: http://www1.eere.energy.gov/hydrogenandfuelcells/fuelcells/ [Accessed 5th June 2013].

Van Herle, J., Horita, T., Kawada, T., Sakai, N., Yokokawa, H. & Dokiya, M. (1996) Low Temperature Fabrication of (Y, Gd, Sm)-Doped Ceria Electrolyte. *Solid State Ionics* 86-88, 1255-1258.

Vincent, A., Luo, J. L., Chuang, K. T. & Sanger, A. R. (2010) Effect of Ba doping on performance of LST as anode in solid oxide fuel cells. *Journal of Power Sources* 195(1), 769-774.

Waldbillig, D., Wood, A. & Ivey, D. G. (2005) Thermal analysis of the cyclic reduction and oxidation behaviour of SOFC anodes. *Solid State Ionics* 176(10), 847-859.

Wang, K., Ran, R. & Shao, Z. (2007) Methane-fueled IT-SOFCs with facile in situ inorganic templating synthesized mesoporous $Sm_{0.2}Ce_{0.8}O_{1.9}$ as catalytic layer. *Journal of Power Sources* 170(2), 251-258.

Wang, Z., Weng, W., Cheng, K., Du, P., Shen, G. & Han, G. (2008) Catalytic modification of Ni–Sm-doped ceria anodes with copper for direct utilization of dry methane in low-temperature solid oxide fuel cells. *Journal of Power Sources* 179(1), 541-546.

Weber, A. & Ivers-Tiffée, E. (2004) Materials and concepts for solide oxide fuel cells (SOFCs) in stationary and mobile applications. *Journal of Power Sources* 127(2), 273-283.

Ye, X. F., Wang, S. R., Wang, Z. R., Hu, Q., Sun, X. F., Wen, T. L. & Wen, Z. Y. (2008) Use of $La_{0.75}Sr_{0.25}Cr_{0.5}Mn_{0.5}O_3$ materials in composite anodes for direct ethanol solid oxide fuel cells. *Journal of Power Sources* 183(2), 512-517.

Yuan, K., Ji, Y. & Chung, J. N. (2009) Physics-based modeling of a low-temperature solid oxide fuel cell with consideration of microstructure and interfacial effects. *Journal of Power Sources*, 194(2), 908-919.

Yoo, K. B. & Choi, G. M. (2009) Performance of La-doped strontium titanate (LST) anode on $LaGaO_3$-based SOFC. *Solid State Ionics* 180(1), 867-871.

Zhu, H. & Kee, R. J. (2008) Modeling distributed charge-transfer processes in sofc membrane electrode assemblies. *Journal of the Electrochemical Society* 155 (7), B715–B729.

Zhu, X., Lü, Z.,Wei, B., Chen, K., Liu, M., Huang, X. & Su, W. (2009) Enhanced performance of solid oxide fuel cells with $Ni/CeO_2$ modified $La_{0.75}Sr_{0.25}Cr_{0.5}Mn_{0.5}O_{3-\delta}$ anodes. *Journal of Power Sources* 190(2), 326-330.

Zhu, X., Lü, Z., Wei, B., Chen, K., Liu, M., Huang, X. & Su, W. (2010) Fabrication and performance of membrane solid oxide fuel cells with $La_{0.75}Sr_{0.25}Cr_{0.5}Mn_{0.5}O_{3-\delta}$ impregnated anodes. *Journal of Power Sources* 195(7), 1793-1798.

Zhy, H. & Kee, R. J. (2008) Modeling Distributed Charge-Transfer Processes in SOFC Membrane Electrode Assemblies. *Journal of the Electrochemical Society* 155(7), B715-B729.

# Chapter 2 – Effective conductivity model development

## 2.1 - Introduction

Solid oxide fuel cells (SOFCs) are devices that convert chemical energy into useful electrical energy in a clean and efficient manner through electrochemical reactions. A SOFC is comprised of two electrodes, the anode and the cathode, and a ceramic electrolyte. The electrodes, where the electrochemical reactions take place, are commonly composites of electron and ion conducting materials characterized by a porous and tortuous microstructure. The governing electrochemical reactions are widely assumed to take place at the percolated triple-phase boundaries (TPBs), or the points where the electronic, ionic and pore phases meet (Cai et al., 2011). To enable and facilitate these reactions the paths connecting the electrode/gas channel and electrode/electrolyte interfaces to the TPBs are required to provide as low a resistance as possible to the passage of ions, electrons and gases, or equivalently, high values of the electronic and ionic conductivities and gas diffusivity, respectively. The objective of this thesis is to develop a model that can be used to determine the effective conductivity of porous composite structures based on their microstructural characteristics and to test its validity on idealized model structures. This allows comparison of the model results against analytical solutions, and represents the first step in developing and demonstrating an effective conductivity model for the more complex porous structures found in SOFC anodes.

Schneider et al. (Schneider et al., 2006) have used Kirchhoff's law of current conservation combined with the discrete element method (DEM) to model the effective conductivity of a sintered packing of spherical particles. The level of overlap between two adjacent particles, which is used to represent the result of the sintering process, is directly proportional to the forces generated by neighboring particles in contact.

A structure consisting of packed particles is initially discretized into a resistor network in this model. The current then flows from the particle in contact with the current collector through the network to the particle in contact with the electrolyte. Each contact in the packed structure is

replaced by a bond resistance which is specific to the two contacting particles and relies on the phase they represent. The nodes comprising the resistor network are therefore centered on each sphere and a set potential is applied to each electrode boundary which, by repeated application of Kirchhoff's law, yields the corresponding current flowing through the electrode. The equivalent or effective resistance of the overall network can then be found as:

$$R_{eq} = V/I. \tag{2.2}$$

where $V$ is the potential applied, $R_{eq}$ the equivalent resistance and $I$ the current.

One limitation of this method, however, is that a real electrode particle, when sintered, can differ greatly from a perfect sphere with overlapping regions, meaning that this technique can only be applied to synthetic structures of spheres. For a real structure found in SOFC electrodes, building a resistor network is not a trivial task due to the non-spherical particle shapes and irregular geometry of the contact surfaces between particles.

To overcome this problem and extend the effective resistance model of Schneider et al. (Schneider et al., 2007) to more realistic SOFC electrode microstructures, a model for the computation of the effective conductivity of porous SOFC electrodes based on a discretized representation of the microstructure is introduced in this chapter.

There have been instances in the literature where the principles inherent to the functioning of the proposed model have been used as the basis of other models. However the novelty of the proposed model lies in the derivation of the resistor network analyzed, and the applicability of the model to real porous, composite structures as well as those created synthetically. For example, Sunde (Sunde, 1995) created a model based on numerically solving Kirchhoff's law of current conservation for a resistor network resulting from scattering predetermined fractions of electrode and electrolyte particles following a Monte-Carlo process on the sites of a three-dimensional cubic lattice. The individual resistances of each network branch are determined by assigning each particle-to-particle contact a finite resistance, based on the pure conductivity of the abundance medium, scaled to the size of the particles and resulting contact area. Particles are

assumed to be perfect spheres as per the work of Schneider et al. (Schneider et al., 2007). This model has the limitation of not being applicable to real SOFC anode microstructures, and poses further limitations with regards to varying the particle size distribution, additionally to making broad assumptions with regards to the contact area between two particles. Jeon et al. (Jeon et al, 2005) have also developed a random resistor network model very similar to that of Sunde (Sunde, 1995) and Schneider et al. (Schneider et al., 2006) where particles are generated as perfect spheres of similar size, and reference Sunde's model to justify the use of a uniform neck size, or contact area between two particles, to determine the individual resistances attributed to each branch of the derived resistor network.

The closest work in the literature to the proposed model is that of Mari et al. (Mari & Dotelli, 2000). In their paper, polycrystalline microstructures are generated using a process called the Voronoi tessellation (Berg et al., 1997) of polyhedras to represent conducting particles as well as a Monte-Carlo distribution of spheres to represent the insulating phase. The structure is then converted to pixels from a statistical formulae defining the average size of a convex hull according to a parameter taken from literature. A cubic grid is then superimposed to the structure and the edges of the cube, each element being 50 pixels in length, and converted into discreet electrical circuits (RC parallel) that are reported to accurately describe the electrical behaviours of the studied materials. Edges falling inside a certain grain are assigned either of the corresponding material impedances, while those lying between particles are considered the material grain boundary contribution. The impedance of the three-dimensional resistance network is then calculated by minimizing the dissipated power, or by applying a transfer-matrix operation. This technique is based on iterative procedures where elements in the matrix are changed whenever a new electrical circuit is added, and the solving of a linear system finally yields the total impedance of the considered network. In order to avoid spurious boundary effects (i.e. lower density), a pre-defined core volume taken as smaller than that used in the Voronoi tessellation is used to perform the overall impedance calculations. The principle drawback of this model however is that assigned resistances are derived from a specific experimental measurement taken from a sample of YSZ/$Al_2O_3$ of a specific composition, and are specifically tailored to analyse the relationship between electrical behaviour and microstructural characteristics of YSZ/$Al_2O_3$ polycrystalline composites. The model therefore needs to be

coupled with tailored experiments to produce accurate results, and is unsuitable for the analysis of a wider array of materials. Furthermore the discretization process employed can cause a loss of information with regards to smaller grains and interstitial effects between particles if the nodes are not properly placed. It is reported in the paper that the discretization level employed in the paper is too coarse at the boundaries, which implies a large computational time for a relatively low number of nodes (~2000 nodes). This is however inevitable in any discretization process, where an optimum discretization level needs to be reached, most commonly determined by means of a sensitivity analysis.

The Resistor Network model reported in this thesis, (ResNet model), can be applied equally to microscopic reconstructions of real and/or synthetic microstructures.

## 2.2 – Origin of the ResNet model

In 2006, Schneider et al. (Schneider et al., 2006) used Kirchhoff's law of current conservation to calculate the electrical conductivity of a packed bed of synthetic spherical particles. They discretized a system of spheres into a network of nodes, each centered at the centroid of the particles comprising the system. Consider the particle system shown in Figure 2.1.

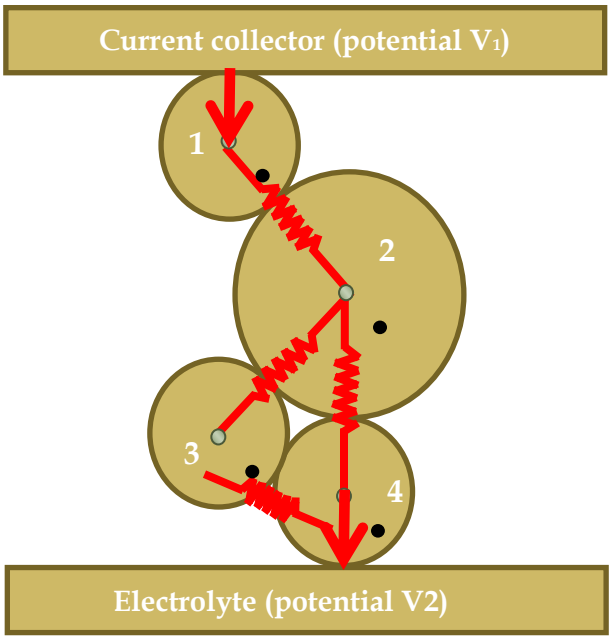


Figure 2.1 – Schematic showing the discretization of a particle packing into a resistor network as per Schneider et al. (Schneider et al., 2006).

The contact between two electrocatalyst or two electrolyte particles is modelled as an electronic or ionic bond resistance, respectively, and attributed an empirical resistance value determined based on a linear approximation of the classical Butler-Volmer kinetic law.

The ensuing calculation used to determine the effective electrode conductivity corresponds to the method of calculation of the internal resistance of a power source. This is found to be a standard procedure in electrical engineering where all internal voltage sources in a network are removed or substituted by a resistance. A macroscopic network response is obtained by imposing the potentials $V_1$ and $V_2$ on current collector and electrolyte respectively and the total current $I$ going through the network is given by Ohm's law.

For the system illustrated in Figure 2.1, this discretization yields the following set of equations, by considering that the current entering any one node is equal to the current exiting the node. The following set of equations can therefore be drawn for each sphere:

Sphere 1- $$i_1 = \frac{V_1 - V_2}{R_{12}} \quad (2.3)$$

Sphere 2- $$0 = \frac{V_2 - V_1}{R_{12}} + \frac{V_2 - V_3}{R_{23}} + \frac{V_2 - V_4}{R_{24}} \quad (2.4)$$

Sphere 3- $$0 = \frac{V_3 - V_2}{R_{23}} + \frac{V_3 - V_4}{R_{34}} \quad (2.5)$$

Sphere 4- $$i_4 = \frac{V_4 - V_2}{R_{24}} + \frac{V_4 - V_3}{R_{34}} \quad (2.6)$$

To facilitate the manipulation of this data, we rewrite the system of equations into a matrix system as follows:

$$\begin{bmatrix} \left(\frac{1}{R_{12}}\right) & \left(-\frac{1}{R_{12}}\right) & 0 & 0 \\ \left(-\frac{1}{R_{12}}\right) & \left(\frac{1}{R_{12}} + \frac{1}{R_{22}} + \frac{1}{R_{24}}\right) & \left(-\frac{1}{R_{23}}\right) & \left(-\frac{1}{R_{24}}\right) \\ 0 & \left(-\frac{1}{R_{23}}\right) & \left(\frac{1}{R_{23}} + \frac{1}{R_{34}}\right) & \left(-\frac{1}{R_{34}}\right) \\ 0 & \left(-\frac{1}{R_{34}}\right) & \left(-\frac{1}{R_{34}}\right) & \left(\frac{1}{R_{24}} + \frac{1}{R_{34}}\right) \end{bmatrix} \begin{pmatrix} V_1 \\ V_2 \\ V_3 \\ V_4 \end{pmatrix} = \begin{pmatrix} i_1 \\ 0 \\ 0 \\ i_4 \end{pmatrix} \quad (2.7)$$

The next step is to substitute the first and last equations for the pre-determined potentials applied to the boundaries of the system. This yields the following system:

$$\begin{bmatrix} 1 & 0 & 0 & 0 \\ \left(-\frac{1}{R_{12}}\right) & \left(\frac{1}{R_{12}} + \frac{1}{R_{22}} + \frac{1}{R_{24}}\right) & \left(-\frac{1}{R_{23}}\right) & \left(-\frac{1}{R_{24}}\right) \\ 0 & \left(-\frac{1}{R_{23}}\right) & \left(\frac{1}{R_{23}} + \frac{1}{R_{34}}\right) & \left(-\frac{1}{R_{34}}\right) \\ 0 & 0 & 0 & 1 \end{bmatrix} \begin{pmatrix} V_1 \\ V_2 \\ V_3 \\ V_4 \end{pmatrix} = \begin{pmatrix} V_{top} \\ 0 \\ 0 \\ V_{bottom} \end{pmatrix} \quad (2.8)$$

The above system is now in the form [A]{X}={B}, where [A] and {B} are known. The inversion of the matrix [A] gives {X}, which is then substituted back into (2.7) gives the current entering and leaving the system at the boundaries. These currents can be added up to find the total current entering and leaving the system,

$$\sum_{top} i_{top} = -\sum_{bottom} i_{bottom} = I \quad (2.9)$$

Allowing for the overall effective conductivity of the system to be found using the following two equations:

$$R_{eq} = V/I \tag{2.10}$$

$$K_{eff} = \frac{I}{V}\frac{h}{A_{electrode}} \tag{2.11}$$

where $h$ is the length of the microstructure and $K_{eff}$ the overall effective conductivity in the direction considered.

## 2.3 – Expansion of Schneider's model to voxel networks

In order to extend the model developed by Schneider we consider a rectangular heterogeneous structure of arbitrary complexity and wish to predict its effective conductivity in a given direction, perpendicular to two of the faces of the structures. Although the current flows in and out of the electrode at two surfaces only, the fact that current can flow in all directions within the structure is captured in the Resnet network model. The first step in determining the equivalent resistance (or effective conductivity) of any structure is the discretization of this structure into cubic elements called voxels (see Figure 2.2). If the space occupied by any one voxel contains more than 50% of a certain material, the voxel is considered to be fully occupied by the material in question. This implies a loss of accuracy, as the structure is indeed being changed during this discretization process. With a high enough resolution however, which will be determined in further sections, the accuracy of the discretized microstructure is sufficient for the context in which it is employed.

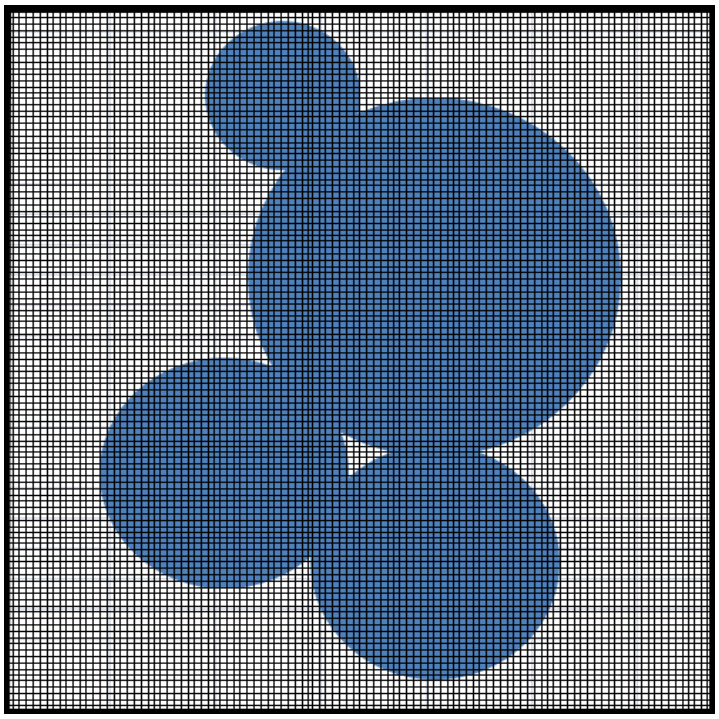

Figure 2.2 – 2D discretization of a system of spheres into pixels.

The typical voxel size used by Cai et al. (Cai et al., 2011) is $1/25^{th}$ of the diameter of the particles (the particles were approximately 1~2 μm in diameter). Once a structure has been discretized, it is transformed into a resistor network, with each voxel represented by a node located at its centre. Due to the fact that the nodes are defined as representing the centroid of each voxel, the space in between two adjacent nodes is occupied by two separate half voxels. The resistance between two adjacent nodes is therefore assigned a value corresponding to the equivalent resistance of the pure material of the two half voxels in series, following Kirchhoff's laws. The resistance between two non-boundary voxel nodes is defined as

$$R_{np} = \frac{1}{2} r_n + \frac{1}{2} r_p \tag{2.12}$$

where $n$ is the index of a non-boundary voxel and $p$ is the index of a neighbouring, non-boundary voxel. $r_n$ and $r_p$, which represent the resistances of voxels $n$ and $p$, respectively, are defined as

$$r_k = \rho_k \frac{l_{vox}}{A_{vox}} \quad , k=n,p \tag{2.13}$$

where $k$ is the voxel index, $\rho_k$ is the resistivity of the pure material occupying voxel $k$, which is given as $1/\sigma_k$, where $\sigma_k$ is the conductivity of the pure material in voxel $k$. $l_{vox}$ is the length of a voxel along the direction of interest (i.e., along the line joining the nodes $n$ and $p$) and $A_{vox}$ is the cross-sectional area of a voxel perpendicular to this direction. In this work, voxels can either be cubic or non-cubic. These equations can only be applied to a system of uniform voxels, meaning that further development would be desirable to improve the computational efficiency of the model. When considering cubic voxels, $l_{vox}/A_{vox} = 1/l_{vox}$. This is different to the work of Schneider et al.; in their model, the resistance of two particles in contact needed to determined separately using a linear approximation of the Butler-Volmer kinetic law (Schneider et al., 2006), whereas here the resistance between two nodes in contact is attributed the resistance of the pure material using equation 2.13.

Boundary voxels in the direction in which the conductivity is being considered need to be treated differently, however, in order to account for the portion of the microstructure between the surface and the boundary node (voxel centre). To achieve this, nodes for the boundary voxels are instead positioned so that they are centred on the voxel face that lies at the surface of the microstructure. In this case, the resistance between a node representing boundary voxel $n$ and its neighbouring node representing a non-boundary voxel $p$ is defined as:

$$R_{np} = r_n + \tfrac{1}{2} r_p \tag{2.14}$$

A voltage difference is applied across the electrode, in the direction in which the conductivity is being measured. This results in a net current flow in this direction, denoted by *I*. Current conservation can then be applied to each voxel or node. The set of linear equations describing current conservation over a network of *q* voxels can be expressed as {x}[a]=[b], where {x} is the conductivity matrix, [a] the potential vector ([a] =$(V_1 \;\; V_2 \; ... \; V_q)^T$) and [b] the resultant current vector, ([b]=$(i_1 \, i_2 \; ... \; i_q)^T$). The only non-zero elements of [b] are those corresponding to voxels on the two surfaces of the structure that are perpendicular to the direction of net current flow. For each voxel *k*, the set of voxels that share a face with *k* is defined as $N_k$. The conductivity matrix is defined as

$$(x)_{kk} = -\sum_{j \in N_k} \frac{1}{R_{kj}} \text{ where } k = 1,...,q \text{ and} \tag{2.15}$$

$$(x)_{kj} = \begin{cases} \dfrac{1}{R_{kj}}, & j \in N_k \\ 0 & j \notin N_k, j \neq k \end{cases} \text{ where } k = 1,...,q \tag{2.16}$$

where *q* is the total number of voxels, *k* and *j* are the voxel indices and $R_{kj}$ the resistance between voxels *k* and *j*.

All boundary voxels at the surface of the electrode where current flows in are given the same arbitrary voltage $V_{in}$ and all boundary voxels at the surface of the electrode where current flows out are given the same arbitrary voltage $V_{out}$, where $V_{in} > V_{out}$. The detailed representation of the

three-dimensional geometry of the microstructure via a 3D network of voxels ensures that the effect of structural anisotropy and heterogeneity is well accounted for in the model.

Upon solving the linear model, the total current entering or leaving the system can then be calculated as

$$\sum_{k \in \mathrm{N}_{in}} i_k = -\sum_{k \in \mathrm{N}_{out}} i_k = I \tag{2.17}$$

where $\mathrm{N}_{in}$ is the set of nodes at the current inlet surface and $\mathrm{N}_{out}$ is the set of nodes at the current outlet surface.

The conductivity of the network is finally given by Ohm's law by dividing the overall current $I$ by the voltage $V = V_{in} - V_{out}$, allowing the overall conductivity $K_{eff}$ to be found from:

$$K_{eff} = \frac{I}{V} \frac{h}{A_{electrode}} \tag{2.18}$$

where $h$ is the electrode thickness, parallel to the current flow, and $A_{electrode}$ is the surface area of the electrode, perpendicular to the current flow.

To demonstrate the working of the model, we will consider a simple 3×3×2 array of voxels as shown in Figure 2.3.

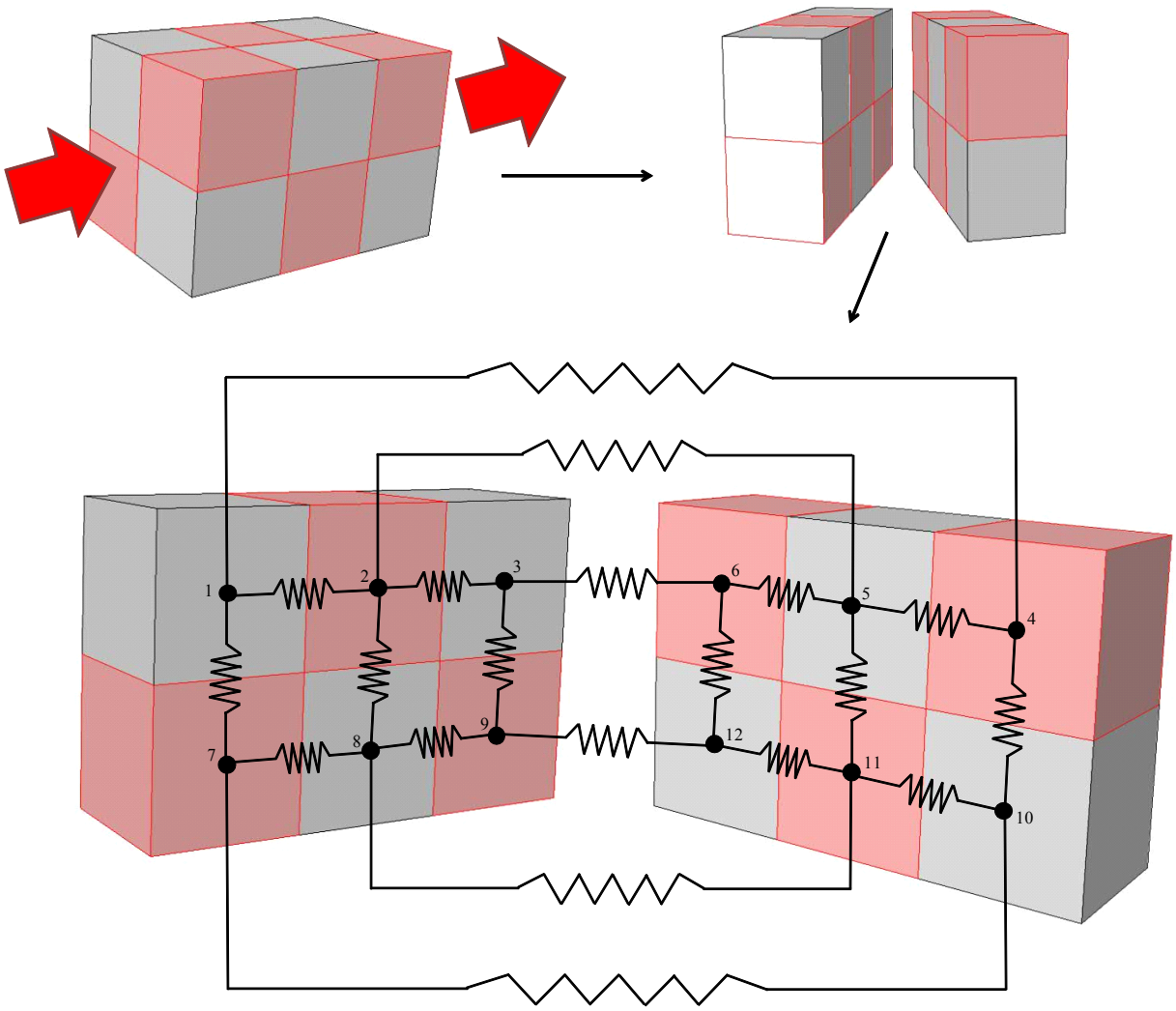


Figure 2.3 – Equivalent resistor network of a 3x2x2 voxel structure, with the nodes positioned at the centre of each voxel. The red and grey voxels represent two materials with different conductivities and the red arrows show the direction in which the equivalent resistance is computed.

As explained above, the resistance between two non-boundary voxels is defined using Equation 2.12 and illustrated by Figure 2.4 and the resistance between two non-boundary nodes is defined using Equation 2.14 and illustrated by Figure 2.5.

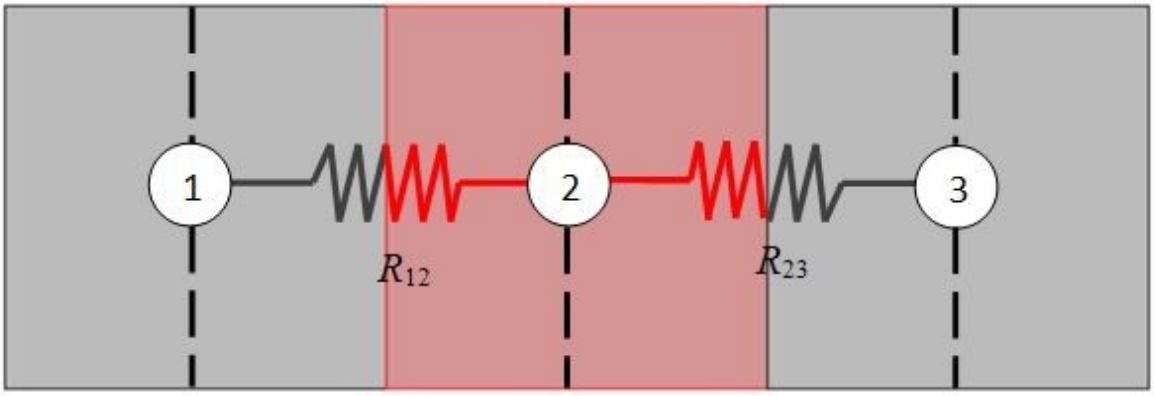


Figure 2.4 – Graphical representation of the distribution of resistance values based on the voxel disposition in the structure comprised of 3x2x2 voxels, the dashed lines representing the voxel space accounted for in the drawn network.

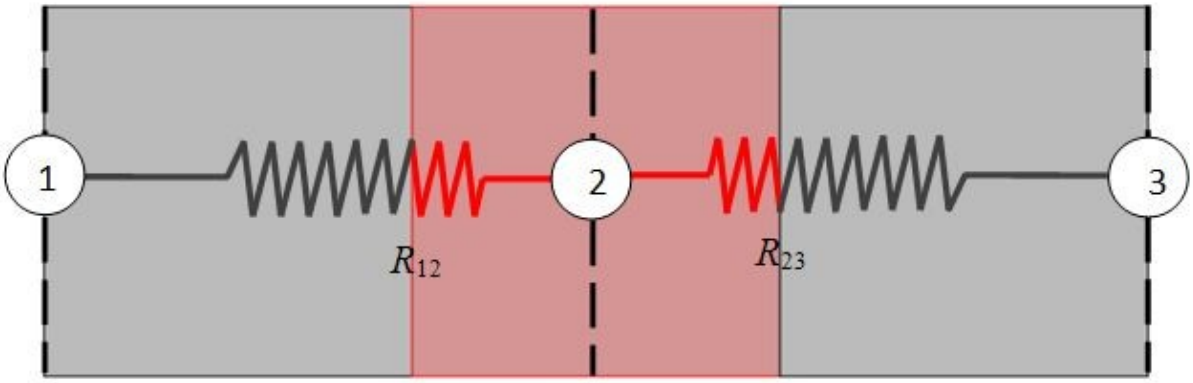


Figure 2.5 – Graphical representation of the modified resistance disposition at the boundaries to account for the whole voxel. In this case $\boldsymbol{R_{12} = R_1 + \frac{1}{2}R_2}$.

The current balance for voxels 1 and 2 of the example considered and illustrated in Figure 2.3 is written as follows:

Voxel 1: $$(V_4 - V_1)\frac{1}{R_{14}} + (V_2 - V_1)\frac{1}{R_{12}} + (V_7 - V_1)\frac{1}{R_{17}} = i_{1,in} \qquad (2.19)$$

Voxel 2: $$(V_5 - V_2)\frac{1}{R_{25}} + (V_1 - V_2)\frac{1}{R_{12}} + (V_3 - V_2)\frac{1}{R_{23}} + (V_8 - V_2)\frac{1}{R_{28}} = 0 \qquad (2.20)$$

In the equations above, the current entering voxel 1 is equal to $i_{1,in}$, and following Kirchhoff's laws the current exiting the same voxel is equal to $i_{i,\ out}$. This current is composed of three components: $i_{14}$, $i_{12}$ and $i_{17}$. Each of these components is defined as $\Delta V/R$, as shown in equations 2.19 and 2.20. For voxels 1, 4, 7 and 10 the sum of currents is equal to $i_{in}$, and for in voxels 3, 6, 9 and 12 the sum of the currents is equal to $i_{out}$, which is the current entering and leaving the system of voxels due to the imposed voltage at the boundary/electrodes of the network. Applying Equations 2.15 and 2.16 to this system yields the resistor network needing to be inversed, in turn yielding the overall current entering and leaving the system. Applying Equation 2.18 finally allows us to extract the overall effective conductivity of the system considered.

These calculations are identical to those performed by Schneider et al in their work (Schneider et al., 2006), the only difference being the fact that nodes are here not centered on spherical particles, but voxels instead. Mari et al. however (Mari et al., 2010) use a transfer-matrix technique (Derrida et al, 1984) which is based on iterative procedures that change the matrix elements whenever a new electrical circuit is added; the total impedance of the system is then obtained by solving a linear system as is the case in this thesis.

## 2.4 – Model implementation

The developed model was implemented using MatLab, in which three FOR loops are used to assign each resistance matrix entry its corresponding resistance. The program checks for the position of the voxel being analyzed through the use of IF statements. Once the resistance matrix has been created, the program obtains the current array by using the backslash command available in MatLab R2010b and later versions. If A is an N-by-N matrix and B is a column vector with N components, or a matrix with several such columns, then X = A \ B is the solution to the equation A • X = B. This is the step that dictates the computational power required for the proposed model to operate. On an Intel® Xeon® octo-core processor @2.4GHz with 24 GB of RAM, the CPU time to compute the current array of a system with $10^6$ voxels is 2.14 hours.

This computational time linearly decreases for a lower number of voxels. It should be noted that in most commercial platforms a similar approach is undertaken to compute the effective

conductivity of a structure (or equivalent resistance) as the algorithms are governed by the same principle of current conservation in each mesh cell. However, when these platforms use an iterative approach to solving the potential (or current) of each cell, if not parameterized properly and the right solver is not employed with optimal settings, these platforms require a large amount of time to reach convergence. This means that, when used on base settings and highly heterogeneous structures and/or singular conductivity values are employed, these platforms require significantly more computational time/power to achieve convergence. The comparison of the computational time required by these platforms and the proposed model is not a fair one unless close attention is paid to the parameterization of these solvers.

## 2.5 – Conclusions

In this Chapter, the derivation of a 3D effective conductivity model is presented, based on Kirchhoff's law of current conservation and series circuits. The model relies on the discretization of a 3D structure into small cubic elements called voxels. The voxelized structure is subsequently discretized into a mixed resistor network, each node positioned at the centre of each voxel. The resistance between two adjacent voxels is assigned a value based on the conductivity of the pure material represented by the voxels, scaled to the space occupied by the path between two nodes; half of one node and half of the other node make up a resistance formed by two resistances in series, each assigned the resistance of half the volume of a voxel. Assigning an arbitrary potential difference between two opposite boundaries of the network allows for a linear set of equations to be solved, yielding the current entering and leaving the system, in turn yielding the effective conductivity of the entire structure to be derived. In the next chapter, the model will be applied to a variety of simple structures, the effective conductivity of which can be derived analytically in order to validate the model.

## 2.6 – References

Archie, G. E. (1942) The electrical resistivity log as an aid in determining some reservoir characteristics. *Transactions of the IME*, 146(1), 54-62.

Aguiar, P, Adjiman, C. S. & Brandon, N.P. (2005) Anode-supported intermediate-temperature direct internal reforming solid oxide fuel cell - II. Model-based dynamic performance and control. *Journal of Power Sources* 147(1), 136-147.

Berg, M., Krevel, M., Overmars & M., Schwarzkopf, O. (1997) Computational Geometry. *Springer-Verlag*, 145.

Bertei, A. & Nicolella, C. (2011) Percolation theory in SOFC composite electrodes: Effects of porosity and aprticle size distribution on effective propeties. *Journal of Power Sources* 196(22), 9429-9436.

Bouvard, D. & Lange, F. F. (1991) Relation between percolation particle coordination in binary powder mixtures. *Acta Metallurgica et Materialia* 39(12), 3038-3090.

Brett, D. J. L., Aguiar, P., Brandon, N. P., Coop, I., Dueck, J., Galloway, R. C., Grande, O., Hayes, G. W., Lillie, K., Mellors, C., Thompson, S., Tilley, A. R. & Wood, A. (2007) Operational Experience of an IT-SOFC/Battery Hybrid System for Automotive Applications. *ECS transactions* 7(1), 113-122.

Brett D. J. L., Aguiar, P. & Brandon, N. P. (2006) System modelling and integration of an intermediate temperature solid oxide fuel cell and ZEBRA battery for automotive applications. *Journal of Power Sources* 163(1), 514-522.

Bruggeman, D. A. G. (1945) Calculation of the various physical constat of heterogeneous substances. I. Delectric constants and conudctivities of mixtures of isotropic substances. *Annalen der Phsik* 24(1), 636-664.

Cai, Q., Adjiman, C. S. & Brandon, N. P. (2010) Investigation of the active thickness of solid oxide fuel cell electrodes using a 3D microstructure model. *Electrochemica Acta* 56(28), 10809-10819.

Cai, Q., Adjiman, C. S. & Brandon, N. P. (2011). Modelling the 3D microstructure and performance of solid oxide fuel cell electrodes: Computational parameters. *Electrochimica Acta* 56(16), 5804-5814.

Cai, W. Z., Tu, S. T. & Gong, J. M. (2005) A Physically Based Percolation Model of the Effective Electrical Conductivity of Particle Filled Composites. *Journal of Composite Materials* 40(23), 2131-2149.

Chen, D., Lin, Z., Zhu, H. & Kee, R. J. (2009) Percolation theory to predict effective properties of solid oxide fuel-cell composite electrodes. *Journal of Power Sources* 191(2), 240-252.

Chen, X. J., Chan, S. H. & Khor, K. A. (2004) Simulation of a composite cathode in solid oxide fuel cells. *Electrochemica Acta* 49(11), 1851-1861.

Choi, H-W., Berson, A., Pharoah, J. G. & Beale, S. B. (2010) Effective transport properties of the porous electrodes in solid oxide fuel cells. *Journal of Power and Energy* 225(2), 183-197.

Derrida, B., Zabolitzky, J. G., Vannimenus & J., Stauffer, D. (1984) A transfer matrix program to calculate the conductivity of random resistor networks. *Journal of Statistical Physics* 36(2), 31-42.

Einstein, A (1926) *Investigations on the theory of the brownian movement*. United States of America, Methuen Co.

Golbert, J., Adjiman, C. S. & Brandon, N. P. (2008) Microstructural modeling of SOFC anodes. *Industrial and Engineering Chemical Research* 47(1), 7693-7699.

Jeon, D. H., Nam, J. H. & Kim, C-J (2005) A random resistor network analysis on anodic performance enhancement of solid oxide fuel cells by penetrating electrolyte structures. *Journal of Power Sources* 139(1), 21-29.

Kazempoor, P., Dorer, V. & Ommi, F. (2009) Evaluation of hydrogen and methane-fuelled solid oxide fuel cell systems for residential applications: System design alternative and parameter study. *International Journal of Hydrogen Energy* 34(20), 8630-8644.

Kishimoto, M., Iwai, H., Saito, M. & Yoshida, H. (2012) Three-Dimensional Simulation of SOFC Anode Polarization Characteristics Based on Sub-Grid Scale Modelling of Microstructure. *Journal of the Electrochemical Society* 159(3), B315-B323.

Landauer, R. (1952) The electrical resistance of binary metallic mixtures. *Journal of Applied Physics* 23(7), 779-784.

Lanzini, A., Santarelli, M. & Orsello, G. (2010) Residential Solid Oxide Fuel Cell Generator Fuelled by Ethanol: Cell, Stack and System Modelling with a Preliminary Experiment. *Fuel Cells* 10(4), 654-675.

Leah, R.T., Brandon, N.P. & Aguiar, P. (2005) Modelling of cells, stacks and systems based around metal-supported planar IT-SOFC cells with CGO electrolytes operating at 500-600 degrees C. *Journal of Power Sources* 145(2), 336-352.

Mari, C. M. & Dotelli, G. (2000) A random resistor model to forecast the electrical properties of crystalline ionic conductor composites. *Solid State Ionics* 136(1), 1315-1319.

Maxwell, J. C (1873) *Treatise of electricity and magnetism*. California: Oxford : Clarendon Press 1.

Mu, D., Liu, Z. S.,Huang, C. & Djilali, N. (2007) Prediction of the effective diffusion coefficient in random porous media using the finite element method. *Journal of Porous Materials* 14(1), 49-54.

Schneider, L. C. R., Martin, C. L., Bultel, Y., Bouvard, D. & Siebert, E. (2007) Discrete modelling of the electrochemical performance of SOFC electrodes. *Electrochemica Acta* 52(1), 314-324.

Schneider, L. C. R., Martin, C. L., Bultel, Y., Dessemond & L., Bouvard, D. (2006) Percolation effects in functionally graded SOFC electrodes. *Electrochemica Acta* 52(9), 3190-3198.

Song, T. W., Sohn, J. L., Kim, J. H., Kim, T. S., Ro, S. T. & Suzuki, K. (2005) Performance analysis of a tubular solid oxide fuel cell/micro gas turbine hybrid power system based on a quasi-two dimensional model. *Journal of Power Sources* 142(1), 30-42.

Stauffer, D. (1994) *Introduction to percolation theory*. 2nd Edition. United Stated of America, Taylor & Francis.

Subramanyan, K. & Diwekar, U. M. (2007) Optimizing model complexity with application to fuel cell based power systems. *Journal of Power Sources* 46(11), 1116-1128.

Sunde, S. (1995) Calculation of Conductivity and Polarization Resistance of Composite SOFC Electrodes from Random Resistor Networks. *Journal of the Electrochemical Society* 142(4), 50-52.

Suzue, Y., Shikazono & N., Kasagi, N. (2008) Micro modeling of solid oxide fuel cell anode based on stochastic reconstruction. *Journal of Power Sources* 184(1), 52-59.

Suzuki, M. & Oshima, T. (1985) Comparison between the Computer-Simulated Results and the Model for Estimating the Coordination Number in a Three-Component Random Mixture of Spheres. *Powder technology* 43(1), 19-25.

Suzuki, M. & Oshima, T. (1985) Co-ordination number of a multi-component randomly packed bed of spheres with size distribution. *Powder technology* 44(3), 213-218.

Suzuki, M. & Oshima, T. (1983) Estimation of the coordination number in a multicomponent mixture of spheres. *Powder technology* 35(2), 159-166.

Tseronis, K., Bonis, I., Kookos, I. K. & Theodoropoulos, C. (2012) Parametric and transient analysis of non-isothermal, planar solid oxide fuel cells. *International Journal of Hydrogen Energy* 37(1), 530-547.

Tseronis, K., Kookos, I. K. & Theodoropoulos, C. (2008) Modelling mass transport in solid oxide fuel cell anodes: a case for a multidimensional dusty gas-based model. *Chemical Engineering Science* 63(23), 5626-5638.

Wishart, J., Dong, Z. & Secanell, M. (2006) Optimization of a PEM fuel cell system based on empirical data and a generalized electrochemical semi-empirical model. *Journal of Power Sources* 161(2), 1041-1055.

Yu, S. & Jung, D. (2010). A study of operation strategy of cooling module with dynamic fuel cell system model for transportation application. *Renewable Energy* 35(11), 2525-2532.

# Chapter 3 – Model validation

## 3.1 – Introduction

Models developed by researchers in a variety of fields are found to have undergone a validation process prior to their use to answer research questions.

In this chapter, the methodology presented previously is applied to simple structures/configurations on a microscopic scale, whose equivalent resistances are known analytically in most cases as well as more complex synthetic microstructures. Computed effective conductivities are compared to those available in literature, when these are not available, the application of a mesh-based discretization combined with solving the Fickian transport equation, computed by the commercial platform COMSOL Multiphysics, gives results with which to compare those given by the ResNet model. In a final instance the model is applied to a synthetic microstructure comprised of randomly packed spheres to check for the solution convergence.

## 3.2 – Model validation against analytical data – simple synthetic structures

To evaluate the ResNet effective conductivity model, sample structures are analyzed. The structures were chosen so that their equivalent resistance could be derived analytically using Kirchhoff's laws, namely by combining equations 2.2, 2.11 and 2.13. The results obtained for 6 sample geometries, that we will call case 1, are illustrated in Table 3.1.

Table 3.1 – Calculated equivalent resistance values of a range of simple model structures obtained using the effective conductivity model and from analytical solutions, where voxels are attributed resistance values corresponding to nickel and a low conductivity material.

| Structure representation | Resistance of a grey voxel (Ω) | Resistance of a red voxel (Ω) | Equivalent resistance in x-direction as given by: | |
|---|---|---|---|---|
| | | | Matlab model (Ω) | Theoretical (Ω) |
| 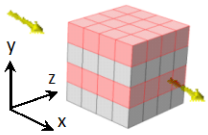 | 1.67 | $4.00 \times 10^{8}$ | 0.833 | 0.833 |
| 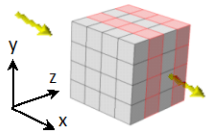 | 1.67 | $4.00 \times 10^{8}$ | 0.833 | 0.833 |
| 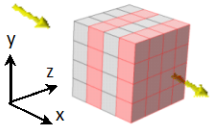 | 1.67 | $4.00 \times 10^{8}$ | $5.00 \times 10^{-7}$ | $5.00 \times 10^{-7}$ |
| 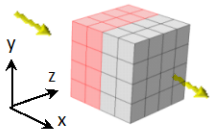 | 1.67 | $4.00 \times 10^{8}$ | $5.00 \times 10^{-7}$ | $5.00 \times 10^{-7}$ |
| 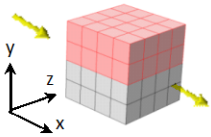 | 1.67 | $4.00 \times 10^{8}$ | 0.833 | 0.833 |
| 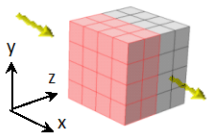 | 1.67 | $4.00 \times 10^{8}$ | 0.833 | 0.833 |

The structures comprise 4×4×4 voxels representing two materials, one with the conductivity of nickel at 1073 K, or 2.4 S/µm (Golbert et al., 2007) which is assigned to the red voxels and one with an arbitrary (low) conductivity of $10^{-8}$ S/µm, assigned to the grey voxels. The resistance values used for each voxel is found using $R = \rho\, l/A$ where R is the resistance in Ohms, $\rho$ is the resistivity in Ohms/µm, $l$ is the voxel length and $A$ is the voxel cross-sectional area in the direction in which the resistance is considered. In these cases the structures are assigned to have a length of 1 µm in every direction, meaning that each voxel has a uniform length of 0.25 µm.

The results predicted by the ResNet model shows good agreement with the analytical solutions for these simple structures. The next step is to analyze the validity of the model against a slightly

more complex structure. As analytical results are needed for a useful comparison, a cylinder is analyzed in case 2. The cylinder chosen is of radius 0.5 µm and length 1 µm and is positioned in a cube of length 1 µm, as the ResNet model is designed to operate on cuboid agglomerations of voxels. The voxels representing the cylinder material are given the conductivity of nickel at 1073 K, and the voxels representing the empty space around the cylinder are given the low arbitrary conductivity used in the previous case. The discretization of a geometry such as a cylinder requires a much finer resolution than that employed in case 1. Figure 3.2 presents the results of this analysis on the structure illustrated in Figure 3.1. Its equivalent resistance is found using $R = \rho\, l/A$ where $l$ is the length of the cylinder (1 µm) and $A$ is the area of the circular boundaries.

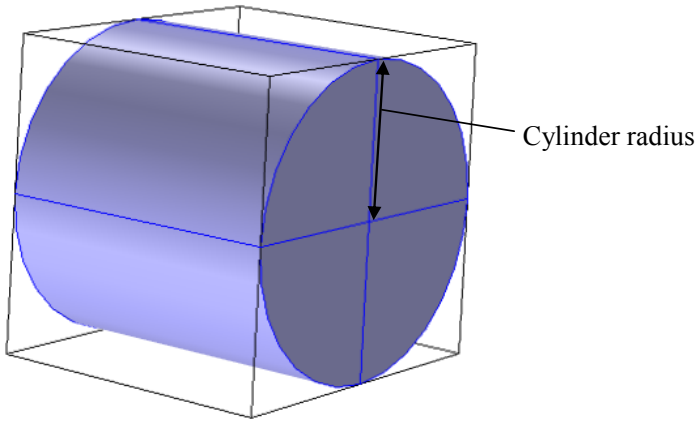


Figure 3.1 - Graphical representation of the cylinder under study with relevant dimensions. When used in the ResNet model, the cylinder is discretized within a cube of length 1µm in which the volume not occupied by the cylinder is defined as an arbitrary material of conductivity $10^{-8}$ S/µm.

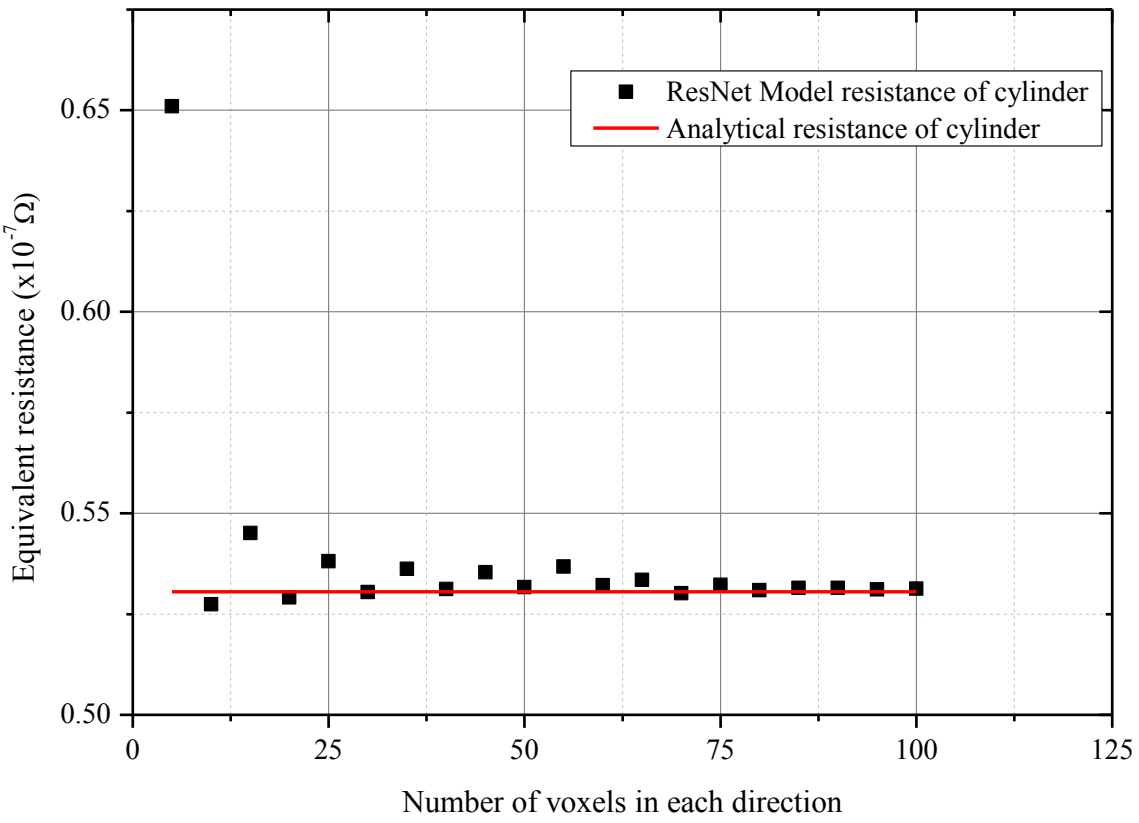


Figure 3.2 – Variation of equivalent resistance for different discretization resolutions. The structure studied is a cylinder of length 1 µm and radius 0.5 µm, discretized within a cube of length 1 µm. The nickel voxels are given the conductivity of nickel at 1073 K and the pore voxels are given a conductivity of $1.0 \times 10^{-8}$ S/µm.

In Figure 3.2, it is apparent that a certain degree of resolution is needed in the discretization process to achieve acceptable agreement with the analytical value. In the case of the cylinder studied, this is achieved for discretizations consisting of at least 60 voxels in each dimension. For coarser resolutions, the difference in resistance between the discretized and the actual structures can be linked to a difference in the calculated volumes of the two structures. This trend is illustrated in Figure 3.3, where the difference between the analytical volume of the cylinder considered and the discretized volume shows how the volume errors follow a similar behaviour to the equivalent resistance errors for an increasing discretization resolution. The use of cylindrical coordinates rather than Cartesian coordinates could overcome this problem, or an

adaptive mesh like that used by COMSOL as will be discussed later. This requires additional work however and is beyond the scope of this thesis.

The analytical volume of the cylinder is calculated using $Volume = h\pi r^2$ where $h$ is the height of the cylinder (1 µm) and $r$ is the radius of the cylinder (0.5 µm). Figure 3.4 shows a plot of the error in equivalent resistance of the discretized cylinder divided by the error in the volume of the discretized cylinder at corresponding resolutions. The grouping of data points around a value of 1 indicates that the errors observed between equivalent resistances obtained with the ResNet model and the analytical solutions are primarily a result of the deviation of the discretized volume from the analytical volume. This arises from the discretization process where a smooth volume is changed into cubes.

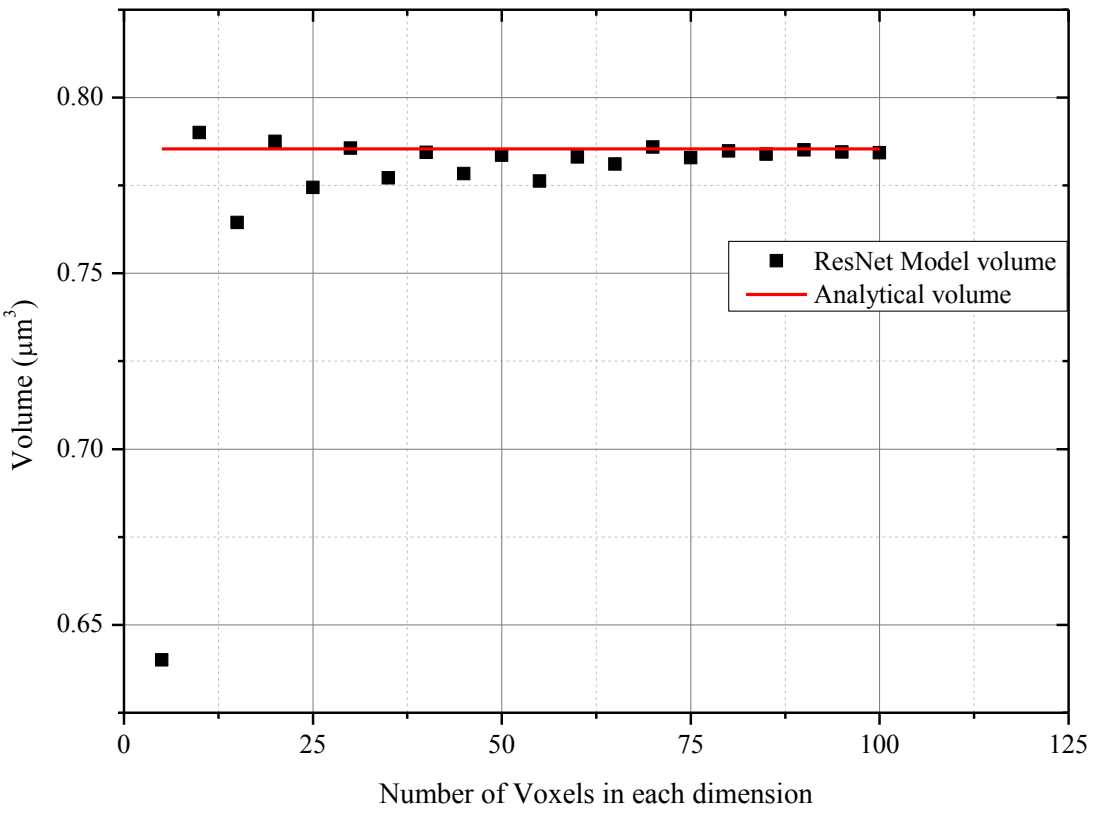


Figure 3.3 – Variation of structure volume for different discretization resolutions. The structure studied is a cylinder of length 1 µm and radius 0.5 µm, discretized within a cube of length 1 µm.

We now consider a more complex geometry. Nelson et al. (Nelson et al., 2011) approximated the geometry of SOFC electrodes by the use of truncated cones connected in series. A truncated cone is thus chosen as case 3. By taking infinitesimally small sections of the truncated cone and assuming a uniform current and potential distribution on each section face, an analytical solution can be derived for the equivalent resistance of this structure. This analytical resistance is given by

$$R_c = \frac{\rho_{Ni} L}{\pi a b} \tag{3.1}$$

where $R_c$ is the equivalent cone resistance, $\rho_{Ni}$ is the resistivity of nickel at 1073 K, $L$ is the length of the cone, $a$ is the inner radius and $b$ is the outer radius (Kai , 2003). The outer radius is fixed at 0.5 µm and the length at 1 µm. Equation 3.1 can be compared to that used to find the equivalent resistance of a cylinder, where $\pi ab$ can be seen as an average surface area which is confirmed by the fact that the equation was obtained by integration.

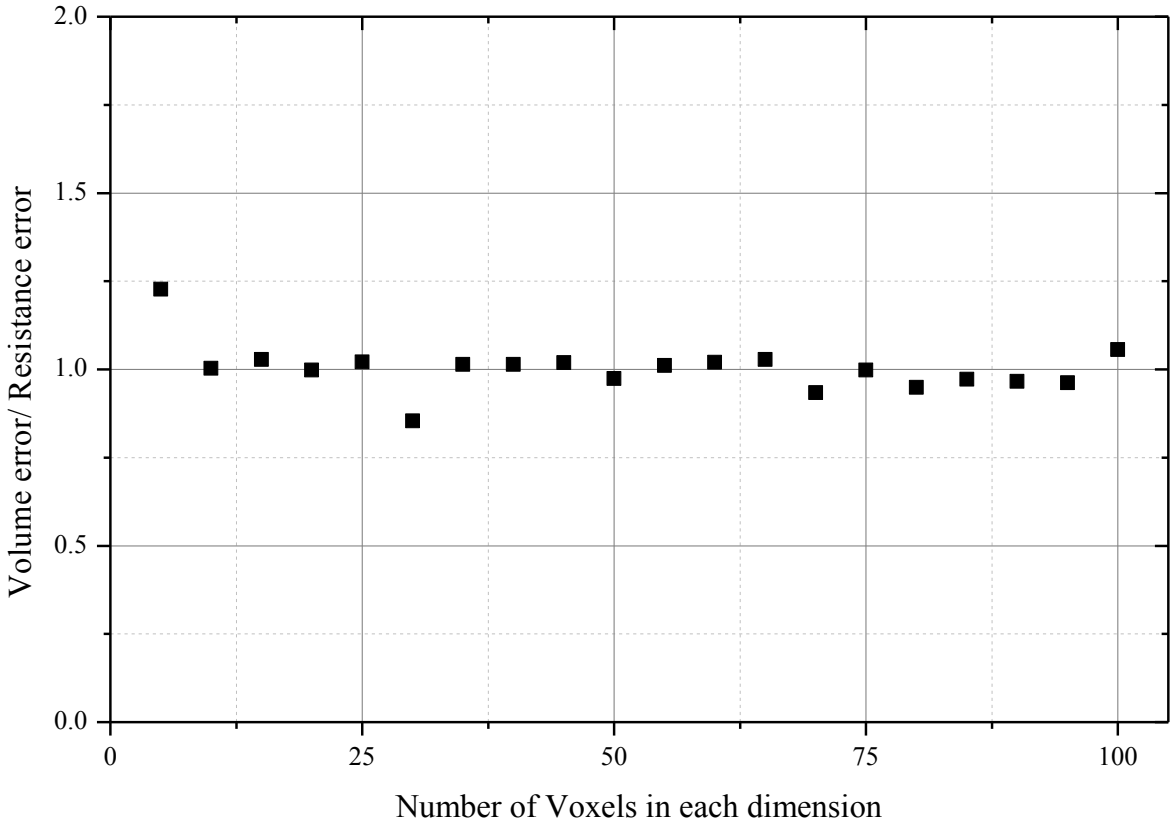


Figure 3.4 – Volume error divided by equivalent resistance error at each discretization resolution for the cylinder of length 1 μm and radius 0.5 μm, discretized within a cube of length 1 μm.

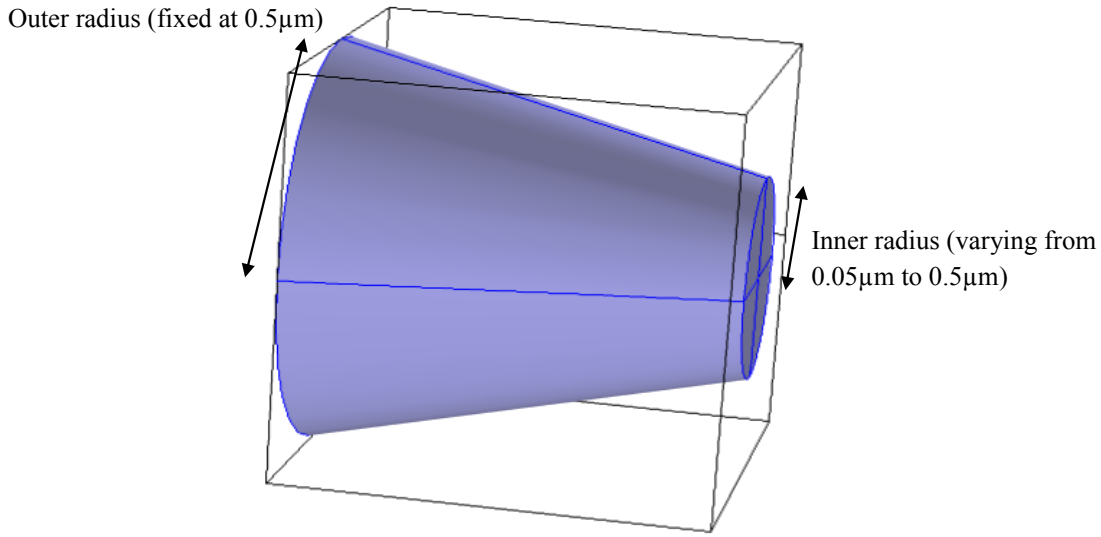


Figure 3.5 - Graphical representation of the cone under study with relevant dimensions. When used in the ResNet model, the cone is discretized within a cube of length 1µm in which the volume not occupied by the cone is defined as an arbitrary material of conductivity $1x10^{-8}$ S/µm.

The cone analyzed is illustrated in Figure 3.5 and is discretized in a cube of non-conductive material, similar to the cylinder used in case 2. Figure 3.6 shows the equivalent resistance of a cone as a function of the smallest radius for different discretization resolutions. In this figure, the computed equivalent resistances given by the ResNet model for different discretization resolutions are compared against those scaled to the volume fraction content of nickel of the chosen discretized structures (this is achieved by multiplying the conductivity of nickel by the volume fraction occupied by the said material in the analyzed structure) as is done in a previously developed model employed by Golbert et al. (Golbert et al., 2007). In all cases, the deviation between the equivalent resistance given by Equation 3.1 and that given by the "scaling" model described above is greater than that between the equivalent resistance obtained with the ResNet model and that given by Equation 3.1. Although a similar trend is observed between the equivalent resistances computed with the proposed model and those predicted by Equation 3.1, an increasing deviation is observed with increasing heterogeneity in the geometry and a decreasing discretization resolution, as expected. In Fig. 3.7 the greatest difference occurs when the inner radius is equal to 0.05 µm and outer radius to 0.5 µm, which can also be thought of in terms of the slope of the cone, defined as $Slope = {}^{\Delta y}/_{\Delta x}$ in this case being $Slope =$

$(0.5 - 0.05)/_1 = 0.45$. It can also be seen that there is a non-linear variation of predicted resistances given by the ResNet model for different discretization resolutions. For example when the structure is discretized into 20×20×20 voxels, the predicted equivalent resistance is lower than the analytical solution for the cases where the inner radius is 0.05 µm, 0.1 µm and 0.15 µm. For larger radii the predicted resistance becomes higher than the analytical solution.

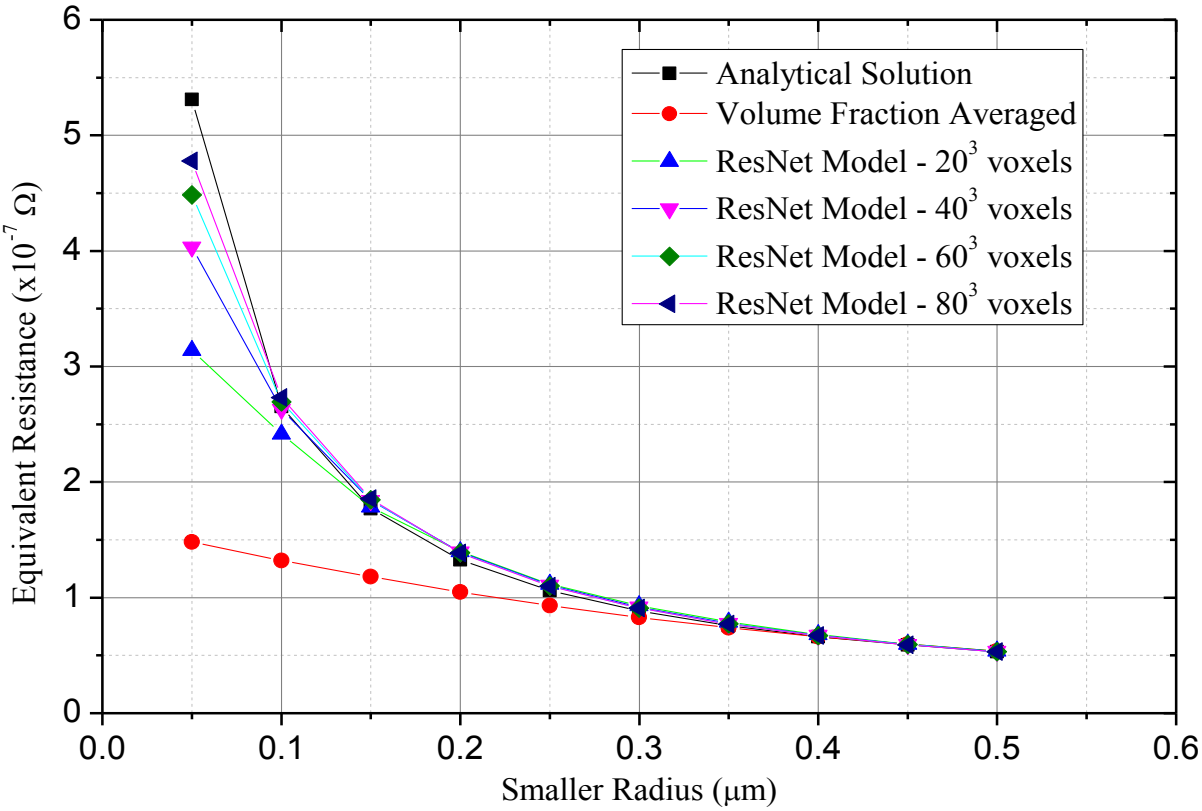


Figure 3.6 - Equivalent resistance of a cone as a function of its smallest radius. The black squares denote the analytical results, results given by averaging the conductivity of pure nickel to the volume fraction of nickel in the discretized structure are denoted by the red circles and the others are results given by the ResNet model using varying numbers of voxels to describe the cone.

One can, from the onset, expect the analytical solution given by equation 3.1 to perform poorly when looking at highly heterogeneous cones due to the assumptions made in deriving it. These assumptions are equivalent to saying that the lines of equipotential, when looking at sections of the cone in the z-axis, are straight and parallel to each other.

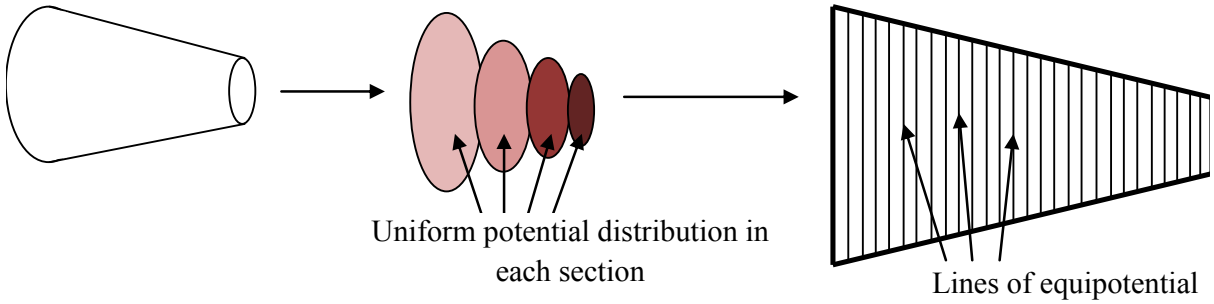


Figure 3.7 – The assumption made by the analytical solution is that the potential is uniformly distributed in each section of the cone.

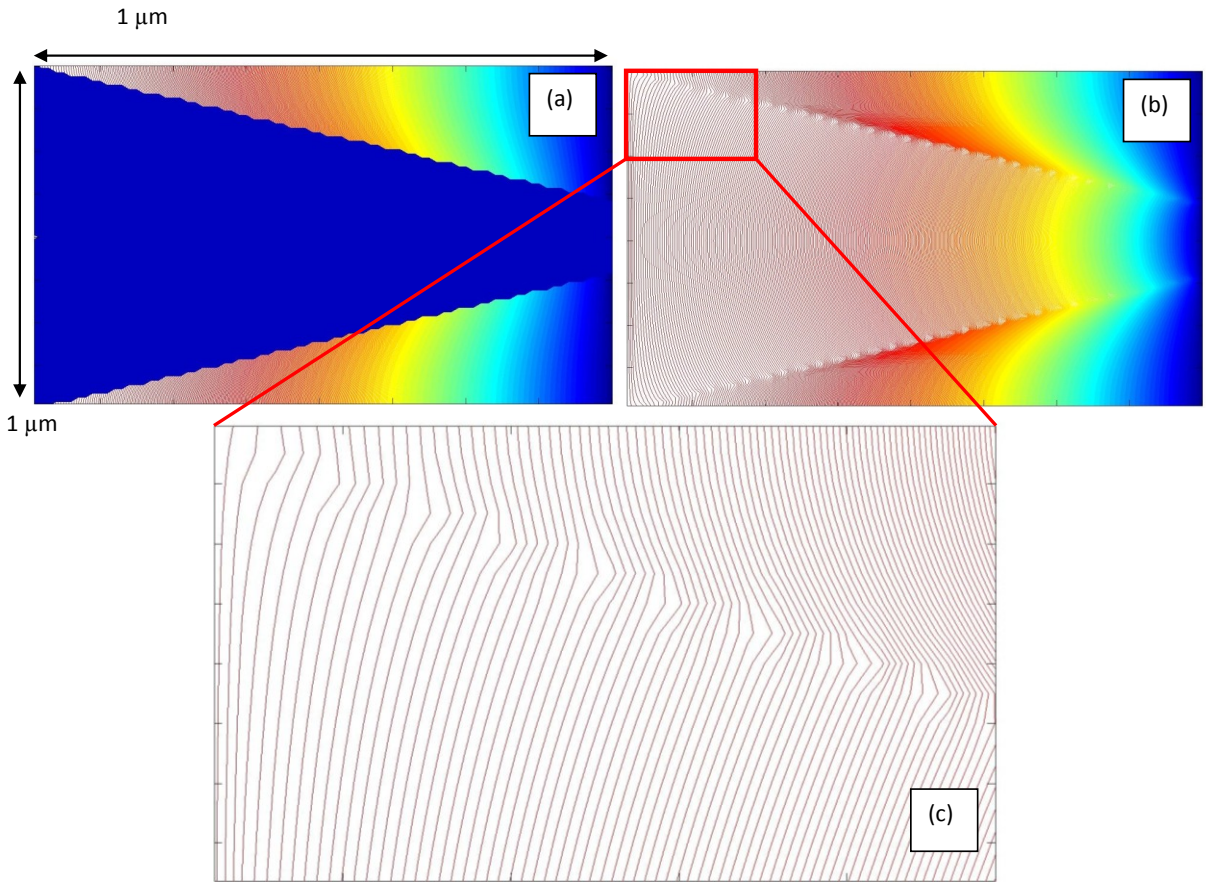


Figure 3.8 – A z-plane section showing the equipotential lines through a cone of slope 0.25 discretized in a cube by 64,000 voxels (40 in each dimension). (a) shows a z-plane section of the discretized cone with the equipotential lines through the cube in which the cone is discretized, (b) shows the equipotential lines through a z-plane section of the structure as a whole and (c) shows a magnified view of the equipotential lines going through the structure at the upper-left boundary.

Figure 3.8 illustrates the assumption made in obtaining the analytical solution, and Figure 3.8 presents a contour plot of the potential array obtained with the ResNet model in the case where the cone has a smaller radius of 0.1µm and is discretized by $80^3$ voxels. This effectively yields a plot of the equipotential lines through the cone when looking at a z-section of the potential matrix, and as can be seen these lines are not straight and parallel, but curve up nearer to the boundaries so as to be perpendicular to them. Based on the data presented in Figure 3.6, alongside the equipotential line distribution shown in Figure 3.8, we can conclude that the

assumptions made in deriving Equation 3.1 render the analytical formulae increasingly inaccurate for truncated cones with increasingly large slopes and hence that the deviations between the ResNet model and the analytical solution observed in Figure 3.6 also reflect the limiting assumptions made in deriving the analytical formulae. As such it is not possible to compare the ResNet model output to an analytical solution for cones of high heterogeneity.

The final analysis of this chapter consists of investigating further the minimum discretization resolution required to achieve convergence. It is understood that, as is the case in any discretization process, an increasing resolution leads to a convergence of results. This is not very clear in Figure 3.8, so the analysis made is presented differently in Figure 3.9 where the equivalent resistances given by the ResNet model for four different cones with slopes increasing from 0.3 to 0.45 in steps of 0.05 are plotted against the discretization resolution used in each case. It can be noticed that the residual difference between the analytical solution and that given by the model increases with increasing slope. These results highlight the residual deviation between the converged equivalent resistance as predicted by the ResNet model and that given by the analytical solution, this difference indeed becomes greater as the slope increases. However, the discretization resolution needed for convergence (the convergence criteria here being defined as a change by less than 1% in two consecutive data points) increases with increasing slope. Indeed, when we plot the minimum resolution required to achieve convergence against slope, a clear trend can be seen showing an increasing discretization resolution required for cones of higher slopes. This trend is shown in Figure 3.9, where the sporadic distribution of data points at low resolutions can be attributed to the nature of the discretization process. Cubic voxels are therefore shown to not handle well large slopes at low resolutions. The solutions to this are either to consider fine enough resolutions when looking at structures containing a certain degree of heterogeneity or anisotropy, or to use either cylindrical coordinates or adaptive meshes.

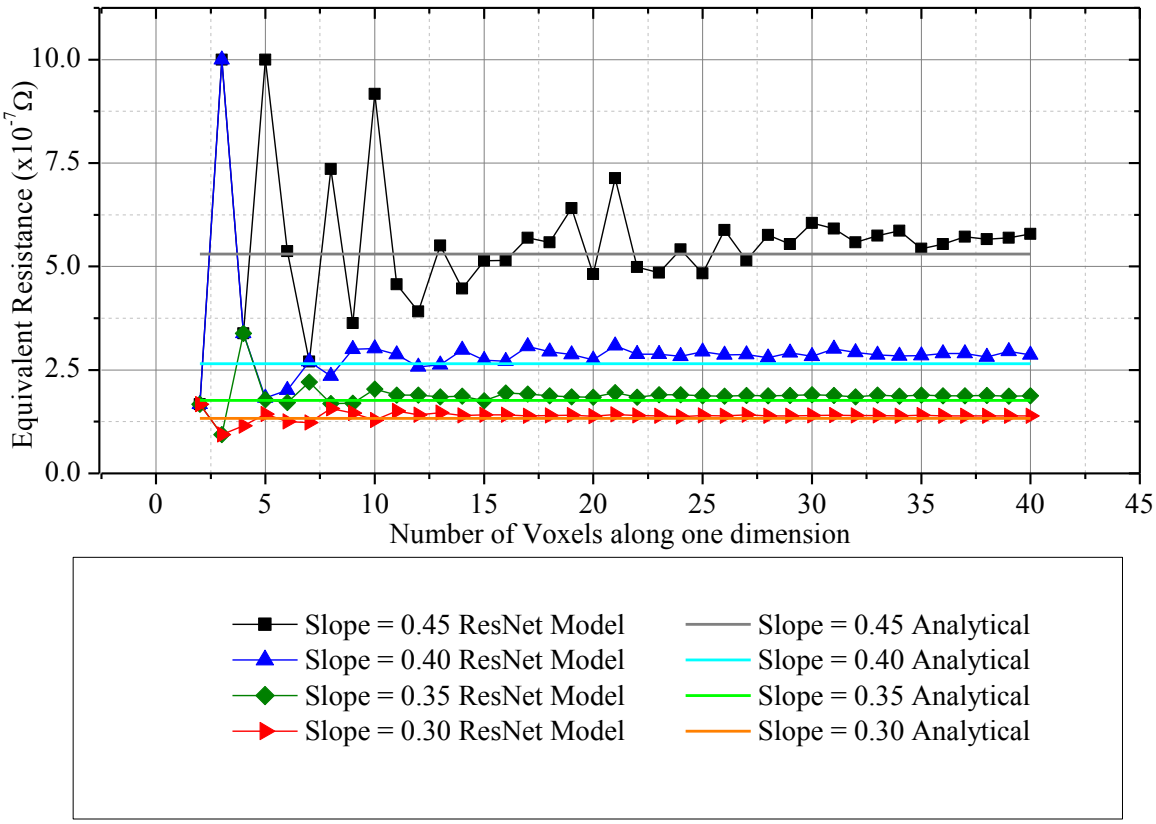


Figure 3.9 –Equivalent resistance of four cones with slopes varying from 0.3 to 0.45. The lines show the analytical solution given by Equation 3.1, and the data points show the equivalent solution given by the ResNet model for each cone at the different discretization resolutions.

Overall it is understood that, although the volume of a cone becomes smaller with a decreasing inner radius, the equivalent resistance of this cone will become larger with a decreasing area of contact with the current collector as this radius decreases. The proposed model is shown to capture this, which is crucial in its application to SOFC anodes due to the tortuous and highly heterogeneous nature of their microstructures.

## 3.3 - Model validation against COMSOL – complex synthetic structures

In the previous section, relatively simple structures made to represent two materials of different conductivity were analyzed and the equivalent resistances of these structures as given by the ResNet model were compared to those given by analytical formulae. In this section more

complex structures are examined and the equivalent resistances as given by the ResNet model are compared to those given by a dynamic mesh discretization and the application of charge conservation equations identical to those used by the ResNet model in COMSOL Multiphysics for the same structures, as analytical solutions are not available.

Nelson et al. (Nelson et al., 2011) approximated the geometry of SOFC electrodes by the use of truncated cones connected in series and this provides an interesting test case. The first type of structure considered is thus a cuboid of essentially non-conductive material containing a truncated cone extruded at each extremity, or effectively a truncated cone with two cylinders at either end sharing the same radius as the face on which they are attached. This structure is illustrated in Figure 3.10. The "conical" structure is given the conductivity of nickel at 1073 K, or 2.4 S/µm (Tseronis et al., 2008) and the rest of the cuboid is given an arbitrarily low conductivity of $10^{-8}$ S/µm.

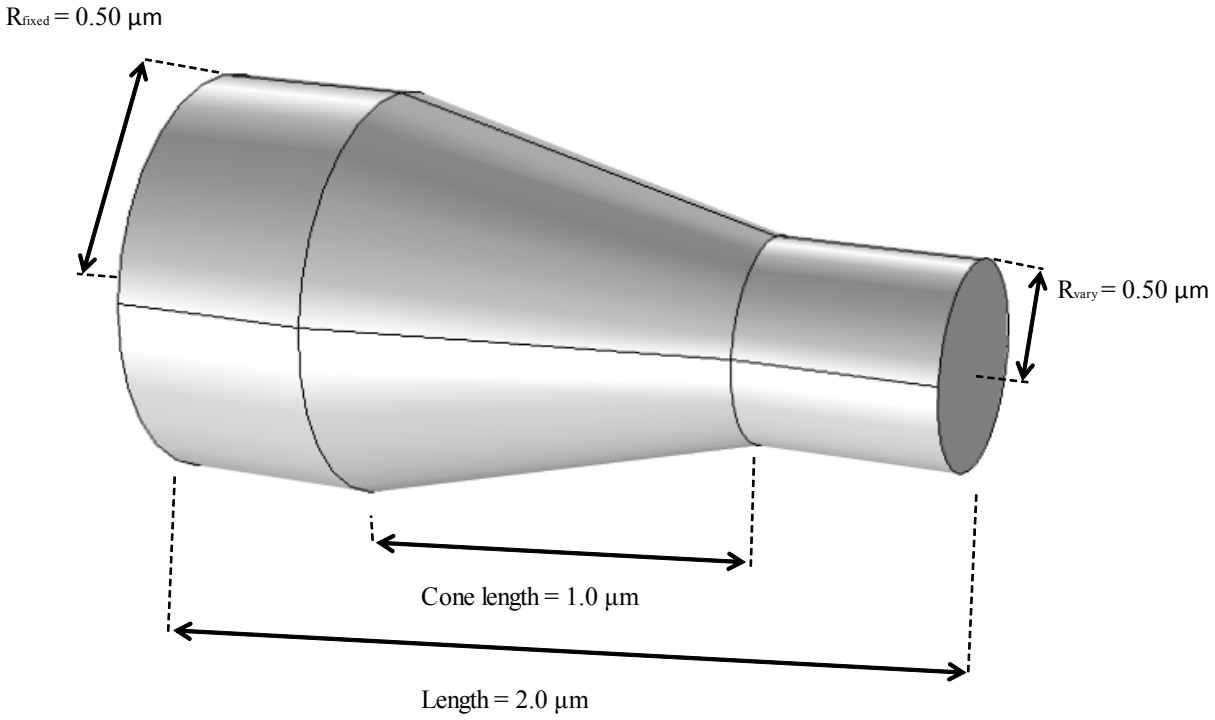


Figure 3.10- Graphical representation of the conical structure under study with relevant dimensions. When used in the ResNet model, the cylinder is discretized within a cuboid of length 2µm in which the volume not occupied by the conical structure is defined as an arbitrary material of conductivity $1x10^{-8}$ S/µm.

The smaller radius (or $R_{vary}$) of the structure illustrated in Figure 3.10 is changed from 0.40 μm to 0.15 μm to investigate the effect of an increasing heterogeneity on the computed equivalent resistance by the ResNet model. A comparison of the equivalent resistance of this structure computed by the ResNet model and that computed by COMSOL is shown in Figure 3.11 as a function of $R_{vary}$.

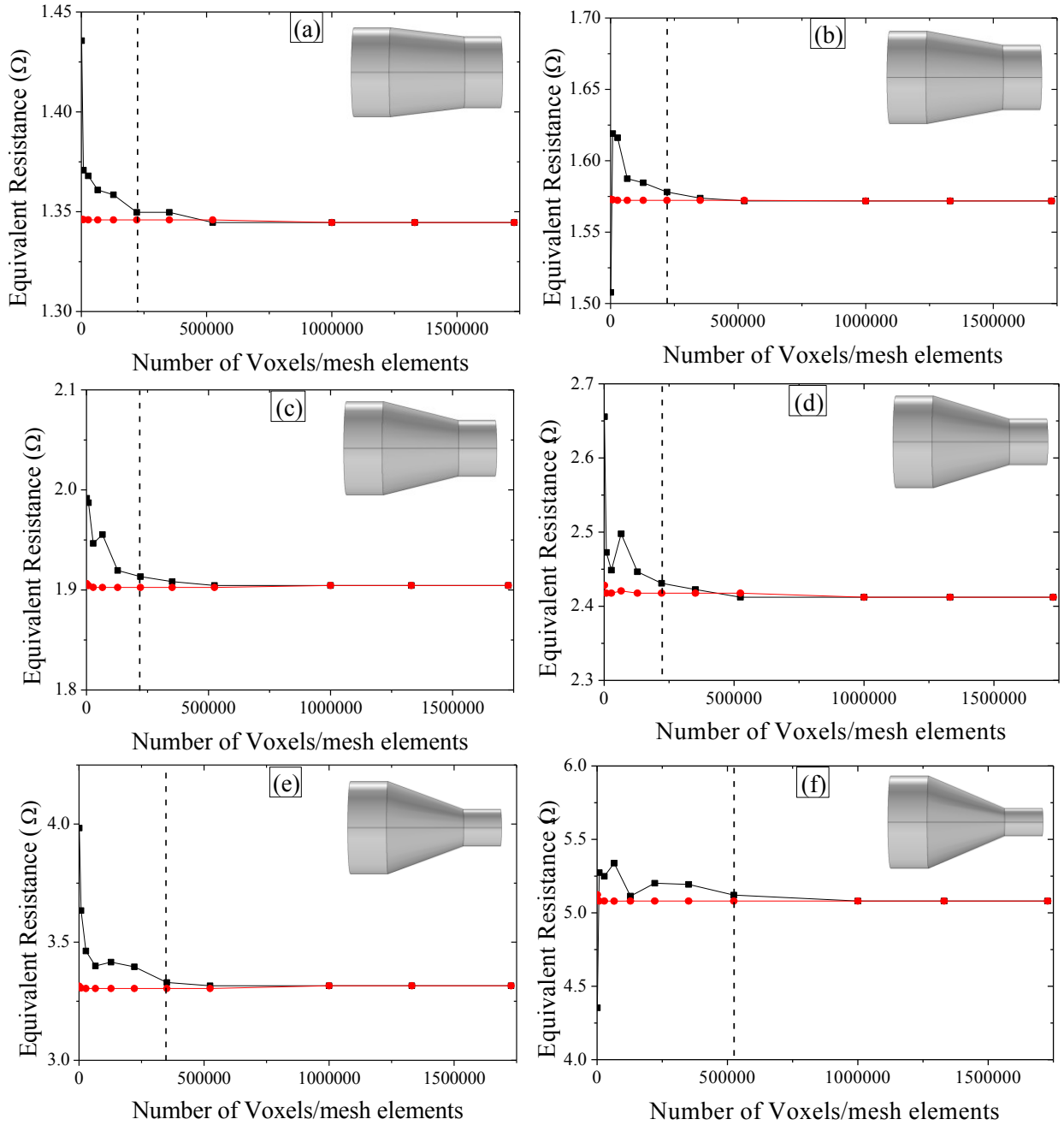


Figure 3.11 – Equivalent resistance of eight conical structures with smaller radii varying from 0.4 to 0.15 µm in steps of 0.05 µm, (a) showing results for $R_{vary}$ = 0.4 µm, (b) for $R_{vary}$ = 0.35 µm, (c) for $R_{vary}$ = 0.3 µm, (d) for $R_{vary}$ = 0.25 µm, (e) for $R_{vary}$ = 0.2 µm and (f) $R_{vary}$ = 0.15 µm respectively. Square symbols indicate the equivalent resistances given by the ResNet model for each cone at the different discretization resolutions and the circle symbols indicate the equivalent resistances given by COMSOL at the corresponding mesh resolutions.

For each structure considered, the discretization resolution of the ResNet model is gradually increased alongside the equivalent mesh resolution used in COMSOL for a relevant comparison. For every structure considered, COMSOL converges at a much lower resolution than the ResNet model. An adaptive tetrahedral mesh is used in COMSOL, meaning that at low meshing resolutions the discretized structure more closely matches the true structure than the cuboidal discretization of ResNet. These differences are illustrated in Figure 3.12.

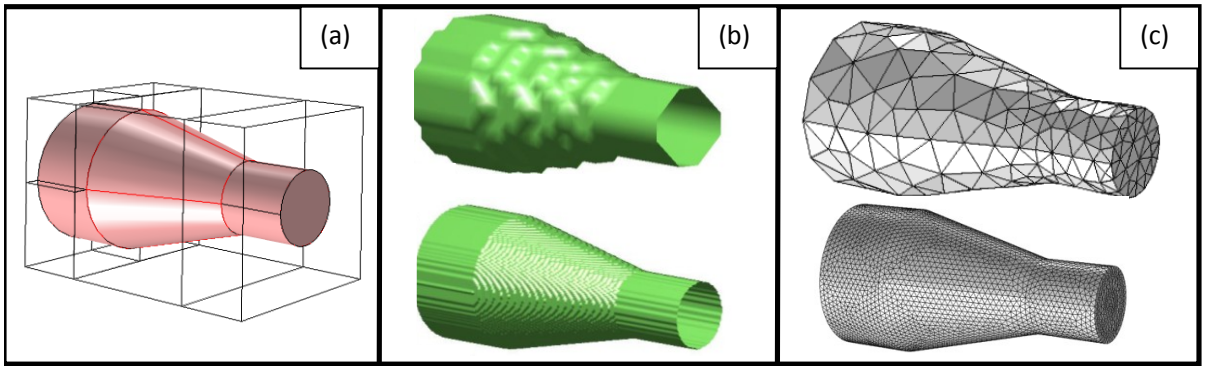


Figure 3.12 - Graphical representation of the discretization process employed by the ResNet model and the meshing approach employed by COMSOL. (a) The original structure as used in COMSOL; (b) the discretized form, with a coarse resolution of 8192 voxels and a fine resolution of 1769472 voxels for use by the ResNet model; (c) the meshed form showing a coarse resolution of 8632 mesh elements and a fine resolution of 1815465 mesh elements for use in COMSOL.

In every scenario considered for case 1, the convergence of the ResNet values with COMSOL values is achieved at gradually higher resolutions as the heterogeneity of the structure increases. For example, when $R_{vary}$ is 0.15 µm, the resolution required for the difference between the equivalent resistance given by the ResNet model and that given by COMSOL to be less than 1% is about 50,000 voxels, whereas the minimum resolution required when this same radius is increased to 0.4 µm (i.e. lower heterogeneity) is about 20,000 voxels. Overall, however, we can conclude that the ResNet model gives results that are matched with those computed by

COMSOL Multiphysics in this first case, provided sufficient voxels are used to properly describe the structure.

To assess the ResNet model further, analyses were next carried out on microstructures sharing an increasing resemblance to real SOFC microstructures, with the end aim of analyzing an actual experimental data set as shown in the following chapter. For the second case study, two hemispheres are modeled with an increasing area of contact (or degree of overlap). This structure is once again positioned in a cuboid element, this time with a fixed length of 1 μm and with width and height equal to the diameters of the two particles. These diameters are increased from 0.5 μm to 0.7 μm, yielding an increase in the degree of overlap $\gamma = 0.5 - R$ from 0 μm to 0.4 μm. The equivalent resistances of these structures are computed for different discretization resolutions by the ResNet model, and compared against those given by COMSOL for the corresponding meshing resolutions in Figure 3.13. In both the COMSOL and ResNet computations, the same phase conductivities are used for both the conducting and non-conducting phases.

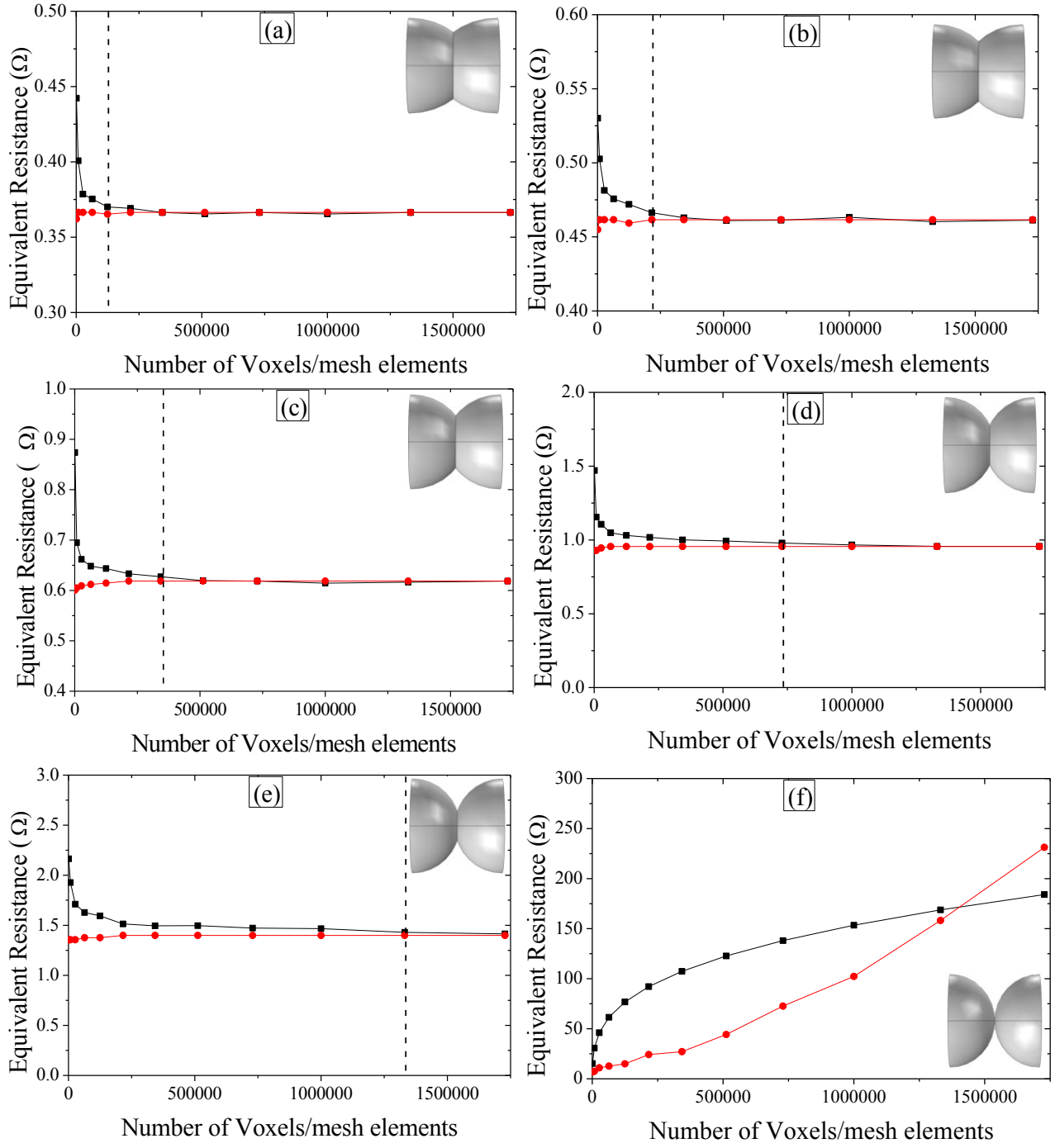


Figure 3.13 – Equivalent resistance of six sets of two semi-spheres in contact with length of overlap varying from 0 to 0.4 μm. (a) shows the results for γ = 0.4 μm, (b) for γ = 0.3 μm, (c) for γ = 0.2 μm, (d) for γ = 0.1 μm, (e) for γ = 0.05 μm and (f) for γ = 0 μm. The square symbols indicate the equivalent resistances given by the ResNet model for each structure at the different

discretization resolutions, and the circle symbols show the equivalent resistances given by COMSOL at the corresponding mesh resolutions.

An analysis of the results shows that the minimum discretization resolution required to ensure a difference of less than 1% between the output of both models increases as the length of overlap decreases, except in the case of tangent spheres ($\gamma$=0). In this case we can see that the solutions diverge (see Fig. 3.14 (f)) and both the ResNet model and COMSOL calculations predict increasing resistances for increasing resolutions. This behavior was investigated further by the author, as well COMSOL technical support (Friedel, 2012) by varying the type of mesh used as well as the position of the nodes of these meshes. Convergence could not be achieved in any of the configurations available, and it was concluded that the issue lies in the definition of the problem itself. Indeed, only a point contact exists, rendering the problem abstract. This point contact is a notional point with an infinitely small area of contact. As both the ResNet model and COMSOL both rely on a discretization of the structure, they both predict increasing values of resistance for increasing mesh resolutions. This is due to the fact that this area is defined as finite after the discretization process, and this value decreases as the resolution increases.

It is therefore concluded that the particular behavior of the results presented in Figure 3.13 (f) are due to the nature of the structure presented as in this case, only a point contact exists, rendering the problem abstract. For all other cases, convergence is achieved, and the resolution required is seen to increase alongside the heterogeneity of the structure. To overcome this issue, it is proposed to clearly define any such point of contact either as a finite area of contact, or a clear disconnect in the electronic pathway. This can be easily achieved at the image reconstruction stage immediately following sampling when real microstructures are considered.

In order to continue to approach real SOFC microstructures, a system of overlapping spheres with a central void (pore space) is analyzed in a third case study. Four quarters-of-spheres are discretized in a cube with a uniform length of 1 μm as shown in Figure 3.14. This cubic element can then be agglomerated into a system of overlapping spheres as shown in Figure 3.16. Before this agglomeration is used in a simulation, it was first chosen to analyze one of these cubic elements by varying the length of overlap of the four quarter-of-spheres, similar to case 2. The

results of these simulations, also performed with an increasing discretization/meshing resolution, are presented in Figure 3.15. These results follow the trend observed in cases 1 and 2, and convergence is obtained in every case for a sufficiently fine resolution. The case where R = 0.52 μm represents the case with the highest heterogeneity, and here convergence is achieved for a resolution of at least 1 million voxels or mesh elements.

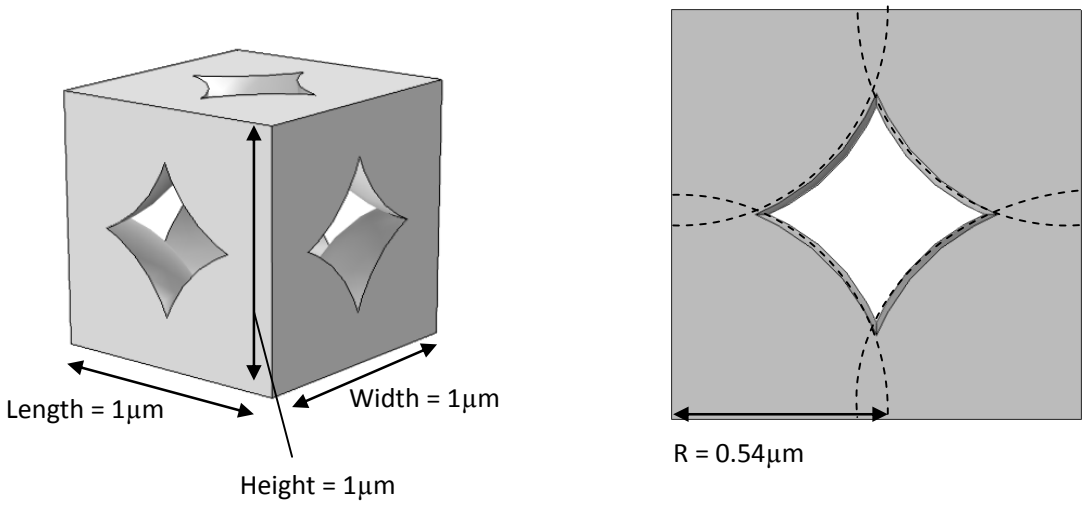


Figure 3.14 - Graphical representation of the four quarters of spheres under study with relevant dimensions. When used in the ResNet model, the structure is discretized within a cuboid of length 1μm in which the volume not occupied by the spherical structure is defined as an arbitrary material of conductivity $1x10^{-8}$ S/μm.

Case 4 represents a number of the structures analyzed in case 3, arbitrarily chosen as that where R = 0.56 μm. Sixty-four elements were combined to create a system consisting of 4×4×4 elements, representing 27 complete spheres and 98 portions of spheres sectioned by the boundaries of the domain. The discretization/meshing resolution was again varied, and as can be seen in Figure 3.17, convergence occurs at around 100,000 voxels. By comparing these results with those presented in Figure 3.15, we would expect this minimum resolution to be proportional to the ratio in sizes between the structure analyzed in case 4 and that presented in case 3. Indeed, this would yield a similar change in volume and hence would represent each "block" with the same accuracy. The uniform length of the structures in case 3 is set to 1 μm, and that in case 4 is scaled up to 4 μm, yielding an enlargement ratio of 1:4. In case 3, the equivalent resistance of

this particular structure converges for a resolution of approximately 25,000 voxels. This corresponds to $1/4^{th}$ of the resolution required for convergence in case 4, confirming the consistency of results given by the ResNet model. This also confirms that the optimum discretization resolution needed by the ResNet model for reliable results solely depends on the heterogeneity of the considered structure. Furthermore, the corresponding resistance of the agglomerated structure is found to be 0.869 Ω/μm calculated using Equation 2.13 and the converged resistance value. Using the converged resistance of structure (d) in Case 3 yields the same effective conductivity of 0.869 Ω/μm. This shows good agreement as this structure was simply tessellated to create the structure analyzed in Case 4, meaning that the effective conductivity should stay the same. However, the behavior of the effective conductivity observed in 3.15 (d) differs from that presented in Figure 3.17. This is attributed to the discretization process; instead of only needing to discretize a single structure as is done in Case 3, an aggregation of 64 structures is now instead discretized by the same number of voxels. This effectively drastically changes the architecture of the microstructure being analyzed, to the point where it becomes impossible to identify each individual "block" at low resolution. The non-monotonic trends observed in the results are attributed to numerical artefacts. Indeed in some cases the discretized structure, albeit being very different from the original structure, is as conductive as that original structure. This means that at some coarse resolutions some structures achieve convergence.

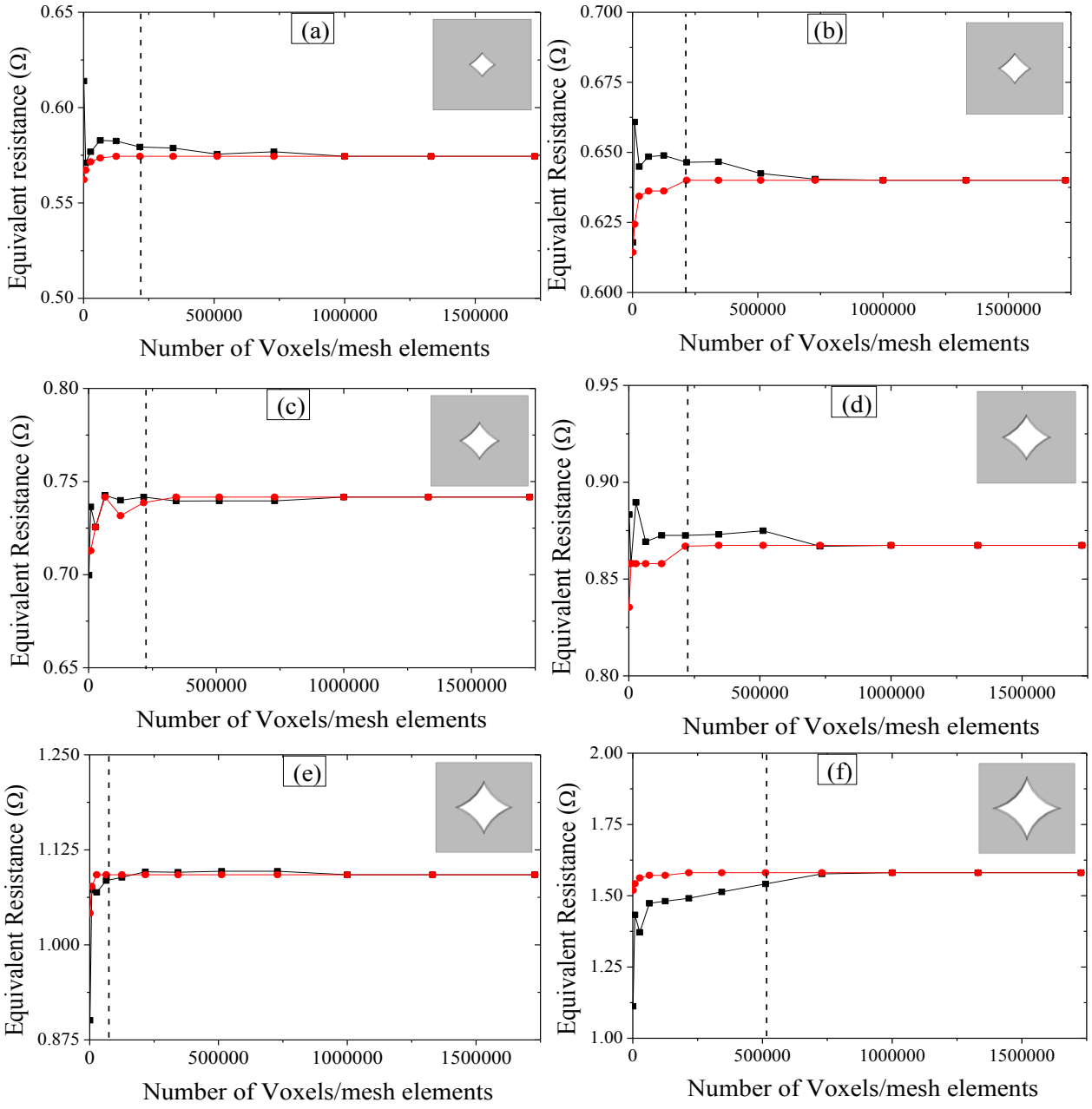


Figure 3.15 – Equivalent resistance between the opposite faces of six sets of four quarter-spheres in contact with radius varying from 0.62 to 0.52 µm in steps of 0.02 µm. (a) shows results for the case where R = 0.62 µm, (b) where R = 0.6 µm, (c) where R = 0.58 µm, (d) where R = 0.56 µm, (e) where R = 0.54 µm and (f) the case where R = 0.52 µm respectively. The square symbols indicate the equivalent resistances given by the ResNet model for each structure at the different

discretization resolutions, and the circle symbols show the equivalent resistances given by COMSOL at the corresponding mesh resolutions.

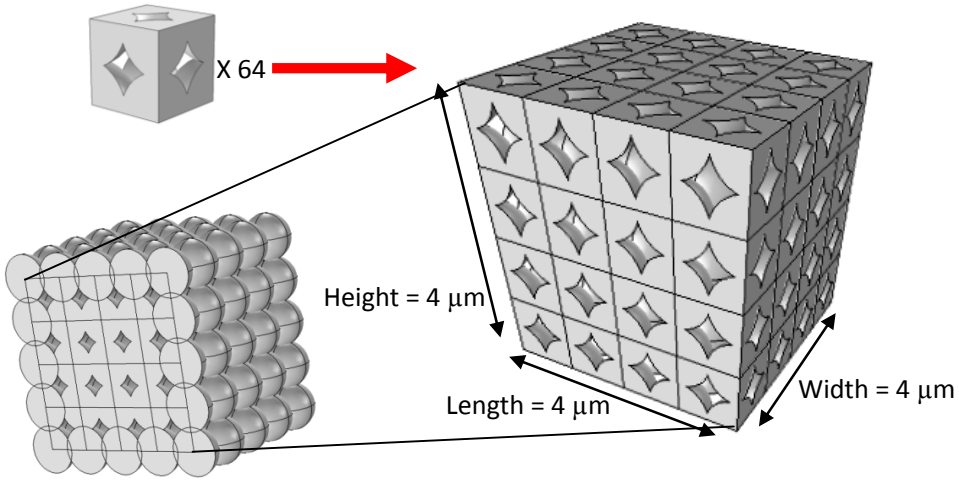


Figure 3.16 - Graphical representation of the sphere array under study made by agglomerating the structures illustrated in Figure 3.14. When used in the ResNet model, the structure is discretized within a cuboid of length 4µm in which the volume not occupied by the spherical structure is defined as an arbitrary material of conductivity $1x10^{-8}$ S/µm.

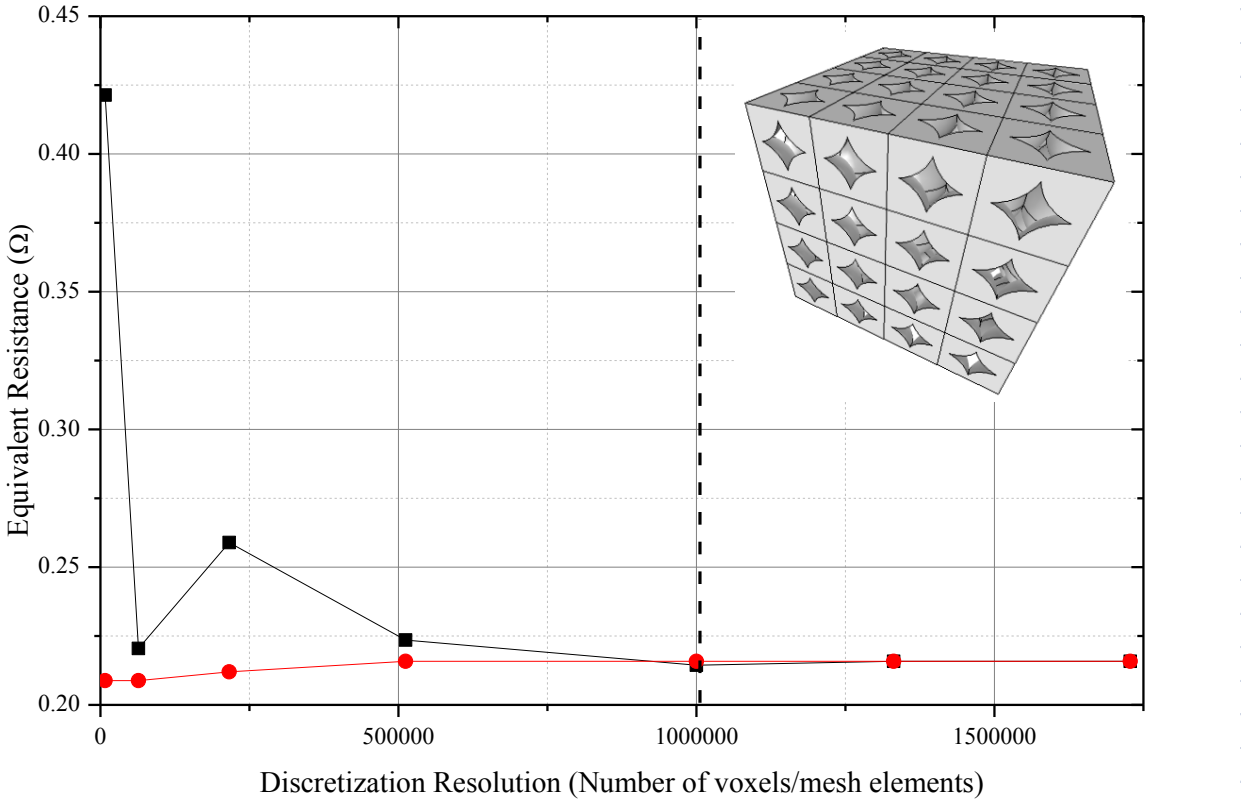


Figure 3.17 - Equivalent resistance of a sphere array as illustrated in Figure 3.16, with a radius of 0.56 µm. The square symbols show the equivalent resistance given by the ResNet model for each structure at the different discretization resolutions and the circle symbols show the equivalent resistance given by COMSOL at the corresponding mesh resolutions.

In all cases considered in this Chapter, COMSOL is seen to converge at much lower discretization resolutions than the ResNet model. This was found to be due to the dynamic discretization process used by COMSOL. In each case, both models required similar computational time for the solution to be formed. This commercial platform is capable of using a direct solver instead of the iterative process already selected in the base settings, but the question of which method is faster is irrelevant here as both approaches use the same fundamental equations. Only the difference in discretization processes causes variations in computed results, the computation of the solution itself is a discipline in itself and both platforms use a different approach.

Now that the ResNet model was shown to agree with COMSOL for a sufficiently high degree of resolution for the cases considered, the behavior of the ResNet model was investigated further by analyzing a final case study.

For this final case study, a system of randomly packed spheres was chosen as the case more closely approaching an SOFC electrode. After packing, the spheres were uniformly enlarged by a factor of 1.2 in order to have a structure approaching a real electrode post-sintering as per the approach of Cai et al. (Cai et al., 2010, 2011). The structure considered has a uniform length of 5 μm and was packed with spheres of diameter 1 μm (only the centre of the spheres are defined as being in the domain) where 40% of the space occupied in the domain represent nickel particles, and in a second instance with a nickel content of 30% by volume. Figure 3.18 illustrates the first of these two structures, before the enlargement factor was applied.

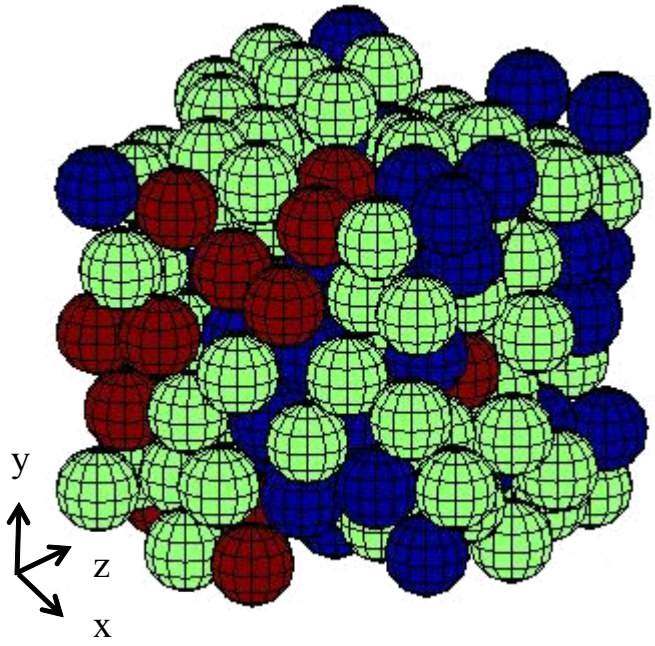


Figure 3.18 – Graphical representation of the particle distribution in a structure of uniform length 5 μm and particle diameter 1 μm post-sintering. Green spheres represent nickel particles, blue spheres represent YSZ particles and red spheres represent pore particles. In this case 40% of the volume occupied in the structure represents Nickel.

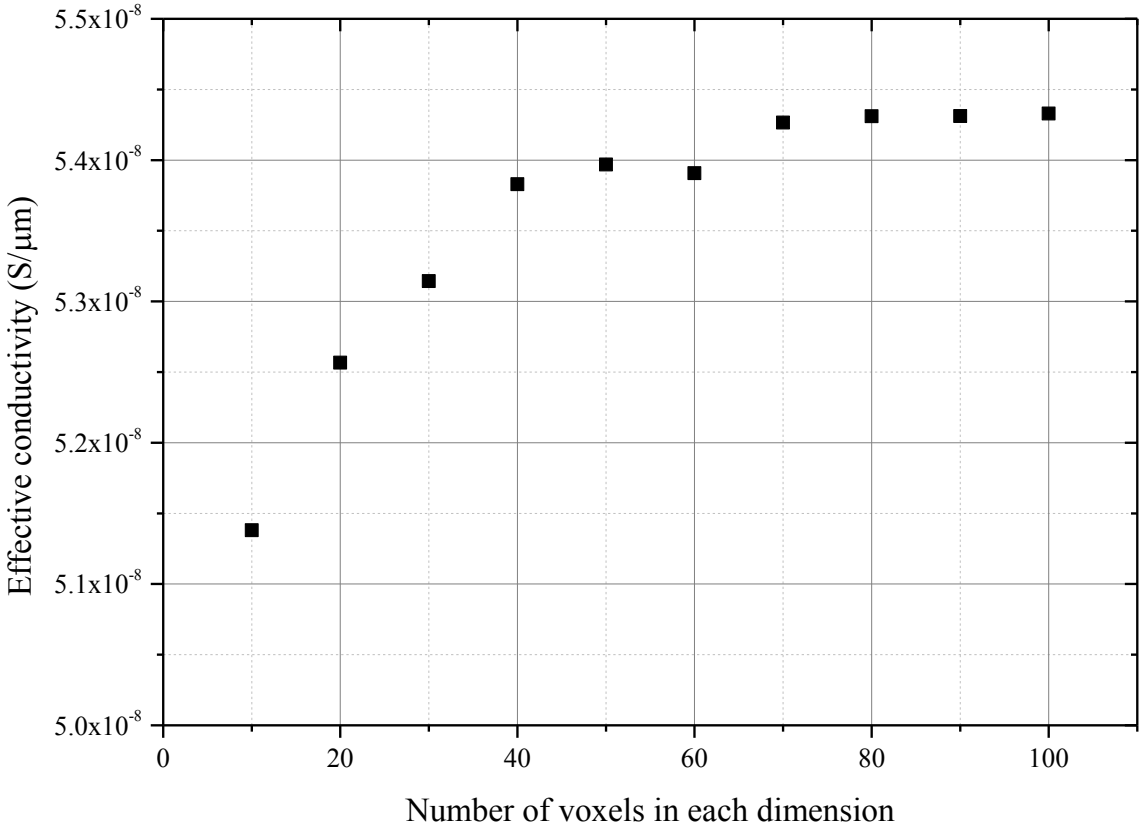


Figure 3.18 - Effective conductivity of a synthetic electrode of length 5 μm with a nickel content of 40% by volume. Spheres of initial diameter of 1 μm are used to discretize the particles, before they are expanded by a factor of 1.2. The square symbols show the effective conductivity given by the ResNet model for this structure at different discretization resolutions.

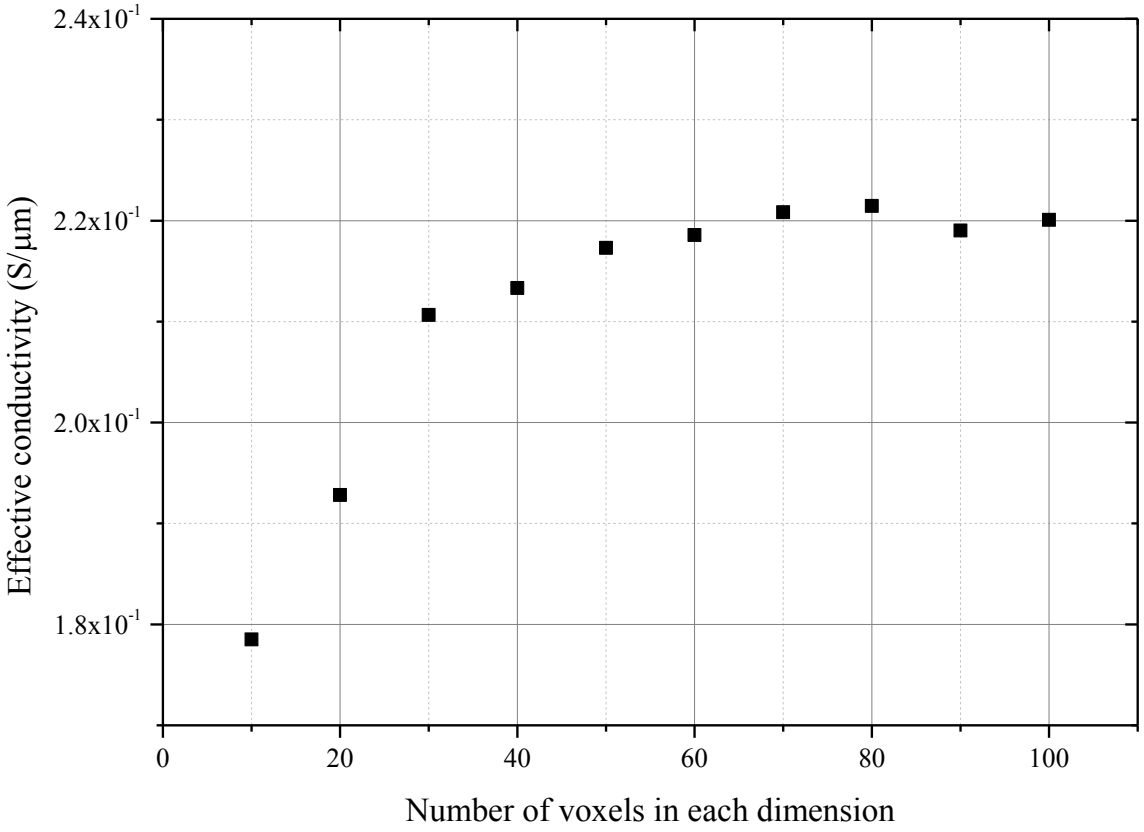


Figure 3.19 - Effective conductivity of a synthetic electrode of length 5 μm with a Nickel content of 30%. Spheres of initial diameter of 1 μm are used to discretize the particles, before they are expanded by a factor of 1.2. The square symbols show the effective conductivity given by the ResNet model for this structure at different discretization resolutions.

The results of the application of the ResNet model to these structures can be found in Figures 3.19-3.20. Convergence was defined as the point when the difference between a data point and the last data point of the series is smaller than 5%, and the data points are seen to converge to a stable value. Figure 3.19 shows a much lower effective conductivity than the other case. This indicates that the microstructure is not conductive in the direction considered due to the particle distribution. Indeed, upon closer inspection of the structure there exists no conductive pathway of nickel particles between the x-boundaries. The 30% sample however is conducting, and this is due to the Monte-Carlo process used in generating the particles and their positions in the structure. It is a good example of how different two structures can be on a microstructural level when generated randomly, whether they have the same characteristics or not. The effective

conductivity of the 40% sample is shown to be conductive by 34.8% than the 30% sample. A larger number of pathways, as can be provided with the particle distribution, is not necessarily sufficient to ensure a higher effective conductivity as these pathways also need to be non-tortuous and provide as high a cross-sectional area as possible.

For the two structures considered, convergence is achieved for a resolution of 50 voxels in each dimension. Looking at how many of these spheres can fit along one side of the domain, and dividing the number of voxels that discretize that side by the number of spheres, shows that the two structures with the same particle size have an optimum value for the number of voxels per particle of 8. It can be concluded from this sample synthetic structure analysis that the optimum discretization required for converged, reliable results is ~10 voxels per particle. It can also concluded that the minimum resolution required for convergence is indeed based on the particle size, as it is analogous to the heterogeneity of the structure.

The data presented in this chapter provides the basis to move forward and tackle real electrode microstructures, where a concluding validation will be made with regards to the ResNet model.

## 3.4 - Conclusions

A numerical technique for calculating the effective conductivity of porous composite microstructures based on Kirchhoff's law of current conservation, the ResNet model, has been applied to microstructures discretized into small cubic elements (voxels). The ResNet model has been developed with the ultimate objective to compute the effective conductivity of real SOFC electrodes, and to be easily combined with a voxel-based model that relates electrochemical performance to microstructure (Golbert et al., 2007).

Structures of increasing level of complexity and resemblance to real SOFC electrode microstructures are considered, and different levels of discretization and meshing resolutions are employed. The results show agreement between the equivalent resistance given by the ResNet Model and analytical solutions for simple structures, as well as for cylinders where agreement

was found above a certain degree of discretization resolution. It was found that, for a truncated cone, an increasing difference between the inner and outer radius leads to a requirement for higher levels of discretization to achieve convergence. It was also shown that the analytical solution commonly used to derive the equivalent resistance of a truncated cone yields errors due to the assumption of uniform potential and current distributions throughout the structure.

The proposed model is also shown to agree with predictions made by COMSOL Multiphysics for four different types of synthetic microstructures, each increasingly approaching the microstructure of actual SOFC electrodes. In each case, it was shown that the discretization resolution required for the difference between results predicted by the ResNet model and those predicted by COMSOL to be less than 1%, increases with the heterogeneity of the structure considered. When a highly heterogeneous microstructure was considered the model was shown to predict converging solutions. It was finally shown that the optimum discretization level for a structure comprised of spherical objects is 10 voxels per particle for reliable results to be obtained, without wasting additional computational power, and that this optimum resolution solely depends on the heterogeneity of the structure considered.

The next sections will conclude the validation of the ResNet model by comparing extracted equivalent resistances of real SOFC anode microstructures to experimental values measured on these same microstructures. Furthermore the ResNet model will be integrated into the electrochemical simulation model for SOFC electrodes previously reported Cai et al. (Cai et al., 2010) to improve the way that this simulation captures electronic transport within the electrode. The validated model is foreseen to have a wide applicability to porous and tortuous structures (including those of SOFC electrodes) to derive the effective conductivity.

## 3.5 - References


Aguiar, P, Adjiman, C. S. & Brandon, N.P. (2005) Anode-supported intermediate-temperature direct internal reforming solid oxide fuel cell - II. Model-based dynamic performance and control. *Journal of Power Sources* 147(1), 136-147.

Brett D. J. L., Aguiar, P. & Brandon, N. P. (2006) System modelling and integration of an intermediate temperature solid oxide fuel cell and ZEBRA battery for automotive applications. *Journal of Power Sources* 163(1), 514-522.

Brett, D. J. L., Aguiar, P., Brandon, N. P., Coop, I., Dueck, J., Galloway, R. C., Grande, O., Hayes, G. W., Lillie, K., Mellors, C., Thompson, S., Tilley, A. R. & Wood, A. (2007) Operational Experience of an IT-SOFC/Battery Hybrid System for Automotive Applications. *ECS transactions* 7(1), 113-122.

Cai, Q., Adjiman, C. S. & Brandon, N. P. (2010) Investigation of the active thickness of solid oxide fuel cell electrodes using a 3D microstructure model. *Electrochemica Acta* 56(28), 10809-10819.

Cai, Q., Adjiman, C. S. & Brandon, N. P. (2011). Modelling the 3D microstructure and performance of solid oxide fuel cell electrodes: Computational parameters. *Electrochimica Acta* 56(16), 5804-5814.

Choi, H-W., Berson, A., Pharoah, J. G. & Beale, S. B. (2010) Effective transport properties of the porous electrodes in solid oxide fuel cells. *Journal of Power and Energy* 225(2), 183-197.

Friedel, S. (2012) COMSOL, personal communication (25th June 2012).

Golbert, J., Adjiman, C. S. & Brandon, N. P. (2008) Microstructural modeling of SOFC anodes. *Industrial and Engineering Chemical Research* 47(1), 7693-7699.

Golbert, J., Adjiman, C. S. & Brandon, N. P. (2007) Microstructural modeling of SOFC andoes. *SOFC -X*, 2041-2047.

Hahn, M., Schwarz, M., Kröplin, B-H. & Wallmersperger, T. (2011) Discrete Element Method for the thermal field: Proof of concept and determination of the material parameters, *Computational Materials Science,* 50(10), 2771-2784.

Isolevich, A., Kornyshev, A. A. & Lehnert, W. (1999). Statistical geometry of reaction space in porous cermet anodes based on ion-conducting electrolytes: Patterns of degradation. *Solid State Ionics*, 124 (3), 221-237.

Jeon, D. H., Nam, J. H. & Kim, C-J (2005) A random resistor network analysis on anodic performance enhancement of solid oxide fuel cells by penetrating electrolyte structures. *Journal of Power Sources* 139(1), 21-29.

Kai, K. (2003). *ESG Physics*. Lecture notes. Massachusetts: Massachusetts Instituted of Technology.

Leah, R.T., Brandon, N.P. & Aguiar, P. (2005) Modelling of cells, stacks and systems based around metal-supported planar IT-SOFC cells with CGO electrolytes operating at 500-600 degrees C. *Journal of Power Sources* 145(2), 336-352.

Mari, C. M. & Dotelli, G. (2000) A random resistor model to forecast the electrical properties of crystalline ionic conductor composites. *Solid State Ionics* 136(1), 1315-1319.

Metcalfe, C., Kesler, O., Rivard, T., Gitzhofer, F. & Abatzoglou, N. (2010) Connected Three-Phase Boundary Length Evaluation in Modeled Sintered Composite Solid Oxide Fuel Cell Electrodes. *Journal of the Electrochemical Society* 157(9), B1326-B1335.

Nelson, G. J., Peracchio, A. A. & Cassenti, B. N. (2011) Analytical Models for SOFC Electrodes with Variable Cross-Section Microstructures. *ECS SOFC XII* 35(1), 913-921.

Schneider, L. C. R., Martin, C. L., Bultel, Y., Bouvard, D. & Siebert, E. (2007) Discrete modelling of the electrochemical performance of SOFC electrodes. *Electrochemica Acta* 52(1), 314-324.

Schneider, L. C. R., Martin, C. L., Bultel, Y., Dessemond & L., Bouvard, D. (2006) Percolation effects in functionally graded SOFC electrodes. *Electrochemica Acta* 52(9), 3190-3198.

Sunde, S. (1995) Calculation of Conductivity and Polarization Resistance of Composite SOFC Electrodes from Random Resistor Networks. *Journal of the Electrochemical Society* 142(4), 50-52.

Terreros, I., Iordanoff, I. & Charles, J. L. (2013) Simulation of continuum heat conduction using DEM domains. *Computational Materials Science* 69(1), 46-52.

Tseronis, K., Bonis, I. & Kookos, I. K. & Theodoropoulos, C. (2012) Parametric and transient analysis of non-isothermal, planar solid oxide fuel cells. *International Journal of Hydrogen Energy* 37(1), 530-547.

Tseronis, K., Kookos, I. K. & Theodoropoulos, C. (2008) Modelling mass transport in solid oxide fuel cell anodes: a case for a multidimensional dusty gas-based model. *Chemical Engineering Science* 63(23), 5626-5638.

Zhang, Y., Xia, C. & Ni, M. (2012) Simulation of sintering kinetics and microstructure evolution of composite solid oxide fuel cells electrodes. *International Journal of Hydrogen Energy* 37(4), 3392-3402.

# Chapter 4 – Application of the ResNet model to a real SOFC anode.

## 4.1 – Introduction

In this chapter, a continuation of earlier work is presented aimed at developing and validating an effective conductivity model applicable to porous, composite SOFC electrode microstructures. In the previous chapters, the ResNet resistor network model was introduced alongside an initial validation against simple cases where effective conductivities were available analytically or in the literature. The model was investigated further by comparing the effective conductivities of more complex structures as computed by the ResNet model to those computed by COMSOL Multiphysics, a commercial modelling platform that relies on a different discretization strategy, for the same set of microstructures. The model is based on the work of Schneider et al. (Schneider et al., 2006) and relies on applying Kirchhoff's law of current conservation. The aggregation methodology of voxels into Volume Elements in the scope of the VOF approach chosen by Golbert et al. (Golbert et al.; 2008) is presented alongside the analysis of a Ni/10ScSZ electrode fabricated by Somalu et al. (Somalu et al., 2011) from which experimental effective conductivity values were extracted and compared to those computed by the ResNet model.

## 4.2 – Integration of Volume Elements

### 4.2.1 – Methodology

A new feature of the model presented in this chapter is the introduction of anisotropic VEs. The conductivity of each volume element in each direction can be obtained by computing the effective conductivity of each VE as an independent structure using the ResNet model, based on resistances at the voxel level. This provides a quantification of the heterogeneity of each VE and thus provides an improvement over the weighted average of conductivities used in earlier work (Golbert et al., 2007; Cai et al., 2011). Importantly, it enables the calculation of effective

conductivities for larger structures, through the two-level discretization into VEs and voxels. The resultant resistance for a VE $v$ along current direction $d$ ($d \in \{x, y, z\}$) is denoted by $S^{VE}_{v,d}$, and given by

$$s^{VE}_{v,d} = \rho_{v,d} \frac{l_{ve,d}}{A^{VE}_{v,d}} \quad , \qquad v=1,\ldots, N_v \text{ and } d \in \{x, y, z\} \tag{4.1}$$

where $\rho_{v,d}$ is the resistivity of VE $v$ in direction $d$ as computed by the ResNet model, $l_{ve,d}$ is the length of a VE along the direction of current flow, $N_v$ is the number of VEs, $A^{VE}{}_{v,d}$ is the cross-sectional area of VE $v$ perpendicular to current flow in direction $d$. The resistance between two adjacent non-boundary VEs $v$ and $w$ or two adjacent boundary VEs $v$ and $w$ is given by

$$S^{VE}_{vw} = \begin{cases} \frac{1}{2} s^{VE}_{v,d} + \frac{1}{2} s^{VE}_{w,d} & w \in \mathrm{N}_w, d = d_{a,vw} \\ 0 & w \notin \mathrm{N}_w \end{cases} \quad , v = 1, \ldots, N_v \tag{4.2}$$

Where $d_{a,vw}$ is the direction perpendicular to the face shared by the two neighbouring VEs $v$ and $w$, and $N_w$ is the set of VEs neighbouring VE $v$. For the case of a boundary VE $v$ and a neighbouring non-boundary VE $w$ it is given by

$$S^{VE}_{vw} = \begin{cases} s^{VE}_{v,d} + \frac{1}{2} s^{VE}_{w,d} & w \in \mathrm{N}_w, d = d_{a,vw} \\ 0 & w \notin \mathrm{N}_w \end{cases} \quad , v = 1, \ldots, N_v \tag{4.3}$$

The resistances are then used to compute an overall resistance matrix $\{X\}$ whose elements are given similarly to Equations 2.15 and 2.16:

$$(X)_{vv} = -\sum_{w \in \mathrm{N}_w} \frac{1}{S^{VE}_{vw}} \quad , v = 1, \ldots, N_v \tag{4.4}$$

$$(X)_{vw} = \begin{cases} \frac{1}{S_{vw}}, & w \in \mathrm{N}_w, w \neq v \\ 0 & w \notin \mathrm{N}_w \end{cases} , v = 1, \ldots, N_v \tag{4.5}$$

Boundary and non-boundary VEs are treated in the same way as their voxel counterparts, as well as the ensuing matrix operations. The set of linear equations describing current conservation over a network of $q$ voxels can be expressed as {X}[A]=[B], where {X} is the conductivity matrix, [A] the potential vector ([A] =$(V_1 \quad V_2 \ldots V_q)^T$) and [B] the resultant current vector, ([B]=$(i_1\, i_2 \ldots i_q)^T$). Upon solving the linear model, the total current entering or leaving the system can be calculated and used in Equation 13 to obtain an overall effective conductivity for the structures considered.

$$K_{eff,d}^{VE} = \frac{I_d^{VE}}{V_d^{VE}} \frac{l_{v,d}}{A_{v,d}} \tag{4.6}$$

The introduction of VEs allows yields three principle advantages to the use of the ResNet model. Firstly, it allows the model to be incorporated in the VOF model developed by Golbert et al. and Cai et al. (Golbert et al., 2008; Cai et al., 2011). Secondly, the aggregation of voxels into VEs allows for a parallelization of the code, speeding up the computational process in solving the system as a whole. Every separate VE can indeed now be solved separately at the same time. Finally, the introduction of VEs allows the ResNet model to be used on the same machine to analyze a much larger structure than before without causing a system crash due to memory problems. It must now be determined what level of aggregation is ideal for use in ensuing computations.

### 4.2.2 – Sensitivity analysis

In the work of Cai et al. (Cai et al., 2010, 2011), it was concluded that a sample taken from an SOFC electrode needs to have a volume equivalent to a cube with its length at least 7.5 times larger than the diameter of the particles used in the fabrication of the electrode, to reach a constant percolated Triple-Phase Boundary (TPB) length per unit volume of electrode. TPB percolation is based on the transport characteristics of materials comprising the electrodes, signifying that the same limits can be used when determining the effective transport properties of

these materials. Another limit determined by Cai et al. (Cai et al., 2010) to obtain reliable TPB densities was that the structure discretization scheme should be based on a $D/l_{vox}$ value of at least 20, with 40 desirable for high accuracy of the simulation results. The particle size used to make these electrodes was 3.0-3.7 μm, meaning that the minimum domain size to be considered for the sample to be representative of the entire structure was 7.5×3.4 = 25.5 μm in each dimension. Following the limits established by Cai et al. (Cai et al., 2010), samples taken from the structures fabricated by Somalu et al. (Somalu et al., 2011) need to be discretized by at least $(7.5\times20)^3 = 150^3 = 3.4\times10^6$ voxels for a reliable analysis to be undertaken with regards to mass and charge transport, and $(7.5\times40)^3 = 300^3 = 2.7\times10^7$ voxels for a highly accurate analysis. Due to the nature of the computations performed, the largest resistance matrix capable of being inverted as a whole without the use of successive iterations is derived from a structure comprised of a maximum of around $120^3$ voxels on the machines used for this thesis. This is found to be solely linked to the RAM available. In order to link the model to the work of Golbert et al. (Golbert et al., 2008), as well as enable the computation of an overall effective conductivity for considered structures, the voxels discretizing the structures are aggregated into larger cuboidal elements, or VEs as introduced earlier in this chapter. This however yields the question of how many voxels should be included in a single VE for a representative computation without being prohibitively computationally expensive.

In order to investigate this discretization limit, three different sets of synthetic SOFC electrodes were selected, with different compositions of Ni, YSZ and pores, as well as different particle sizes for analysis by the ResNet model. Electrodes were created in a similar way to the previous chapter by randomly packing a box with spheres representing the three phases, removing the spheres representing the pore phase once the box was densely packed, and expanding Ni and YSZ particles along the radius of the spheres by a factor of 1.2 (Golbert et al., 2008) to mimic the enlargement effect of the sintering process on the particles during the manufacturing of the electrodes. In case 1, electrodes were generated using particles of diameter 0.6 μm and volume fraction contents of Ni, YSZ and pore of respectively 15.77%, 72.71% and 11.53%. In case 2, the same particle size was used but with volume fraction contents of 34.15%, 54.39% and 11.46% and finally in case 3 for the same particle size, volume fraction contents of 63.81%, 24.97% and 11.22% were generated. These volume fractions were arbitrarily chosen with the

aim of capturing electrodes with a range of nickel contents. Somalu et al. (Somalu et al., 2011) experimentally determined the percolation threshold content for nickel volume fraction in the solid phase to be around 30% when analyzing their samples of Ni/10Sc1CeSZ and Ni/10ScSZ thick films at 700$^{o}$C (see figure below).

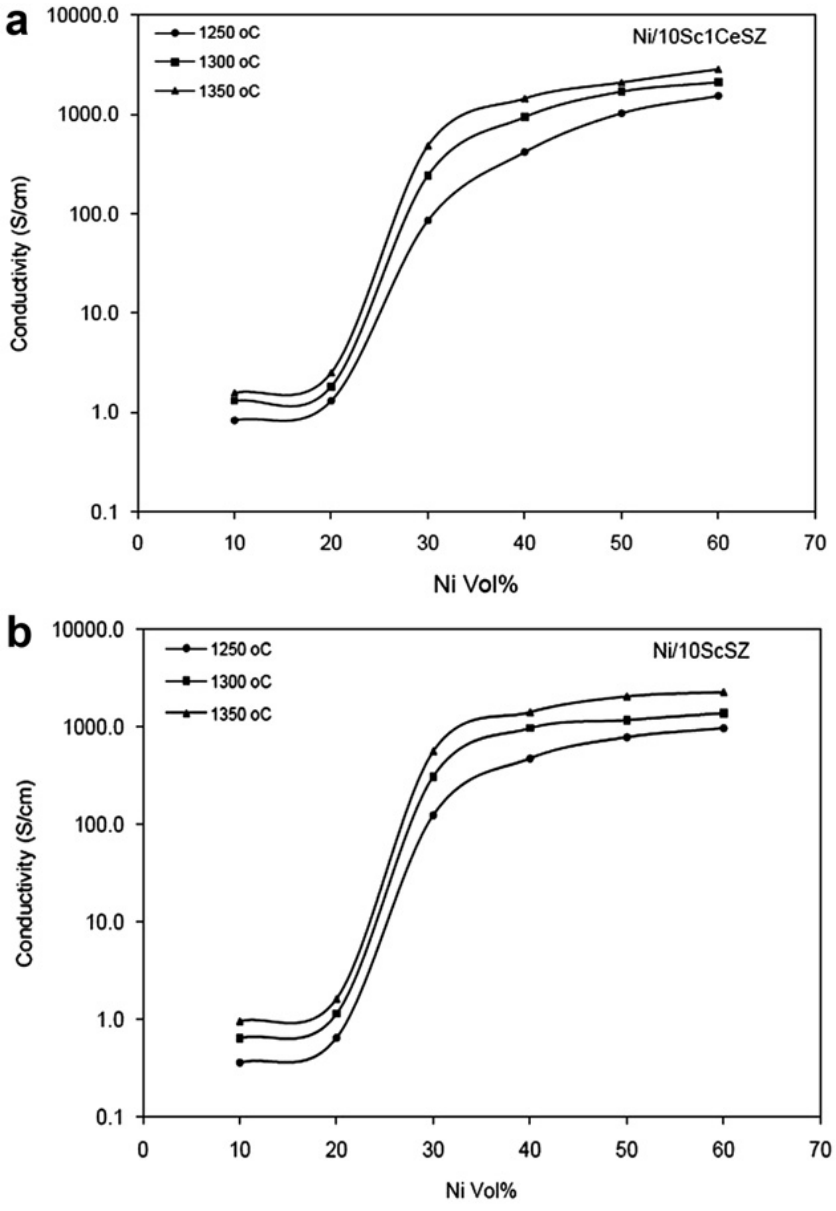


Figure 4.1 – Variation of electrical conductivity of (a) Ni/10Sc1CeSZ and (b) Ni/10ScSZ anode films of approximately 30 μm in thickness measured at 700$^{o}$C as a function of Ni content and sinter temperature, reported by Somalu et al. (Somalu et al., 2011).

In light of these results, the previously mentioned volume contents of nickel were chosen as such in order to capture electrodes below the percolation threshold of 30%, at the threshold itself and above it. In each case, 5 microstructures were randomly generated with identical volume fractions and particle sizes. Each microstructure is understood to be unique due to the inherent heterogeneity of the 3D percolation paths of the electronic, ionic and gas conducting phases within the microstructure. For all the three cases, each of the electrode structures generated was cubic in shape of uniform size 5 μm, and were discretized by $100^3$ voxels in each dimension of diameter 1 μm. Figure 4.2 illustrates one randomly selected microstructure of each case considered.

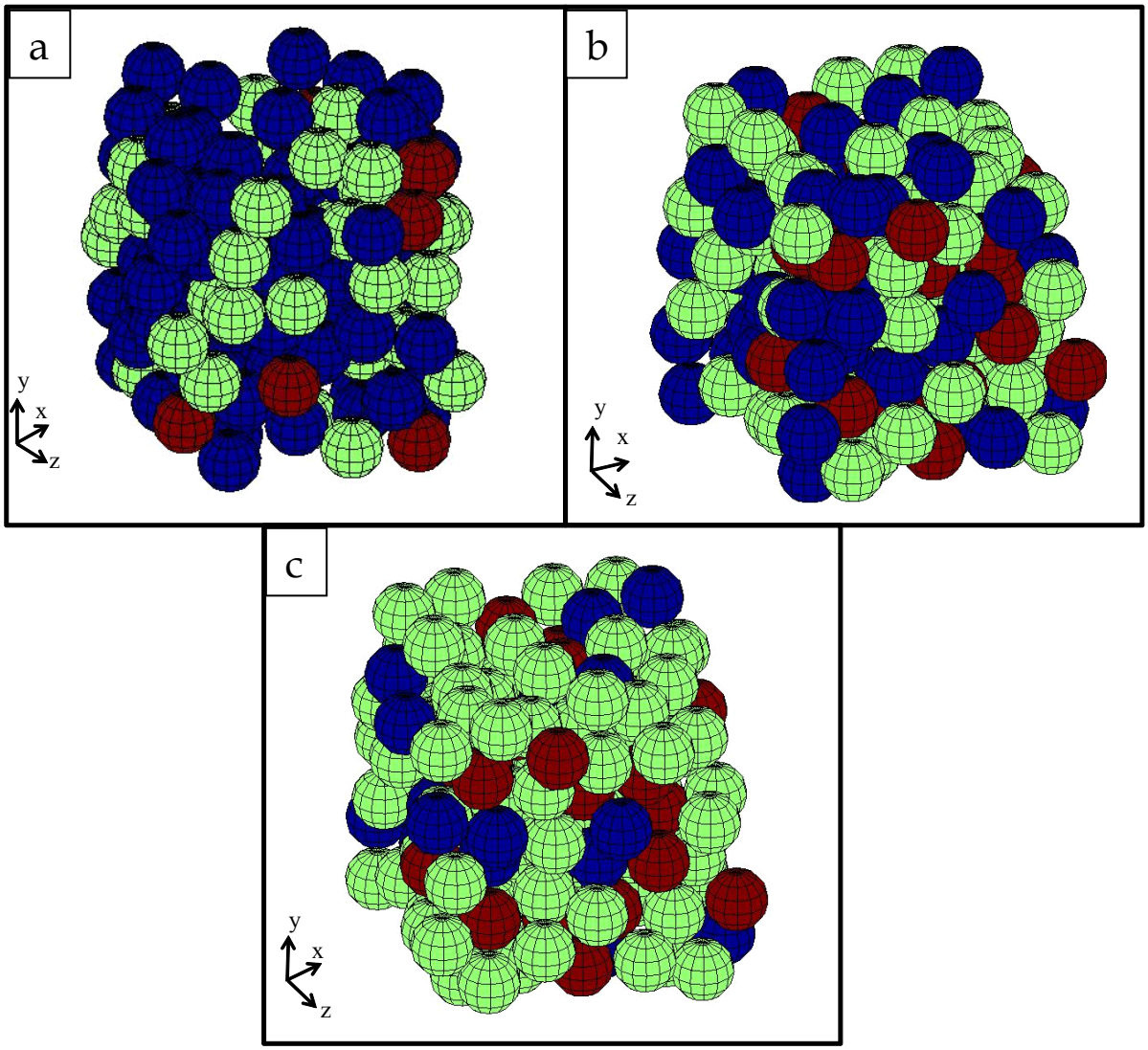


Figure 4.2 – Graphical representation of the particle distribution for each case considered when determining an optimum aggregation resolution. Green spheres represent nickel particles, blue spheres represent YSZ particles and red spheres represent pore particles. In the first instance (a) the nickel phase occupies 15.77% of the volume, YSZ 72.71% and pores 11.53%. In (b), the nickel phase occupies 34.15% of the volume, YSZ 54.39% and pores 11.46%. In (c), nickel occupies 63.81%, YSZ 24.97% and pores 11.22%.

In each case, the ResNet model was applied to each microstructure with 9 separate aggregation levels; $1^3$ voxel per VE, $2^3$ voxels per VE, $4^3$ voxels per VE, $5^3$ voxels per VE, $10^3$ voxels per VE,

$20^3$ voxels per VE, $25^3$ voxels per VE, $50^3$ voxels per VE and $100^3$ voxels per VE. Figures 4.3 to 4.5 present the results of this analysis, showing the variation of effective conductivities of each of these individual microstructures as computed by the ResNet model for increasing levels of aggregation resolution. The cases where the voxels are aggregated into $1^3$ VEs and $100^3$ VEs are effectively equivalent to the computation being carried out without the introduction of VEs. When the entire structure comprises $100^3$ voxels, as is the case where $100^3$ voxels are contained within a single VE, the derived effective conductivity of the one VE corresponds to that of the entire structure. At the lowest level of aggregation, ie when when $1^3 = 1$ voxel is contained in each VE, the computation performed is identical to that on $100^3$ voxels, as each VE will simply be assigned the effective conductivity of the pure material which it represents, resulting in an identical effective conductivity to the above case. Hence the data points at each extremity of the plots presented in Figures 4.3 to 4.5 are the same for each microstructure. The results represented by these data points can be seen as the most accurate as demonstrated in previous sections due to the fact that these results are those which were obtained using the highest degree of resolution considered. Two conclusions can be drawn from the analysis of these results. The first is that two electrodes with similar composition characteristics can yield very different effective conductivities. This implies significant variations in the size and distribution of electronically conducting pathways within these electrodes brought upon by the fabrication/generation process of real and synthetic electrodes, already established in the literature by Golbert et al. (Golbert et al., 2008) and Cai et al. (Cai et al., 2010, 2011) amongst others. When considering the representation of the particle distribution shown in Figure 4.2, it is clear that the random positioning of particles of different phases accounts for these differences in effective electronic conductivities. The ResNet model captures the effect of the random distribution in a way that the naked eye cannot. To illustrate this point the reader is referred to the conductivities of structures 3 and 4 in Figure 4.4, which consistently differ by almost 600%. A second conclusion that can be drawn is the dependency of the overall effective conductivity of any one structure on the aggregation resolution employed in the application of the proposed model. In Figures 4.3 to 4.5 predicted effective conductivities of every structure analyzed vary with respect to aggregation resolution, in some cases by a factor of 2.

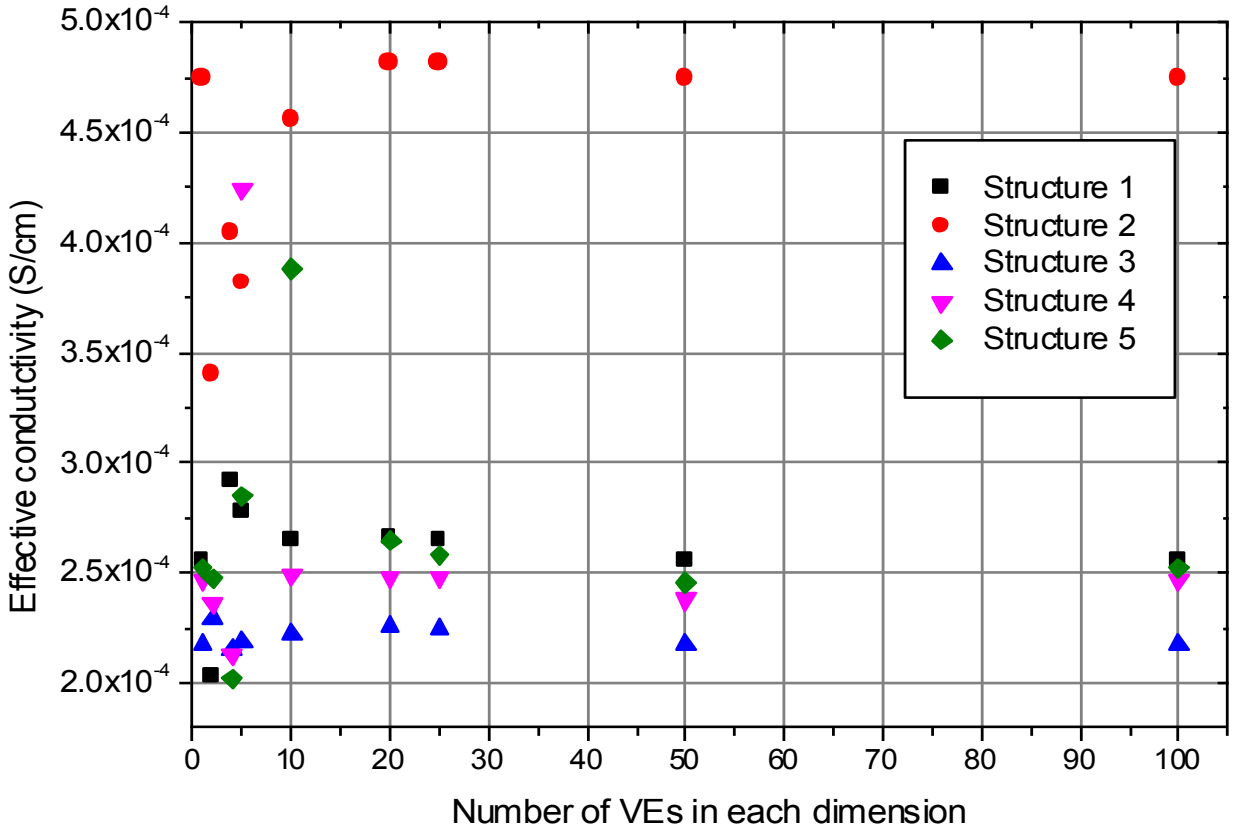


Figure 4.3- Effective conductivity of the electrodes of Case 1 representing volume fraction contents of Ni, YSZ and Pore respectively of 15.77%, 72.71% and 11.53%. The electrodes are cubic, of size 5 μm. Each electrode is initially discretized by $100^3$ voxels which are subsequently aggregated into VEs.

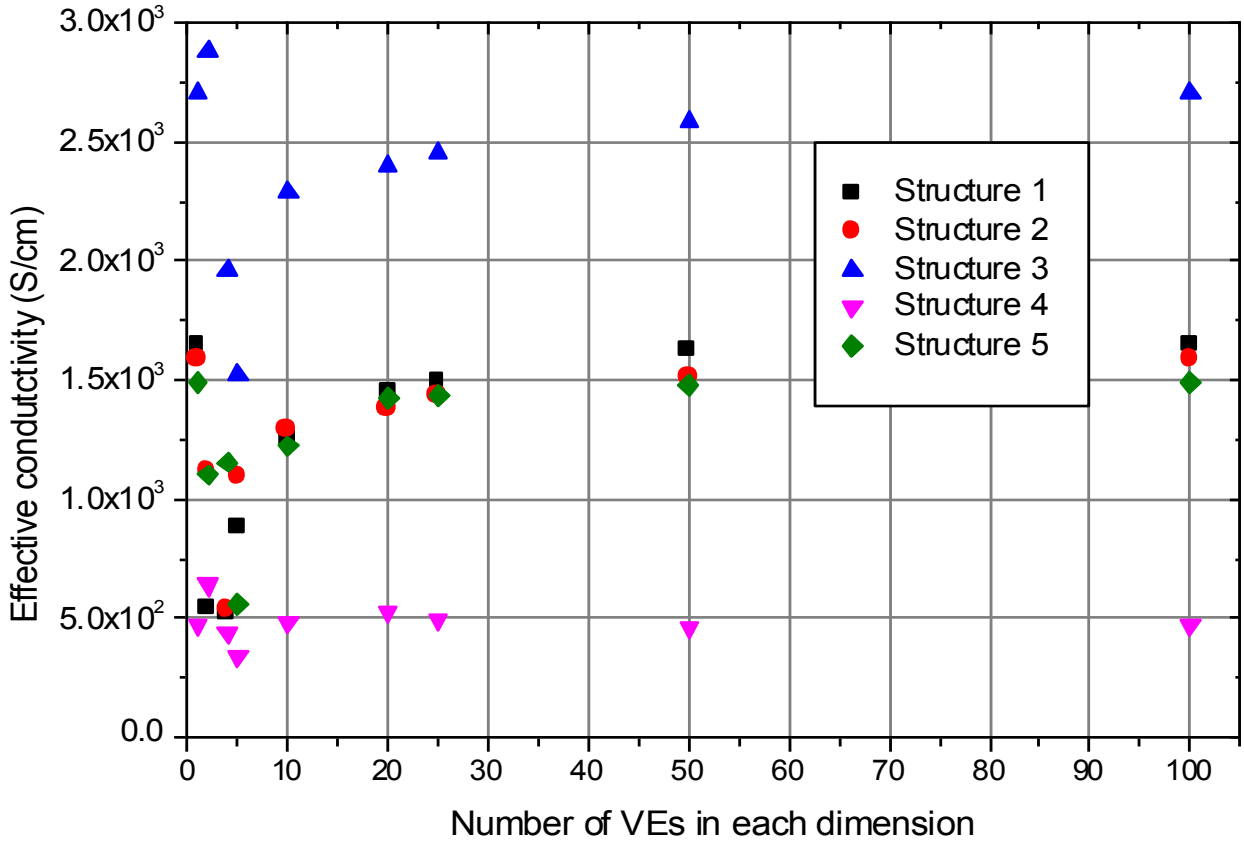


Figure 4.4- Effective conductivity of the electrodes of Case 2 representing volume fraction contents of Ni, YSZ and Pore respectively of 34.15%, 54.39% and 11.46%. The electrodes are cubic, of size 5 μm. Each electrode is initially discretized by $100^3$ voxels which are subsequently aggregated into a gradually larger number of VEs.

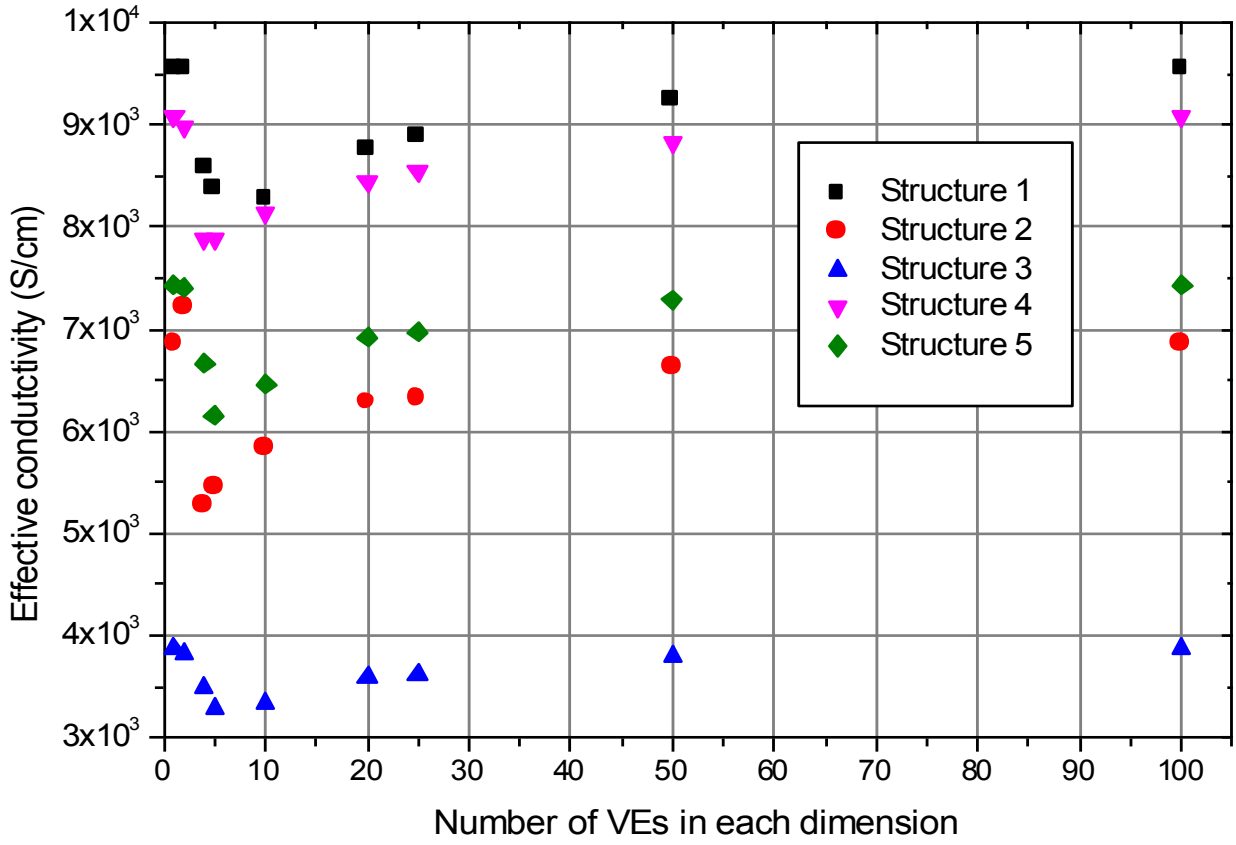


Figure 4.5- Effective conductivity of the electrodes of Case 3 representing volume fraction contents of Ni, YSZ and Pore respectively of 63.81%, 24.97% and 11.22%. The electrodes are cubic, of size 5 μm. Each electrode is initially discretized by $100^3$ voxels which are subsequently aggregated into a gradually larger number of VEs.

Figures 4.6 and 4.7 illustrate in more detail why two microstructures with the same composition can have significantly different effective conductivities. Figure 4.6 illustrates structures 3 and 4 of Case 2, showing in Figure 4.6 (a) and (c) the un-modified structures of structure 3 and 4, and in Figure 4.6 (b) and (d) the same structures highlighting the connected nickel paths in the direction in which the conductivity is being considered. Figure 4.7 depicts x-y views of the same percolated structures with limiting bottlenecks in the nickel pathways highlighted. Overlaid on the structure are the nickel path skeletons, obtained by repeatedly removing pixels from the edges of particles and particle bulks in a binary image until they are reduced to single-pixel wide shapes. The algorithm applied is a thinning algorithm established by Zhang and Suen (Zhang & Suen, 1984) and is well established in the literature. With the removal of unconnected particles,

it can be seen that structure 4 of Case 2 presents a higher degree of limitation in the available pathways for electron conduction, where three critical bottlenecks can be identified visually. The skeletonized path network of structure 3 is found to be 89.3 μm in length, as opposed to 42.2 μm for structure 4. Effective conductivities of both structures at the highest considered aggregation resolutions differ by a factor of 5.78 and their percolating path lengths by a factor of 2.12. Structure 3 therefore presents a much higher number of pathways for charge transfer, agreeing with the conclusions of Cai et al. (Cai et al., 2011) and the theory that spatial differences in particle distributions of each structure are responsible for variations in effective conductivities derived from these structures.

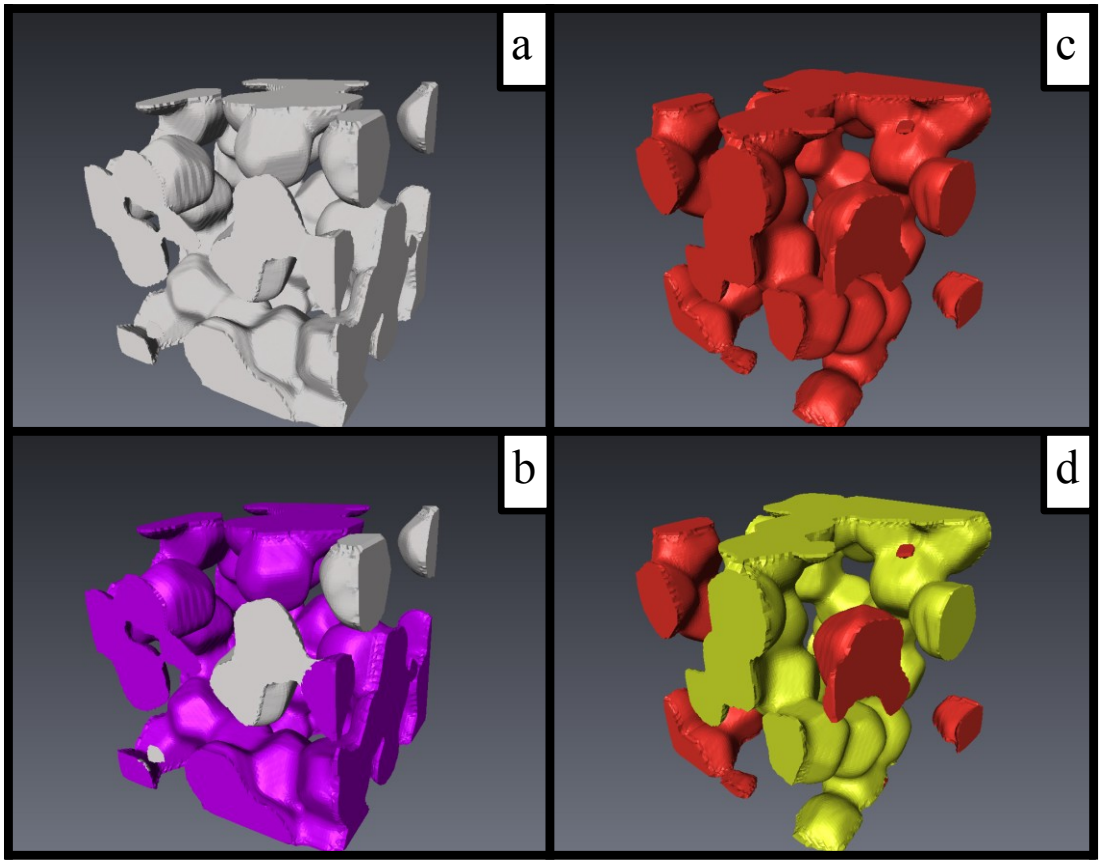


Figure 4.6- Graphical representation of the electrodes 3 and 4 of case 2. a) and b) show electrode 3 and in b) the purple shows the connected nickel paths in the direction in which the conductivity is being considered. c) and d) show electrode 4, and in d) the yellow shows the connected nickel paths in the direction in which the conductivity is being considered.

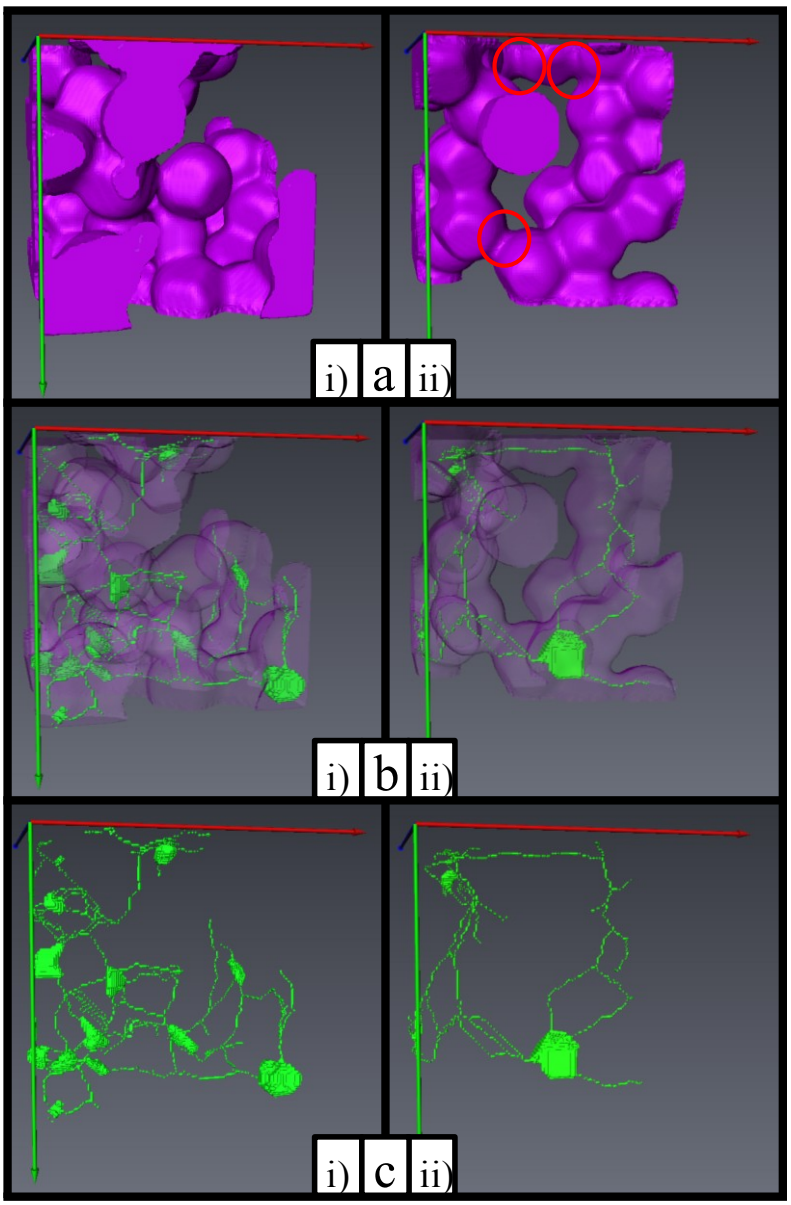


Figure 4.7- Graphical representation of the connected pathways of electrodes 3 and 4 of case 2, illustrated respectively by i) and ii). a shows the percolated structures of the electrodes, b shows the skeleton of the electron path through the electrodes in green superimposed on the structure, and c shows the skeleton of the electron paths alone. The red arrows show the x-axis, the green arrows show the y-axis and the blue arrow the z-axis. The red circles show the charge-limiting bottle-necks of electrode 4, yielding a lower conductivity.

In order to understand why any single structure yields different effective conductivities based on the different aggregation levels employed, Figure 4.8 shows how the aggregation of voxels into

VEs on a 2-dimensional slice taken from structure 3 of Case 2 affects the overall conductivity of the sample slice. It is important to note that although the presented figure and analysis is carried out on a 2-dimensional slice of the full structure, the findings can be extrapolated to the entire 3-D domain. In this figure, if a VE shows at least one connecting pathway in the x-direction, it is coloured blue. If it shows at least one connecting pathway in the y-direction, it is coloured yellow. If a VE is found to contain at least one connecting pathway in both the x- and y-directions it is accordingly coloured green. As shown in Figure 4.8, the lowest level of aggregation (i.e. 1 VE for the entire structure, as in Figure 4.8 (a)) yields a nominally insulating structure in the x-direction, whereas for the next three aggregation levels (i.e. $2^2$, $4^2$ and $5^2$ VEs, as in Figure 4.8 (b) – (d)) connecting VEs enable current flow through the structure. The next two levels of aggregation (i.e. $10^2$ and $20^2$ VEs, as in Figure 4.7 (e) and (f)) cut the pathways off again, yielding a nominally non-conductive structure in the x-direction. The nominal effective conductivity of the 2D slice as a function of the aggregation level therefore undergoes a non-linear variation in which a peak occurs at intermediate levels of aggregation. Extrapolating this analysis to a 3 dimensional level, it can be understood how merging equations 2.15 and 2.16 with equations 4.4 and 4.5 cause this aggregation process to in turn create and close conducting pathways depending on the resolutions used. This accounts for the non-linear variation of the effective conductivities obtained from structures analyzed in Cases 1 to 3, in which sporadic peaks and troughs are observed for any level of aggregation of $10^3$ voxels per VE and below. From the data presented in Figures 4.3 to 4.5, it is concluded that the optimum discretization level for any given structure is $5^3$ voxels per VE, as this is the point after which conductivity values do not change by more than 5%. This corresponds to $l_{ve}/l_{vox} = 5$. Additionally this limit is understood to be independent of the volume fraction content of each phase characterizing the electrodes analyzed, as well as the size of particles comprising these electrodes. Using a higher ratio would waste computational power, as results would not change significantly. A lower resolution would yield a much larger difference in results, as the aggregation process could have closed or opened a large number of connecting pathways.

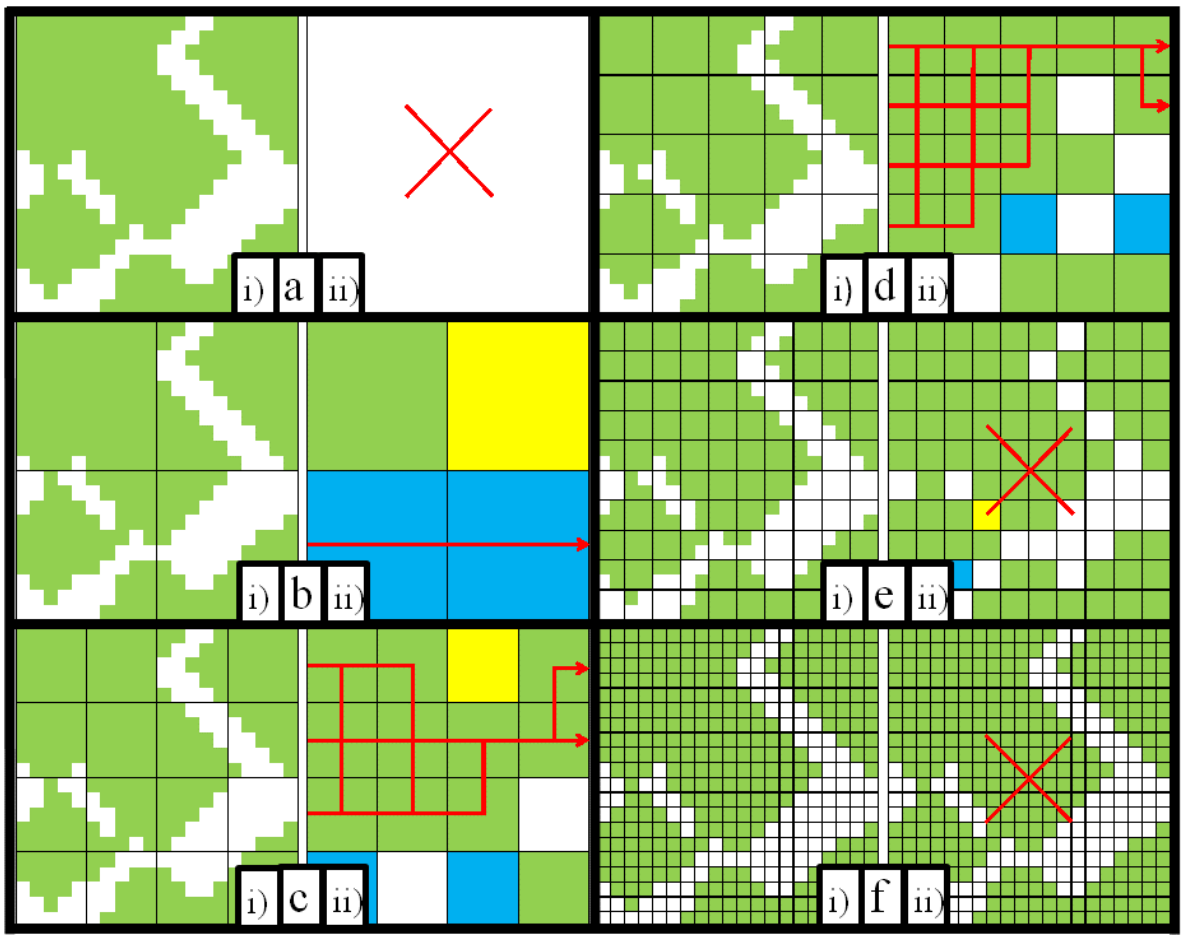


Figure 4.8- Graphical representation of a 2 dimensional slice of structure 3 used in Case 2. The slice selected is comprised of 20x20 voxels, which are aggregated into 1 VE (a), $2^2$ VEs (b), $4^2$ VEs (c), $5^2$ VEs (d), $10^2$ VEs (e) and $20^2$ VEs (f). In each case, i) shows the original structures superimposed by the VE aggregation layout, and ii) shows the aggregated structure. Green blocks represent voxels, or VEs, that show conducting pathways in the x and y directions, blue blocks represent VEs that only have conducting pathways in the x direction, and yellow blocks represent VEs that only have conducting pathways in the y direction. The red arrows show conducting pathways in the aggregated structures which are conductive in the x direction, and the red crosses mark the structures which are not conductive in the x direction.

## 4.3 - Case study of real electrode – skeletonized path analysis

In a previously published paper by Somalu et al. (Somalu et al., 2011), SOFC anodes were fabricated with increasing contents of nickel and characterized. The experimental in-plane conductivities of these structures were measured by the authors, which can be seen as analogous to the effective conductivity of the structures with the assumption of homogeneity throughout the electrode. Somalu et al. concluded that the electronic conductivity percolation threshold for Ni/10ScSZ anodes was established at approximately 30% solid volume content of nickel. A portion of the microstructure of one of the 30% anodes used in the analysis carried out by Somalu et al. (Somalu et al., 2011) was reconstructed using Focused Ion Beam (FIB) extraction followed by distinct tomographical segmentation processes. It is evident that a rigorous validation of the model requires the use of an accurate real microstructure which can only be achieved from a detailed analysis of the image acquisition and segmentation process. This is, however, not the focus of this chapter. Instead, the aim here was to first investigate the behavior of the ResNet model when applied to a real SOFC electrode. In this case, a standard procedure of imaging analysis was used, followed by the tomographical segmentation process established within Imperial College to obtain the 3D microstructure of the Ni/10ScSZ anode with 30% Nickel content fabricated by Somalu et al. (Somalu et al., 2011). The process is initiated by applying contrast filters coupled with Edge-preserving smoothing and Gaussian smoothing filters. Histogram segmentations and a selection of tools grouping pixels based on their binary value, or their shade, finalizes the 3d reconstruction. Figure 4.9 illustrates the reconstructed microstructure.

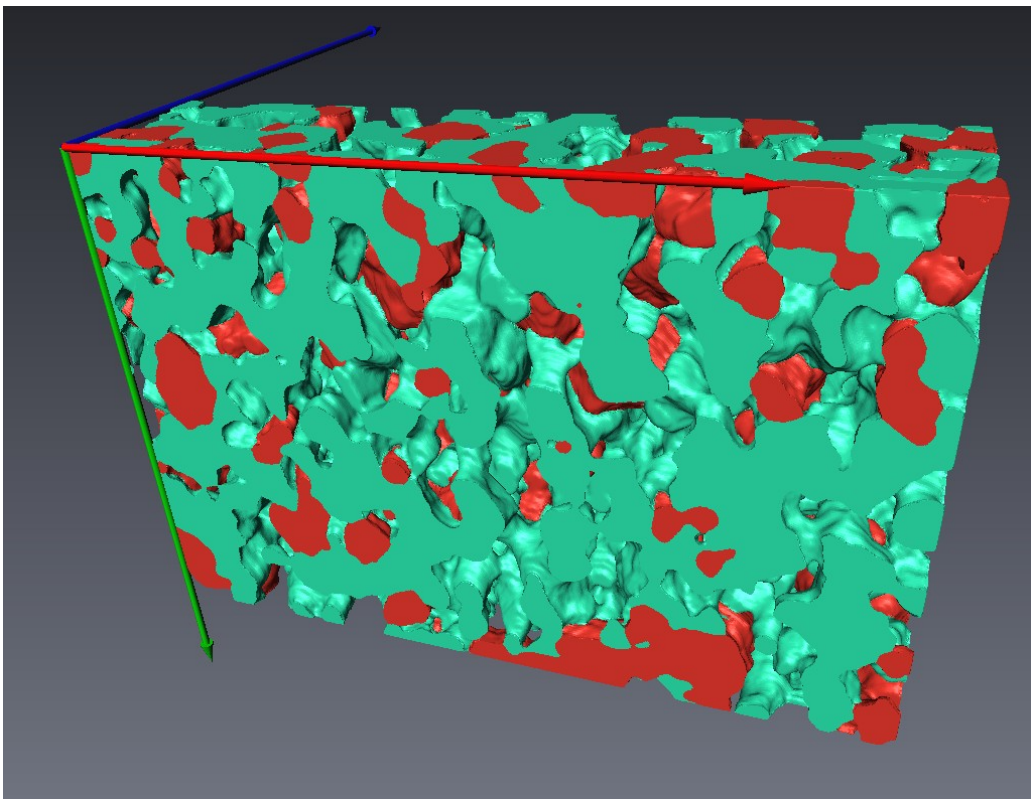

Figure 4.9- Graphical representation of the reconstructured microstructure extracted from a Ni/10ScSZ anode sample with 30% nickel content. The red arrow represents the x-axis, the green arrow the y-axis and the blue arrow the z-axis. Red portions of the microstructure represent nickel particles, green portions represent ScSZ particles and the empty areas represent pores.

The microstructure analyzed was found to be 26.93 μm, 18.19 μm and 6.42 μm thick respectively in the x, y and z directions. The volume fraction of nickel, extracted from the reconstructed microstructure, was found to be 28.4%, close to the experimental value design of 30%. An analysis of the structure using an aggregation resolution of $5^3$ voxels per VE and a nickel conductivity value of $2.4\times10^6$ S/m (Cai et al., 2010) yielded effective conductivities in the x, y and z directions of $5.74\times10^{-2}$ S/m, $1.24\times10^5$ S/m and $1.59\times10^6$ S/m respectively. In comparison to the conductivity of pure nickel, this data suggests that the nickel network in the sample is not percolated in the x direction, relatively poorly percolated in the y direction and relatively strongly percolated in the z direction. Figure 4.8 illustrates in turn the full and percolated particle network in the y and z directions, alongside a representation of the

skeletonized path of these particle networks. An observation of the percolated network and skeletonized paths confirms these conclusions. A higher number of connecting pathways can be seen to connect the z-boundaries of the microstructure than the y-boundaries, and no connection can be seen between the x-boundaries. As stated earlier, Cai et al. (Cai et al., 2010) established that for a sample structure to be representative of the entire microstructure, the minimum size to be considered is 7.5 times the average particle size. These anodes were fabricated using commercial Ni/10ScSZ particles of around 3.0-3.7 μm in diameter, meaning that the minimum electrode sample size to ensure a representative structure is ≈ 25 μm in each dimension. It is therefore evident that the sample dimensions were not appropriate for it to be representative of the entire anode. Furthermore, the z size of this structure is equivalent to just two particle diameters, such that only two particles need be connected to provide a current path, which can be seen in Figure 4.10. If the sample was larger in the z-direction, it is possible that pathways could then become connected in the other two dimensions. In the work of Somalu et al. (Somalu et al., 2011) electrodes containing 30% nickel showed effective conductivity measurements in the range of $1.0\times10^{4}$ – $1.0\times10^{5}$ S/m at 700$^{o}$C. In conclusion, obtained results are consistent with initial observations carried out prior to the application of the ResNet model, and underline the importance of using a sample volume representative of the considered electrodes for a relevant analysis.

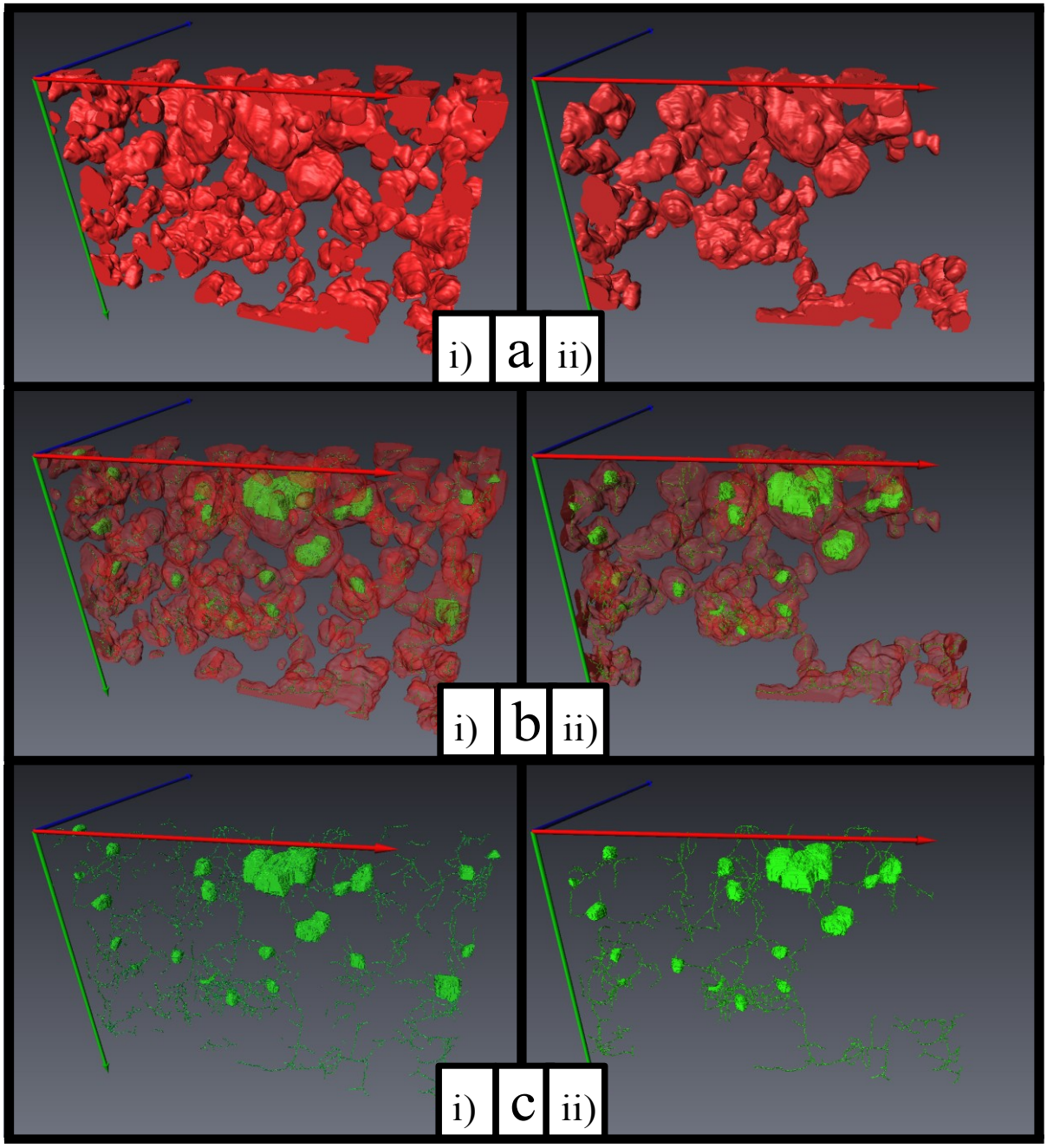


Figure 4.10- Graphical representation of the nickel network extracted from a Ni/10ScSZ anode sample with 30% nickel content. The red arrow represents the x-axis, the green arrow the y-axis and the blue arrow the z-axis. The full network is illustrated by i) in contrast to the percolated particles shown in ii). a shows a shaded view of the structures, b a transparent view of the structures overlaid with the skeletonized paths of this network, and c the skeletonized paths alone.

## 4.4 – Conclusions

A numerical technique for calculating the effective conductivity of porous composite microstructures has been developed and presented in a previous chapter. This model, the ResNet model, is based on Kirchhoff's law of current conservation of current and is applied to microstructures discretized into small cubic elements called voxels. This allows for actual electrodes to be analyzed, as well as synthetic microstructures. The aggregation of these voxels into Volume Elements enables the model to be used on large structures, as experimentally extracted microstructures are typically relatively large data sets.

By analyzing the behaviour of the effective conductivity model when run on several synthetic microstructures of various compositions it was determined that the optimum aggregation resolution when integrating VEs in the ResNet model is $5^3$ voxels per VE, corresponding to $D/l_{ve}$ = 5. This limit is shown to be independent of particle size, already accounted for in the voxel discretization limit established in previous chapters, and phase volume fractions. Additionally, by extracting electron pathway skeletons from the analyzed microstructures, it was shown that the deviation of effective conductivities between two electrodes generated with identical composition characteristics are a result of variations in the spatial distributions of electronically-conducting particles within the electrodes. By analyzing the aggregation process on a 2 dimensional slice of one of the analyzed structures and extrapolating the observations to a 3D structure, it was also shown that this process can in turn open and then close conducting pathways with an increasing aggregation level, yielding a non-linear behaviour of the extracted effective conductivities as a function of aggregation resolution.

As a final case study a real SOFC anode taken from the work of Somalu et al. (Somalu et al., 2011) was analyzed with the established aggregation limit. Results yielded effective conductivities in the x, y and z directions of $5.74\times10^{-2}$ S/m, $1.24\times10^{5}$ S/m and $1.59\times10^{6}$ S/m respectively, consistent with observations made on the microstructure itself alongside the extracted skeletonized electron pathways. These results showed that the size of the sample considered in relation to the particle sizes extracted by Somalu et al. (Somalu et al., 2011) in fabricating these electrodes is not consistent with limits established by Cai et al. (Cai et al., 2011),

supporting the findings of both of these authors, and finally underlining the importance of selecting a sample following these limits for a relevant study.

The next step is an in-depth analysis of image extraction and reconstruction techniques with the aim of extracting representative microstructures of the electrodes fabricated by Somalu et al. (Somalu et al., 2011) in order to apply the model to representative portions of these microstructures. A comparison between computed effective conductivities of these microstructures obtained with the ResNet model and experimental values extracted by Somalu et al. (Somalu et al., 2011) will allow final validation of the ResNet model. Furthermore, the ResNet model will be integrated into the electrochemical model developed by Golbert et al. (Golbert et al., 2008) to investigate the sensitivity of effective electronic conductivity on current generation, and therefore the performance, of SOFC anodes.

## 4.5 - References

Aguiar, P, Adjiman, C. S. & Brandon, N.P. (2005) Anode-supported intermediate-temperature direct internal reforming solid oxide fuel cell - II. Model-based dynamic performance and control. *Journal of Power Sources* 147(1), 136-147.

Asinari, P., Calì, M., Von Spakovsky, M.R & Kasula, B.V. (2007) Direct numerical calculation of the kinematic tortuosity of reactive mixture flow in the anode layer of solid oxide fuel cells by the lattice Boltzmann method. *Journal of Power Sources* 170(2), 359-375.

Bertei, A. & Nicolella, C. (2011) Percolation theory in SOFC composite electrodes: Effects of porosity and aprticle size distribution on effective propeties. *Journal of Power Sources* 196(22), 9429-9436.

Brett, D. J. L., Aguiar, P., Brandon, N. P., Coop, I., Dueck, J., Galloway, R. C., Grande, O., Hayes, G. W., Lillie, K., Mellors, C., Thompson, S., Tilley, A. R. & Wood, A. (2007)

Operational Experience of an IT-SOFC/Battery Hybrid System for Automotive Applications. *ECS transactions* 7(1), 113-122.

Brett D. J. L., Aguiar, P. & Brandon, N. P. (2006) System modelling and integration of an intermediate temperature solid oxide fuel cell and ZEBRA battery for automotive applications. *Journal of Power Sources* 163(1), 514-522.

Cai, Q., Adjiman, C. S. & Brandon, N. P. (2010) Investigation of the active thickness of solid oxide fuel cell electrodes using a 3D microstructure model. *Electrochemica Acta* 56(28), 10809-10819.

Cai, Q., Adjiman, C. S. & Brandon, N. P. (2011). Modelling the 3D microstructure and performance of solid oxide fuel cell electrodes: Computational parameters. *Electrochimica Acta* 56(16), 5804-5814.

Choi, H-W., Berson, A., Pharoah, J. G. & Beale, S. B. (2010) Effective transport properties of the porous electrodes in solid oxide fuel cells. *Journal of Power and Energy* 225(2), 183-197.

Golbert, J., Adjiman, C. S. & Brandon, N. P. (2008) Microstructural modeling of SOFC anodes. *Ind Eng Chem Res* 47(1), 7693-7699.

Kazempoor, P., Dorer, V. & Ommi, F. (2009) Evaluation of hydrogen and methane-fuelled solid oxide fuel cell systems for residential applications: System design alternative and parameter study. *International Journal of Hydrogen Energy* 34(20), 8630-8644.

Lanzini, A., Santarelli, M. & Orsello, G. (2010) Residential Solid Oxide Fuel Cell Generator Fuelled by Ethanol: Cell, Stack and System Modelling with a Preliminary Experiment. *Fuel Cells* 10(4), 654-675.

Leah, R.T., Brandon, N.P. & Aguiar, P. (2005) Modelling of cells, stacks and systems based around metal-supported planar IT-SOFC cells with CGO electrolytes operating at 500-600 degrees C. *Journal of Power Sources* 145(2), 336-352.

Nelson, G. J., Peracchio, A. A. & Cassenti, B. N. (2011) Analytical Models for SOFC Electrodes with Variable Cross-Section Microstructures. *ECS SOFC XII* 35(1), 913-921.

Schneider, L. C. R., Martin, C. L., Bultel, Y., Bouvard, D. & Siebert, E. (2007) Discrete modelling of the electrochemical performance of SOFC electrodes. *Electrochemica Acta* 52(1), 314-324.

Schneider, L. C. R., Martin, C. L., Bultel, Y., Dessemond & L., Bouvard, D. (2006) Percolation effects in functionally graded SOFC electrodes. *Electrochemica Acta* 52(9), 3190-3198.

Somalu, M. R., Yufit, V., Cumming, D., Lorente, E. & Brandon, N.P. (2011) Fabrication and characterization of Ni/ScSZ cermet anodes for IT-SOFCs. *International Journal of Hydrogen Energy* 36(9), 5557-5566.

Song, T. W., Sohn, J. L., Kim, J. H., Kim, T. S., Ro, S. T. & Suzuki, K. (2005) Performance analysis of a tubular solid oxide fuel cell/micro gas turbine hybrid power system based on a quasi-two dimensional model. *Journal of Power Sources* 142(1), 30-42.

Subramanyan, K. & Diwekar, U. M. (2007) Optimizing model complexity with application to fuel cell based power systems. *Journal of Power Sources* 46(11), 1116-1128.

Tseronis, K., Bonis, I. & Kookos, I. K. (2012) Parametric and transient analysis of non-isothermal, planar solid oxide fuel cells. *International Journal of Hydrogen Energy* 37(1), 530-547.

Tseronis, K., Kookos, I. K. & Theodoropoulos, C. (2008) Modelling mass transport in solid oxide fuel cell anodes: a case for a multidimensional dusty gas-based model. *Chemical Engineering Science* 63(23), 5626-5638.

Vivet, N., Chupin, S., Estrade, E., Richard A., Bonnamy, S., Rochais, D. & Bruneton, E., (2011) Effect of Ni content in SOFC Ni-YSZ cermets: A three-dimensional study by FIB-SEM tomography. *Journal of Power Sources* 196(23), 9989-9997.

Vivet, N.,Chupin, S.,Estrade, E.,Piquero, T.,Pommier, P. L., Rochais, D. & Bruneton, E. (2011) 3D Microstructural characterization of a solid oxide fuel cell anode reconstructed by focused ion beam tomography. *Journal of Power Sources* 196(18), 7541-7549.

Wishart, J., Dong, Z. & Secanell, M. (2006) Optimization of a PEM fuel cell system based on empirical data and a generalized electrochemical semi-empirical model. *Journal of Power Sources* 161(2), 1041-1055.

Yu, S. & Jung, D. (2010). A study of operation strategy of cooling module with dynamic fuel cell system model for transportation application. *Renewable Energy* 35(11), 2525-2532.

Zhang, T. Y. & Suen, C. Y. (1989) A fast parallel algorithm for thinning digital patterns. *Communications of the ACM* 27(3), 236-239.

# Chapter 5 – Relationship between microstructural parameters and performance of both synthetic and actual SOFC anodes.

## 5.1 – Introduction

Alongside the requirement for fuels and reaction products to be transported effectively by SOFC electrodes, there is also a need to provide a large percolated TPB length in the electrode. The number and lengths of TPB pathways alone is not sufficient however to characterize an electrode microstructure and thus, to properly model the transport and electrochemical processes in these porous composites, a comprehensive understanding of the percolated solid and pore-phase networks is required.

To better understand these networks, the generation of 3D synthetic microstructures provides the opportunity to investigate the influence of a variety of microstructural parameters on performance such as particle size, electrode thickness, phase volume fractions, phase surface and interface areas, phase connectivity and tortuosity as well as TPB path lengths and densities, by coupling them with electrochemical models.

Mass/charge transport and electrochemical models can be applied directly to a discretized electrode microstructure to provide the capability to model the impact of electrode geometry on mass/charge transport and electrochemical performance of porous, composite SOFC electrodes without providing these models with empirical parameters such as tortuosity, particle size, and porosity, which can be non-trivial to determine on experimental electrodes. Only a few studies, however, have been reported to date that link microstructural properties to electrochemical performance. Initially, multi-species gas transport in a SOFC anode was modelled using the Lattice Boltzmann Method (LBM) on a 2D scale based on a 2D micrograph of an anode (Joshi et al., 2007). Later, the LBM method was improved via the incorporation of a six-step kinetic electrochemical oxidation mechanism to enable the study of electrochemical performance (Grew et al., 2010). Suszue et al. (Suzue et al., 2008) went on to use the LBM method on 3D SOFC anode microstructures to model the transport phenomena and electrochemical reactions using

stochastic correlation reconstruction yielding 3D potential and current distributions through the electrode. In this work, Fickian and Knudsen diffusion are assumed to drive gas diffusion, and charge-transfer kinetics are modeled using the Butler-Volmer equation. Kishimoto et al. (Kishimoto et al, 2012a, 2012b) made use of the dusty-gas model (DGM) to simulate the gaseous diffusion of hydrogen and steam but the simple Butler-Volmer equation was found to not always be valid when considering the charge-transfer rates in SOFC electrodes due to the fact that the equation was originally derived to describe reactions that take place at the surface of metal electrodes in electrolyte solutions (Gorte & Vohs, 2011) in which the rate determining step is single electron charge transfer. The Butler-Volmer equation exhibits linear behaviour for the current-voltage response according to the low-field (low overpotential) approximation. The slope of this line, occurring at low over-potentials, defines the charge-transfer resistance. Making use of an iterative approach, the electrochemical simulation can be used to match the low-overpotential gradient with the experimentally derived charge-transfer resistance from experimental data. Using this approach, the corresponding length specific exchange current can be derived. To overcome this many researchers investigated the charge-transfer rate in SOFC electrodes with Ni-YSZ cermet anodes in both anodic and cathodic regimes, and developed a modified version of the Butler-Volmer equation used by Kishimoto et al. in their model. This thesis uses the simpler version of the Butler-Volmer equation due to the fact that the simulations presented are carried out within the assumptions validating the approach (i.e. low over-potential). Golbert et al. (Golbert et al., 2007) in their work use the volume-of-fluid (VOF) method to analyze 3D SOFC electrode microstructures and model the transport of electronic, ionic and gas phase species, as well as electrochemical reactions. The modeling framework developed by these authors has provided a platform to link electrode design parameters to microstructural properties and overall electrode performance. Microstructures analyzed by this model can either be synthetically generated by randomly packing a discreet domain with spheres representing the electronic, ionic and pore phases followed by simulated sintering, or reconstructed microstructures obtained with FIB-SEM or X-ray computed tomography (XCT) techniques. The structure in question is then discretized into small cubic elements called voxels, followed by an aggregation of these voxels into discrete volumes called volume-elements (VEs). Each volume $i$ is assigned a vector of volume fractions, $f_i$, whose elements $f_{i,k}$ define the volume fraction content of material $k$ in VE $i$. Following this definition, a VE where any single phase fraction lies

between 0 and 1 contains a phase interface. This methodology can capture exact interface information through discrete volume data and enable the representation of complex multiphase structures alongside continuous phase boundaries which as well suited for conduction/diffusion. Cai et al. (Cai et al., 2011) investigated the range of computational parameters within which the model developed by Golbert et al. (Golbert et al., 2007) can be used. The effect of the level of resolution/aggregation of voxels and VEs for microstructure analysis and electrochemical/transport modeling was examined, and an optimum number of VEs was found to be $25^3$ VEs per structure, as well as the minimum electrode length required for the microstructure to be considered representative of an entire electrode, reported to be $L/D \geq 7.5$ . Indeed, Iwai et al. (Iwai et al., 2010) and Shearing et al. (Shearing et al., 2010) reconstructed 3D microstructures from FIB-SEM characterization of SOFC anodes and reported variations in the volume fractions of Ni and YSZ for samples from the same electrode, implying the need for a larger sample size to ensure that the sample was representative of the entire electrode. This limit was established as being $10\mu m^3$ by Shearing et al. (Shearing et al., 2010) for the microstructure that they considered, though this is not necessarily applicable to anodes of different compositions or particle size distributions. Cai et al. (Cai et al., 2011) reported that the extracted structure dimensions should be at latest 7.5 times the mean particle diameter. However this limit was found by investigating the behaviour of TPB length density with respect to increasing domain size, and parameters such as phase conductivity were not considered. This limit can therefore only be used to ensure that the sample of a given microstructure is representative of the whole with regards to the length of percolated TPBs . In order to select a microstructure portion that can be characterized as comprehensively representative, phase volume fraction, particle size distribution and phase conductivity must also be considered. In this Chapter the effect of domain size on effective conductivity will be investigated in order to determine the minimum microstructure portion size that should be characterized if it is to be representative of the structure as a whole with regards to effective conductivity. Alongside this analysis, the effect of particle size, electrode composition, porosity and sintering factor or on effective conductivity will be determined.

It was shown in the work of Cai et al. (Cai et al, 2010) that the abundance of TPBs is one primary factor determining the performance of an SOFC electrode using the electrochemical

model based on the Butler-Volmer equation developed by Golbert et al. (Golbert et al., 2007), and in this Chapter the impact of effective conductivity will also be determined. Finally the effects of electrode composition and particle size on current density will be investigated.

## 5.2 – Representative sample volume.

In order to determine what sample volume should be considered for this to be representative of the whole anode in terms of its effective conductivity, families of synthetic microstructures were generated by initially packing a domain with spheres using a Monte-Carlo process. The spheres generated represent electronically conductive particles, ionically conductive particles, and pore former particles. After packing, the particles were uniformly enlarged by a factor of 1.2 to represent sintering (Cai et al., 2010), and pore former particles removed. This is to enable the formation of bottlenecks between contacting particles. To investigate the effect of domain size on effective conductivity, the microstructures were generated with increasing ratios of length (L) over particle diameter (D), with each dimension of the sample volume kept as a constant ratio of the length, hence increasing the domain size uniformly. Four different particle sizes were considered; 0.5 μm, 1 μm, 2 μm and 4 μm. In order to ensure that no other factor than the variation of domain size was responsible for the behavior of effective conductivity, particles were generated with a uniform size. In each case, the microstructures had a 43.5% volume content of nickel, 35% volume content of YSZ and 21.5% porosity. Due to the Monte-Carlo process used to generate the structures, families of up to 300 structures were generated to obtain statistically reliable results. As the L/D ratio of the structures increased, the number of structures required for statistically reliable results decreased (defined as the point where standard deviations fall below 10% of the ensemble mean average), with the highest L/D ratio considered only requiring the generation of 30 structures. Following the particle generation phase, the structures were discretized into voxels following the limits established in previous chapters, and by Cai et al. (Cai et al., 2010), i.e. 20 voxels per particle diameter. This discretization was followed by an aggregation of voxels into Volume Elements (VEs), at a level of $5^3$ voxels in each VE, determined as the optimum resolution in the previous chapter. Figure 5.1 shows the x-direction effective conductivities of these structures, as given by the ResNet model, and Figure 5.2 shows the same data but for the case where particles of diameter 1 μm showing effective conductivities

in the y and z-directions. Conductivities are here presented in S/μm to simplify data representation.

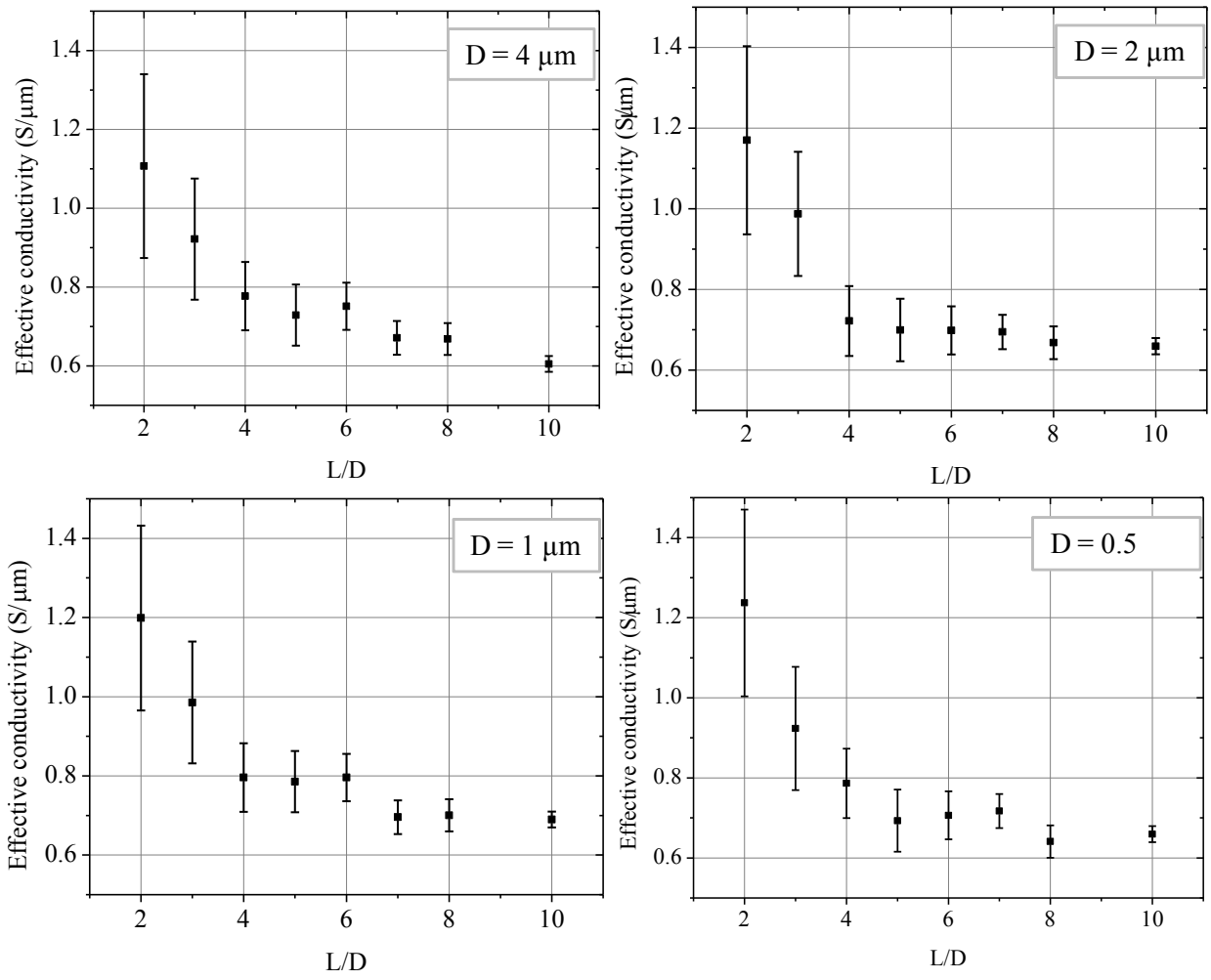


Figure 5.1 – Effective conductivity as a function of L/D for families of structures with a 43.5% volume content of nickel, 35% volume content of YSZ and 21.5% porosity for four different particle sizes. All conductivities presented are computed in the x-direction.

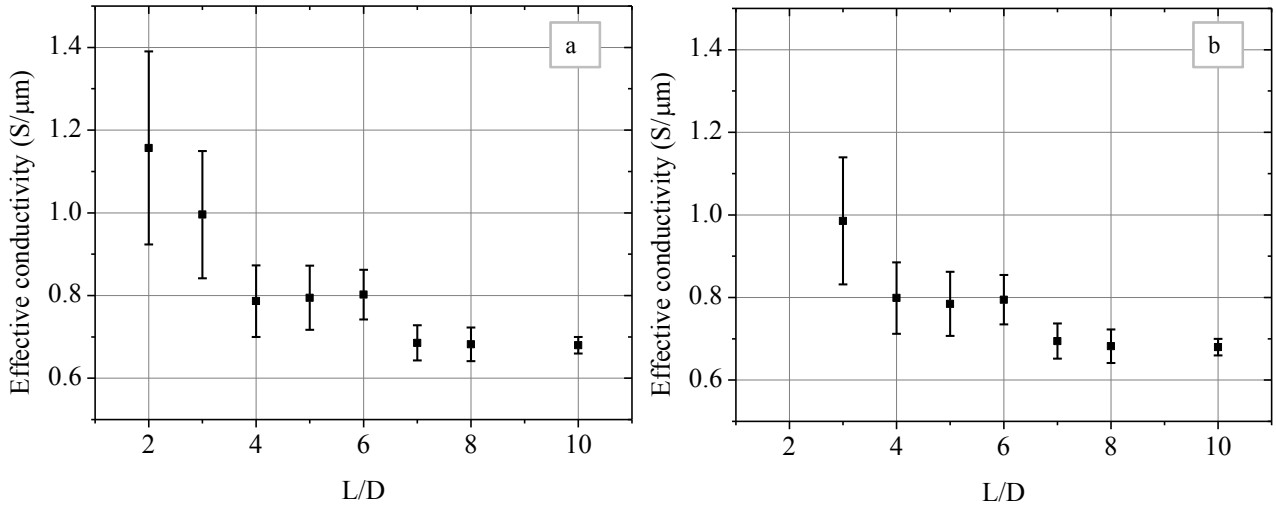


Figure 5.2 - Effective conductivity as a function of L/D for families of structures with a 43.5% volume content of nickel, 35% volume content of YSZ and 21.5% porosity. Particle diameter is 1 μm and conductivities are shown in the y-direction (a) and the z-direction (b).

By setting the convergence criteria as the point at which results come within less than 5% of the last data point, Figure 5.1 shows that for each particle size considered, this convergence is achieved at an L/D ratio of 7. Figure 5.2 shows that each of the x, y and z-direction conductivities are similar within a 2-4% margin due to the random process used in generating the electrodes, the high number of structures used to achieve statistically reliable results and uniform structure sizes, and therefore conclusions drawn from the behaviour of effective conductivities in the x-direction can also be applied to that in the y or z-directions. The analysis also shows a gradual decrease of effective conductivity and standard deviation for an increasing domain size, starting at an average value of 1.19 S/μm to a converged value of 0.73 S/μm. The decrease in standard deviation can be attributed to the Monte-Carlo process used in generating the microstructures. For smaller particle "boxes", it is less likely to achieve the same volume fraction content in each phase and therefore deviations in electronic phase volume contents are more important, yielding larger variations in effective conductivity. Effective conductivities are found to be relatively independent of particle size, with similar behaviours and values of extracted effective conductivities observed for each particle size. The larger effective conductivities for

smaller structures are in part attributed to the less tortuous paths for charge transport in these structures than in the larger structures. It can indeed be understood that, as the domain size increases, the length of each conducting path between the relevant boundaries increases to an even higher extent, as they expand in all three dimensions rather than just one dimension. The formation of a web of paths causes the resistance of the microstructures to increase non-proportionally to their size, in turn increasing the effective conductivities of these structures. The figure below shows three different microstructures at three different L/D ratios to illustrate the expansion of conducting path networks with increasing domain sizes, with the skeletonized nickel paths highlighted within each structure.

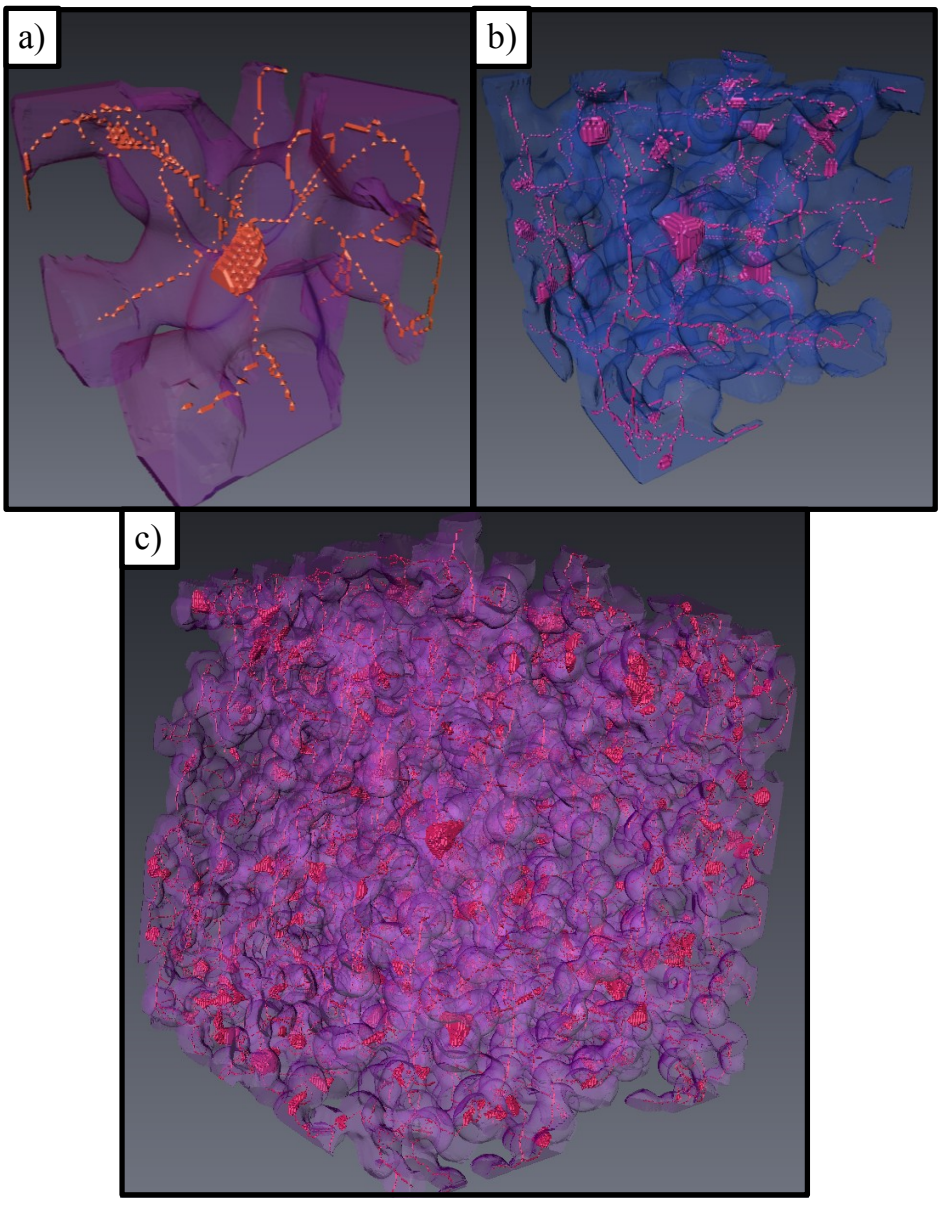

Figure 5.3 – Graphical representation of sample microstructures at L/D = 2 (a), L/D = 5 (b) and L/D = 10 (c), with the skeletonized paths highlighted in each microstructure.

By measuring the skeletonized paths of these structures, an attempt to better understand the link between the size of the microstructure and the overall path length was conducted, but revealed a linear increase of overall path length with microstructure size. This means that the larger path lengths found in larger structures does not account for the decrease in conductivity measured. No tangible result could be drawn from this analysis, as the network path length in itself is not a sufficient characteristic to describe and quantify the effective conductivity of these model structures. Attempts were also made to calculate the tortuosity of the samples. Most models in the literature rely on the porosity to determine the tortuosity of a porous microstructure, rendering them inadequate for use in this analysis due to the fact that porosity is kept constant in each dataset.

Instead, a more straight forward explanation is proposed for the gradual decrease of average effective conductivity for increasing L/D ratios. The problem is reversed to explain why the effective conductivity of the model structures increases for decreasing domain sizes. At smaller microstructure sizes, as little as 5-10 particles fill the domain with a random distribution of particles of all phases using weighted probabilities. This means that the entire domain can effectively be filled with nickel particles, yielding a high effective conductivity which in turn raises the average value for the family of structures. The high deviation of effective conductivities observable in Figure 5.1 provides evidence of this. As the L/D ratio increases, this spread decreases, in turn decreasing the average computed value. At low L/D ratios, there exist a large number of structures comprised of only nickel for instance, as opposed to structures at higher L/D ratios, which are comprised of much more particles, and are therefore more statistically stable.

From this analysis it can be concluded that the optimum L/D ratio to be considered for a microstructure to be representative of an entire anode when considering effective conductivity is L/D = 7. In the analysis of Cai et al., this optimum L/D ratio was found to be 7.5 when the structures were simply elongated, rather than uniformly expanding, and by considering TPB percolation (Cai et al., 2010). In order to determine if this ratio is the same when the structures uniformly increase in size, the same analysis is carried out on the structures generated for the

analysis presented above. The TPB length density value is computed following a percolation analysis of the entire voxelized structure using a percolation algorithm (Stauffer & Aharony, 1997), and shown in the figure below.

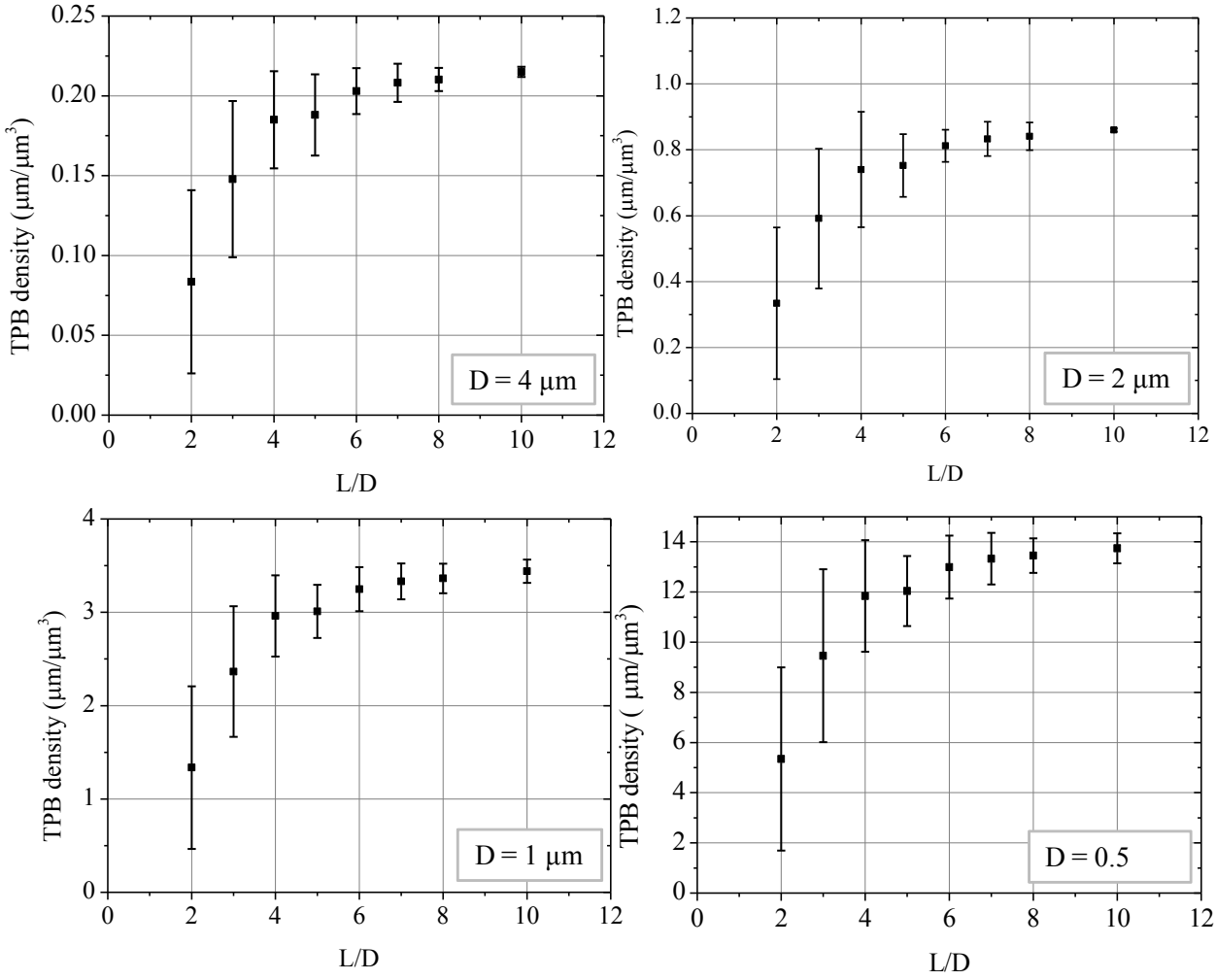


Figure 5.4 – TPB density as a function of L/D for families of structures with a 43.5% volume content of nickel, 35% volume content of YSZ and 21.5% porosity for four different particle sizes.

As shown in the figure above, it can be seen that the limits established by Cai et al. (Cai et al., 2010) are indeed consistent with structures increasing in size uniformly. Convergence can be seen to arise at an L/D ratio of > 7. TPB densities however are seen to be dependent on particle size, which is a well understood phenomenon due to the increased surface area and particle

contact area when particle sizes decrease (Cai et al., 2010). A particle diameter of 0.5 μm yields an average converged TPB density of 13.74 $\mu m/\mu m^2$, as opposed to 0.215 $\mu m/\mu m^2$ for particle diameters of 4 μm.

## 5.3 – Effect of microstructural parameters on effective conductivity.

It has now been established that particle diameter does not impact the effective conductivity of the model structures generated, based on the results shown in Figure 5.1. Next the impact of porosity was considered. To conduct this analysis, families of 50 microstructures were generated using the same discretization and aggregation resolutions as previously, with an L/D ratio of 7, particle diameters of 1 μm, a fixed ratio of nickel to YSZ particles of 4.8:4, and a varying porosity. The effective conductivities of these structures, as computed by the ResNet model, are presented in the figure below.

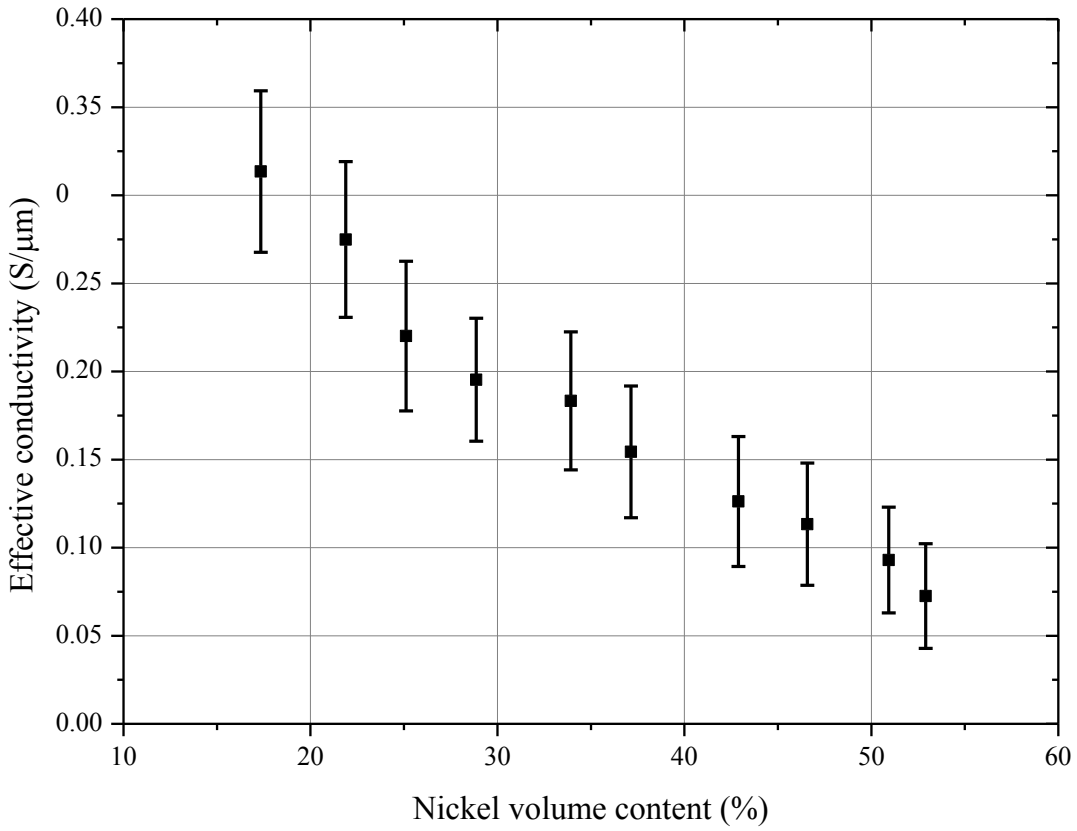


Figure 5.5 – Effective conductivity as a function of porosity for structures with an L/D ratio of 7, particle diameters of 1 μm and a fixed ratio of nickel to YSZ particle diameters of 4.8:4. All conductivities presented are computed in the x-direction.

The effective conductivity of these structures is seen to steadily decrease as porosity increases, due to the decreasing volume content of electronically conductive particles. The lowest case of porosity considered is 16% and yields an average effective conductivity of 0.325 S/μm. This steadily decreases to 0.0755 S/μm for a porosity of 53%. By plotting the nickel volume fraction content of these microstructures against porosity, as shown in Figure 5.6, it can be established that the effective conductivity of Ni-YSZ modeled structures is dependent on the porosity only when this porosity affects the volume fraction content of nickel. Indeed, the figure below shows that decreasing the porosity proportionally decreases the volume fraction content of nickel. The behaviour of nickel volume fraction with regards to porosity is found to mirror that of effective conductivity with regards to porosity.

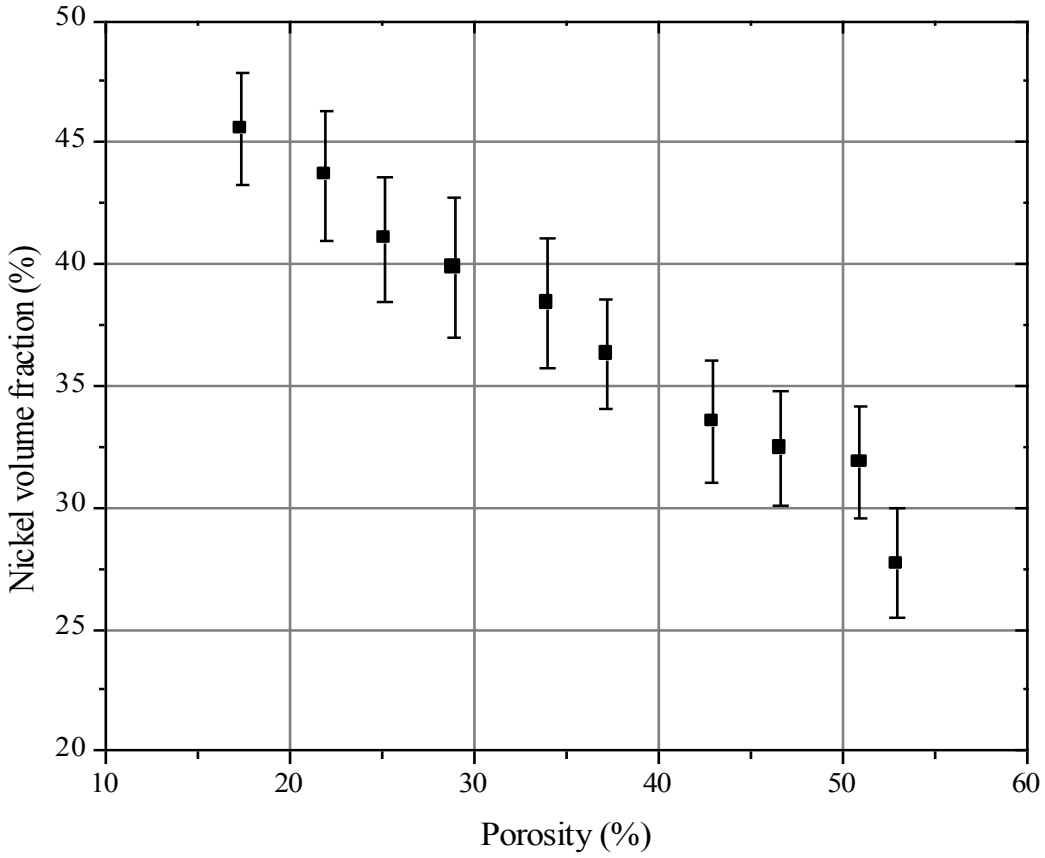


Figure 5.6 – Nickel volume fraction content against porosity for structures with an L/D ratio of 7, particle diameters of 1 μm and a fixed ratio of nickel to YSZ particle diameters of 4.8:4.

Varying the volume content of nickel, while keeping porosity constant, provides further insight into the impact of nickel content on electrode effective conductivity. Figure 5.7 shows how effective conductivity varies with regards to nickel content in structures with the same characteristics as previously, and a constant (arbitrary) porosity of 40%.

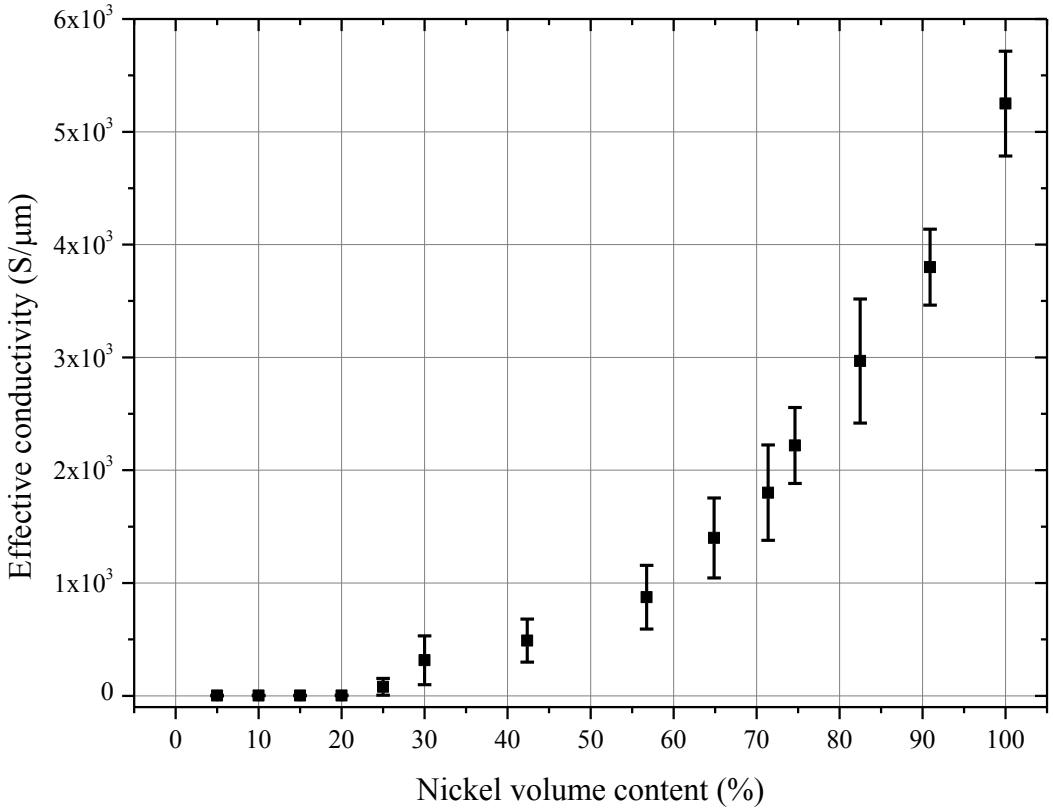


Figure 5.7 - Effective conductivity as a function of nickel volume fraction for structures with an L/D ratio of 7, particle diameters of 1 μm and a fixed porosity of 40%. All conductivities presented are computed in the x-direction, similarly to the work of Somalu et al. (Somalu et al., 2011).

The results presented in the figure above shows that, as the nickel volume fraction content increases in the solid phase of a model SOFC anode microstructure, the effective conductivity steadily increases until the nickel content in the solid phase reaches 30 vol%, after which the effective conductivity is seen to exponentially increase to a maximum of 0.792 S/μm. A steady increase of standard deviation is also noted in the structures generated, until a nickel content of around 70% is reached in the solid phase. This deviation is thought to come from the occasional formation of isolated nickel aggregations within the generated microstructures that do not contribute to effective conductivity. The conductivity of pure nickel at 1073 K is 2.4 S/μm, showing the dramatic impact that 40the microstructure has on the effective conductivity. By plotting these values on a log graph, a comparison can be made between the computed results and values available in the literature. To enable a comparison as reliable as possible, as well as

provide the opportunity for subsequent validation of the ResNet model, computed values are compared against those obtained by Somalu et al. in the Imperial group from experimental analyses (Somalu et al., 2011). This also allows for the effective conductivity of the same structures used by Somalu et al. to be computed by the ResNet model and compared to experimental measurements, as presented in Figure 5.10.

These authors fabricated Ni/10ScSZ and Ni/10Sc1CeSZ SOFC cermet anode films sintered at 1250°C, 1300°C and 1350°C and determined their conductivity using a 4-point van der Pauw technique (Somalu et al., 2011) at 700°C. The results of their investigation are compared to the output of the ResNet model and the volume fraction average model used by Golbert et al. in Figure 5.8.

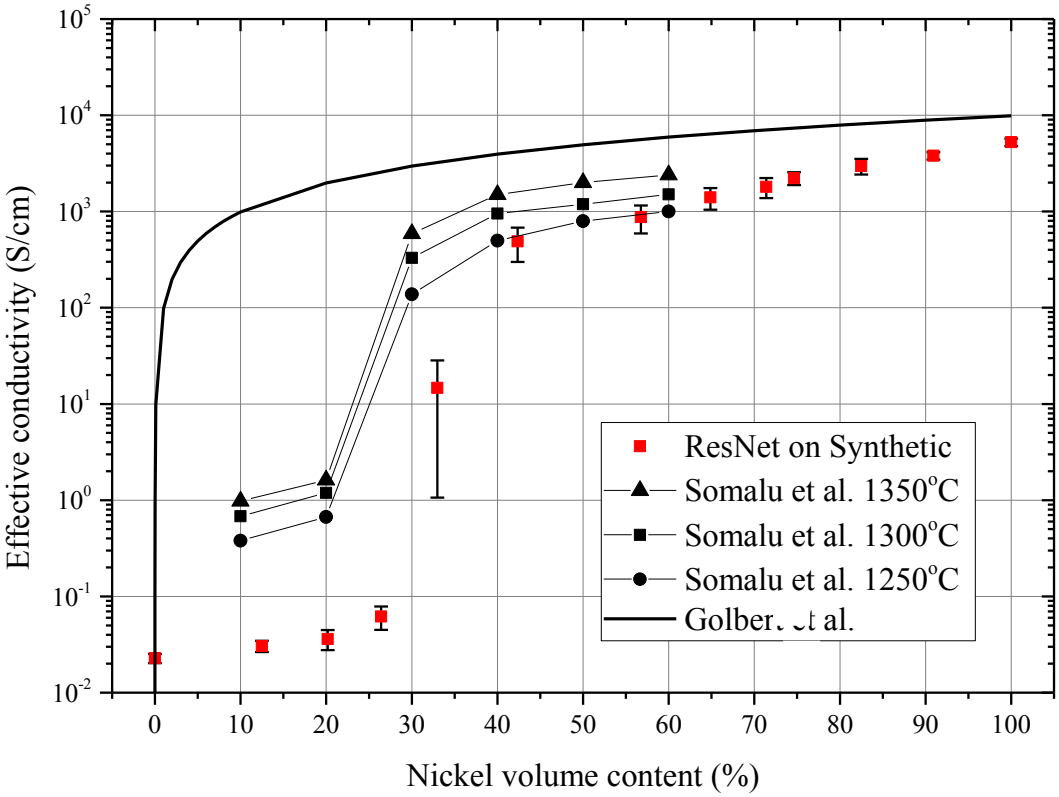


Figure 5.8 – Variation of effective conductivity of Ni/10ScSZ anode films measured at 700°C as a function of Ni content and sinter temperature as reported by Somalu et al. (Somalu et al., 2011) compared to the effective conductivity as a function of Nickel volume fraction for synthetic structures with an L/D ratio of 7, particle diameters of 1 μm and a fixed porosity of 41.2%,

similarly to the real structures. All conductivities presented are computed in the x-direction, in line with the work of Somalu et al. (Somalu et al., 2011).

Both the experimental analysis and ResNet prediction find a steep increase in electrical conductivity at around 30 vol% nickel content, found to be the percolation threshold for nickel as reported by Somalu et al. (Somalu et al., 2011) and the literature (Dees et al., 1987). Before this threshold, average electrical conductivities lay at around 0.05 S/cm before increasing by 4 to 5 orders of magnitude past the 30 vol% threshold. The results also show an increasing spread of conductivities in families of structures approaching the percolation threshold, highlighting the sensitivity of the conductivity to the local distribution of particles when the structure is close to the percolation limit. At this threshold, the conducting material within the structure is as likely to connect the two opposite boundaries of interest than not, and as the nickel content increases past this threshold, connections are more and more likely to be made through the electrode, eventually yielding a conductive anode at every generation or fabrication. Effective electrical conductivities as predicted by the ResNet model on synthetic structures are found to be lower than those obtained by Somalu et al. in their experiments for all cases, with closest agreements occurring at nickel above the percolation threshold. At low nickel contents, results computed by the ResNet model deviate by as much as 1500% to those obtained by Somalu et al. on structures sintered at $1350^{o}$C, and at high nickel contents deviations reach on average 200%. For structures sintered at $1250^{0}$C however, agreement is found for structures above the percolation threshold. These results highlight the importance of modelling the sintering process as accurately as possible, as well as considering realistic particle size distributions as opposed to uniform particle sizes. A combination of higher bottleneck sizes and non-uniform particle distributions in the real electrodes accounts for the higher electrical conductivities obtained experimentally by Somalu et al. In all cases, the volume-averaged approach used by Golbert et al. is found to yield a gross over-estimation of the effective conductivity at all considered volume fractions, and does not capture the percolation threshold.

To confirm that the aggregation resolution used is indeed the optimum resolution for this investigation, and study the impact of changing this resolution on the computed effective conductivities, a similar analysis was carried out by changing the aggregation resolution to $2^3$ voxels, and $10^3$ voxels, in each VE. Figure 5.9 illustrates the results of this analysis.

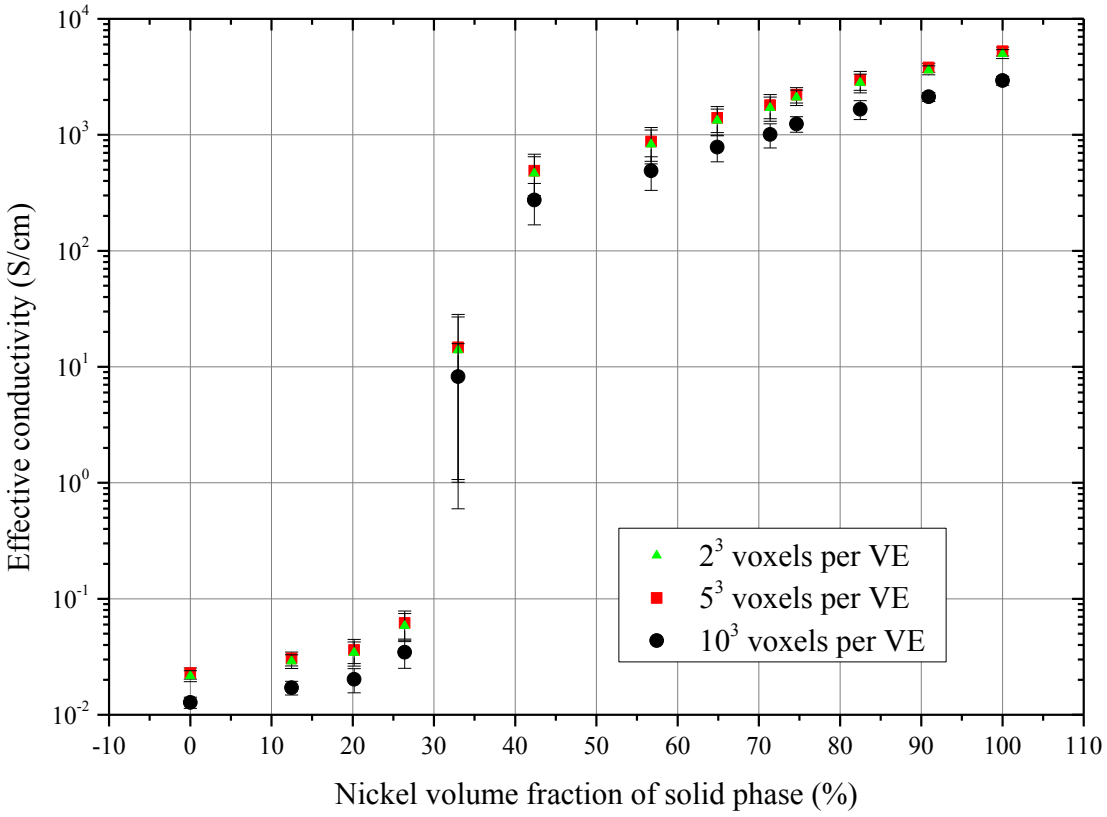


Figure 5.9 - Variation of effective conductivity of families of synthetic SOFC anode microstructures as a function of nickel volume fraction for synthetic structures with an L/D ratio of 7, particle diameters of 1 µm and a fixed porosity of 41.2%. Values computed using aggregation resolutions of $2^3$ voxels per VE, $5^3$ voxels per VE and $10^3$ voxels per VE are compared. All conductivities presented are computed in the x-direction.

The data presented in the above figure shows an average deviation of 22% between effective conductivities computed using an aggregation resolution of $5^3$ and $10^3$ voxels per VE, and a deviation of around 4% between those computed using resolutions of $5^3$ and $2^3$ voxels per VE. This confirms that the resolution used for the study presented in Figure 5.7 is indeed the optimum resolution, as increasing this resolution further yields a relatively small change in computed results, and decreasing it causes an important deviation. Values obtained using the lower resolution were found to be lower than those using a resolution of $5^3$ voxels per VE, also in line with results presented in the previous chapter.

Now that it has been established that the model parameters used for this investigation are well understood, a final validation of the ResNet model is presented. By segmenting the anodes fabricated by Somalu et al. (sintered at 1300$^{o}$C and used for the conductivity measurements presented in Figure 7), using a FIB microscope and reconstructing their 3D microstructures through the use of contrast filters coupled with Edge-preserving smoothing and Gaussian smoothing filters, histogram segmentations and a selection of tools grouping pixels based on the binary value, or shade of the pixels, the conductivity of 30%, 40% and 50% nickel volume content samples can be determined using the ResNet model. Following earlier analyses, for a microstructure to be representative of the entire anode, the samples need to be 7 times larger than the average particle size used during fabrication in every dimension. Tariq et al. (Tariq et al., 2013) determined that in these samples the average particle size is 1.2 μm, meaning that for a sample to be representative, a minimum sample size of 8.4×8.4×8.4 μm is required. The samples considered were therefore cut to sizes of 10.95×10.95×10.95 μm. The pixel size as given by the microscope was 30×30×30 nm, giving 365 voxels in each direction. These were then aggregated into VEs at the level of $5^3$ voxels per VE. The effective conductivity of both structures was computed by the ResNet model, and compared in the next figure to experimental measurements and the conductivity of synthetic structures as predicted by the ResNet model.

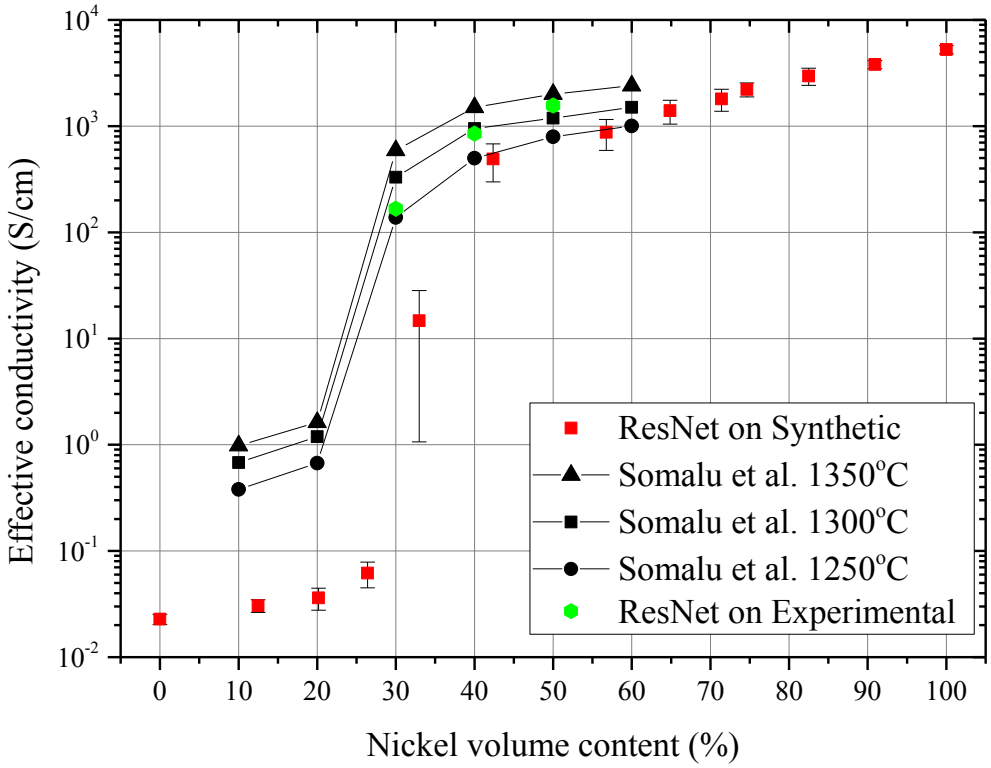


Figure 5.10 - Variation of effective conductivity of Ni/10ScSZ anode films measured at 700°C as a function of Ni content and sinter temperature as reported by Somalu et al. (Somalu et al., 2011) compared to the effective conductivity of 2 samples taken from these anodes as computed by the ResNet model, following FIB segmentation and image reconstruction. The samples were cut to sizes of 10.95×10.95×10.95 μm, and constituted $365^3$ voxels. Also presented are the effective conductivities as computed by the ResNet model as a function of nickel volume fraction for synthetic structures with an L/D ratio of 7, particle diameters of 1 μm and a fixed porosity of 41.2%. All conductivities presented are computed in the x-direction.

The data presented in the above figure shows good agreement between the experimentally derived effective conductivity of 40% and 50% nickel volume content Ni/10ScSZ anode films by Somalu et al. and that computed by the ResNet model on samples taken from the same microstructures, sintered at 1350°C. The 40% sample shows a similarity of 56.7% between experimental and simulated results and the 50% sample a 78.1% similarity, in contrast to the model used by Golbert et al. (Golbert et al., 2007) who predicts effective conductivities that diverge by more than 600% when looking at the same samples. The 30% sample however shows

a higher deviation from experimental results. This is due to the sample being very close to the percolation threshold, and one could expect a different sample at this same threshold to yield a different conductivity, closer or further from the value obtained experimentally. This is clearly seen in the synthetic structure families at 30% nickel, where deviations of conductivities reach 1500%. The relatively small divergence observed between effective conductivities predicted by the ResNet model and those measured experimentally for the sample above the percolation threshold can be attributed to the random particle configuration, as they fall within the standard deviation window predicted by the ResNet model when looking at families of synthetic structures. This in effect not only validates the ResNet model, but also validates the approach chosen by Somalu et al. in their measurements of effective conductivity (Somalu et al., 2011), the particle size distribution extraction technique used by Tariq et al. (Tariq et al., 2013) and finally the image segmentation and reconstruction techniques used by Kishimoto et al. (Kishimoto et al., 2013). However, the results presented highlight the importance of correctly modelling the sintering process used for fabricating SOFC electrode and the particle size distribution as found in the real electrode due to an observed average difference of 43% between the effective conductivities predicted by the ResNet model on experimental and synthetic microstructures. Also, it is understood that in real electrodes, particles are not perfectly spherical, also highlighted by the results. Table 1 shows the effective electrical conductivity as predicted by ResNet model on the four experimental data sets in each dimension.

Table 5.1 – Effective electrical conductivity in all dimensions as computed by the ResNet model of Ni/10ScSZ anode films Somalu et al. (Somalu et al., 2011) for three different compositions.

| Sample nickel content | x-conductivity | y-conductivity | z-conductivity |
|---|---|---|---|
| 30% | $0.007\times10^3$ S/cm | $0.0183\times10^3$ S/cm | $0.0247\times10^3$ S/cm |
| 40% | $0.858\times10^3$ S/cm | $0.911\times10^3$ S/cm | $0.782\times10^3$ S/cm |
| 50% | $1.522\times10^3$ S/cm | $1.755\times10^3$ S/cm | $1.411\times10^3$ S/cm |

The table above shows an average variation of less than 3% between the x-conductivities of these samples and their averaged x, y and z-conductivities above the percolation threshold. As found for synthetic structures, the experimental structures cut to a representative size show similar conductivities in all dimensions, validating the criteria determining the representativeness

of sample size derived in this thesis. The 30% sample shows a larger deviation of conductivities in each dimension, due to the nickel content being at the percolation threshold.

As explained in previous sections, there has been much interest in creating models to represent the geometrical changes undergone by particles comprising these anodes during sintering and long term operation. The process employed in this model is understood to be relatively simple, the uniform expansion of every particle steadily increasing the contact area between the neck size of two particles in contact. An increase in sintering factor, the factor by which particles are uniformly enlarged to model sintering, effectively increases the cross-sectional area of conducting pathways, in turn yielding a higher volume fraction of nickel and effective conductivity. The following figure shows the effect varying the sintering factor has on the effective conductivity of families of 50 structures with a composition of 43.5% nickel, 35% YSZ and 21.5% porosity, particle diameters of 1 μm and an L/D ratio of 7.

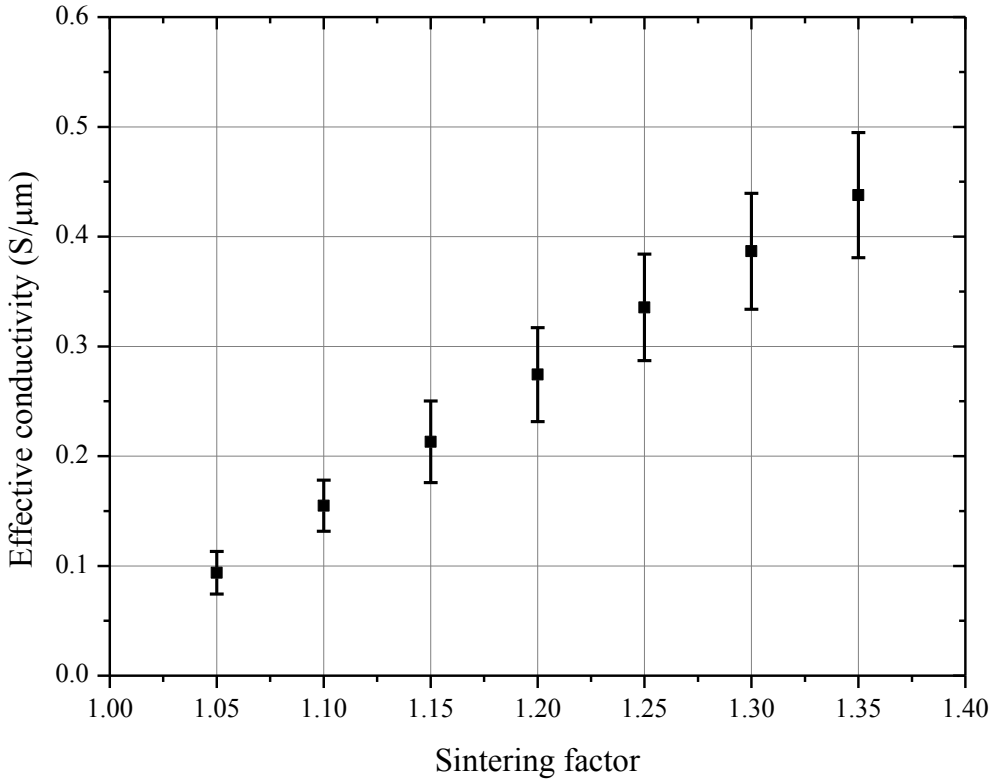


Figure 5.11 - Effective conductivity as a function of sintering factor for structures with an L/D ratio of 7, particle diameters of 1 μm and a 43.5% volume content of nickel, 35% volume content of YSZ and 21.5% porosity.

The data presented in Figure 5.11 shows that increasing the sintering factor, or particle enlargement factor, causes a proportional increase in effective conductivity, with a steady increase in standard deviation. The steady rise in effective conductivity is expected, as sintering increases the contact area between contacting particles and enlarges the conducting pathways from one boundary to the other. The observed slow increase in standard deviation can be attributed to the fact that, at lower sintering factors, the paths will in general be poorly conductive, regardless of particle distribution, whereas when this factor increases, the higher resulting conductivities are more dependent on the particle distribution within the synthetic anodes; the addition or subtraction of a conducting pathway with a large cross-sectional area will have a larger impact on overall effective conductivity than the addition or subtraction of a conducting pathway with a smaller cross-section.

In the work of Cai et al. (Cai et al., 2011), varying this expansion coefficient and looking at the current densities generated in synthetic microstructures using the VOF electrochemical model developed by Golbert et al. (Golbert et al., 2007) showed an optimum value of 1.2 with drops of current densities above and below this value. This behaviour was found to mirror that of the TPB densities extracted from these samples.

To further investigate the behaviour of SOFC anodes at the percolation threshold, families of structures were generated with a 20.1% nickel content, 38.7% YSZ content and 41.2% porosity. The particles comprising these structures are 1 μm in diameter as in previous cases, with an L/D ratio gradually increasing from 2 to 10.

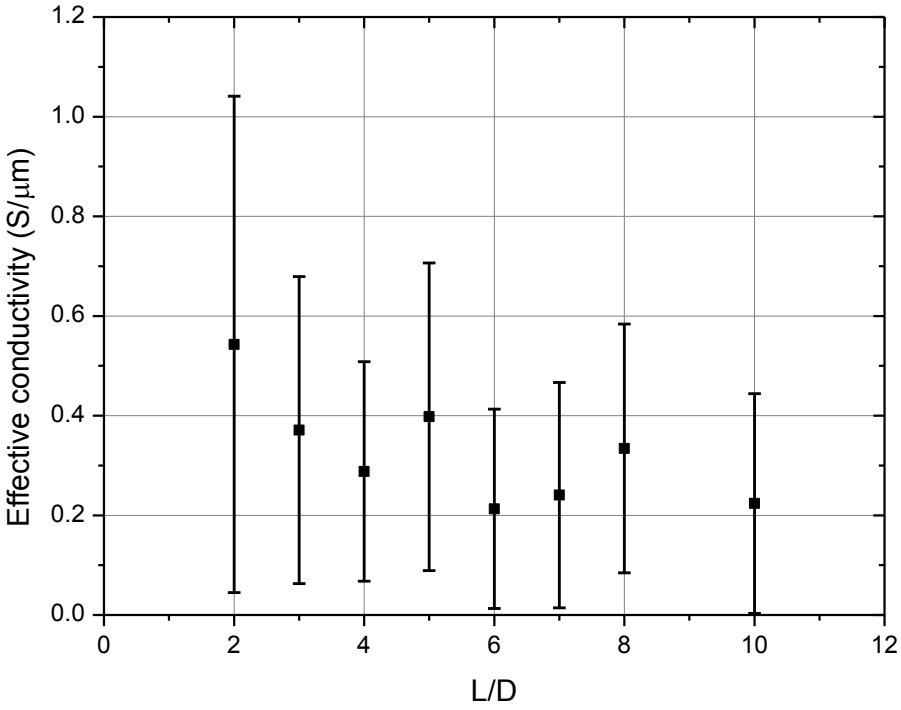


Figure 5.12 - Effective conductivity as a function of L/D for families of structures with a 20.1% nickel content, 38.7% YSZ content, 41.2% porosity and comprising particles of diameter 1 μm.

By comparing the data presented above to that presented in Figure 5.1, a larger spread of results for each L/D ratio is observed at a nickel content of 20.1%, occupying 30 vol% of the solid phase. The average effective conductivity lies around 0.3 S/μm, with each data point showing a spread of almost 100%. This means that at each L/D ratio, structures are either electronically connected or disconnected, depending on the distribution of particles within the electrodes. At this composition the average effective conductivity as predicted by the ResNet model does not converge to a stable value, demonstrating the unpredictable behaviour of SOFC anodes where the electronic phase lies at the percolation threshold. The large spread of error bars illustrates how different one electrode can be from another despite sharing identical fabrication parameters, when the content of nickel in the solid phase is close to 30%. Structures are indeed as likely to be conductive than not.

Now that the effects of microstructural parameters have on effective conductivity have been explored, the effect of effective conductivity on current density generation will be investigated.

## 5.4 – Effect of microstructural parameters on electrochemical performance

In this section the effect of effective conductivity on current generation, as given by the VOF model developed by Golbert et al. (Golbert et al., 2008), is investigated. The structures generated for the analysis presented in Figure 5.1, are analyzed using this model at over-potentials of 50 mV due to the limiting assumption of the Butler-Volmer equation being able to represent accurately the current-voltage behaviour of the SOFC anode at low over-potentials, as explained in Chapter 1. We have chosen this particular over-potential because the experimental measurements carried out to determine the exchange-current density were undertaken at 50 mV. The results of these simulations are illustrated below.

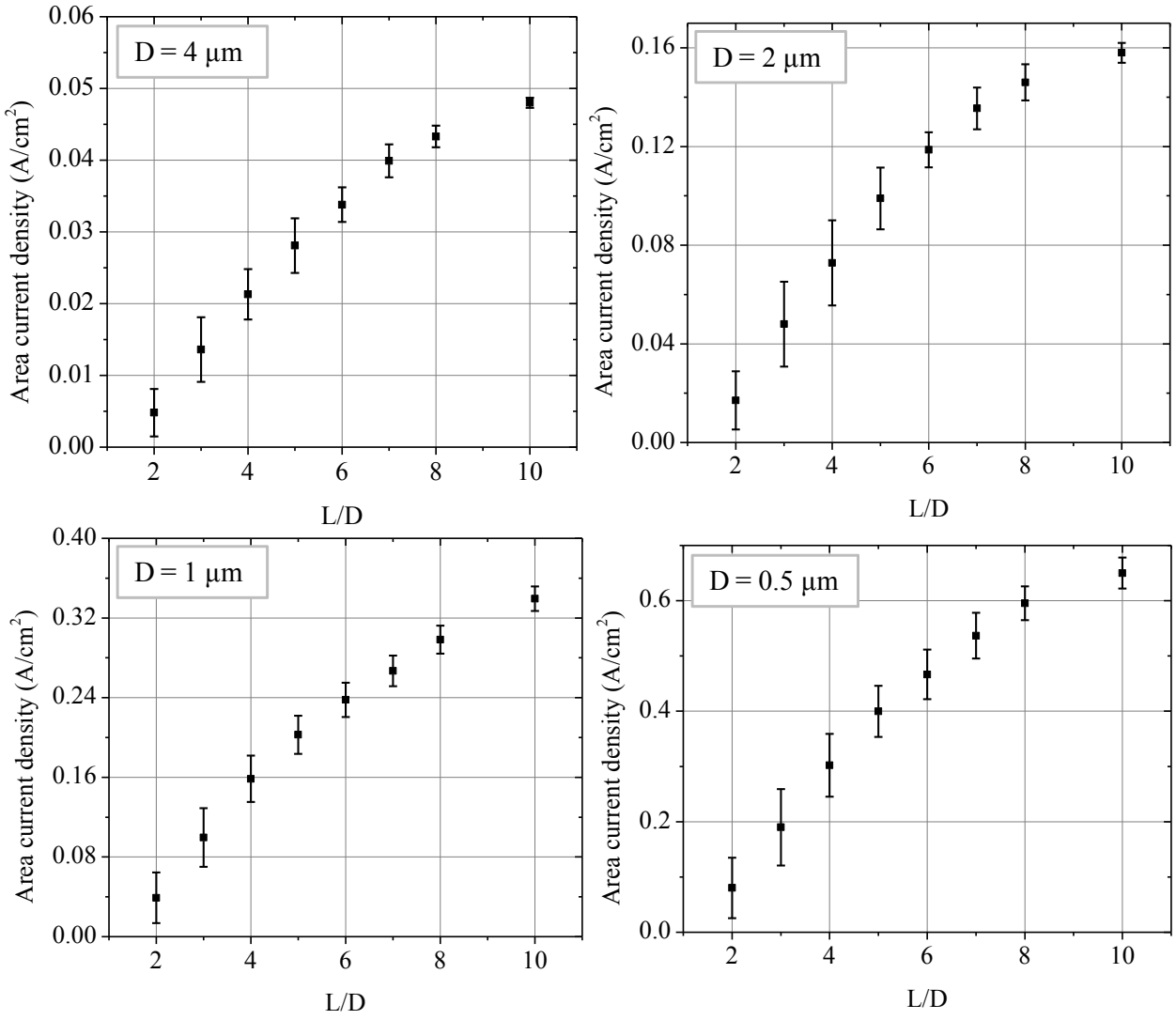


Figure 5.13 – Area current density as a function of L/D for families of structures with a 43.5% volume content of nickel, 35% volume content of YSZ and 21.5% porosity for four different particle sizes.

The analysis presented in Figure 5.13 shows that a smaller particle size enhances the current density generation capabilities of the anode, due in part to the higher number and length of TPB paths within the electrode. The increase in current density is due to the increase in the sum of the percolated TPB length as L/D increases (Cai et al., 2011).

The ResNet model is now introduced into the VOF model; the effective conductivity of each VE is calculated using the ResNet model as opposed to the volume fraction average used previously

by Cai et al. and Golbert et al. (Cai et al., 2010, 2011; Golbert et al., 2007). The entire domain and each VE being cubic, the average effective conductivity in each dimension is the same for every family of structure analyzed. Due to this fact, instead of dimensionalizing the equations governing the VOF model to enable the application of dimension specific conductivities to the model, the first attempt simply consisted of using the x-conductivity of the VEs instead of the volume-fraction averaged conductivity in ensuing computations.

The difference found in generated current densities through the incorporation of the ResNet model was of the order of only 0.001%, meaning that the results are nearly identical to those presented in Figure 5.12. This is in part due to the fact that, at the level of aggregation employed, most VEs are either completely contained in a particle or a pore, in which cases the volume fraction averaged and ResNet derived effective conductivity value are essentially identical. Only the effective conductivity of VEs situated at the boundary of two phases are affected by the model used in their calculation. Also, the nickel composition of the families of structures considered is 41.5%, which is above the percolation threshold reported earlier, meaning that a large portion of the microstructure is occupied by the electronically conducting phase. This further decreases the possible difference in conductivities given by the two models due to the relative abundance of charge-carrying paths; the number of VEs containing a critical charge-carrying juncture are limited.

This suggests that, under the conditions examined, i.e. at 1073 K and at an overpotential of 50mV, and with a well percolated (and therefore conducting) nickel microstructure, the effective conductivity of the nickel phase of an SOFC anode has little or no impact on current generation. Low conductivities, however, are expected to inhibit the anodes ability to transfer current from the reaction sites to the current collector. A sensitivity analysis was therefore carried out on families of 300 simple structures made of particles with a diameter of 1 μm, an L/D ratio of 2, and a 43.5% volume content of nickel, 35% volume content of YSZ and 21.5% porosity. The figure below shows the effect of varying the conductivity of the 'nickel' phase from $1.0x10^{-10}$ S/μm to $1.0x10^{0}$ S/μm. The ResNet model was used alongside the volume fraction averaged approach to determine how the use of each model impacts the predicted electrochemical performance of model structures while varying the conductivity of the nickel phase.

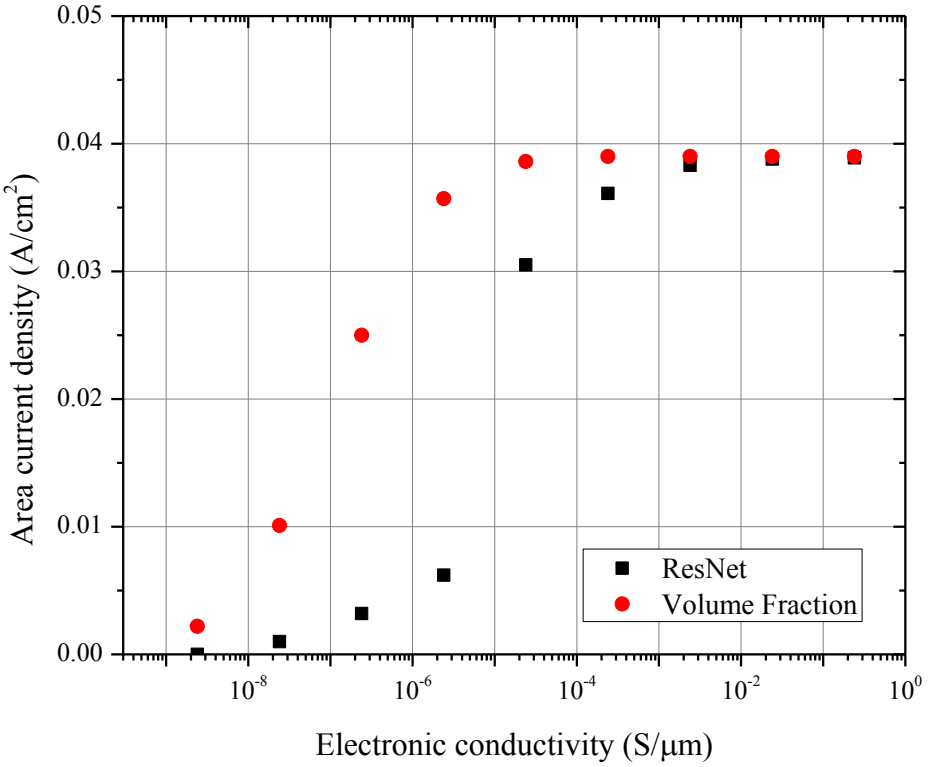


Figure 5.14 - Area current density as a function of electronic conductivity for families of structures with an L/D ratio of 2, a 43.5% volume content of 'electronic phase', 35% volume content of YSZ, 21.5% porosity and particles of diameter 1 μm.

The data presented above shows that the conductivity of the electronic phase needs to reach a value < $10^{-3}$ S/μm before the area current density starts to drop when using the ResNet model, and < $10^{-5}$ S/μm when using volume averaged conductivity. This analysis shows that the effective conductivity of SOFC anodes under standard operating conditions is a parameter that has a relatively small effect on the performance of these electrodes. The analysis also demonstrates that using a volume fractioned average electrical conductivity in the VOF model is a suitable approximation for nickel anodes, if they are properly percolated.

However, the results presented above show also that the ResNet model could be used to compute the effective ionic conductivity of a family of synthetic microstructures for use in the VOF model, where the use of the ResNet model could be expected to have a more significant effect on electrochemical performance than when used on the electronic phase, reflecting the lower conductivity of the YSZ and hence the greater sensitivity of current density to local ionic

conductivity paths. Figure 5.15 shows the effective ionic conductivities of families of microstructures of increasing L/D ratios with a 43.5% volume content of nickel, 35% volume content of YSZ and 21.5% porosity for particles with a diameter of 1 μm, and Figure 5.16 the area current density generated by these microstructures using the computed effective ionic conductivities.

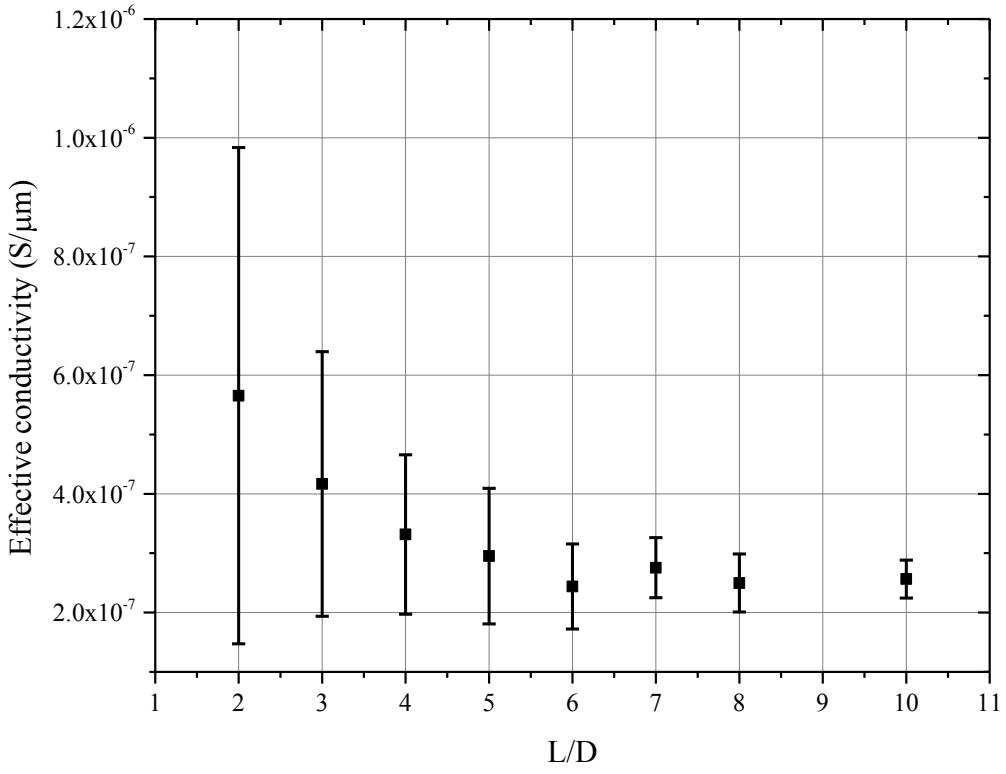


Figure 5.15 – Effective ionic conductivity as a function of L/D for families of structures with a 43.5% volume content of nickel, 35% volume content of YSZ and 21.5% porosity with particles of diameter 1 μm. All conductivities presented are computed in the x-direction.

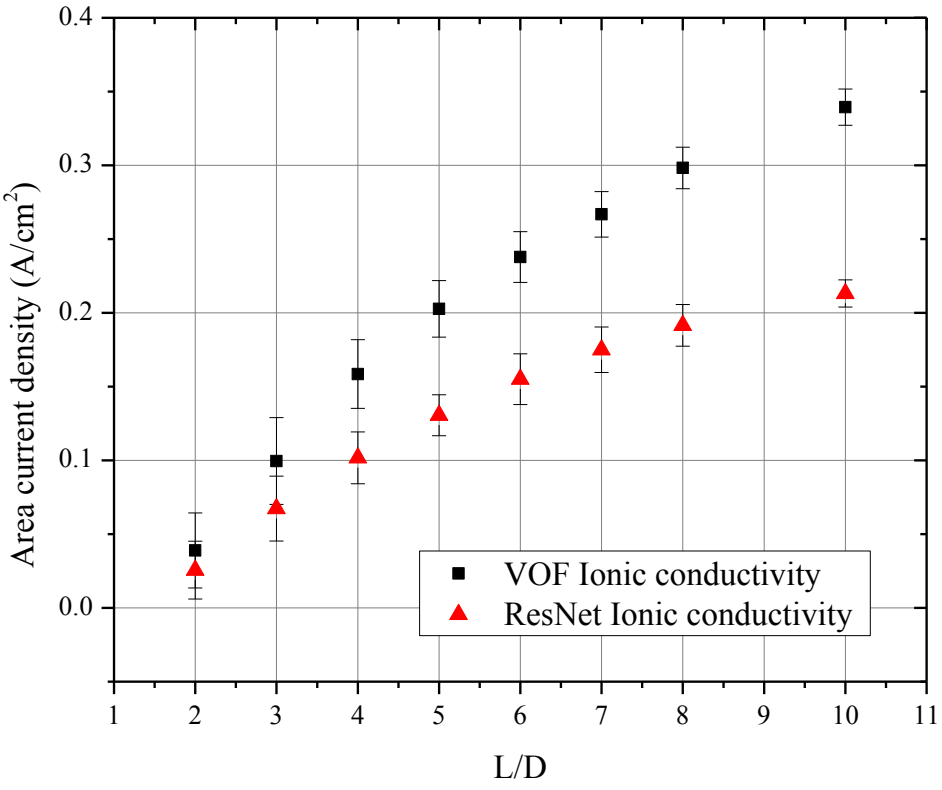


Figure 5.16 – Area current density as a function of L/D for families of structures with a 43.5% volume content of nickel, 35% volume content of YSZ and 21.5% porosity with particles of diameter 1 μm. The VOF model is initially employed using volume fraction averaged ionic conductivities, before integrating the effective ionic conductivities as computed by the ResNet model.

Figures 5.15 and 5.16 show that, by integrating the ResNet model into the VOF model for the computation of ionic conductivities, generated current densities gradually drop for increasing microstructure sizes by a factor of as much as 63.9% for the largest structure considered. Figure 5.15 shows that the converged effective ionic conductivity is $2.44\times10^{-7}$ S/μm, with a large spread of conductivities at low L/D ratios. This is in part due to the scale chosen to represent the results, and because at low L/D ratios some electrodes generated are only comprised of conducting particles while other can be only comprised of non-conducting particles. The conductivity of pure YSZ at 1073 K is $4.28\times10^{-6}$ S/ μm (Cai et al., 2010), and as the structures studied have a YSZ content of 35%, the ionic conductivity used by the VOF model when the volume fractioned approach is chosen is $0.35\times4.28\times10^{-6} = 1.5\times10^{-6}$ S/μm. The value computed by the ResNet

model is lower by a factor of 6.14, which accounts for the lower current density predicted by the VOF model when using the conductivities generated by the ResNet model. These current densities are seen to deviate at a steadily increasing extent as the L/D ratios of the structures increase. It is understood that as the structures increase in size, the mean total percolated TPB lengths increase. However, the ratio of active TPB sites to inactive sites due to poor ionic conductivities is presumed to increase with increasing domain size, with TPB sites located further away from the electrolyte being able to conduct less ionic species to and from these sites and the electrolyte, which would correlate with results shown in Figure 5.15.

It can therefore be seen that the current densities as computed by the VOF model are much more sensitive to the effective conductivity of the ionic phase than the electronic phase in Ni-YSZ electrodes. For cathode materials where the electronic phase has a lower conductivity, the model can be expected to have an impact on computed current generations. To better understand this sensitivity, an analysis of the effect of varying the ionic conductivity when using the VOF model is presented in the figure below.

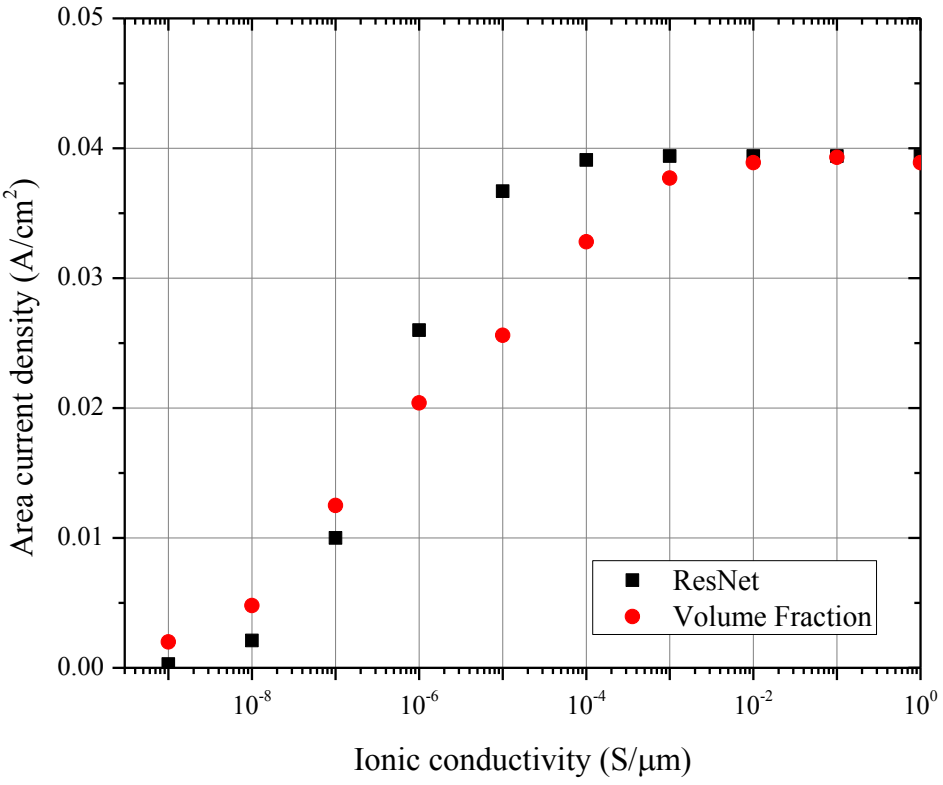


Figure 5.17 - Area current density as a function of ionic conductivity for families of structures with an L/D ratio of 2, a 43.5% volume content of nickel, 35% volume content of YSZ, 21.5% porosity and particles of diameter 1 μm. All conductivities presented are computed in the x-direction.

The conductivity of pure YSZ in the VOF model at 1073 K is set to $4.28\times10^{-6}$ S/μm (Cai et al, 2010), a value lying within the transition region of the graph above. Using both the ResNet and volume fractioned average approach for conductivity measurements, the VOF model shows that current generation is sensitive to ionic conductivity values lower than $10^{-3}$ S/μm. Current densities are seen to steadily drop until ionic conductivity values reach around $10^{-9}$ S/μm, meaning that conductivity variations between these two boundaries have a direct impact on current generation capabilities of these synthetic SOFC microstructures. Poor ionic conductivities are indeed understood to impede the transport of ions to and from reaction sites which slows down the reaction rate and decreases the amount of current being able to be generated by the synthetic electrodes. The model is therefore concluded to be most useful in the case where SOFC anodes operating in these conditions are considered in the ionic phase.

Electronic conductivities under these conditions are found to not be a limiting parameter, whereas ionic conductivities are found to directly influence the current density generation capabilities of SOFC anodes.

## 5.5 – Conclusion

In this Chapter the ResNet model was used to investigate the impact of several microstructural parameters on the effective conductivity of synthetic SOFC anode microstructures. The parameters considered for analysis were particle diameter, material composition, porosity and sintering factor. The following key conclusions were reached.

An L/D value of 7 was determined to be sufficient for electrode samples to be representative of the whole electrode microstructure in terms of effective conductivity, a finding supporting the research of Cai et al. who reported an L/D ratio of 7.5 for a structure to be representative when looking at percolated TPB densities (Cai et al., 2011) in structures of increasing length. This ratio was also confirmed when TPB densities were extracted from the microstructures of uniformly increasing size, and was found to be independent of particle size.

Results showed a steady decrease in effective conductivity as the porosity increased, due to the decreasing nickel volume fraction content of the synthetic microstructures. Analysis on microstructures of increasing nickel volume fraction in the solid phase and constant porosity revealed a slow increase in effective conductivity before a 30% phase fraction was reached, after which effective conductivities exponentially increase. Plotting these values on a log scale allowed comparison of the output of the ResNet model and experimental conductivity values obtained by Somalu et al. (Somalu et al., 2011) on Ni/10ScSZ and Ni/10Sc1CeSZ SOFC cermet anode films sintered at 1250$^{o}$C, 1300$^{o}$C and 1350$^{o}$C, showing good agreement between the predicted and measured conductivity values. An aggregation level of $5^3$ voxels per VE was determined to be optimum to follow the variation in conductivity across the nickel percolation threshold, consistent with conclusions from previous chapters.

A final validation of the ResNet model was achieved by extracting representative microstructures from three samples used by Somalu et al. when measuring experimental effective conductivities,

and using the ResNet model to compute their effective conductivities. Good agreement was found between the experimentally derived effective conductivity of 40% and 50% nickel volume content Ni/10ScSZ anode films by Somalu et al. and that computed by the ResNet model on samples taken from the same microstructures, sintered at 1300$^{o}$C. The sample with 30% nickel in the solid phase shows a higher deviation, attributed to the nickel content being close the percolation threshold, shown by the deviation of conductivities in the x, y and z-dimension of this sample. This enabled a validation of the ResNet model, the approach chosen by Somalu et al. in their measurements of effective conductivity, Somalu et al., 2011) the particle size distribution extraction technique used by Tariq et al. (Tariq et al., 2013) and finally the image segmentation and reconstruction techniques used by Kishimoto et al. (Kishimoto et al., 2013).

Studies of synthetic microstructures showed a proportional increase in effective conductivity with sintering factor, due to the enlargement of the bottleneck size between contacting particles. This increased the cross-sectional area of conducting pathways in the synthetic microstructures which directly influenced the transport properties of the electrodes.

Incorporation of the ResNet model into the electrochemical model developed by Golbert et al. (Golbert et al., 2007) to predict the electrochemical performance of SOFC anodes showed that, for nickel based anodes, the volume fraction model is adequate to predict electrode performance as the electronic conductivity of SOFC anodes, under operating conditions, is not a parameter whose variation greatly impacts the current generation characteristics of the electrodes.

It was however established that the electrochemical performance was sensitive to the local ionic conductivity within the electrode, and therefore use of the ResNet model is recommended to predict the effective ionic conductivity.

## 5.6 – References

Abel, J., Kornyshev, A. A. & Lehnert, W. (1997) Correlated resistor network study of porous solid oxide fuel cell anodes. *Journal of the Electrochemical Society* 144(12), 4253-4259.

Ali, A., Wen, X., Nandakumar, K., Luo, J. & Chuang, K.T. (2008) Geometrical modelling of microstructure of solid oxide fuel cell composite electrodes. *Journal of Power Sources*, 185(2), 961-966.

Brune, A., Lajavardi, M., Fisler, D., Wagner, J. B. Jr. (1998) The electrical conductivity of yttria-stabilized zirconia prepared by precipitation from inorganic aqueous solutions. *Solid State Ionics* 106, 89-101.

Cai, Q., Adjiman, C. S. & Brandon, N. P. (2010) Investigation of the active thickness of solid oxide fuel cell electrodes using a 3D microstructure model. *Electrochemica Acta* 56(28), 10809-10819.

Cai, Q., Adjiman, C. S. & Brandon, N. P. (2011). Modelling the 3D microstructure and performance of solid oxide fuel cell electrodes: Computational parameters. *Electrochimica Acta* 56(16), 5804-5814.

Chan. S. H., Chen, X. J. & Khor, K. A. (2004) Cathode Micromodel of Solid Oxide Fuel Cell. *Journal of the Electrochemical Society*, 151(1), A164-A172.

Chen, K., Chen, X., Lü, Z., Ai, N., Huang, X. & Su, W. (2008) Performance of an anode-supported SOFC with anode functional layers. *Electrochemica Acta* 53(1), 7825-7830.

Dees, D. W., Claar, T. D., Easler, T. E., Fee, D. C., Mrazek, F. C., 1987, Conductivity of porous NI/ZRO2-Y2O3 cermets. *Journal of the Electrochemical Society* 134(9), 2141-2146.

Gorte R. J. & Vohs J. M. (2011) Catalysis in Solid Oxide Fuel Cells. *Annual Review of Chemical and Biomolecular Engineering* 2, 9-30.

Golbert, J., Adjiman, C. S. & Brandon, N. P. (2008) Microstructural modeling of SOFC anodes. *Ind Eng Chem Res* 47(1), 7693-7699.

Golbert, J., Adjiman, C. S. & Brandon, N. P. (2007) Microstructural modeling of SOFC andoes. *SOFC -X*, 2041-2047.

Gostovic, D., Smith, J.R., Kundinger, D.P., Jones, K.S. & Wachsman, E.D. (2007) Three-Dimensional Reconstruction of Porous LSCF Cathodes. *Electrochemical and Solid-State Letters* 10(12), B214-B217.

Grew, K.N., Joshi, A.S., Peracchio, A.A. & Chiu, W.K.S. (2010) Pore-scale investigation of mass transport and electrochemistry in a solid oxide fuel cell anode. *Journal of Power Sources* 195(8), 2331-2345

Grew, K.N., Peracchio, A.A., Izzo, J.R. & Chiu, W.K.S. (2009) Nondestructive Imaging and Analysis of Transport Processes in the Solid Oxide Fuel Cell Anode. *ECS Transations, Solid Oxide Fuel Cells 11 (SOFC-XI) – Part 3. The Electrochemical Society*, USA, 1861.

Hernández-Pacheco, E., Singh, D., Hutton, P.N., Patel, N. & Mann, M.D. (2004) A macro-level model for determining the performance characteristics of solid oxide fuel cells. *Journal of Power Sources* 138(1), 174-186

Hirt, C.W. & Nichols, B.D. (1981) Volume of fluid (VOF) method for the dynamics of free boundaries. *Journal of Computational Physics*, 39(1), 201-225.

Iwai, H., Shikazono, N., Matsui, T., Teshima, H. Kishimoto, M., Kishida, R.,Hayashi, D., Matsuzaki, K., Kanno, D., Saito, M., Muroyama, H., Eguchi, K., Kasagi, N. & Yoshida, H. (2010) Quantification of SOFC anode microstructure based on dual beam FIB-SEM technique. *Journal of Power Sources* 195(4), 955-961.

Izzo, J.R., Joshi, A.S., Grew, K.N., Chiu, W.K.S., Tkachuk, A., Wang, S.H. & Yun, W. (2008) Nondestructive Reconstruction and Analysis of SOFC Anodes Using X-ray Computed

Tomography at Sub-50 nm Resolution. *Journal of the Electrochemical Society* 155(5), B504-B508.

Joshi, A.S., Grew, K.N., Peracchio, A.A. & Chiu, W.K.S. (2007) Lattice Boltzmann modeling of 2D gas transport in a solid oxide fuel cell anode. *Journal of Power Sources* 164(2), 631-638.

Kenney, B., Valdmanis, M., Baker, C., Pharoah, J. G. & Karan, K. (2009) Computation of TPB length, surface area and pore size from numerical reconstruction of composite solid oxide fuel cell electrodes. *Jounral of Power Sources*, 189(2), 1051-1059.

Kishimoto, M., Iwai, H., Saito, M. & Yoshida, H. (2012) Three-Dimensional Simulation of SOFC Anode Polarization Characteristics Based on Sub-Grid Scale Modelling of Microstructure. *Journal of the Electrochemical Society* 159(3), B315-B323.

Kishimoto, M., Iwai, H., Saito, M. & Yoshida, H. (2012) Quantitative evaluation of solid oxide fuel cell porous anode microstructure based on focused ion beam and scanning electron microscope technique and prediction of anode overpotentials. *Journal of Power Sources* 186(10), 4555-4563.

Metcalfe, C., Kesler, O., Rivard, T., Gitzhofer, F. & Abatzoglou, N. (2010) Connected Three-Phase Boundary Length Evaluation in Modeled Sintered Composite Solid Oxide Fuel Cell Electrodes. *Journal of the Electrochemical Society* 157(9), B1326-B1335.

Rhazaoui, K., Cai, Q., Adjiman, C.S., Brandon, N.P. (2013) Towards the 3D Modelling of the Effective Conductivity of Solid Oxide Fuel Cell Electrodes – Part 1: model structures. *Chem. Eng. Sci.* 99, 161-170.

Sanyal, J., Goldin, G.M., Zhu, H. & Kee, R.J. (2010) A particle-based model for predicting the effective conductivities of composite electrodes. *Journal of Power Sources*, 195(19), 6671-6679.

Shearing, P.R., Cai, Q., Golbert, J.I., Yufit, V., Adjiman, C.S. & Brandon, N.P. (2010) Microstructural analysis of a solid oxide fuel cell anode using focused ion beam techniques coupled with electrochemical simulation. *Journal of Power Sources* 195(15), 4804-4810.

Shearing, P.R., Gelb, J., Brandon & N.P. (2010) X-ray nano computerised tomography of SOFC electrodes using a focused ion beam sample-preparation technique. *Journal of the European Ceramic Society* 30(8), 1809-1814.

Schneider, L. C. R., Martin, C. L., Bultel, Y., Bouvard, D. & Siebert, E. (2007) Discrete modelling of the electrochemical performance of SOFC electrodes. *Electrochemica Acta* 52(1), 314-324.

Schneider, L. C. R., Martin, C. L., Bultel, Y., Dessemond & L., Bouvard, D. (2006) Percolation effects in functionally graded SOFC electrodes. *Electrochemica Acta* 52(9), 3190-3198.

Shikazono, N., Kanno, D., Matsuzaki, K., Teshima, H., Sumino, S. & Kasagi, N. (2010) Numerical Assessment of SOFC Anode Polarization Based on Three-Dimensional Model Microstructure Reconstructed from FIB-SEM Images. *Journal of the Electrochemical Society* 157(2), B665-B672.

Stauffer, D., Aharony, A. (1994) *Introduction to Percolation Theory*. 2nd Edition. London, Taylor & Frances Inc.

Sussman, M. & Puckett, E.G. (2000) A Coupled Level Set and Volume-of-Fluid Method for Computing 3D and Axisymmetric Incompressible Two-Phase Flows. *Journal of Computational Physics*, 162(2), 301-337.

Suzue, Y., Shikazono & N., Kasagi, N. (2008) Micro modeling of solid oxide fuel cell anode based on stochastic reconstruction. *Journal of Power Sources* 184(1), 52-59.

Tariq, F., Shearing, P., Yufit, V., Gelb, J., Bradley, R., Withers, P., Brandon, N., 2012, Lithium Ion Batteries: 3-D Multi-scale Tomography. *ECS Meeting Abstracts*, MA2012-02 802.

Versteeg, H.K. & Malalasekera, W. (2007) *An Introduction to Computational Fluid Dynamics: The Finite Volume Method*, 2nd Edition, London, Pearson Educational Ltd.

Wilson, J.R., Kobsiriphat, W., Mendoza, R., Chen, H.Y., Hiller, J.M., Miller, D.J., Thornton, K., Voorhees, P.W., Adler, S.B. & Barnett, S.A. (2006) Three-dimensional reconstruction of a solid-oxide fuel-cell anode. *Nature Materials* 5(1), 541-544.

Yousuf, M., Sahu, P.C. & Rajan, K.G. (1986) High-pressure and high-temperature electrical resistivity of ferromagnetic transition metals: Nickel and iron. *Physical Review* B 34, 8086-8100.

Zhu, H. & Kee, R.J. (2003) A general mathematical model for analyzing the performance of fuel-cell membrane-electrode assemblies. *Journal of Power Sources* 117(1), 61-74.

# Chapter 6 – Conclusions and future work

## 6.1 – Conclusions

This thesis presents the development, validation and use of an effective conductivity model on synthetic and real Ni-YSZ SOFC anodes to determine the impact of microstructural parameters on cell performance.

It is widely acknowledged that the electrode microstructure of SOFCs plays a key role in all aspects of cell performance from mechanical integrity to electrochemical performance. The relationship between this microstructure and overall cell performance has been the focus of much attention in recent years, and there still remains little agreement in the literature as to what constitutes a "good" microstructure.

Advances in modeling and tomography techniques have enabled not only a direct quantification of electrode microstructures, allowing direct access to a number of microstructural parameters including the distribution and length of triple phase boundary points, but also the link between these parameters and cell performance to be better understood.

A key parameter in the functioning and modeling of SOFCs is the electrical conductivity of the anode. This parameter is also one that can and has been measured accurately experimentally in the literature, allowing for the validation of a theoretical model to be carried out. In system models to date however, this parameter is usually attributed an empirical value or approximated using simple models that do not take into account the highly tortuous and porous nature of microstructures comprising these anodes.

At the time of writing this thesis, no effective conductivity model exists in the literature that has been validated against experimental data when considering porous, composite microstructures, nor are there any that can operate efficiently with computational flexibility on real and synthetic microstructures.

Using Kirchhoff's laws of current conservation, a 3D resistor model was developed and presented, the ResNet model. The model relies on the discretization of a real or synthetic

microstructure into small cuboidal elements called voxels, which are subsequently aggregated into Volume Elements. Nodes of the resistor network are centered at the centroid of each voxel, and upon solving a linear set of equations the effective conductivity of the desired structure can be derived.

Using simple geometric shapes, the effective conductivity of which can be derived analytically or found in the literature by attributing the material in question a pre-defined electric conductivity, the reliability and validity of the model was investigated. Results showed a good agreement when using a sufficiently fine discretization resolution.

Using the model on more complex structures, and comparing computed conductivities with those as predicted by COMSOL Multiphysics, a commercial modeling platform, resulted in good agreement when employing a sufficiently fine discretization resolution. The required discretization resolution was found to increase with increasing structural heterogeneity. When considering spherical particles, an optimum discretization limit of $D/L_{vox} = 10$ was established.

Implementing VEs into the ResNet, and looking at large families of synthetic microstructures created by randomly packing a box with spheres representing the electronic, ionic and pore phases where sintering is modeled by uniformly expanding the particles by a factor of 1.2, allowed for the optimum aggregation level of $5^3$ voxels in each VE to be determined.

The segmentation and acquisition of the 3D microstructure of a Ni/10ScSZ anode of size 26.93 μm × 18.19 μm × 6.42 μm with 30% of the solid phase occupied by nickel showed the importance of selecting a sample size representative of the entire anode considered. Applying the ResNet model to the reconstructed microstructure showed good electrical conductivities in the y and z-directions, but the length of the sample proved too high for connectivity in the x-direction. The extraction of the skeletonized nickel paths within the electrodes proved to be an additional tool in better understanding the behavior of current transport within these structures.

In order to determine what sample size one must consider for the sample to be representative of an entire anode when considering effective conductivity, families of up to 300 structures were generated with varying compositions, particle diameters, and structure sizes to achieve statistical invariance of results. The uniform microstructure size for which effective conductivities as computed by the ResNet model are seen to converge at $L/D = 7$.

Using this criteria for sample representativeness as well as the optimum discretization and aggregation resolutions determined previously, the ResNet model was used to investigate the effect of particle diameter, material composition, porosity and sintering factor on effective conductivity. Particle diameters are seen to have relatively poor influence on effective conductivities, whereas an increase in nickel content as well as sintering factor was shown to directly correlate to a proportional increase in effective electronic conductivity. Varying the nickel content of the solid phase at a fixed porosity allowed for a comparison to be made between predictions by the ResNet model on families of synthetic structures and measurements in the literature. Good agreement was found and a similar S-trend observed with a percolation threshold at a 30% nickel volume fraction in the solid phase.

Two Ni/10ScSZ SOFC anode microstructures were extracted and reconstructed by Dr F. Tariq and Dr M. Kishimoto in the Imperial College group. The electrodes were fabricated by Dr M. Somalu who also experimentally determined their effective electronic conductivities. Application of the ResNet model to these datasets provided the first comparison between theoretically predicted and experimentally extracted effective conductivities of real SOFC anodes. The mean particle size comprising these electrodes was extracted by F. Tariq, ensuring that a representative sample size was used. Excellent agreement was obtained between computed and experimentally derived effective conductivities.

The ResNet model was therefore validated using two real SOFC anode samples, with agreement agreement between measured electronic conductivity, and predicted electronic conductivity using the ResNet model on 3D datasets of the actual electrode microstructures. This also validated the approach of Somalu et al. in their experimental measurements, Kishimoto et al. in their image reconstruction techniques and Tariq et al. in their image acquisition techniques (Somalu et al., 2011; Tariq et al., 2012; Kishimoto et al., 2013).

The effect of a selection of microstructural parameters having been studied and quantified on the electrical effective conductivity of sample SOFC anode microstructures, the impact of effective conductivity on current density generation was also investigated using the Volume-of-Fluid approach and an electrochemical model developed by Golbert et al. and Cai et al. (Golbert et al, 2007, Cai et al, 2010). This model previously approximated the effective conductivity of analyzed structures by averaging the electrical conductivity of a pure material by the volume

fraction content of that material in each VE. Coupling the ResNet and VOF models allowed for the tortuous nature of SOFC anodes to be taken into account when computing effective conductivities, but no change was found between past and present instances of the VOF model when looking at generated current densities on families of structures with varying compositions, size and particle size. A sensitivity analysis of the effect of electrical conductivity on current density confirmed the relatively low influence electrical conductivity has on cell performance for Ni-YSZ SOFC anodes; the conductivity of nickel only starts having an influence on predicted current densities after dropping by almost 4 orders of magnitude. The TPB densities extracted from analyzed synthetic microstructures however were found to mirror the behaviour of current density.

The ResNet model was also applied to the ionic phase of the same microstructures generated for the previous study, and current densities as predicted by the original VOF model were found to around double those predicted by the VOF+ResNet model. Indeed, the ionic conductivity predicted by the ResNet model is lower than that predicted by the volume-fraction approach, and this lower effective ionic conductivity was found to have a significant impact on current densities predicted by the VOF model.

Therefore, when predicting electrochemical performance using the VOF approach, use of the ResNet model is therefore recommended to predict the effective ionic conductivity of SOFC anodes, but it is not generally needed to predict the electronic conductivity and a simple volume-fractioned average model is sufficiently accurate for most cases. Additionally, the ResNet model is recommended for use in SOFC cathodes, where the electronic conductivity is much lower and microstructural variations have an impact on simulated current densities.

Throughout the work presented in this thesis, the ResNet model extracted the conductivity of samples in x, y and z-directions. The VE solver in the VOF model however was built uni-dimensionally, so it was chosen to assign each VE the conductivity corresponding to the x-direction instead of dimensionalizing the VOF model equations and program code due to the statistical nature of the analyses undertaken, the cubic nature of the structures and the random process used in their generation.

## 6.2 - Future work

The effective conductivity model developed in this study has the potential to be applied to a wide variety of microstructures and macrostructures of varying nature in a wide range of fields. In this section, future studies of SOFC microstructures and electrochemical models will be considered.

The ResNet model is suggested to be used for the prediction of ionic conductivity in Ni-YSZ SOFC anodes, and more work should be done on better understanding the link between ionic conductivity and cell performance both experimentally and theoretically.

To further validate the model and investigate the effect of numerical artifacts, it is suggested to extract 3D microstructures from every sample fabricated by Dr. Somalu for a comprehensive comparison between computed electronic conductivities and experimentally measured ones.

The code written describing the model can be improved in terms of computational efficiency, and it is suggested to change the language from MatLab to C or C++, enabling the use of High Performance Computer (HPC) clusters. This would enable the model to analyze structures discretized by an increasing number of voxels and/or VEs, allowing larger structures to be looked at. Overall, a worthwhile project would be to create a stand-alone software package that would automatically reconstruct a real 3D microstructure from segmented images and run both the ResNet model and the VOF model on the reconstructured microstructure in an efficient way.

The ResNet model is recommended to be used on SOFC cathodes, where the electronic conductivity is lower and where the microstructure has a greater role in limiting the performance of the cell due to variations of the electronic conductivity.

Dimensionalizing the governing equations of the VOF model would allow for the tortuous nature of SOFC anodes to be captured with more precision, especially when looking at a small number of structures and when a statistical study is not being carried out.

Percolated TPB densities were found to directly govern the behaviour of SOFC anodes and their performance, therefore the recommendation is made to develop a TPB percolation model that does not rely on percolation theory, but one that extracts actual TPB lengths from real or synthetic electrodes for integration in the VOF model. Moreover, understanding the factors that

affect TPB lengths and densities is essential when characterizing SOFC anodes as good or poor performers.

Finally, a more robust gas transport model is also proposed for development, as the flow of gases through these porous anodes is another key parameter able to limit the performance of SOFC anodes.

## 6.3 – Dissemination

### 6.3.1 – Papers published or submitted

Brandon, N. P., Adjiman, C. S., Cai, Q., Clagyue, R., Marquis, A., Rhazaoui, K., Shearing, P., Modeling Solid Oxide Fuel Cell Electrochemistry in Three Dimensions. *ECS Meetings*, MA2011 1897, May 2011, Montreal, Canada.

Rhazaoui, K., Cai, Q., Adjiman, C. S., Brandon, N. P., 2013, Towards the 3D modeling of the effective conductivity of solid oxide fuel cell electrodes: I. Model development. *Chem Eng Sci* 99(1), 161-170.

Rhazaoui, K., Cai, Q., Adjiman, C. S., Brandon, N. P., 2013, Towards the 3D modeling of the effective conductivity of solid oxide fuel cell electrodes: II. Complex synthetic microstructures. *Comp Eng Sci* (2013, under review).

Rhazaoui, K., Cai, Q., Adjiman, C. S., Brandon, N. P., 2013, Towards the 3D modeling of the effective conductivity of solid oxide fuel cell electrodes: III. Large experimental microstructure. *In preparation* (2013, under review).

Rhazaoui, K., Cai, Q., Adjiman, C. S., Brandon, N. P., 2013, Towards the 3D modeling of the effective conductivity of solid oxide fuel cell electrodes: IV. Model validation and electrochemical modeling. *In preparation* (2013, under review).

Rhazaoui, K., Cai, Q., Shearing, P., Adjiman, C. S., Brandon, N. P., 2011, Solid Oxide Fuel Cell Electrode 3D Microstructure and Performance Modeling. *ECS Meetings*, MA2011-01 973.

Tariq, F., Kishimoto, M., Yufit, V., Rhazaoui, K., Somalu, M., Brandon, N. P., 2013, 3D imaging and quantification of interfaces in SOFC anodes. *In preparation* (2013, under review).

### 6.3.2 – Conference contributions

Rhazaoui, K. R., Cai, Q., Adjiman, C.S., Brandon, N.P.
Resistance modeling of a Solid Oxide Fuel Cell Anode
Fuel Cell Supergen Meeting, Loughborough, United Kingdom, February 2011.

Rhazaoui, K. R., Cai, Q., Adjiman, C.S., Brandon, N.P.
Solid Oxide Fuel Cell Electrode 3D microstructure and performance modeling
H2 Energy Research Student Symposium, October 2011, London, United Kingdom.

Rhazaoui, K. R., Cai, Q., Adjiman, C.S., Brandon, N.P.
3D modeling of the effective conductivity of solid oxide fuel cell electrodes.
7th International Hydrogen and Fuel conference, December 2011, Birmingham, United Kingdom.

Rhazaoui, K. R., Cai, Q., Adjiman, C.S., Brandon, N.P.
3D modeling of the effective conductivity of solid oxide fuel cell electrodes: I. Model development. ModVal 9, Sursee, Switzerland. April 2012.

Rhazaoui, K. R., Cai, Q., Adjiman, C.S., Brandon, N.P.
3D modeling of the effective conductivity of solid oxide fuel cell electrodes: II. Model validation. ModVal 10, Stuttgart, Germany. March 2013.

### 6.3.3 – Poster presentations

Rhazaoui, K. R., Cai, Q., Adjiman, C.S., Brandon, N.P.
3D modeling of SOFCs. 219th ECS meeting, SOFC XII, May 2011, Montreal, Canada.

Rhazaoui, K. R., Cai, Q., Adjiman, C.S., Brandon, N.P.
3D modeling of the effective conductivity of solid oxide fuel cell electrodes.
10th European SOFC Forum, June 2012, Luzern, Switzerland.

Rhazaoui, K. R., Cai, Q., Adjiman, C.S., Brandon, N.P.
3D modeling of the effective conductivity of solid oxide fuel cell electrodes.

ChemEngDayUK 2013, March 2013, London, United Kingdom.